Inhomogeneous Chamber States in Screw Spindle Vacuum Pumps

Zur Erlangung des akademischen Grades eines

Dr.-Ing.

von der Fakultät Maschinenau der

Technischen Universität Dortmund

genehmigte Dissertation

Heiko Pleskun, M. Sc.

aus

Warstein

Tag der mündlichen Prüfung: 15.10.2024

1. Gutachter: Prof. Dr.-Ing. Andreas Brümmer

2. Gutachter: Prof. Dr.-Ing. Peter F. Pelz

Dortmund, 2024

Acknowledgements

Die vorliegende Arbeit entstand während meiner Tätigkeit als wissenschaftlicher Mitarbeiter am Fachgebiet Fluidtechnik der Technischen Universität Dortmund. An dieser Stelle möchte ich mich bei allen bedanken, die mich während meiner Arbeit unterstützt haben.

Mein besonderer Dank gilt Herrn Prof. Dr.-Ing. Andreas Brümmer, dem Leiter des Fachgebiet Fluidtechnik, für die persönliche Betreuung und Förderung sowie für die Begleitung meines wissenschaftlichen Werdegangs. Dabei stand seine Tür für mich immer offen, sodass zahlreiche konstruktive Gespräche und Anregungen maßgeblich zum Erfolg dieser Arbeit beigetragen haben und ich auch darüber hinaus in dieser Zeit viel gelernt habe. Herrn Prof. Dr.-Ing. Peter Pelz danke ich für die Übernahme des Koreferats.

Ein großer Dank gilt allen Mitarbeitenden des Fachgebiet Fluidtechnik, die mich in all den Jahren begleitet haben. Vielen Dank für die tolle Zeit! Ich habe mir öfter sagen lassen, dass man mein Lachen von überall hören konnte. Ohne euch hätte ich aber nicht so viel gelacht. Neben der zwischenmenschlichen Ebene waren aber auch die vielen inhaltlichen Diskussionen die ich mit euch geführt habe sehr wertvoll. Dabei möchte ich mich besonders bei der Arbeitsgruppe Vakuum bedanken. Von Christopher Huck habe ich bereits in meiner Zeit als studentische Hilfskraft viel gelernt und er hat durch seinen Forschungsantrag meine Stelle als wissenschaftlicher Mitarbeiter am Fachgebiet Fluidtechnik ermöglicht und mich in der Anfangszeit begleitet. Timo Jünemann möchte ich dafür danken, dass er jederzeit alles stehen und liegen gelassen hat, um mit mir einen fixen Gedanken zu durchdenken.

Weiterhin möchte ich mich bei meinen studentischen Helfern für ihr hohes Engagement und die intensive Arbeit bedanken. Dabei möchte ich Tobias Bode besonders hervorheben, der mich in meiner Zeit am längsten begleitet hat und ohne dessen Programmierkünste ich vermutlich immer noch nicht fertig wäre. Darüber hinaus möchte ich mich auch bei Ralf van de Straat und Kevin Weidler bedanken, die mir bei der Realisierung des Versuchstands geholfen haben. Ilona Kokott möchte ich für die Hilfe in bürokratischen Angelegenheiten danken.

Nicht zuletzt gilt ein großer Dank meiner Familie für die Unterstützung und die Ermöglichung meines Werdegangs. Ganz besonders danke ich meiner Frau Sina und meiner Tochter Amy für das mir entgegengebrachte Verständnis, die bedingungslose Unterstützung und die schönste Ablenkung, die ich mir vorstellen kann.

Essen im November 2024

Heiko Pleskun

Supported by:

on the basis of a decision
by the German Bundestag

Supported by the Federal Ministry for Economic Affairs and Energy (BMWi) on the basis of a decision by the German Bundestag, AiF, IGF No.: 19859 N/1.

I gratefully acknowledge the computing time provided on the Linux HPC cluster at Technical University Dortmund (LiDO3), partially funded in the course of the Large- Scale Equipment Initiative by the German Research Foundation (DFG) as Project No. 271512359.

Zusammenfassung

In der vorliegenden Arbeit werden inhomogene Druckverteilungen in Arbeitskammern von Schraubenspindelvakuumpumpen (SSVP) untersucht, die durch eine Überlagerung einer Schleppströmung und einer druckgetriebenen Strömung insbesondere bei niedrigen Kammerdrücken und hohen Drehzahlen auftreten. Infolge der Rotation wird in den Arbeitskammern ein Massenstrom in Richtung der bewegten Rotorzähne hervorgerufen, der im Profileingriff aufgestaut wird. Daraufhin stellt sich ein Druckgradient in entgegengesetzter Richtung ein, der diesen kompensiert. In der Arbeitskammer ist der statische Druck demzufolge ortsabhängig. Dieser Mechanismus führt zu einer deutlichen Vergrößerung der anliegenden Spaltmassenströme, da die Spalteintrittsdichte infolge der lokalen Druckerhöhung größer ist als bei einer homogenen Arbeitskammer. Beim Ansaugvorgang führt die inhomogene Druckverteilung dazu, dass weniger Masse in die Maschine angesogen werden kann und daraus folgend der Füllungsgrad reduziert ist.

Zur Berechnung der inhomogenen Druckverteilung wird die Arbeitskammer zunächst als Rechteckkanal abstrahiert, bei dem alle Wände (z.B. Rotorzahnflanken) eine Wandgeschwindigkeit entsprechend der kinematischen Beziehungen aufweisen. Anschließend wird eine eindimensionale Differenzialgleichung formuliert, die auf einer Überlagerung der Massenströme einer Druck- und einer Schleppströmung basieren. In Abhängigkeit der Gasverdünnung, der Geometrie und der Gas-Oberflächen-Interaktion ergibt sich ein Schließungsproblem, das separat mithilfe analytischer Lösungen und mit Ergebnissen der Direct-Simulation Monte Carlo (DSMC) Methode gelöst wird.

Das eindimensionale Modell wird in zweifacher Hinsicht validiert. Zum einen wird ein Vakuumprüfstand zur experimentellen Validierung errichtet, bei dem die Inhomogenität in einer Arbeitskammer über drei Druckmessstellen erfasst wird. Dabei zeigt sich eine gute Übereinstimmung zwischen Messungen und Modell. Zum anderen werden dreidimensionale numerische Strömungssimulationen (CFD) durchgeführt, die die Zulässigkeit einer Reduktion des Modells auf eine eindimensionale Strömung bestätigen. Mit instationären CFD-Simulationen wird außerdem die Kammerfüllung mit einem sich ausdehnenden Rechennetz untersucht. Durch eine Dimensionsanalyse wird gezeigt, dass die Inhomogenität in der Arbeitskammer sowohl für die Kammerfüllung als auch in gekapselten Arbeitskammern auf je einer Kurve zusammenfallen, sodass analytisch bestimmbare Funktionale abgeleitet und anschließend in die Kammermodelsimulationssoftware *KaSim* implementiert werden.

Abschließend wird eine Testmaschine simuliert und mit bereits vorhandenen Messergebnissen verglichen. Dabei können die Simulationsergebnisse von SSVPs mithilfe des inhomogenen Modells von Arbeitskammern deutlich verbessert werden. Dadurch, dass die Maschine in Betriebspunkten höherer Kammerinhomogenität deutlich ineffizienter ist, eignet sich die Auswertung der Funktionale in Abhängigkeit des geforderten Betriebspunktes zur Grobauslegung neuer Maschinen.

Abstract

In the present work, inhomogeneous pressure distributions in working chambers of screw spindle vacuum pumps (SSVP) are investigated, which occur due to a superposition of a drag-driven and a pressure driven flow, especially at low chamber pressures and high rotational speeds. As a result of the rotation, a mass flow is caused in the working chambers in the direction of the moving rotor teeth, which is dammed up in the profile engagement. This causes a pressure gradient in the opposite direction, which compensates for this. The static pressure in the working chamber is therefore location-dependent. This mechanism leads to a significant increase in the applied gap mass flow rates, since the gap entry density is greater than in a homogeneous working chamber due to the local pressure increase. During the filling process, the inhomogeneous pressure distribution means that less mass can be sucked into the machine and the filling efficiency is reduced as a result.

To calculate the inhomogeneous pressure distribution, the working chamber is first abstracted as a rectangular channel in which all walls have a wall velocity corresponding to the kinematic relationships. Subsequently, a one-dimensional differential equation is formulated, which is based on a superposition of the mass flow rates of a pressure-driven flow and a drag-driven flow. Depending on the gas rarefaction, the geometry and the gas-surface interaction, a closure problem arises, which is solved separately using analytical solutions and results from the direct simulation Monte Carlo (DSMC) method.

The one-dimensional model is validated in two ways. On the one hand, a vacuum test rig is set up for experimental validation, in which the inhomogeneity in a working chamber is measured via three pressure measurement points. This shows good agreement between measurements and model. On the other hand, three-dimensional computational fluid dynamics (CFD) simulations are carried out, which confirm the admissibility of a reduction of the model to a one-dimensional flow. Transient CFD simulations are also used to investigate the chamber filling process with an expanding computational mesh. By dimensional analysis, it is shown that the inhomogeneity in the working chamber coincides on one curve each for both chamber filling and encapsulated working chambers, so that analytically determinable functionals are derived and implemented in the chamber model simulation software *KaSim*.

Subsequently, a test machine is simulated and compared with existing measurement results. It is obtained that the simulation results of SSVPs can be significantly improved with the help of the inhomogeneous model of working chambers. Since the machine is significantly more inefficient at operating points with higher chamber inhomogeneity, the evaluation of the functionals depending on the required operating point is suitable for a rough design of new machines.

Table of Contents

Abstract V

Symbols and Abbreviations XI

1 Introduction 1
- 1.1 Dry-Running Screw Spindle Vacuum Pumps . . . 3
  - 1.1.1 Classification and Working Principle . . . 3
  - 1.1.2 Simulation of Screw Vacuum Pumps . . . 6
- 1.2 Investigation of Gas Flows . . . 8
  - 1.2.1 Poiseuille Flow . . . 8
  - 1.2.2 Couette Flow . . . 9
  - 1.2.3 Thermal Creep Flow . . . 9
  - 1.2.4 Mixed Flows . . . 10
- 1.3 Gas-Surface Interactions . . . 10

2 Aim of the Work and Approach 13

3 Basics of Rarefied Gas Dynamics 15
- 3.1 Molecular Model . . . 15
- 3.2 Conservation Laws . . . 16
- 3.3 Principle of Relativity . . . 17
- 3.4 Binary Collisions . . . 18
- 3.5 Kinetic Gas Theory . . . 20
  - 3.5.1 Macroscopic Gas Properties . . . 22
  - 3.5.2 Distribution Function . . . 24
  - 3.5.3 Boltzmann Equation . . . 26
  - 3.5.4 Maxwell-Boltzmann Distribution . . . 27
  - 3.5.5 Gas-Surface Interactions . . . 28
- 3.6 Macroscopic Conservation Equations . . . 30
  - 3.6.1 Continuum Model . . . 31
  - 3.6.2 Velocity Slip and Temperature Jump . . . 32
  - 3.6.3 Dimensional Analysis and Simplifications . . . 33

4 Numerical Methods 37
- 4.1 Computational Fluid Dynamics (CFD) . . . 37

4.1.1 Discretisation . . . 37
4.1.2 Boundary Conditions . . . 40
4.2 Direct Simulation Monte Carlo (DSMC) Method . . . 41
4.2.1 Algorithm . . . 42
4.2.2 Particle Movement . . . 43
4.2.3 Boundary Conditions . . . 43
4.2.4 Binary Collisions . . . 45
4.2.5 Macroscopic Properties . . . 45
4.2.6 Error Estimation . . . 46

5 Working Chambers in Vacuum Spindle Pumps 47
5.1 Kinematics and Geometric Abstraction . . . 47
5.2 Dimensional Analysis . . . 49
5.3 Thermodynamic Model for Closed Chambers . . . 50
5.4 Strouhal Number for Open Chambers . . . 52

6 Reduced Flow Rates 53
6.1 Poiseuille Flow . . . 53
6.1.1 Slip Regime . . . 54
6.1.2 Transitional Regime . . . 59
6.1.3 DSMC Model . . . 60
6.1.4 Validation . . . 61
6.1.5 Contour Plots . . . 64
6.2 Couette Flow . . . 65
6.2.1 Properties of the Couette Flow . . . 66
6.2.2 Hydrodynamic Regime . . . 67
6.2.3 Slip Regime . . . 68
6.2.4 Free Molecular Regime . . . 69
6.2.5 Transitional Regime . . . 72
6.2.6 Validation . . . 74
6.2.7 Contour Plots . . . 76
6.3 Applications and Application Limits . . . 79
6.3.1 Poiseuille Flow . . . 79
6.3.2 Couette Flow . . . 80
6.3.3 Couette-Poiseuille Flow . . . 81

7 Inhomogeneous Chamber States 83
7.1 CFD Model . . . 83
7.2 Validation of the 1D Model . . . 84
7.3 Approximative Functions Depending on the Dimensionless Pressure Gradient . . . 91

8 Experimental Investigations 95
8.1 Test Rig . . . 95
8.2 Sensors . . . 98
8.3 Method of Measurement . . . 99
8.4 Leakage . . . 99

8.5 Uncertainty . . . 101
8.5.1 Pressure . . . 102
8.5.2 Temperature . . . 102
8.5.3 Rotational Speed . . . 104
8.5.4 Geometry . . . 104
8.5.5 Uncertainties of Dimensionless Numbers . . . 104
8.6 1D Modelling of the Test Rig . . . 104
8.7 Comparison Between Measurements and 1D Model Simulation . . . 106
8.8 Conclusion . . . 114

9 Transient Chamber Filling 115
9.1 Domain and Boundary Conditions . . . 115
9.2 Error Estimation . . . 117
9.3 Strouhal Number . . . 118
9.4 Comparison Between Transient and Quasi-Static Chamber Filling . . . 124

10 Chamber Model Simulation 127
10.1 The Simulation Tool *KaSim* . . . 127
10.2 Inhomogeneous Chamber States . . . 131
10.3 Gap Flow Models . . . 133
10.3.1 Theoretical Mass Flow Rates . . . 133
10.3.2 Friction Models . . . 134
10.4 Geometry Model . . . 137
10.4.1 Mathematical Rotor Description . . . 139
10.4.2 Volume Curves and Opening Areas . . . 141
10.4.3 Housing Gap . . . 142
10.4.4 Radial Gap . . . 142
10.4.5 Blow Hole . . . 143
10.4.6 Inter-Lobe Gap . . . 143
10.5 Simulation of a Test Machine . . . 144

11 Conclusion and Outlook 149

Bibliography 153

Appendix 163

A Proof of Couette Flow Properties 165
A.1 Shape Factor . . . 165
A.2 High Wall Velocities . . . 165
A.3 Superposition Principle . . . 166

B DSMC Data 167

C Experimental Setup 171

D Measurement Data 173

Symbols and Abbreviations

Symbols

Latin letters

symbol	unit	explanation	equation
A	m^2	area	(3.36)
b	m	closest approach of molecular trajectories	(3.19)
$\boldsymbol{b}$	$\mathrm{N\,kg^{-1}}$	specific body force	(3.93)
c_p	$\mathrm{J\,kg^{-1}\,K^{-1}}$	specific isobaric heat capacity	(3.48)
c_s	$\mathrm{m\,s^{-1}}$	isentropic speed of sound	(3.55)
c_v	$\mathrm{J\,kg^{-1}\,K^{-1}}$	specific isochoric heat capacity	(3.46)
$\mathfrak{c}$	$\mathrm{m\,s^{-1}}$	molecular speed	(3.12)
$\boldsymbol{\mathfrak{c}}$	$\mathrm{m\,s^{-1}}$	molecular velocity	(3.9)
$\boldsymbol{\mathfrak{c}}'$	$\mathrm{m\,s^{-1}}$	molecules' thermal velocity	(3.30)
c_m	$\mathrm{m\,s^{-1}}$	most probable molecular speed	(3.81)
$\overline{\mathfrak{c}}$	$\mathrm{m\,s^{-1}}$	average molecular velocity	(3.29)
$\mathcal{C}$	$\mathrm{m\,s^{-1}}$	speed of light	(3.1)
C		integration constant	(3.76)
C_0	-	reduced mass flow rate	(5.15)
D	m	diameter	(5.2)
$\mathfrak{d}$	m	molecular diameter	(3.18)
e	$\mathrm{J\,kg^{-1}}$	specific internal energy of a system	(3.45)
E	J	internal Energy of a system	(3.50)
$\mathcal{E}$	J	energy of a molecule	(3.43)
Eu	-	Euler number	(3.119)
f	$\mathrm{m^{-6}\,s^3}$	velocity distribution function	(3.56)
f	-	function	(5.23)
f	$\mathrm{s^{-1}}$	frequency	(5.1)
$\mathcal{F}$	N	force	(3.36)
$\boldsymbol{\mathcal{F}}$	N	force vector	(3.2)
$\mathfrak{F}$	-	velocity distribution function in normal direction	(3.85)
$\mathfrak{f}$	$\mathrm{m^{-3}\,s^3}$	Maxwell Boltzmann velocity distribution function	(3.78)
$\mathfrak{f}$	-	number of molecules' internal degrees of freedom	(3.49)
F	-	interpolation function	(10.30)
F_N	-	number of equivalent particles	(4.29)

symbol	unit	explanation	equation
Fr	-	Froude number	(3.120)
g	-	geometric ratio	(5.16)
g	$\mathrm{m\ s^{-2}}$	gravitational acceleration	(3.70)
G	-	reduced flow rate	(5.18)
h	m	height	(5.6)
h	$\mathrm{J\,kg^{-1}}$	specific enthalpy of a gas	(3.47)
H	-	shape factor	(6.43)
i	-	lobe ratio	(10.9)
$\boldsymbol{I}$	-	unit tensor	(3.65)
J	$\mathrm{m^{-6}\ }s^2$	collision integral	(3.69)
J	-	shape factor	(6.46)
k	$\mathrm{J\,K^{-1}}$	Boltzmann constant $k = 1.38064852 \cdot 10^{-23}\,\mathrm{J\,K^{-1}}$	(3.42)
Kn	-	Knudsen number	(3.111)
L	m	channel length	(5.9)
L	m	characteristic length	(3.115)
$\bar{\mathfrak{l}}$	m	molecular mean free path	(3.33)
ℓ	m	equivalent free path	(3.103)
$\boldsymbol{l}$	m	lever	(10.6)
$\mathbb{L}$	$\mathrm{Pa\ m^3\ s^{-1}}$	leakage	(8.1)
$\mathcal{L}$	$\mathrm{kg\ m^2\ s^{-1}}$	angular momentum vector	(10.6)
m	kg	mass	(5.11)
$\dot{m}$	$\mathrm{kg\,s^{-1}}$	mass flow rate	(5.17)
M	-	Mach number	(3.113)
$\boldsymbol{\mathcal{M}}$	$\mathrm{kg\,m\ s^{-1}}$	momentum vector	(3.2)
$\mathfrak{m}$	kg	molecular mass	(3.1)
n	$\mathrm{m^{-3}}$	number density	(3.26)
$\boldsymbol{n}$	-	unit normal vector	(3.82)
N	-	number (of molecules)	(3.26)
$\dot{N}$	$\mathrm{s^{-1}}$	number flux	(3.62)
$\mathcal{N}$	-	shape function	(4.3)
$\mathcal{O}$	-	origin	(3.3)
p	Pa	pressure	(3.38)
p_{ch}	Pa	mass averaged pressure in a vacuum chamber	(5.11)
p^*_{ch}	Pa	pressure in the middle of a vacuum chamber	(5.11)
$\boldsymbol{P}$	Pa	pressure tensor	(3.63)
P	-	probability	(4.49)
$\mathcal{P}$	-	dimensionless pressure gradient	(5.21)
Po	-	Poiseuille number	(6.138)
Pr	-	Prandtl number	(3.110)
q		macroscopic quantity	(3.58)
$\mathfrak{q}$		molecular quantity	(3.58)
$\dot{q}$	$\mathrm{W\,m^{-2}}$	heat flux	(3.87)
$\dot{\boldsymbol{q}}$	$\mathrm{W\,m^{-2}}$	heat flux vector	(3.67)

symbol	unit	explanation	equation
$\dot{Q}$	W	heat flow	(10.2)
r	m	radius	(6.55)
R	m	radius	(6.55)
R	J kg^{-1} K^{-1}	specific gas constant	(3.42)
r_f	-	refinement factor	
Re	-	Reynolds number	(3.121)
s	m	rotor lead	(5.1)
s		standard deviation	(4.59)
S	-	shape factor	(6.44)
$\boldsymbol{S}$	-	tangential surface tensor	(3.104)
$\mathcal{S}$	-	surface	(3.97)
St	-	Strouhal number	(5.29)
t	s	time	(3.2)
T	K	temperature	(3.40)
T	-	shape factor	(6.45)
$\boldsymbol{\mathcal{T}}$	kg m^2 s^{-2}	torque vector	(10.6)
u_0	-	speed ratio	(5.14)
u	m s^{-1}	macroscopic velocity in flow direction	(6.2)
$\boldsymbol{u}$	m s^{-1}	macroscopic velocity vector	(3.29)
$\mathfrak{u}$	m s^{-1}	molecular velocity in a certain direction	(3.73)
U	m s^{-1}	wall velocity	(3.102)
v	m s^{-1}	velocity	(3.4)
V	m^3	volume	(3.26)
w	m	width	(5.7)
$\mathcal{W}$	J	work	(3.50)
x	m	space coordinate	(5.28)
$\boldsymbol{x}$	m	space coordinate vector	(3.56)
y	m	space coordinate	(5.28)
z	m	space coordinate	(5.28)
Z	-	number of starts	(5.7)

Greek letters

symbol	unit	explanation	equation
α	-	accommodation coefficient	(3.87)
α	rad	rotation angle	(10.12)
α_{CL}	rad	cut lens angle	(5.10)
β	rad	polar angle	(10.50)
γ	-	heat capacity ratio	(3.49)
δ	-	gas rarefaction parameter	(5.13)
ε	-	small parameter	(6.14)
ζ	-	temperature jump coefficient	(3.109)

symbol	unit	explanation	equation
η	-	cross-section ratio	(6.1)
λ	$\mathrm{W\,kg^{-1}\,K^{-1}}$	heat conductivity	(3.100)
μ	$\mathrm{Pa\,s}$	dynamic viscosity	(3.23)
ν	$\mathrm{s^{-1}}$	collision frequency	(6.67)
Π	-	pressure ratio	(5.12)
ρ	$\mathrm{kg\,m^{-3}}$	density	(3.41)
σ	$\mathrm{m^2}$	collision cross section	(3.14)
σ	-	slip coefficient	(3.106)
$\boldsymbol{\tau}$	Pa	stress tensor	(3.65)
ϕ	$\mathrm{m\ s^{-1}}$	dimensionless velocity field	(6.70)
ϕ		physical property	(4.3)
ϕ	-	phase angle	(10.12)
Φ	rad	tooth pitch angle	(10.11)
φ	rad	helix angle	(5.3)
φ	rad	angle	(10.45)
χ	rad	deflection angle	(3.21)
ψ	rad	wrap angle	(10.46)
ω	-	viscosity index	(3.23)
ω	$\mathrm{s^{-1}}$	angular frequency	(3.6)
Ω	-	domain	(3.97)
Ω	$\mathrm{rad^2}$	unit solid angle	(3.15)

Abbreviations and Indices

abbreviation	explanation
+	only positive values
*	post collisional value
*	normalized value
0	rest state, dimensionless value
1,2	different states / molecules
∞	initial state
1D	one-dimensional
3D	three-dimensional
ax	axial
b	bottom
bh	blow hole
c	collision
C	Couette
cf	centrifugal
cell	value is related to the cell
CFD	computational fluid dynamics

abbreviation	explanation
CFL	Courant-Friedrich-Levy
ch	chamber
circ	circumferential
cl	clearance
cl	(superscript) related to the clearance area
CL	Cercignani-Lampis
CLL	Cercignani-Lampis-Lord
cm	centre of mass
d	diffuse
DSMC	direct simulation Monte Carlo
e	end
ec	epicycloid
eff	effusion
et	epitrochoid
EAC	energy accommodation coefficient
Eq.	equation
Eqs.	equations
Fig.	figure
Figs.	figures
GR	gate rotor
h	housing
h	horizontal
H_2	hydrogen
hc	hypocycloid
HP	high pressure
i	inner
i	incident molecule
i	counter
il	inter-lobe
in	inlet value
in	internal
j	counter
l	left
LP	low pressure
max	maximum value
min	minimum value
mod	model
MR	main rotor
n	counter
n	normal
N_2	nitrogen
NTC	no time-counter
o	outer

abbreviation	explanation
out	outlet value
P	Poiseuille
pc	pitch circle
r	reflected molecule
r	relative
r	rotor
r	right
r	radial
R	rotor
ref	reference
Ref.	reference
Refs.	references
rot	rotational
s	scoop
s	sound
s	start
SM	Smolochowski
SSVP	screw spindle vacuum pump
SVW	Saint Venant and Wantzel
t	tangential
t	total
t	top
T	test
th	thermal
Tab.	table
Tabs.	tables
th	theoretic
TMAC	tangential momentum accommodation coefficient
tr	translational
tr	trailing
trans	transitional
U	unknown
v	vertical
VHS	variable hard-sphere
vib	vibrational
w	wall

Math symbols

abbreviation	explanation
a	scalar value
$\boldsymbol{a}$	vector or tensor
$\lvert(\ )\rvert$	absolute value
$\lVert(\ )\rVert$	magnitude or norm
$(\dot{\ })$	time derivative
$(\bar{\ })$	average value
$(\tilde{\ })$	variable belongs to a local coordinate system
$\in$	is element of
$\forall$	for all
$\exists$	if there exists
∂	partial differential
d	total differential
exp( )	exponential function
ln( )	natural logarithm
Γ	gamma function
max( )	maximum
min( )	minimum
$\mathbb{N}$	set of natural numbers
$\mathbb{R}$	set of real numbers
Δ	difference, Laplace operator
$\boldsymbol{\nabla}$	gradient vector
$\int$	integral
$\sum$	sum

1 Introduction

Today, vacuum technology plays a central role both in research and in industrial applications. The word *vacuum* is derived from the Latin word *vacuus*, which means *empty*, *void* and describes a space in absence of matter. As it is not technically possible to create a perfect vacuum, the International Organisation for Standardisation (ISO) provides the following definition:

> "Vacuum [is a] commonly used term to describe the state of a rarefied gas or the environment corresponding to such a state, associated with a pressure or a molecular density below the prevailing atmospheric level."[1]

The first proof that air is also matter was provided by Galilei in 1613, who weighed a glass bottle containing compressed air or air at atmospheric pressure and determined a density value. From this it could be concluded that if air can be regarded as matter with mass, it can also be removed from a container. The first proof of this was provided by Torricelli in 1644, who filled a glass tube sealed on one side with mercury and immersed it in a water bath with the sealed end facing upwards so that the open end was wetted with water. The mercury did not leak completely into the water bath, but a vacuum formed at the upper end of the glass tube. Pascal repeated the experiment in 1646 with other liquids and found that the maximum height of the liquid in the glass tube is inversely proportional to the respective density. Together with Descartes, he developed the idea of being able to determine the air pressure p at different heights. In 1650, Guericke invented a pump whose seals and valves were sealed with water, which he used to evacuate a spherical container. Because of this historical experiment, such machines are still called pumps today instead of compressors, which is usually associated with incompressible media.[2]

Although the first vacuum pump was invented very early on, the physical phenomena had not been understood well yet. In 1835 Clapeyron[3] presents a formula that is today called the ideal gas law which relates the pressure of a certain gas to its respective density and temperature. In 1856 Krönig[4] presents a relation of the pressure based on a kinetic theory, where the gas is described as a large number of submicroscopic particles (atoms and molecules) that have a mass and a velocity. This theory was refined by Clausius[5] in 1857 and connects the kinetic theory with the ideal gas law and he investigates the concept of a mean free path of molecules, which is the mean length a molecule travels until it collides with another molecule. This is inversely proportional to the pressure of a gas. In 1860 Maxwell[6] proposes a mathematical relationship for the velocity distribution of particles in an equilibrium state depending on their average kinetic energy and in 1871 Boltzmann[7] proved, that the particle model fulfils the laws of thermodynamics. In 1909 Knudsen[8] showed in experiments of pressure driven flows through pipes in a vacuum that the flow behaviour can be characterized by a dimensionless ratio which is today called the Knudsen number Kn. This defines the ratio

TAB. 1.1 Definition of flow regimes according to the Knudsen number by Beskok[10].

flow regime	continuum	rarefied gas		
		slip flow	transitional flow	molecular flow
Knudsen number	$Kn < 0.01$	$0.01 \leq Kn \leq 0.1$	$0.1 \leq Kn \leq 10$	$Kn > 10$
gas rarefaction parameter	$\delta > 100$	$100 \geq \delta \geq 10$	$10 \geq \delta \geq 0.1$	$\delta < 0.1$

of the mean free path of the molecules to a characteristic length of a geometry. Alternatively the gas rarefaction parameter δ is often used in the literature which is inversely proportional to the Knudsen number. In case of tubes the diameter is chosen as characteristic length and therefore the Knudsen number shows the ratio of intermolecular collisions to collisions of molecules with the surrounding wall. This characterises the mechanism of momentum and energy transport, which is dominated by intermolecular collisions for small Knudsen numbers, so that the gas can be regarded as a continuum. With large Knudsen numbers, the momentum and energy transport is mainly described by collisions of the molecules with the walls, so that this is considered a molecular flow. Due to the different dynamic behaviour of gases depending on the Knudsen number, a classification according to the Knudsen number is made. An example is given in Tab. 1.1. Therefore, a continuum is defined for $Kn < 0.01$ where intermolecular collisions dominate. Typically such a flow can be calculated by means of a continuum model but a slip on the wall occurs proportional to the molecular free path, that can be neglected for $Kn < 0.01$. For $Kn > 0.1$ the flow must be described by means of the kinetic theory of gases and for $Kn > 10$ intermolecular collisions can often be neglected. Gases for which the mean free path is a non-negligible quantity are called rarefied. In contrast, one speaks of a dilute gas when the mean free path is much greater than the molecular diameter which is of the order of 10^{-10} m.[9]

Nowadays, a variety of vacuum pumps with different mechanisms of action for different flow regimes are developed. The pressure range of technically produced vacuums now extends over more than 15 decades (10^{-10} Pa - 10^{5} Pa), so that a classification into different vacuum ranges depending on the pressure has been established as shown in Tab. 1.2 with rounded values for the number density (number of particles per unit volume) and the mean free path. The vacuum regimes are subdivided into low (rough) vacuum ($>$ 100 Pa), medium (fine) vacuum (0.1 Pa - 100 Pa), high vacuum (10^{-6} Pa - 0.1 Pa), ultra-high vacuum (10^{-9} Pa - 10^{-6} Pa) and extreme-high vacuum ($< 10^{-9}$ Pa).[1] The generation of technical vacuums is an elementary component of many industrial and scientific applications. In particular, the generation of clean, oil-free vacuums plays an important role, for example in the semiconductor, pharmaceutical, chemical and food industries, but also in scientific applications such as mass spectroscopy. For these purposes, the development of dry-running vacuum pumps has been driven forward in the recent past, so that contamination by auxiliary fluids such as oil can be avoided.[2]

TAB. 1.2 Pressure ranges of vacuum technology with corresponding values of the number density and mean free path for air at 300 K rounded on full decades[1].

vacuum regime	rough	fine	high	ultra-high	extreme-high
pressure [Pa]	$10^{5} - 10^{2}$	$10^{2} - 10^{-1}$	$10^{-1} - 10^{-6}$	$10^{-6} - 10^{-9}$	$< 10^{-9}$
number density [m^{-3}]	$10^{25} - 10^{22}$	$10^{22} - 10^{19}$	$10^{19} - 10^{14}$	$10^{14} - 10^{11}$	$< 10^{11}$
mean free path [m]	$10^{-7} - 10^{-4}$	$10^{-4} - 10^{-1}$	$10^{-1} - 10^{4}$	$10^{4} - 10^{7}$	$> 10^{7}$

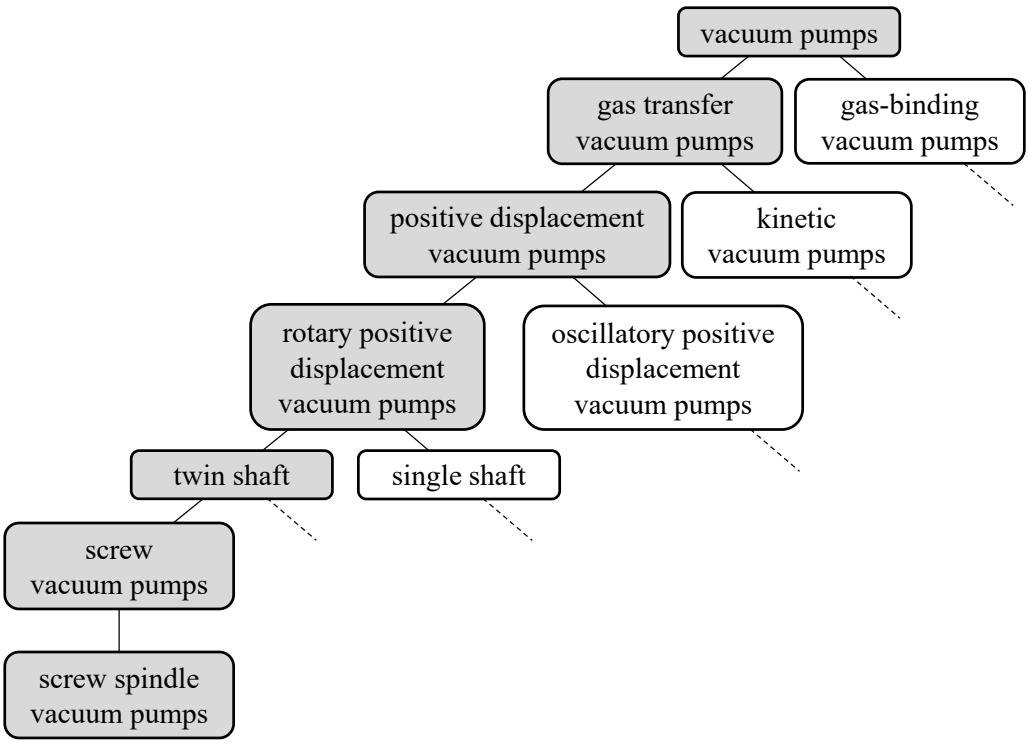

FIG. 1.1 Classification of the screw vacuum pump according to its operation principle.[2,12]

1.1 Dry-Running Screw Spindle Vacuum Pumps

The focus of the present work is the thermodynamic simulation of dry-running screw spindle vacuum pumps (SSVP), which have become increasingly important in recent years because they are able to produce technically clean vacuums and at the same time have a good tolerance to dirt particles and small quantities of liquid. As few machine parts are required due to the design, the assembly and maintenance effort of these machines is comparatively low. Together with their high suction speeds (up to 2500 m^3/h) these machines are particularly interesting for industrial purposes. They offer pressure ranges from 0.1 Pa to atmospheric pressure and are therefore settled in the low and fine vacuum. In many applications they are used as fore vacuum pumps in combination with roots pumps or other vacuum pumps for high suction speeds in the fine or high vacuum regime.[2] The most important quantity for rotary positive displacement vacuum pumps is the suction speed, which describes the volume flow on the low pressure side. The lowest pressure that can be reached in a recipient with a vacuum pump without external leakage is called ultimate pressure.[11]

1.1.1 Classification and Working Principle

The classification of vacuum pumps is typically performed according to the operation principle and design type as shown in Fig. 1.1. A first subdivision can be made according to the principle of gas transfer and gas-binding vacuum pumps. Gas-binding vacuum pumps make use of absorption, adsorption, condensation and diffusion mechanisms to store gas within the pumps. Gas-transfer vacuum pumps transfer the gas through the pump and can be subdivided in kinetic vacuum pumps and positive displacement vacuum pumps. While kinetic vacuum pumps exert momentum to the gas molecules in the direction of flow, positive displacement vacuum pumps enclose the gas in a working chamber, compress it by reducing its volume and expel it under higher pressure. This is done in

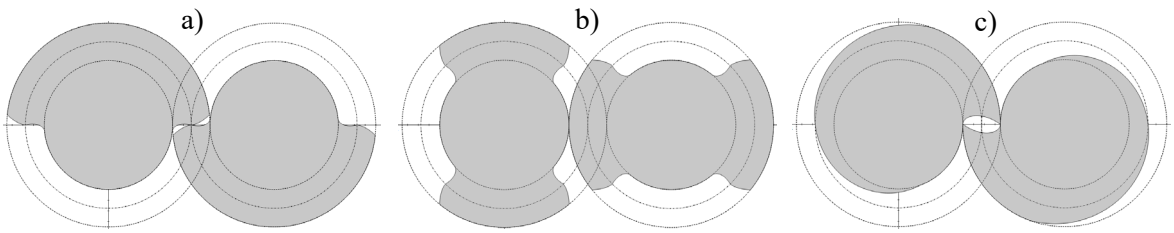

FIG. 1.2 Typical rotor profiles for SSVPs: a) symmetrical single start cycloid profile b) symmetrical two start cycloid profile c) asymmetric single start quimby profile

a cyclic manner either by an oscillatory or by a rotary movement. Rotary positive displacement vacuum pumps can be either single shaft or twin shaft and the screw spindle vacuum pump is a subset of the twin shaft screw vacuum pumps. The last distinction is made because SSVPs have wrap angles much larger than 360° due to the large pressure ratios and therefore require a different profile shape than is usually used for screw compressors. However, Nadler[13] showed that standard compressor profiles can also be used for vacuum pumps when they are operated as blowers.[2]

A further classification can be made on the basis of the rotor profile. Like all screw machines, SSVPs can be described by their face section, which is then twisted in the axial direction. This can be symmetrical and asymmetrical. Similar to a gear wheel, a meshing condition of the two rotors is described by a curve that connects the inner circle with the outer circle and divides the face section into a full profile and grooves. The number of grooves within one face section equals the number of teeth and is also called number of starts. The working chamber is then formed in the grooves between the rotors and the housing. In a symmetrical arrangement, the teeth of the face section are mirror-symmetrical as shown in Fig. 1.2. This means that the formed working chambers can be clearly assigned to a rotor. The tooth flanks are usually generated in a similar way to gear wheels with involutes or cycloids, whereby the profile near the inner circle is closed by means of envelopes. Symmetrical profiles can be used in single start and two start configurations. Rotors with single start profiles offer larger grooves leading to a better ratio of fluid volume swept to the construction volume and better properties regarding gap sizes and leakage paths. Two start rotors, on the other hand, are almost free of imbalance, which makes them particularly interesting for high-speed pump applications.[14,15]

To be able to run dry, the two rotors must run without contact. For this purpose, gaps between the rotors and the housing are essential, but these have an unfavourable effect on the thermodynamic process. Most of these operational gaps can be adjusted via the clearance. However, all symmetrical profiles also have a blowhole, which occurs between the rounding of the tooth tip and the intersecting edge of the housing due to the profile. With asymmetrical profile arrangements it is possible to reduce or even completely close this blowhole on one side while it is enlarged on the other side. This can even lead to a complete connection between the working chambers of both rotors. This is done for the quimby profile, as inner circle and outer circle are connected with a trochoid on one side and with an archimedean spiral on the other side. Therefore, in the ideal profile the tip of the trochoid touches the intersection edge of the housing and thus the blowhole on one side is closed and the whole working chamber is formed on both rotors limited by the inner circle and the spiral. The quimby profile is restricted to a single start rotor as otherwise a complete bypass from the high pressure side to the low pressure side would be established for large wrap angles. As the wrap angle

for compressors above atmospheric pressure is typically smaller than 360°, almost all rotor types there exploit the asymmetric configuration[16–23]. For screw spindles, asymmetrical profiles can also mean increased manufacturing costs, as they often have an undercut[15].[24]

Finally, a further classification can be made on the basis of internal compression. The simplest design is the isochoric machine, whereby the gas is only compressed by a backflow of gas through the gaps. At low intake pressures, this is the worst case in terms of energy. The use of isochoric rotors can be improved considerably in terms of energy by compressing against an end plate. In this way, the volume of the discharge chamber is first reduced before the gas is pushed out. This procedure is usually used in the area of compressors that have a low wrap angle. With a larger wrap angle, the disadvantage here is that a large part of the gas is then only transported without being compressed. On the one hand, this leads to a pure transport phase, similar to the isochoric machine, in which compression only occurs via gap backflows, which is energetically unfavourable. On the other hand, the majority of the compression only takes place locally in the high-pressure working chamber, which means that there occur extremely high gas temperatures due to the large compression ratios. Therefore, the machine cooling can be challenging. Furthermore, small outlet areas are required for the use of an end plate, which leads to larger fluid velocities that increase throttling effects and pulsations due to the cyclic process. Furthermore, the discharge of process-related liquid quantities is made more difficult, for example in the chemical industry.[2]

Modern SSVPs usually realise internal compression via a variable rotor lead[14,15,25–27]. Since the chamber volume scales with the lead, continuous compression can be achieved in this way from closing the working chamber on the low-pressure side to opening the working chamber on the high-pressure side. The compression heat is thus distributed over a larger area of the machine and can be dissipated more efficiently. This reduces temperature peaks on the high-pressure side. Additionally by reducing the lead the same number of chambers require a shorter rotor length which has a positive effect on rotor dynamics and the size of the machine. Furthermore, an end plate is no longer required, which eliminates the disadvantages mentioned above[2]. The design of the ideal rotor pitch is part of various optimisation efforts.[22,28,29] The internal compression ratio is often designed for intake pressures around 300 mbar to reduce over-compression at high intake pressures, which can affect the maximum torque required. As there are often problems with pressure relief valves in dry-running machines, they are often dispensed with in order to reduce the maintenance effort considerably[2]. An idea to overcome this problem is to increase the gap heights on the suction side in order to increase gap flows for high intake pressures. As the sealing effect of gaps increases at a lower pressure due to changed fluid mechanical conditions, the overall power consumption of the machine can be improved this way[14]. There exist further ideas to realise internal compression for example due to change of rotor diameter along the axis leading to conical rotors with either parallel or non-parallel axes[27,30].

Figure 1.3 shows an example for a modern screw spindle vacuum pump with abstracted machine parts. The rotors have a symmetric single start profile with a decreasing lead from low-pressure side to high-pressure side. The working chambers are filled both axially and radially. When the rotor continues to rotate, the trailing rotor tooth closes the working chamber. When the rotor continues to rotate, the fluid is conveyed axially and compressed by the successive reduction of the chamber volume. At the end of the working process, the leading rotor tooth opens the working chamber at a low volume on the high pressure side, so that the fluid can be discharged. The housing is

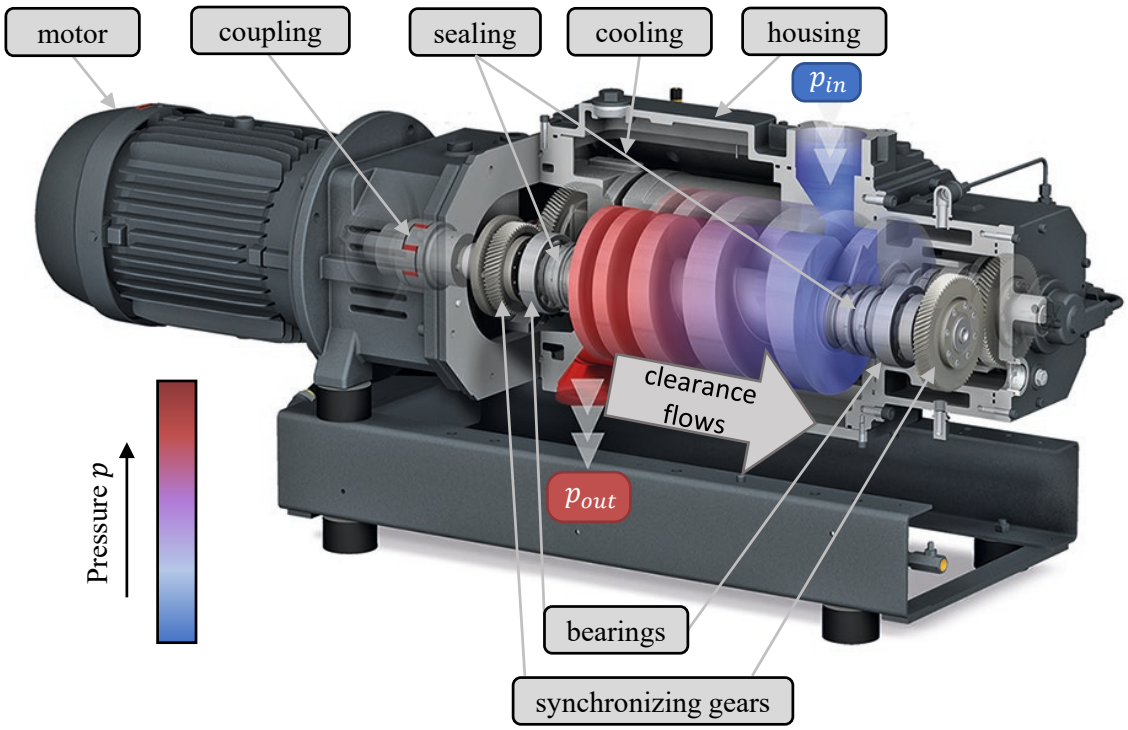

FIG. 1.3 Sketch of an SSVP with working principle.[31,32]

water-cooled via cooling channels. However, there are also concepts for air cooling in which a fan is placed on the shaft and blows air over cooling fins. The main rotor is driven by an electric motor and synchronisation gears are used to drive the female rotor and enable contactless operation. Seals between the bearings and the working chamber prevent contamination of the process gas with oil. For particularly clean processes, seal gas can also be used, but this has a negative effect on the machine's performance. Usually, an internal oil circuit is also installed and driven by the shaft to supply the bearings and the gearbox with oil and to dissipate the heat generated. In addition to the bearing concept presented here, the rotors can also be cantilevered. This makes the rotor dynamics more difficult, but on the one hand the sealing of the low-pressure side is significantly simplified and on the other hand cleaning can be carried out without dismantling the bearings in processes including dirt particles[15].

1.1.2 Simulation of Screw Vacuum Pumps

Since prototyping is very time-consuming and expensive, predicting machine behaviour is of utmost importance. For this purpose, there are various approaches at different levels of complexity. The simplest level is based on analytical approaches, which usually make many simplifications and therefore serve to estimate orders of magnitude in order to carry out a rough design[33]. Ohbayashi et al.[34] investigated an analytical approach to estimate the suction speed for isochoric machines based on an isothermal approach by means of predefined dimensionless flow rates. Rohe[35] developed an analytical function for estimating the ultimate pressure of an SSVP using a series connection approach of pump stages. Nevertheless, for more complex models this needs to be solved by means of numerics. The model of a series of pump stages can be extended to calculate the suction speed in steady-state and is mainly used for screw spindles when conveying incompressible media, but has also been applied on SSVPs[28]. This can be seen as a simplified version of the chamber model

simulation, which can generally be used to calculate positive displacement machines by abstracting them through one or more fluid volumes and different connections. Such a simulation tool named *KaSim*[13,36] based on mass and energy balance has been developed at the Chair of Fluidics at TU Dortmund University. A sketch of a chamber model for an SSVP with a symmetric two start cycloid profile is shown in Fig. 1.4. The different chambers are fluid volumes that are enclosed between the rotors and the housing and connected by gaps. The clearance between the rotor and the housing forms the housing gap and connects to adjacent chambers on the same rotor. The clearance between both rotors can be divided in the radial gap and the inter-lobe gap according to their shape. The radial clearance is placed between the inner diameter of one rotor and the the outer diameter of the other rotor and also connects chambers on the same rotors. The inter-lobe clearance is formed by the minimum distance between the lobes of both rotors. It connects both chambers on the same rotor and chambers of both rotors. The blow hole is the only gap that is given by the profile and not by a clearance and connects adjacent chambers of different rotors. Each chamber has a time dependent volume carrying mass and energy in axial direction. The fluid state inside the chamber is typically assumed to be homogeneous and is changed by mass and energy flows due to the gaps and heat can also be exchanged with the rotors and the housing due to temperature differences of fluid and solid. The characteristic properties of an operating point can be calculated by means of a time-stepping method via a work cycle. Therefore, the fluid state in each time step is changed by the change of volume and by inflowing and outflowing mass and energy flow rates due to the connections. On the low and high pressure side the chamber gets filled or discharged due to connections to the suction or discharge port respectively. The chamber model method is established in the simulation of rotary positive displacement machines[36–40] and is also applied for SSVPs[24,28,35,41,42]. Nevertheless, comparisons to measurements show remaining deviations of the operation performance at low intake pressures that need to be improved[28,41]. The quality of the method depends above all on the modelling depth of the gap flows[22,35,43,44]. Particularly in the case of rarefied gap flows, many investigations have been carried out to determine the respective mass flow rates as a function of given boundary conditions[12,35,41,45–50]. Furthermore, modelling of heat transfers[35,42] can be important. While outlet throttling impacts the machine when an end plate is used[2,51], Stratmann[41] found out that this can be neglected without an end plate. He further investigated inlet throttling for large intake pressures in SSVPs, where a back flow from leading chambers can lead to a pressure rise in the suction chamber before it is closed. He was not able to investigate the chamber filling process for low intake pressures where gas rarefaction effects dominate.

A more detailed simulation approach is provided by multi-dimensional transient fluid dynamics simulations. These simulations are typically based on a continuum assumption, which is quickly violated in vacuum pumps due to the narrow gaps and the associated large Knudsen numbers at low pressure ranges. For moderate Knudsen numbers in the slip regime (Tab. 1.1), the continuum model can still be used if the boundary conditions at the walls are adjusted[52,53]. For more rarefied gases, a coupling with solvers based on the kinetic theory of gases would be needed. A coupling of such methods is under investigation[54,55], nevertheless, this is not yet state of the art in commercial solvers and extremely time-consuming. Huck[12,48] calculated mass flow rates of single gaps using the stochastic Direct Simulation Monte Carlo (DSMC) method which sometimes took several days on a computing cluster. For compressors in the continuum regime such coupling is not needed and although the mesh generation is challenging for rotary positive displacement machines[56–58] these

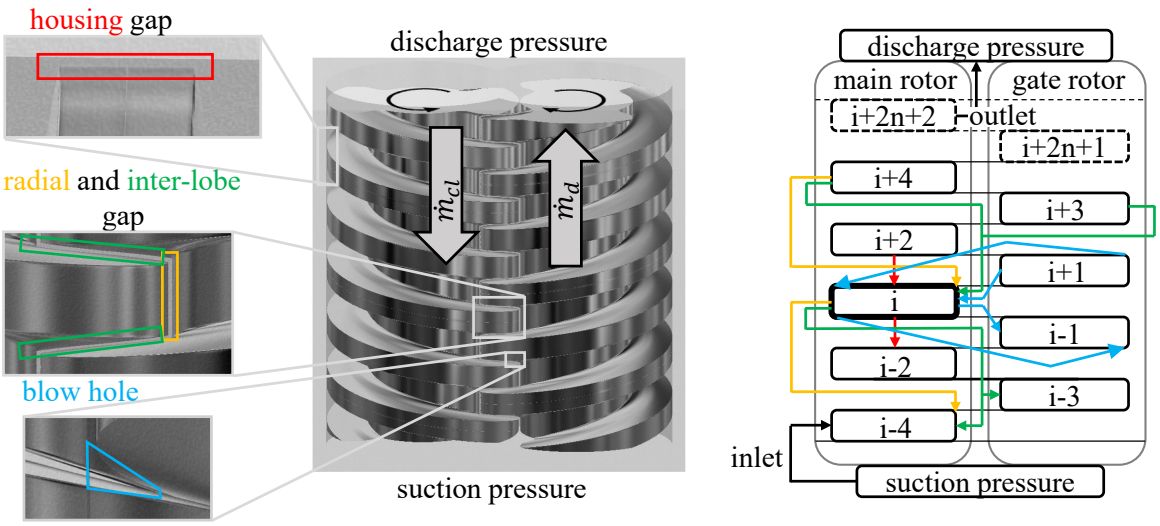

FIG. 1.4 Sketch of an SSVP with two start cycloid profile and the corresponding gaps.

simulations have been successfully carried out since several years [59–64]. But even in the continuum regime the high wrap of SSVPs would be problematic due to the large amount of chambers and clearances that need to be meshed.

In the free molecular regime Nadler[65] simulated a roots pump that operates in fine and high vacuum by means of a test particle method where single molecules are simulated without intermolecular collisions where no mesh is needed. This method is not sufficient for SSVPs that also reach atmospheric pressure.

1.2 Investigation of Gas Flows

In addition to simulating the entire machine, it can also be useful to restrict oneself to partial aspects and investigate these specifically. Therefore, in this section investigations about internal flows for different driving forces are presented.

1.2.1 Poiseuille Flow

A main driving force for flows is a pressure difference causing a fluid to flow from high pressure to low pressure. Hagen and Poiseuille[66] derived an analytical solution for the resulting mass flow rate for such a flow through a pipe in the laminar continuum regime. Therefore, a pressure-driven flow through a channel or pipe is widely called Poiseuille flow. Maxwell[67] derived a solution for slightly rarefied gases predicting a velocity slip at the wall. Measurements in the whole range of the gas rarefaction have been done by Knudsen[8]. These results are reproduced by simulations based on the kinetic gas theory by Loyalka[68] and later by Sharipov[69]. Numerical and experimental investigations for a rarefied Poiseuille flow through short pipes have been carried out by Lilly et al.[70]

The pressure-driven flow between parallel plates in the continuum regime is found in almost any textbook for fluid dynamics, see for example Refs. [66, 71, 72]. For rarefied gas flows this is investigated by Cercignani et al.[73,74], Loyalka et al.[75–77] and Sharipov[78] with different methods based on the kinetic gas theory. Analytical solutions for the mass flow rate in the slip regime are provided by

Arkilic[79], Sharipov[78] and Graur et al.[80] and experimental investigations are carried out by Ewart et al.[81,82].

Analytical solutions in the continuum regime for other cross sections can be found in Ref. [72]. Varoutis et al.[83] provide numerical and experimental investigations for rarefied gases through channels with circular, square, triangular and trapezoidal cross sections. Numerical and analytical approaches for channels with circular and elliptic cross sections are also investigated by Zhvick and Friedlander[84]. For the slip regime different analytical solutions for a flow through a rectangular channel are derived by Méolans et al.[85] and Titarev and Shakhov[86]. The latter also derived an analytical solution for the free molecular regime. In the transitional regime solutions are provided by Sharipov[87,88] as tabulated data.

For converging or diverging channels an analytical solution for the continuum regime is provided by Jeffrey and Hamel[66]. Measurements for rarefied gas flows are made by Graur and Ho[89] and Hemadri et al.[90].

An upper limit for adiabatic frictionless mass flow rates is provided by Saint Venant and Wantzel[91]. This can be used for estimations in compressible flows, where the maximum flow velocity in a constant or converging channel is limited by the speed of sound.

1.2.2 Couette Flow

Another driving force causing a fluid flow is shear stress. Due to a movement of a wall, fluid is dragged in direction of the wall movement. This phenomenon occurs in any machine and is often investigated in the context of a flow between coaxial cylinders where the inner cylinder is rotating. Experimentally this is widely studied to investigate gas properties related to fluid friction.[92–94] Also a flow between parallel plates with relative tangential movement can be considered. In the continuum regime, this fundamental flow is found in any fluid mechanics text book[66] and is called Couette flow named by the physicist who originally formulated the problem. For rarefied gases both the flow between parallel plates and coaxial cylinders is widely investigated in the literature[78,95–100].

An analytical solution for a Couette flow in a rectangular channel in the continuum regime is derived by Rowell and Finlayson[101] to describe the flow in a screw viscosity pump.

1.2.3 Thermal Creep Flow

Reynolds[102] investigated that a temperature gradient causes a fluid flow from cool to warm and named this flow thermal transpiration. Furthermore, he noticed that a temperature gradient can cause a pressure gradient with a zero net mass flow rate for finite inlet and outlet reservoirs in steady state. Therefore, the two driving forces cancel each other out. In his velocity slip condition on the walls, Maxwell[67] could also explain this phenomenon by non-equilibrium conditions of slightly rarefied gases and derived a solution based on a velocity slip that leads to a superposition of both Poiseuille and thermal transpiration mass flow rate. Nowadays this is a rather named thermal creep flow and is numerically investigated by Sharipov[103] in a flow through a pipe. A superposition of a Poiseuille and thermal creep flow between parallel plates is investigated by Sharipov and Siewert[104–106]. Numerical solution for a flow through a rectangular channel in the whole range of the gas rarefaction for such flows is also provided by Sharipov as tabulated data[88].

1.2.4 Mixed Flows

Fukui und Kaneko[107–109] derived based on the kinetic theory of gases, that the total mass flow rate in a channel caused by mixed driving forces (Poiseuille, Couette and thermal creep) can be calculated by superposition of the mass flow rates caused by the individual forces. They exploited this to calculate the behaviour of rarefied gas flows in slider bearings. Alexander et al.[110] use a similar approach and compare their results with numerical simulations of the DSMC method. Li and Hsieh[111] present an analytical solution for the flow in a single screw extruder pump where the flow is calculated by a laminar Couette-Poiseuille flow for high viscous fluids. Sharipov et al.[112] use a similar approach in the context of rarefied gases to simulate the operation behaviour of a Holweck pump. Similarly Huck[12,47,48] calculates the mass flow rates in the gaps of vacuum pumps. A comparison to experimental results shows that the model fits perfectly for rarefied gases, but fails in the continuum limit as the predicted fluid velocity exceeds the limit of the speed of sound. He additionally performs simulations based on the kinetic gas theory for the gap flows where he notices that there is no clear distinction between the flow in the gaps and the connected reservoirs in rarefied gases when there are moving walls applied.

For compressible channel flows with constant cross-section, analytical solutions exist for adiabatic frictional flows (Fanno flow) and for diabatic frictionless flows (Rayleigh flow). Shapiro[113,114] develops a one-dimensional differential equation with which a channel flow can be determined numerically for compressible frictional and diabatic flows with a change in cross-section. Müller[46] uses this differential equation and extends this model for rarefied pressure-driven gas flows by using Sharipov's flow coefficients for the friction closure problem in plane channels. Jünemann[49] extends this model so that a diabatic Couette-Poiseulle flow with variable cross-section in the entire range of gas rarefaction can be calculated, as occurs, for example, in the radial gap of SSVPs. He also takes into account flow separations[50] on the basis of an analogy to the Jeffrey Hamel flow.

1.3 Gas-Surface Interactions

The works presented in the previous section are related to a full heat and momentum exchange of the gas molecules with the wall. Maxwell[67] was the first who predicted a velocity slip between gas and wall for rarefied gases, that is increased if molecules that collide with the wall keep part of their tangential velocity leading to a reduced shear stress. This phenomenon is widely modelled with the so-called tangential momentum accommodation coefficient (TMAC) which is a dimensionless number depending on the pair of the gas and surface material[115,116]. Similarly a reduced heat flux can be obtained by non-complete heat exchange which is modelled with the so-called energy accommodation coefficient (EAC)[115,117]. Different models exist with slightly different definitions of these coefficients as described in detail in Sec. 3.5.5. The idea is that the coefficients for the gas-surface interactions can be obtained by measurements. Therefore, Arkilic et al.[79,118,119] developed a measurement technique to extract the TMAC in a plane Poiseuille flow for rarefied gases by comparison to analytical solutions. A similar approach is used by Graur et al.[120]. Missoni et al.[121] compare simulation results to measurements of a thermal creep flow to extract the TMAC and EAC. Gabis et al.[93], Loyalka[122] and Bentz et al.[94] use a spinning rotor gauge experiment to extract the TMAC. Acharya et al.[116,123–125] developed a procedure via disc spin-down time to extract the TMAC for different gas-surface material combinations and provide an overview about many works and results about this topic in Ref. [116].

Based on given parameters for the gas-surface interactions Sharipov provides dimensionless flow rates in tabulated form for Poiseuille flow and thermal creep flow through parallel plates[126] and through long tubes[127] for different combinations of gas surface-interactions with the result that the Poiseuille flow is mainly affected by the TMAC and hardly by the EAC. Furthermore, he derived slip coefficients for the continuum model by comparison to the kinetic gas theory[128]. Cercignani et al. use a variational approach based on the kinetic gas theory to provide reduced flow rates as tabulated data of a rarefied Poiseuille flow[129] and Couette flow[95] between parallel plates that have different TMACs.

In addition to the effect that the shear stress can be reduced by incomplete accommodation, surface roughness can even cause molecules to be scattered back in the opposite direction, leading to an increased shear stress. The effect of surface roughness is investigated experimentally by Lilly et al.[130]. Analytic surface roughness models are presented by Aksenova and Khalidov[131–133]. Zhang et al.[134] investigate the effect of surface roughness in a plane Poiseuille flow for rarefied gases and Yan et al.[135] simulate this behaviour for pipe flows while Su et al.[136] simulate the effect of surface roughness in the flow of slider bearings. Further numerical investigations are performed by Sazhin[137–139] where the surface roughness is abstracted geometrically with a surface structure in periodic patterns. In summary surface roughness leads to a comparably higher friction and thus to lower flow rates through the channel.

As already mentioned for slider bearings, rarefied gas flows do not only exist in vacuum application, but also in micro and nano electro-mechanical systems (MEMS/NEMS)[140]. An overview of different applications and phenomena is given by Narendran et al.[141] and Taassob et al.[142]. A critical review about the different measurement techniques for microfluidics is given by Morini et al.[143].

2 Aim of the Work and Approach

Improving the efficiency of commonly used machines is a high priority, especially in the context of climate change. As prototyping is expensive, numerical optimisation is an effective tool which requires a good and efficient representation of the machine performance. However, currently no simulation tool is able to adequately represent the operation behaviour of screw spindle vacuum pumps (SSVP) at all operating points. Today the chamber model simulation still seems to have the highest potential in terms of accuracy and efficiency. Furthermore, by using sub-models, individual loss mechanisms can be identified and specifically minimised in order to improve the machine performance.

Currently, investigations show a good agreement between simulation and experiment in the range of high suction pressures, whereas the machine's performance is predicted to be too good at low suction pressures. Improved models for the gap mass flow rates lead to an improvement of the simulation results, but these alone cannot solve the problem. From Huck's[12] findings that the wall velocity in the context of rarefied gas flows has a great influence on the mass flow rate and that this can also affect the fluid state in the reservoirs it can be concluded that the assumption of homogeneous working chambers is violated at low suction pressures. The movement of the rotors causes a Couette flow in the direction of rotation within the chamber. Due to the encapsulation of the working chamber, this mass flow is dammed up so that a pressure gradient is caused in the opposite direction. An analogy can be made by the friction dominated flow in extruder pumps. The effect of inhomogeneous chamber states in SSVPs in the context of a chamber model is sketched in Fig. 2.1. An expected pressure distribution p normalised by the respective average chamber pressure p_{ch} is visualized by a colour map. As a consequence an inhomogeneous pressure distribution within the chamber causes higher mass flow rates for the adjacent gaps as these scale with the inlet density. Furthermore, it can be deduced that an inhomogeneous chamber state leads to an incomplete chamber filling. Although Stratmann[41] investigated the chamber filling process in the continuum regime, he was not able to investigate this for rarefied gases.

The aim of this work is to develop a fluid mechanical model with which the pressure distribution in working chambers can be efficiently determined as a function of the respective influencing parameters for both the chamber filling process as well as for encapsulated chambers, so that it can be easily implemented in chamber model simulation. For this purpose, the chamber is geometrically abstracted and a dimensional analysis is performed in order to reduce the number of parameters to be considered without reducing the generality. Since the influence is expected particularly in the range of low chamber pressures, the model must be able to represent rarefied gas flows. According

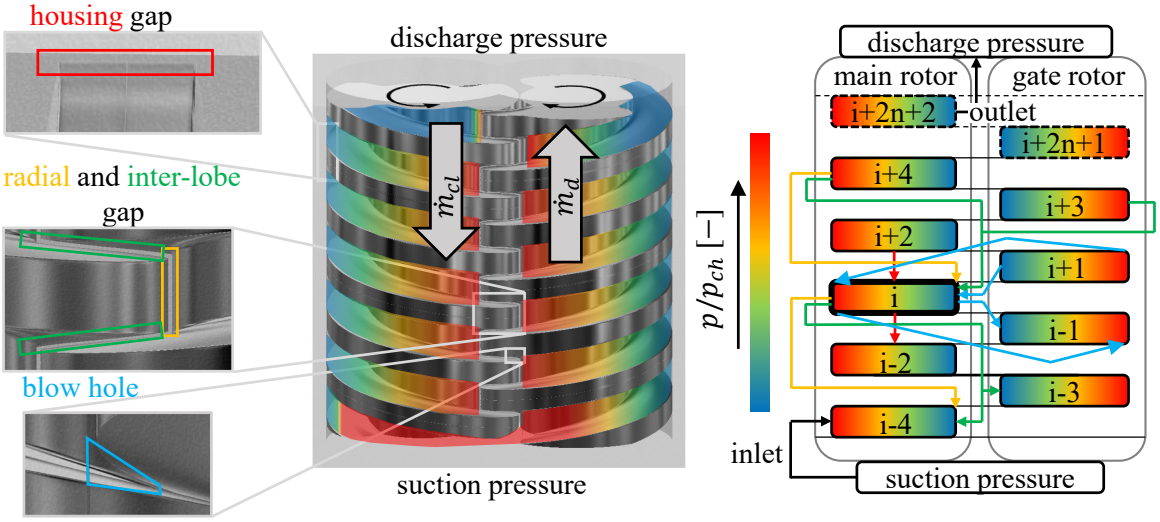

FIG. 2.1 Sketch of an SSVP with a two start cycloid profile and the corresponding gaps with inhomogeneous chambers.

to the literature the pairing of gas and surface material also needs to be taken into account. For experimental validation a test rig is constructed.

Furthermore, the chamber filling for low suction pressures is investigated. While it is assumed for closed working chambers that the chamber is in a steady-state, transient simulations are carried out for the open working chamber using computational fluid dynamics (CFD), because the chamber volume continuously changes with time.

Both the results of the open and the closed chamber are reduced to approximative functionals of a dimensionless number via regression analysis. This dimensionless number is calculated by means of the machine dimensions, the operation point and the average chamber state. The functionals are implemented into the chamber model simulation software *KaSim* developed at the Chair of Fluidics at TU Dortmund University. The operation performance of a test machine is simulated and compared with measurement results to prove that the models are suitable to improve the simulation results of the whole machine.

3 Basics of Rarefied Gas Dynamics

> "If, in some cataclysm, all of scientific knowledge were to be destroyed, and only one sentence passed on to the next generations of creatures, what statement would contain the most information in the fewest words? I believe it is the atomic hypothesis (or the atomic fact, or whatever you wish to call it) that all things are made of atoms—little particles that move around in perpetual motion, attracting each other when they are a little distance apart, but repelling upon being squeezed into one another. In that one sentence, you will see, there is an enormous amount of information about the world, if just a little imagination and thinking are applied."[144]

With this introduction Richard P. Feynman started his lectures on physics at the California institute of Technology. And especially when dealing with rarefied gas dynamics the consideration of the molecular model is important as many phenomena cannot be explained with continuum assumptions. Fortunately not all other scientific knowledge is destroyed, thus there are many basics that can be used to make use of this *atomic hypothesis*. Therefore, in this chapter at first the molecular model is presented leading to the conservation laws which are needed when molecules interact with each other. For a large amount of molecules the kinetic theory of gases is explained which connects the molecular model with the macroscopic properties that are also used in the continuum model.

3.1 Molecular Model

First of all it is convenient to present the molecular model, where atoms consist of a nucleus with protons and neutrons in a sphere of about 10^{-15} m and a cloud of electrons around in a larger sphere of about 10^{-10} m. While the nucleus is held together by weak and strong nuclear forces, the electrons are kept by electromagnetic forces. Such an atom is modelled as a sphere with a molecular mass $\mathfrak{m}$ and a diameter $\mathfrak{d}$. The atom has a velocity vector $\mathfrak{c}$ leading to a momentum $\boldsymbol{\mathcal{M}} = \mathfrak{m}\mathfrak{c}$ and a kinetic energy $\mathcal{E}_{\mathrm{tr}} = \mathfrak{m}\mathfrak{c}^2/2$. Due to the electromagnetic forces different molecules can attract each other by van der Waals forces and repel each other if their nuclear shells interact as shown in Fig. 3.1. Often an even more simplified model is convenient when dealing with gases, where the spheres are considered to be rigid bodies. In this case there is no attractive potential and a penetration of nuclear shells is omitted.[9,115,144]

While noble gases like helium or argon are electromagnetically neutral, most other gases build molecules where two or more atoms are kept together, like nitrogen or oxygen which are the main ingredients of air. Although it is obviously incorrect in physics such a molecule is also successfully modelled as a sphere albeit including internal energy modes. So next to the translational kinetic energy

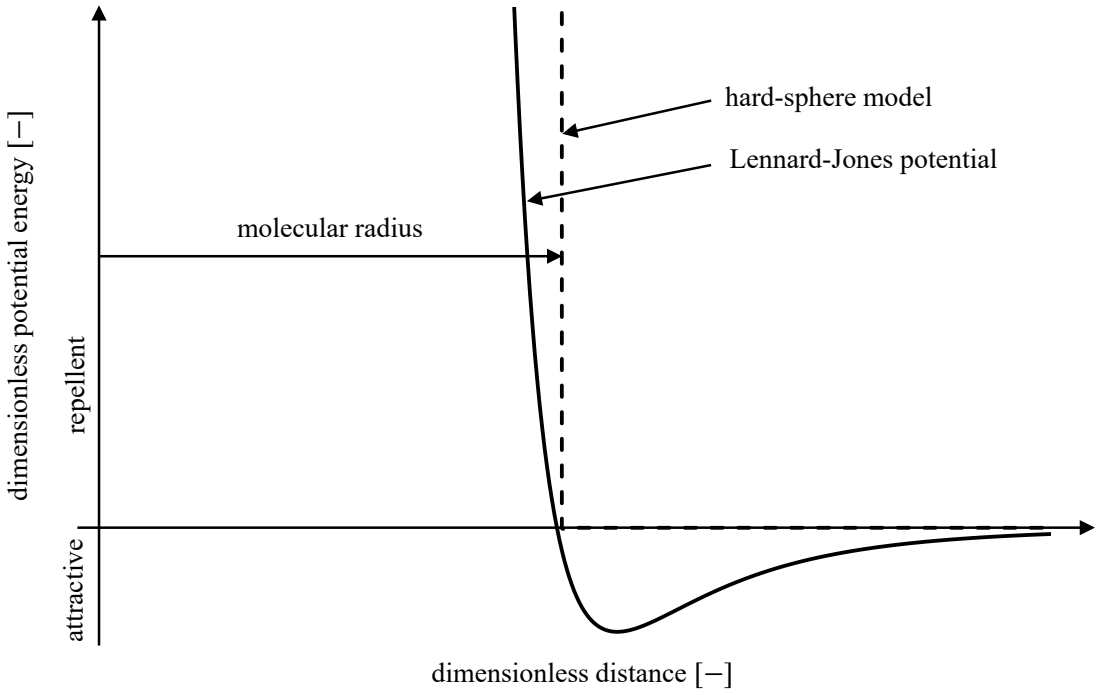

FIG. 3.1 Molecular energy potentials between two molecules according to Lennard-Jones and a rigid body (hard-sphere) model.

there is a rotational kinetic energy $\mathcal{E}_{\mathrm{rot}}$ due to a rotation around the molecules' centre of mass with two degrees of freedom $\mathfrak{f}$ in case of diatomic molecules like oxygen, nitrogen or hydrogen and three rotational degrees of freedom for more than two atoms like carbon dioxide. Additionally there can be a vibrational energy $\mathcal{E}_{\mathrm{vib}}$ if the atoms' distance within the molecule fluctuates. Therefore, there is a kinetic energy mode due to the internal movement and a potential energy mode as the molecular forces depend on their distance. Thus, for diatomic molecules there are two additional degrees of freedom. The probability that the internal energy modes are stimulated depends on the possible quantum states with higher probability for more degrees of freedom with increasing energy[144]. Therefore, vibrational modes are often neglected for air at ambient temperature[115].

3.2 Conservation Laws

The exchange of different energy modes of molecules leads to the conservation laws. It is a fundamental observation that energy is conserved which means that energy is constant and can just be converted from kinetic energy to potential energy or transferred from molecule to molecule in a reversible way. Since Einstein's[145] discovery it is clear that mass is also a potential energy with the relation $\mathcal{E} = \mathfrak{m}\mathcal{C}^2$ and that the mass of a particle is related to its rest mass $\mathfrak{m}_0$ and its ratio of movement speed to the speed of light $\mathcal{C}$:

$$\mathfrak{m} = \frac{\mathfrak{m}_0}{\sqrt{1 - \mathfrak{c}^2/\mathcal{C}^2}} \tag{3.1}$$

Nevertheless, as the velocities considered in this work are all small compared to the speed of light, mass is considered to be a conserved quantity as well and a change of the molecular mass is neglected.

Finally, with Newton's first two axioms a third conserved quantity is identified which is the momentum $\boldsymbol{\mathcal{M}}$ with the statements, that the momentum is constant in the absence of forces and that the rate of change equals the sum of the present forces $\boldsymbol{\mathcal{F}}$:

$$\frac{\mathrm{d}\boldsymbol{\mathcal{M}}}{\mathrm{d}t} = \sum \boldsymbol{\mathcal{F}} \tag{3.2}$$

His third axiom *action equals reaction* means that if two particles are supposed, with one particle pushing with a certain force against the other, the second particle will push on the first one with equal force in opposite direction in the same line. With these fundamental assumptions the world of classical mechanics can principally be explained from molecular scales to planetary scales, as a set of particles can be considered where all internal forces cancel out and only the forces on the surface need to be considered, acting on the centre of mass. Nevertheless, most phenomena in reality are too complex for detailed descriptions. As already mentioned for the internal energy modes, classical mechanics fails to explain the subatomic scales where quantum mechanics need to be taken into account, and to describe interplanetary and larger scales the general theory of relativity is needed.[144]

3.3 Principle of Relativity

This work is limited to the use of the Galilean principle of relativity for classical mechanics at speeds much lower than the speed of light. The principle of relativity is an important statement that ensures that a physical observation does not depend on the observer. Therefore, two different coordinate systems with origins $\mathcal{O}$ and $\tilde{\mathcal{O}}$ can be considered with coordinates $\boldsymbol{x}$ and $\tilde{\boldsymbol{x}}$ respectively. At some time t $\tilde{\mathcal{O}}$ is located at a distance $\boldsymbol{r}$ and it is moved with a constant velocity $\boldsymbol{v}$ relative to $\mathcal{O}$. The question is whether the description of Newton's laws delivers equal results from both coordinate systems. Considering a constant mass m the equality

$$m\frac{\mathrm{d}^2\boldsymbol{x}}{\mathrm{d}t^2} = \boldsymbol{\mathcal{F}} = m\frac{\mathrm{d}^2\tilde{\boldsymbol{x}}}{\mathrm{d}t^2} \tag{3.3}$$

must hold. This can be proved with the relations

$$\frac{\mathrm{d}\tilde{\boldsymbol{x}}}{\mathrm{d}t} = \frac{\mathrm{d}}{\mathrm{d}t}(\boldsymbol{x} - \boldsymbol{r}) = \frac{\mathrm{d}\boldsymbol{x}}{\mathrm{d}t} - \boldsymbol{v} \tag{3.4}$$

and

$$\frac{\mathrm{d}^2\tilde{\boldsymbol{x}}}{\mathrm{d}t^2} = \frac{\mathrm{d}^2\boldsymbol{x}}{\mathrm{d}t^2} \tag{3.5}$$

since $\mathrm{d}\boldsymbol{v}/\mathrm{d}t = \boldsymbol{0}$. Thus, any reference frame moved with an arbitrary constant velocity $\boldsymbol{v}$ with $v = \|\boldsymbol{v}\| \ll \mathcal{C}$ can be used to observe the same forces, but all observed velocities are relative to $\boldsymbol{v}$. This is not true if the reference frame is accelerated with $\mathrm{d}\boldsymbol{v}/\mathrm{d}t \neq \boldsymbol{0}$. This leads to the observation of pseudo forces. An example is the centrifugal force

$$\mathcal{F}_{\mathrm{cf}} = m\omega^2 r \tag{3.6}$$

in rotating systems where ω is the angular frequency and r is the distance from the rotation axis.[144]

3.4 Binary Collisions

With the previous statements it is possible to describe collisions between two molecules 1 and 2 and calculate their post-collisional velocities $\mathfrak{c}_1^*$ and $\mathfrak{c}_2^*$ depending on their pre-collisional properties $\mathfrak{m}_1$ and $\mathfrak{m}_2$ and $\mathfrak{c}_1$ and $\mathfrak{c}_2$. Their masses remain constant due to conservation of mass. At first, elastic collisions are assumed. Therefore, the momentum and energy equation read

$$\mathfrak{m}_1\mathfrak{c}_1 + \mathfrak{m}_2\mathfrak{c}_2 = \mathfrak{m}_1\mathfrak{c}_1^* + \mathfrak{m}_2\mathfrak{c}_2^* = (\mathfrak{m}_1 + \mathfrak{m}_2)\mathfrak{c}_{\mathrm{cm}} \tag{3.7}$$

$$\mathfrak{m}_1\mathfrak{c}_1^2 + \mathfrak{m}_2\mathfrak{c}_2^2 = \mathfrak{m}_1\mathfrak{c}_1^{*2} + \mathfrak{m}_2\mathfrak{c}_2^{*2} \tag{3.8}$$

where $\mathfrak{c}_{\mathrm{cm}}$ is the velocity of the centre of mass at the moment when both molecules collide and is constant during the collision. With the definition of the pre- and post-collisional relative velocities

$$\mathfrak{c}_{\mathrm{r}} = \mathfrak{c}_1 - \mathfrak{c}_2 \quad \mathfrak{c}_{\mathrm{r}}^* = \mathfrak{c}_1^* - \mathfrak{c}_2^* \tag{3.9}$$

the pre- and post-collisional velocities can be written relative to the centre of mass:

$$\mathfrak{c}_1 = \mathfrak{c}_{\mathrm{cm}} + \frac{\mathfrak{m}_2}{\mathfrak{m}_1 + \mathfrak{m}_2}\mathfrak{c}_{\mathrm{r}} \quad \mathfrak{c}_2 = \mathfrak{c}_{\mathrm{cm}} - \frac{\mathfrak{m}_1}{\mathfrak{m}_1 + \mathfrak{m}_2}\mathfrak{c}_{\mathrm{r}} \tag{3.10}$$

$$\mathfrak{c}_1^* = \mathfrak{c}_{\mathrm{cm}} + \frac{\mathfrak{m}_2}{\mathfrak{m}_1 + \mathfrak{m}_2}\mathfrak{c}_{\mathrm{r}}^* \quad \mathfrak{c}_2^* = \mathfrak{c}_{\mathrm{cm}} - \frac{\mathfrak{m}_1}{\mathfrak{m}_1 + \mathfrak{m}_2}\mathfrak{c}_{\mathrm{r}}^* \tag{3.11}$$

Inserting this into the energy equation it is obtained that the magnitude of the relative velocity

$$\mathfrak{c}_{\mathrm{r}} = \mathfrak{c}_{\mathrm{r}}^* \tag{3.12}$$

remains constant. The last unknown to calculate the post-collisional relative velocity vector is the deflection angle χ between pre- and post-collisional relative vector which is sketched in Fig. 3.2 where the trajectories of pre- and post-collisional velocity vectors are shown in the collision plane. This collision plane is parallel to the relative pre-collision vector and contains the centre of mass.[9,146]

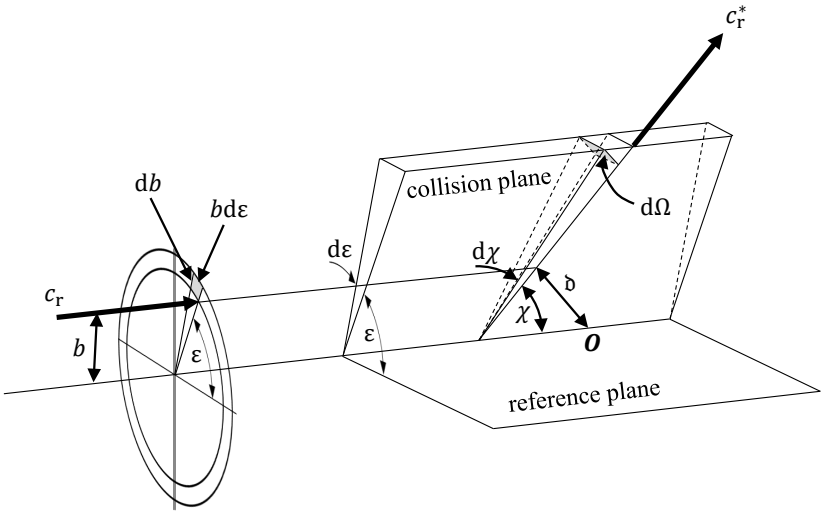

FIG. 3.2 Representation of the collision plane in the relative frame of the centre of mass.

According to this sketch the post-collision velocity vector can be calculated[9]:

$$\mathfrak{c}_{\mathrm{r}}^{*} = \mathfrak{c}_{\mathrm{r}} \begin{pmatrix} \cos\chi \\ \sin\chi\cos\varepsilon \\ \sin\chi\sin\varepsilon \end{pmatrix} \tag{3.13}$$

In order to calculate the deflection angle χ in a binary collision apart from the translational velocities of the collision partner, two impact parameters are required. That is the closest approach b of the two undisturbed trajectories in the centre of mass and the angle ε between an arbitrary reference plane and the collision plane. The differential cross-section is defined by

$$\sigma \, \mathrm{d}\Omega = b \, \mathrm{d}b\mathrm{d}\varepsilon \tag{3.14}$$

with the unit solid angle

$$\mathrm{d}\Omega = \sin\chi \, \mathrm{d}\chi\mathrm{d}\varepsilon \tag{3.15}$$

about the relative post-collision vector $\mathfrak{c}_{\mathrm{r}}^{*}$ so that

$$\sigma = \frac{b}{\sin\chi} \left| \frac{\mathrm{d}b}{\mathrm{d}\chi} \right| \tag{3.16}$$

and the total collision cross-section σ_{t} is defined as[9]:

$$\sigma_{\mathrm{t}} = \int_{0}^{4\pi} \sigma \, \mathrm{d}\Omega = 2\pi \int_{0}^{2\pi} \sigma \sin\chi \, \mathrm{d}\chi \tag{3.17}$$

Assuming the simplest molecular model of hard spheres the closest approach of two molecules is the average value of their respective diameters $\mathfrak{d}_1$ and $\mathfrak{d}_2$

$$\mathfrak{d} = \frac{\mathfrak{d}_1 + \mathfrak{d}_2}{2} \tag{3.18}$$

and therefore the distance b in Fig. 3.2 is

$$b = \mathfrak{d} \sin\theta_A = \mathfrak{d} \cos\left(\frac{\chi}{2}\right) \tag{3.19}$$

with the solution of the total cross section

$$\sigma_{\mathrm{t}} = \pi\mathfrak{d}^2 \tag{3.20}$$

and the deflection angle

$$\chi = 2 \arccos\left(\frac{b}{\mathfrak{d}}\right) \quad . \tag{3.21}$$

A more realistic model is the so-called variable hard sphere model (VHS), where the collision cross-section is proportional to the inverse power of the relative velocity. Thus, with increasing relative kinetic energy $\mathcal{E}_{\mathrm{tr,r}}$ there is a relative decrease in the repellent forces leading to a smaller deflection

which is modelled with an effective smaller collision cross-section σ_t. The VHS model can be defined as

$$\frac{\sigma_\mathrm{t}}{\sigma_\mathrm{t,ref}} = \left(\frac{\mathfrak{d}}{\mathfrak{d}_\mathrm{ref}}\right)^2 = \left(\frac{\mathfrak{c}_\mathrm{r,ref}}{\mathfrak{c}_\mathrm{r}}\right)^{2\xi} = \left(\frac{\mathcal{E}_\mathrm{tr,r,ref}}{\mathcal{E}_\mathrm{tr,r}}\right)^{\xi} \tag{3.22}$$

where the subscript ref denotes reference values of a certain temperature T_ref and $\xi = \omega - 1/2$ depends on the gas and represents the proportional relationship of the macroscopic quantities dynamic viscosity μ and temperature T with a power law[9]:

$$\mu = \mu_\mathrm{ref}\left(\frac{T}{T_\mathrm{ref}}\right)^{\omega} \tag{3.23}$$

The total collision cross section for the VHS model can be calculated as

$$\sigma_\mathrm{t} = \pi d_\mathrm{ref}^2 \frac{\left(2kT_\mathrm{ref}/\mathfrak{m}\mathfrak{c}_\mathrm{r}^2\right)^{\omega-1/2}}{\Gamma\left(5/2-\omega\right)} \tag{3.24}$$

where the Gamma function is defined as[9]:

$$\Gamma(j) = \int_0^\infty x^{j-1}\exp(-x)\,\mathrm{d}x \tag{3.25}$$

If molecules with internal degrees of freedom are considered, the pre-collisional and post-collisional internal energy must be considered in the energy balance Eq. (3.8), leading to a different relative post-collision velocity magnitude c_r. Typically an equipartition of energy modes is assumed leading to the Larsen-Borgnakke model, where the distribution of the total energy of both molecules on translational and internal modes is solved by statistical methods leading to an equipartition at average in many collisions. When the post-collision magnitude of the relative velocity $\mathfrak{c}_\mathrm{r}^*$ is known, the deflection angle is calculated according to Eq. (3.21). The complexity of the atomic model depends on the physical phenomena which need to be described. The models presented here are suitable for the simulation of friction dominated gas flows at moderate temperature levels. For diffusion phenomena, for example, the assumption of hard spheres leads to errors which can be corrected by adjusting the deflection angle. For chemical reaction processes, electron charges or quantum mechanic models need to be taken into account.[9,146–148]

3.5 Kinetic Gas Theory

The kinetic theory of gases connects the macroscopic observations to the microscopic molecular movement. According to the theory a gas consists of a large number N molecules per unit volume V which is typically defined by the number density

$$n = \frac{N}{V}\ . \tag{3.26}$$

These molecules move through space in perpetual motion where they carry mass, momentum and energy and collide with each other, where they exchange momentum and energy in each collision. The time-scale of the macroscopic processes is set by the mean collision time which is the mean time between two intermolecular collisions with the reciprocal value being the mean collision rate or collision frequency ν per molecule. To quantify this collision frequency it is convenient to consider

a test molecule with velocity $\mathfrak{c}_\mathrm{T}$ in a field of Δn molecules with velocity $\mathfrak{c}$ with the corresponding relative velocity $\mathfrak{c}_\mathrm{r}$. With these definitions a relative frame can be chosen, where the test molecule moves in a time interval Δt much shorter than the mean collision time while the field molecules are stationary as sketched in Fig. 3.3. The test molecule would collide with any field molecule which has its centre within the cylinder of the volume $\sigma_\mathrm{t}\mathfrak{c}_\mathrm{r}\Delta t$ where σ_t is the total collision cross-section. In a dilute gas where the molecular size is much smaller than the average distance between the molecules ($\mathfrak{d} \ll n^{-1/3}$) the restriction on Δt can be neglected and the number of collisions per unit time with the field molecules is $\Delta n \sigma_\mathrm{t} \mathfrak{c}_r$.[9]

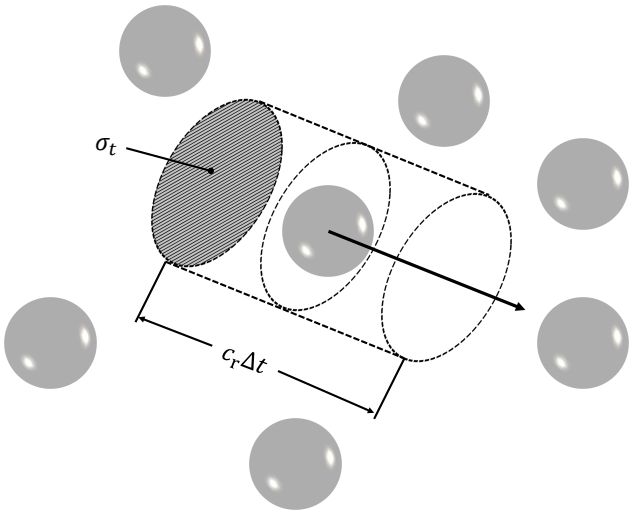

FIG. 3.3 Effective volume swept out by moving test molecule relative to stationary field molecules.

By summing over all velocity classes of molecules, the mean collision frequency is obtained[9]:

$$\nu = \sum \Delta n \sigma_\mathrm{t} \mathfrak{c}_r = n\overline{\sigma_\mathrm{t}\mathfrak{c}_\mathrm{r}} \tag{3.27}$$

The average number of collisions per unit time and unit volume is therefore given by

$$N_c = \frac{1}{2} n\nu = \frac{1}{2} n^2 \overline{\sigma_\mathrm{t}\mathfrak{c}_\mathrm{r}} \tag{3.28}$$

while the factor of one half is due to the fact that each collision involves two molecules. The mean free path $\bar{\mathfrak{l}}$ is the average distance travelled by a molecule between two collisions and must be defined in a frame of reference where the gas is at rest. The macroscopic stream velocity $\boldsymbol{u}$ of the centre of mass in a single species gas equals the sum of all molecular velocities

$$\boldsymbol{u} = \sum \mathfrak{c} = \bar{\mathfrak{c}} \tag{3.29}$$

with the molecules' thermal velocities $\mathfrak{c}'$ defined in the reference frame at rest

$$\mathfrak{c}' = \mathfrak{c} - \boldsymbol{u} \tag{3.30}$$

and the thermal molecular speed

$$\mathfrak{c}' = \|\mathfrak{c}'\| = \sqrt{\mathfrak{c}_x'^2 + \mathfrak{c}_y'^2 + \mathfrak{c}_z'^2}\ . \tag{3.31}$$

Therefore, the mean free path is the average of the thermal molecular speed[I] divided by the collision frequency

$$\bar{\mathfrak{l}} = \frac{\overline{\mathfrak{c}'}}{\nu} \tag{3.32}$$

which can be solved for hard sphere molecules to[9]

$$\bar{\mathfrak{l}} = \frac{1}{\sqrt{2}\pi n \mathfrak{d}^2} \,. \tag{3.33}$$

3.5.1 Macroscopic Gas Properties

Chapman and Enskog[9] derived independently the dependency of the macroscopic coefficient of dynamic viscosity μ to the molecular diameter. For the hard sphere model this can be expressed as

$$\mu = \frac{5\mathfrak{m}\overline{\mathfrak{c}'}}{\sqrt{2048}\mathfrak{d}^2} \tag{3.34}$$

leading with Eq. (3.33) to a mean free path of

$$\bar{\mathfrak{l}} = \frac{32}{5\pi}\frac{\mu}{n\mathfrak{m}\overline{\mathfrak{c}'}} \,. \tag{3.35}$$

In the literature[2,78,83,87,90,139] a simplification is often performed with $\frac{32}{5\pi} \approx 2$ leading to an error of about 1.85 % which can be justified with the simplification of the model itself.

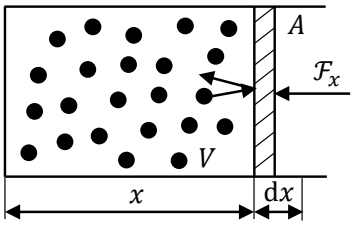

FIG. 3.4 Molecules of a gas in a cylinder with a frictionless piston.

Due to the large amount of molecules and the fact that mass, momentum and energy are conserved in any collision, it is convenient to assume that a gas at rest without forces acting on them is in an equilibrium state after some time during which the average velocity in each direction is zero and all energy modes are equally distributed. If such a state is assumed in a box with a frictionless piston according to Fig. 3.4, the force $\mathcal{F}_x$ equals the momentum change of the number of molecules hitting the piston

$$\mathcal{F}_x = \frac{\mathrm{d}\mathcal{M}_x}{\mathrm{d}t} = n\mathfrak{m}\overline{\mathfrak{c}_x'^2}A \tag{3.36}$$

where the number of molecules hitting the piston area A in a time t is $N = nA\overline{\mathfrak{c}'_{x,+}}t$ with $\overline{\mathfrak{c}'_{x,+}}$ being the average molecular velocity in positive x direction.[144] With the assumption that there is no preferred molecular direction

$$\overline{\mathfrak{c}_x'^2} = \frac{1}{3}\overline{\mathfrak{c}_x'^2 + \mathfrak{c}_y'^2 + \mathfrak{c}_z'^2} = \frac{1}{3}\overline{\mathfrak{c}'^2} \tag{3.37}$$

[I] Note, that although the average of the thermal velocity is zero, the average of the thermal speed is not.

and the definition of the pressure

$$p = \frac{\mathcal{F}}{A} \tag{3.38}$$

this can be written as

$$p = \frac{2}{3} n \frac{\overline{\mathfrak{m}\mathfrak{c}'^2}}{2} = \frac{2}{3} n \overline{\mathcal{E}'_{\mathrm{tr}}} \, . \tag{3.39}$$

From macroscopic observations it is known that for ideal gases such as air, this is related to the change of macroscopic temperature T leading to the ideal gas law

$$p = \rho R T = n k T \tag{3.40}$$

where

$$\rho = n\mathfrak{m} \tag{3.41}$$

is the macroscopic gas density, k is the universal Boltzmann constant and

$$R = \frac{k}{\mathfrak{m}} \tag{3.42}$$

is the specific gas constant. Thus, the macroscopic temperature is related to the average kinetic energy of the gas molecules:

$$\frac{3}{2} k T = \overline{\mathcal{E}'_{\mathrm{tr}}} \tag{3.43}$$

Similarly, a temperature depending on internal molecular energy modes can be defined as

$$\overline{\mathcal{E}_{\mathrm{in}}} = \frac{\bar{\mathfrak{f}}}{2} k T_{\mathrm{in}} \tag{3.44}$$

with $T_{\mathrm{in}} = T$ in a molecular thermal equilibrium state. Therefore, the mass specific internal energy of the gas e is defined as

$$e = c_v T = \frac{n}{\mathfrak{m}} \left(\overline{\mathcal{E}'_{\mathrm{tr}}} + \overline{\mathcal{E}_{\mathrm{in}}} \right) = \frac{n}{\mathfrak{m}} \overline{\mathcal{E}} \tag{3.45}$$

with the isochoric heat capacity

$$c_v = \frac{3 + \bar{\mathfrak{f}}}{2} R \, . \tag{3.46}$$

Furthermore, the thermodynamic variable enthalpy

$$h = e + \frac{p}{\rho} = c_p T \tag{3.47}$$

can be defined with the isobaric heat capacity

$$c_p = \frac{5 + \bar{\mathfrak{f}}}{2} R \tag{3.48}$$

and the heat capacity ratio

$$\gamma = \frac{c_p}{c_v} = \frac{5 + \bar{\mathfrak{f}}}{3 + \bar{\mathfrak{f}}} \tag{3.49}$$

where $\bar{\mathfrak{f}}$ is the average number of degrees of freedom. As stated in Sec. 3.1, the probability of higher internal energy modes depends on the molecular energy which is related to the macroscopic temperature. Although the number of degrees of freedom $\mathfrak{f}$ is a non-negative integer for one molecule, not all molecules have the same energy level and therefore the average number on a macroscopic

scale can be seen to be a continuous function of temperature $\bar{\mathfrak{f}}(T) \in [0, \mathfrak{f}_{\max}]$, where $\mathfrak{f}_{\max}$ is the maximum number of internal degrees of freedom depending on the molecule.[144]

If an isentropic compression of the gas by the piston in Fig. 3.4 is assumed, the work $\mathcal{W}$ done is

$$\mathrm{d}\mathcal{W} = -\mathcal{F}_x \, \mathrm{d}x = -pA \, \mathrm{d}x = -p \, \mathrm{d}V = \mathrm{d}E \tag{3.50}$$

which changes the internal energy of the gas $E = \rho V e$. Combining Eqs. (3.26), (3.39) and (3.49) it is obtained that the pressure times the volume is related to the internal energy

$$pV = (\gamma - 1)E \tag{3.51}$$

and combined with Eq. (3.50) it is obtained via integration that

$$pV^{\gamma} = \text{const} \tag{3.52}$$

if the change of state is isentropic. Although energy is transferred from molecule to molecule in a reversible way, macroscopic changes in state are irreversible which is due to the large amount of molecules and intermolecular collisions. This leads to chaotic movements and the probability that the initial state is reached again tends to zero. Therefore, in macroscopic processes irreversible phenomena like friction are observed leading to heat. This macroscopic phenomenon is called entropy, which can only be reduced in a system via heat exchange.[144] Nevertheless, especially for engineering purposes the consideration of isentropic processes is important in order to determine physical limits. One macroscopic phenomenon that is often approximated by an isentropic process is the propagation speed of sound waves

$$c_{\mathrm{s}} = \sqrt{\frac{\mathrm{d}p}{\mathrm{d}\rho}} \, . \tag{3.53}$$

if a constant mass is assumed, Eq. (3.52) can also be written as

$$\frac{p}{\rho^{\gamma}} = \text{const} \tag{3.54}$$

and with the help of the ideal gas law in Eq. (3.40) the isentropic speed of sound is given by

$$c_{\mathrm{s}} = \sqrt{\gamma R T} \, . \tag{3.55}$$

3.5.2 Distribution Function

Although molecules are discrete particles carrying discrete values of mass, momentum and energy, due to their large quantity it is convenient to describe them mathematically with a distribution function

$$f(t, \boldsymbol{x}, \boldsymbol{\mathfrak{c}}) = \frac{\mathrm{d}N}{\mathrm{d}\boldsymbol{x}\mathrm{d}\boldsymbol{\mathfrak{c}}} \, . \tag{3.56}$$

Therefore, an incremental phase space element is considered, which is based on the assumption that in a small space element $\mathrm{d}\boldsymbol{x}$ there is still a large number of molecules that move with different

velocity classes $\mathfrak{c}$. The normalisation is chosen in a form that the integral over the velocity space delivers the number density n per space increment:

$$n(t,\boldsymbol{x}) = \frac{\mathrm{d}N}{\mathrm{d}\boldsymbol{x}} = \int_{\mathbb{R}^3} f(t,\boldsymbol{x},\mathfrak{c})\ \mathrm{d}\mathfrak{c} \tag{3.57}$$

With such a distribution function it is possible to calculate moments. Therefore, a molecular quantity $\mathfrak{q}$ is multiplied with the distribution function and the product is integrated over the velocity space. The result is the average molecular quantity $\overline{\mathfrak{q}}$ multiplied with the number density n giving the volume specific macroscopic quantity $q(t,\boldsymbol{x})$ at space increment $\boldsymbol{x}$ and time t[115]:

$$q(t,\boldsymbol{x}) = \int_{\mathbb{R}^3} \mathfrak{q} f(t,\boldsymbol{x},\mathfrak{c})\ \mathrm{d}\mathfrak{c} \tag{3.58}$$

Thus in accordance with Eq. (3.41) the density of the gas is given by

$$\rho = \int_{\mathbb{R}^3} \mathfrak{m} f\ \mathrm{d}\mathfrak{c}\ . \tag{3.59}$$

Similarly the integral volume specific momentum can be derived by

$$\rho\boldsymbol{u} = \int_{\mathbb{R}^3} \mathfrak{m}\mathfrak{c} f\ \mathrm{d}\mathfrak{c} = \int_{\mathbb{R}^3} \mathfrak{m}\left(\mathfrak{c}' + \boldsymbol{u}\right) f\ \mathrm{d}\mathfrak{c} \tag{3.60}$$

with $\overline{\mathfrak{c}'} = \boldsymbol{0}$ according to Eq. (3.30). The volume specific total energy is

$$\rho e_\mathrm{t} = \rho\left(e + \frac{u^2}{2}\right) = \int_{\mathbb{R}^3} \left(\mathfrak{m}\frac{\mathfrak{c}^2}{2} + \mathcal{E}_\mathrm{in}\right) f\ \mathrm{d}\mathfrak{c} = \int_{\mathbb{R}^3} \left(\mathfrak{m}\frac{\left(\mathfrak{c}' + \boldsymbol{u}\right)^2}{2} + \mathcal{E}_\mathrm{in}\right) f\ \mathrm{d}\mathfrak{c} \tag{3.61}$$

which includes the specific kinetic energy due to the macroscopic velocity $\boldsymbol{u}$ with $\overline{\mathfrak{c}'\boldsymbol{u}} = \overline{\mathfrak{c}'}\boldsymbol{u} = \boldsymbol{0}$.[115]

Similarly the respective fluxes of the macroscopic quantities can be considered. The molecular number flux in normal direction n to an arbitrary surface with surface area increment $\mathrm{d}A_\mathrm{n}$ is defined as[9]

$$\frac{\mathrm{d}\dot{N}_\mathrm{n}}{\mathrm{d}A_\mathrm{n}} = \int_{\mathbb{R}^3} \mathfrak{c}\cdot\boldsymbol{n} f\ \mathrm{d}\mathfrak{c} = \int_{\mathbb{R}^3} \mathfrak{c}_\mathrm{n} f\ \mathrm{d}\mathfrak{c}\ . \tag{3.62}$$

The momentum flux is obtained by

$$\int_{\mathbb{R}^3} \mathfrak{m}\mathfrak{c}\mathfrak{c} f\ \mathrm{d}\mathfrak{c} = \rho\boldsymbol{u}\boldsymbol{u} + \boldsymbol{P} \tag{3.63}$$

where the first term on the right hand side is the advective momentum transport with stream velocity and the second term is the pressure tensor

$$\boldsymbol{P} = \int_{\mathbb{R}^3} \mathfrak{m}\mathfrak{c}'\mathfrak{c}' f\ \mathrm{d}\mathfrak{c} \tag{3.64}$$

which is typically divided into an isotropic part related to the static pressure p and a stress tensor $\boldsymbol{\tau}$ with

$$\boldsymbol{P} = p\boldsymbol{I} - \boldsymbol{\tau} \tag{3.65}$$

where $\boldsymbol{I}$ is the unit tensor. In the same way the macroscopic energy flux is obtained with

$$\int_{\mathbb{R}^3} \left(\mathfrak{m}\frac{\mathfrak{c}^2}{2} + \mathcal{E}_{\text{in}} \right) \mathfrak{c} f \, \mathrm{d}\mathfrak{c} = \rho e_{\text{t}} \boldsymbol{u} + \boldsymbol{P} \cdot \boldsymbol{u} - \dot{\boldsymbol{q}} \tag{3.66}$$

where

$$\dot{\boldsymbol{q}} = \int_{\mathbb{R}^3} \left(\mathfrak{m}\frac{\mathfrak{c}'^2}{2} + \mathcal{E}_{\text{in}} \right) \mathfrak{c}' f \, \mathrm{d}\mathfrak{c} \tag{3.67}$$

is a kinetic expression of the heat flux vector which describes the diffusive energy flux. The first term on the right hand side is the advective energy transport due to stream velocity and the last term is the energy flux related to the pressure tensor. The derivation for gas mixtures is omitted here and can be found for example in Refs. [9, 115].

3.5.3 Boltzmann Equation

In order to describe transport phenomena on a molecular level based on the distribution function, it is convenient to describe its rate of change. Assuming thermal molecular equilibrium and neglecting chemical reactions this can be described by the Boltzmann equation in the following form[2]

$$\frac{\mathrm{d}f}{\mathrm{d}t} = \frac{\partial f}{\partial t} + \mathfrak{c} \cdot \frac{\partial f}{\partial \boldsymbol{x}} + \frac{\partial \mathfrak{c}}{\partial t} \cdot \frac{\partial f}{\partial \mathfrak{c}} = J(ff^*) \tag{3.68}$$

where the total change of the distribution function with time is referred to the local change with time plus the advection of the distribution function in space and the change of the distribution function due to the advection in velocity space by mass specific external forces $\boldsymbol{b} = \frac{\mathrm{d}\mathfrak{c}}{\partial t}$. The right hand side is the so-called collision integral, which describes the change of the distribution function due to intermolecular collisions containing an integral over the whole velocity space, which makes the equation unsolvable in its most general form[9]. Analytical solutions are possible for the free molecular flow, where no intermolecular collisions occur. Otherwise the collision integral needs to be replaced by simplified models. The widely used Bhatnagar-Gross-Krook[149] model is based on the fact that any gas tends to an equilibrium state if no external forces are applied. Therefore, during intermolecular collisions on average, molecules with a higher energy level will transfer energy to molecules with a lower energy level, thus, the distribution function f relaxes towards some equilibrium state f^0:

$$J(ff^*) \approx \nu(f^0 - f) \tag{3.69}$$

This term increases with increasing difference from the unrelaxed distribution function f to the equilibrium state f^0 and with increasing collision frequency ν. Similar to the variable hard sphere model, diffusion phenomena are represented insufficiently with this model. Therefore, in the literature extensions to this model are available, like the Shakhov[150] model or the ES-BGK[151] model which is extended to polyatomic gases in Ref. [152]. A procedure to solve the Boltzmann equation numerically in a deterministic way is presented in Refs. [78, 153] and is omitted here, as the stochastic DSMC method is used in this work, which is explained in Sec. 4.2.

3.5.4 Maxwell-Boltzmann Distribution

If the gas is in an equilibrium state, collisions do not change the distribution function and therefore the right hand side vanishes. A distribution function satisfying such a state was developed by Maxwell, which can be explained by gravitational forces in the atmosphere. On planet earth the main impact of gravity leads to an effective constant acceleration g of all molecules towards the planet's centre of mass. In the absence of other external forces, this is balanced by a pressure difference in radial direction (height z) leading to[144]:

$$\mathrm{d}p = -\mathfrak{m} g n \, \mathrm{d}z \; . \tag{3.70}$$

Combined with the ideal gas law of Eq. (3.40) the following expression is obtained

$$\frac{\mathrm{d}n}{\mathrm{d}z} = -\frac{\mathfrak{m} g n}{kT} \tag{3.71}$$

and the solution assuming isothermal conditions is found by

$$n = n_0 \exp\left(-\frac{\mathfrak{m} g z}{kT}\right) = n_0 \exp\left(-\frac{\text{potential energy of each atom}}{kT}\right) \tag{3.72}$$

where n_0 is a reference number density at an arbitrary position $z = 0$. An explanation why there are fewer molecules at higher regions in the atmosphere than on the ground, is that not all molecules contain the same kinetic energy. A molecule that reaches a potential energy on a certain height must contain the same amount of kinetic energy on the ground moving in upward direction. Therefore, the ratio of number of molecules reaching a potential energy of height z must be the same that have the kinetic energy on the ground leading to

$$\frac{n}{n_0} = \exp\left(-\frac{\mathfrak{m} g z}{kT}\right) = \exp\left(-\frac{\mathfrak{m}\mathfrak{u}^2}{2kT}\right) \tag{3.73}$$

where $\mathfrak{u} = \mathfrak{c}_z^+ > 0$ is the upward velocity needed to reach height z. With the help of Eqs. (3.62) and (3.73) and the definition $f^0 = n\mathfrak{f}$ it is obtained that the number flux reaching the plane of height z must have the following form:

$$\int_{\mathfrak{u}}^{\infty} \mathfrak{u}\mathfrak{f}(u) \, \mathrm{d}\mathfrak{u} = \text{const} \cdot \exp\left(-\frac{\mathfrak{m}\mathfrak{u}^2}{2kT}\right) \tag{3.74}$$

which can be differentiated with respect to $\mathfrak{u}$:

$$\mathfrak{f}(\mathfrak{u}) \, \mathrm{d}\mathfrak{u} = C \exp\left(-\frac{\mathfrak{m}\mathfrak{u}^2}{2kT}\right) \, \mathrm{d}\mathfrak{u} \tag{3.75}$$

With the help of Eq. (3.57) the integration term

$$C = \sqrt{\frac{\mathfrak{m}}{2\pi kT}} = \frac{1}{\sqrt{2\pi RT}} \tag{3.76}$$

is found using the condition

$$\int_{-\infty}^{\infty} \exp\left(-x^2\right) \, \mathrm{d}x = \sqrt{\pi} \; . \tag{3.77}$$

Therefore, a distribution function is derived where the kinetic energy of a molecule in one direction is related to the average kinetic energy of each degree of freedom. Using the thermal velocities of the molecules, the reference frame at rest in a local equilibrium can be used where a Gauss normal distribution similar to Eq. (3.75) is found in each direction, which is the so-called Maxwell-Boltzmann distribution[2,78,144]:

$$\mathfrak{f}(\mathfrak{c}) = \mathfrak{f}(\mathfrak{c}_x)\mathfrak{f}(\mathfrak{c}_y)\mathfrak{f}(\mathfrak{c}_z) = \left(\frac{\mathfrak{m}}{2\pi kT}\right)^{3/2} \exp\left(-\frac{\mathfrak{m}\mathfrak{c}'^2}{2kT}\right) = \left(\frac{\mathfrak{m}}{2\pi kT}\right)^{3/2} \exp\left(-\frac{\mathfrak{m}\,(\mathfrak{c}-\boldsymbol{u})^2}{2kT}\right) \tag{3.78}$$

This distribution function has the property that the average molecular velocity in each direction is zero. Nevertheless, it is very unlikely that the velocity in all directions at the same time is zero. Therefore, in order to get a distribution function for the magnitude of the molecular velocity, Eq. (3.78) can be transformed into spherical coordinates and integrated over the spherical unit surface as the magnitude does not depend on the direction. The result is

$$\mathfrak{f}(\|\mathfrak{c}'\|) = \frac{4\pi}{(2\pi RT)^{3/2}}\mathfrak{c}'^2 \exp\left(-\frac{\mathfrak{m}\mathfrak{c}'^2}{2kT}\right) \ . \tag{3.79}$$

The average molecular speed already implicitly used in Sec. 3.5.1 is calculated by

$$\overline{\mathfrak{c}'} = \int_0^\infty \mathfrak{c}'\mathfrak{f}(\mathfrak{c}')\ \mathrm{d}\mathfrak{c}' = \sqrt{\frac{8RT}{\pi}} \tag{3.80}$$

and the most probable molecular speed c_m is obtained by setting the derivative to zero[154,155]:

$$\frac{\partial \mathfrak{f}(\mathfrak{c}')}{\partial \mathfrak{c}'} = 0 \Rightarrow c_\mathrm{m} = \sqrt{2RT} \tag{3.81}$$

Comparing Eqs. (3.55) and (3.81) it is obtained that the isentropic speed of sound differs from the most probable molecular speed by the factor $\sqrt{\gamma/2}$.

3.5.5 Gas-Surface Interactions

As stated at the beginning of the chapter, everything is made of atoms which can just be in different thermodynamic states. Thus, for example, rotors or a casing consist of a large number of molecules that are kept together by intermolecular forces. So when a gas molecule collides with a surface molecule, this could just be seen as a binary collision where the surface molecule on average will keep its position and the gas molecule will be reflected back into the flow field. In order to describe this for an average state, Maxwell[67] considered two limiting cases. The simplest model states that the surface molecules are so densely arranged that a gas molecule is only reflected specularly in an elastic collision like a beam of light on a mirror, where its normal velocity is reversed and its tangential velocity is maintained. According to this model, the gas molecules would be in an equilibrium state with the surface molecules, and the resulting heat flow and shear stress on the wall would be zero and only normal stresses can be transferred. The velocity vector $\mathfrak{c}_\mathrm{r}$ of the reflected molecule is therefore

$$\mathfrak{c}_\mathrm{r} = \mathfrak{c}_\mathrm{i} - 2(\mathfrak{c}_\mathrm{i} \cdot \boldsymbol{n})\boldsymbol{n} \tag{3.82}$$

where $\mathfrak{c}_\mathrm{i}$ is the incident velocity vector of the molecule before the collision and $\boldsymbol{n}$ is the inward normal vector of the surface. This model is in contradiction with macroscopic observations which

arises from the fact that surfaces are rough on a microscopic scale compared to the molecular diameter and that the average energy of the surface molecules can differ from those of the gas molecules. The other limiting case Maxwell considered is the so-called diffuse scattering model, where the surface is again considered to be a plane from the macroscopic view, but the reflected velocity vector is defined by the local equilibrium of the wall and independent of the incident velocity vector. Therefore, the tangential velocity components $\mathfrak{c}_{\mathrm{t},1}$ and $\mathfrak{c}_{\mathrm{t},2}$ are given in accordance to Eqs. (3.78) as

$$\mathfrak{f}(\mathfrak{c}_{\mathrm{t},i}) = \frac{1}{\sqrt{2\pi R T_\mathrm{w}}} \exp\left(-\frac{\mathfrak{m}\mathfrak{c}_{\mathrm{t},i}'^2}{2kT_\mathrm{w}}\right) \tag{3.83}$$

with $i \in [1,2]$ and $\mathfrak{c}_{\mathrm{t},i}' = \mathfrak{c}_{\mathrm{t},i} - U_{\mathrm{t},i}$ where $U_{\mathrm{t},i}$ is the wall velocity in the respective tangential direction and T_w is the wall temperature. The velocity component normal to the wall is restricted to positive values with

$$\mathfrak{f}^+(\mathfrak{c}_\mathrm{n}) = \frac{1}{\sqrt{2\pi R T_\mathrm{w}}} \exp\left(-\frac{\mathfrak{m}\mathfrak{c}_\mathrm{n}'^2}{2kT_\mathrm{w}}\right) \quad \mathfrak{c}_\mathrm{n}' > 0 \tag{3.84}$$

which can be calculated using the number flux condition Eq. (3.62) and integrating over the half space for positive values of $\mathfrak{c}_\mathrm{n}' = \mathfrak{c}_\mathrm{n} - U_\mathrm{n}$, where U_n is the normal component of the wall velocity. A distribution function $\mathfrak{F}$ that only refers to positive values of $\mathfrak{f}^+(\mathfrak{c}_\mathrm{n}')$ can be defined as

$$\mathfrak{F}(\mathfrak{c}_\mathrm{n}') = C\mathfrak{c}_\mathrm{n}' \exp\left(-\frac{\mathfrak{c}_\mathrm{n}'^2}{2RT_\mathrm{w}}\right) = \frac{\mathfrak{c}_\mathrm{n}'}{RT_\mathrm{w}} \exp\left(-\frac{\mathfrak{c}_\mathrm{n}'^2}{2RT_\mathrm{w}}\right) \tag{3.85}$$

where the constant C is found using the normalisation condition

$$\int_0^\infty \mathfrak{F}(\mathfrak{c}_\mathrm{n})\, \mathrm{d}\mathfrak{c}_\mathrm{n} = 1\ . \tag{3.86}$$

Furthermore, Maxwell[67] suggested that a portion of molecules α is scattered diffusely and a portion of molecules $1-\alpha$ is specular reflected, where α is called the accommodation coefficient. Smoluchowski[117] introduced a thermal accommodation coefficient

$$\alpha_\mathrm{th}^\mathrm{SM} = \frac{\dot{q}_\mathrm{i} - \dot{q}_\mathrm{r}}{\dot{q}_\mathrm{i} - \dot{q}_\mathrm{w}} \tag{3.87}$$

where $\dot{q}_\mathrm{i}$ and $\dot{q}_\mathrm{r}$ are the energy fluxes normal to the wall of the incident and reflected molecules, while $\dot{q}_\mathrm{w}$ is the energy flux under complete diffuse conditions. By analogy accommodation coefficients α_n and α_t can be defined as normal and tangential momentum accommodation coefficients respectively:

$$\alpha_\mathrm{n} = \frac{p_\mathrm{i} - p_\mathrm{r}}{p_\mathrm{i} - p_\mathrm{w}} \quad \alpha_\mathrm{t} = \frac{\tau_\mathrm{i} - \tau_\mathrm{r}}{\tau_\mathrm{i} - \tau_\mathrm{w}} \tag{3.88}$$

According to Eq. (3.65) p and τ are the normal and tangential components of the momentum flux. For complete specular reflection all accommodation coefficients are zero and for complete diffuse scattering all accommodation coefficients are equal to one. The idea is that all accommodation coefficients can be defined through macroscopic quantities that can be measured where it is implicitly supposed that these values are independent from each other, which is not the case.[146]

Therefore, Cercignani and Lampis[156] proposed a different model where the average tangential and normal velocity components of the reflected components are prescribed. The tangential momentum accommodation coefficient is defined as

$$\alpha_\mathrm{t} = \frac{\mathfrak{c}'_{\mathrm{t,i}} - \overline{\mathfrak{c}}'_{\mathrm{t,r}}}{\mathfrak{c}'_{\mathrm{t,i}}} \tag{3.89}$$

which is equal to α_t in Eq. (3.88). The tangential momentum accommodation coefficient is defined in ranges $0 \leq \alpha_\mathrm{t} \leq 2$ where $\alpha_\mathrm{t} > 1$ refers to back scattering[127]. The energy accommodation coefficient (EAC) of the normal velocity is defined as

$$\alpha_\mathrm{th} = \frac{\mathfrak{c}'^2_{\mathrm{n,i}} - \overline{\mathfrak{c}}'^2_{\mathrm{n,r}}}{\mathfrak{c}'^2_{\mathrm{n,i}}} \ . \tag{3.90}$$

Lord[157] additionally defined accommodation coefficients for internal energy modes. For the rotational energy with angular velocity ω the accommodation coefficient reads as follows:

$$\alpha_\mathrm{rot} = \frac{\omega_\mathrm{i}^2 - \overline{\omega}_\mathrm{r}^2}{\omega_\mathrm{i}^2} \tag{3.91}$$

The model with internal energy accommodation is called Cercignani-Lampis-Lord (CLL) model and is verified with beam scattering experiments in Ref. [158].[146]

As this work is limited to isothermal considerations, the energy accommodation coefficients do not significantly impact the distribution function and by neglecting a wall movement in normal direction, the impact of the tangential momentum accommodation coefficient (TMAC) remains.[126,127]

3.6 Macroscopic Conservation Equations

The Boltzmann equation can also be used to build moments or macroscopic average values. If this is done for the conservation of mass, momentum or energy, these conservative quantities cannot be "created" nor "destroyed" in collision processes (see Sec. 3.2). Thus, on a macroscopic scale intermolecular collisions cannot act as a source or sink and the collision integral must vanish. Therefore, applying moments with the conservation of mass to the Boltzmann equation, the respective macroscopic equation is obtained using Eqs. (3.59) and (3.60):

$$\frac{\partial \rho}{\partial t} + \boldsymbol{\nabla} \cdot (\rho \boldsymbol{u}) = 0 \tag{3.92}$$

With Eqs. (3.60), (3.63) and (3.65) the macroscopic equation for the conservation of momentum is obtained by

$$\frac{\partial (\rho \boldsymbol{u})}{\partial t} + \boldsymbol{\nabla} \cdot (\rho \boldsymbol{u}\boldsymbol{u}) + \boldsymbol{\nabla} p = \boldsymbol{\nabla} \cdot \boldsymbol{\tau} + \rho \boldsymbol{b} \tag{3.93}$$

with

$$\int_{\mathbb{R}^3} \boldsymbol{b} \frac{\partial \mathfrak{m} \mathfrak{c} f}{\partial \mathfrak{c}} \, \mathrm{d}\mathfrak{c} = \rho \boldsymbol{b} \ . \tag{3.94}$$

Finally, the macroscopic equation for conservation of energy is obtained using Eqs. (3.61), and (3.66):

$$\frac{\partial (\rho e_\mathrm{t})}{\partial t} + \boldsymbol{\nabla} \cdot (\rho e_\mathrm{t} \boldsymbol{u}) = -\boldsymbol{\nabla} \cdot (p \boldsymbol{u}) + \boldsymbol{\nabla} \cdot (\boldsymbol{\tau} \cdot \boldsymbol{u}) + \boldsymbol{\nabla} \cdot \dot{\boldsymbol{q}} + \rho \boldsymbol{b} \cdot \boldsymbol{u} \tag{3.95}$$

$$\int_{\mathbb{R}^3} \boldsymbol{b} \frac{\partial \mathfrak{m} \mathfrak{c}^2 f}{2 \partial \mathfrak{c}} \, \mathrm{d}\mathfrak{c} = \rho \boldsymbol{b} \cdot \boldsymbol{u} \; . \tag{3.96}$$

The macroscopic conservation equations derived in this section are without loss of generality, because no further model equations have been introduced. As the conservation laws are in differential form, they are valid for infinitesimally small volumes. By integrating over a finite volume the integral form of the conservation equations is obtained. Furthermore, using Gauss's theorem[159] and the Leibniz-Reynolds transport theorem[160] the equations can be generalised for volumes $\Omega(t)$ that change with time. Therefore, the integral conservation equation of mass reads

$$\frac{\mathrm{d}}{\mathrm{d}t} \int_{\Omega(t)} \rho \, \mathrm{d}V + \oint_{\mathcal{S}(t)} \rho (\boldsymbol{u} - \boldsymbol{v}_{\mathcal{S}}) \cdot \boldsymbol{n} \, \mathrm{d}A = 0 \tag{3.97}$$

where $\mathcal{S}(t)$ is the surface of Ω and $\boldsymbol{v}_{\mathcal{S}}$ is the respective surface velocity with the surface outward normal vector $\boldsymbol{n}$. For a constant volume this equation reads as follows: *The change of mass with respect to time in a given volume equals the sum of the mass flow rates through the volume's surface.* For non-constant volumes the mass additionally changes due to the density times the change of volume, which equals the density times the volume swept by the surface area times the surface velocity in normal direction similar to Fig. 3.3. In the same manner the momentum equation can be written as

$$\frac{\mathrm{d}}{\mathrm{d}t} \int_{\Omega(t)} \rho \boldsymbol{u} \, \mathrm{d}V + \oint_{\mathcal{S}(t)} \rho \boldsymbol{u} (\boldsymbol{u} - \boldsymbol{v}_{\mathcal{S}}) \cdot \boldsymbol{n} \, \mathrm{d}A = - \oint_{\mathcal{S}(t)} p \boldsymbol{n} \, \mathrm{d}A + \oint_{\mathcal{S}(t)} \boldsymbol{\tau} \cdot \boldsymbol{n} \, \mathrm{d}A + \int_{\Omega(t)} \rho \boldsymbol{b} \, \mathrm{d}V \tag{3.98}$$

and the energy equation reads as follows:

$$\frac{\mathrm{d}}{\mathrm{d}t} \int_{\Omega(t)} \rho e_{\mathrm{t}} \, \mathrm{d}V + \oint_{\mathcal{S}(t)} \rho e_{\mathrm{t}} (\boldsymbol{u} - \boldsymbol{v}_{\mathcal{S}}) \cdot \boldsymbol{n} \, \mathrm{d}A = - \oint_{\mathcal{S}(t)} p (\boldsymbol{u} \cdot \boldsymbol{n}) \, \mathrm{d}A + \oint_{\mathcal{S}(t)} \boldsymbol{u} \cdot (\boldsymbol{\tau} \cdot \boldsymbol{n}) \, \mathrm{d}A + \oint_{\mathcal{S}(t)} \dot{\boldsymbol{q}} \cdot \boldsymbol{n} \, \mathrm{d}A + \int_{\Omega(t)} \rho \boldsymbol{b} \cdot \boldsymbol{u} \, \mathrm{d}V \tag{3.99}$$

This set of equations forms the basis for the numerical calculation using Computational Fluid Dynamics (CFD) explained in Sec. 4.1 and the chamber model simulation in Chap. 10.

3.6.1 Continuum Model

In the previous chapter, no limiting assumptions were made from the transfer of the Boltzmann equation to the macroscopic conservation equations. Thus, if the integral values are known, the set of equations is valid in the whole range of the gas rarefaction. This fact will be used when a simplified model is presented in order to calculate the inhomogeneous chamber states in Sec. 5.3. Nevertheless, in most cases it is necessary to solve a closure problem to determine the internal energy e, the stress tensor $\boldsymbol{\tau}$ and the heat flux vector $\dot{\boldsymbol{q}}$. As already stated in Sec. 1.2, a continuum can be assumed when the mean free path is much smaller than the characteristic length of the surrounding geometry ($\bar{l} \ll L$). With Eq. (3.32) this typically leads to large values for the collision frequency and therefore to high relaxation rates towards a molecular equilibrium. Therefore, an equipartition of energies as stated in Sec. 3.5.1 is a valid assumption for continuum flows and Eq. (3.45) can be used for the specific internal energy e as long as the fluid can be considered an ideal

gas. In order to calculate the heat flux vector, typically Fourier's law of heat conduction is used with

$$\dot{\boldsymbol{q}} = \lambda \boldsymbol{\nabla} T \tag{3.100}$$

where λ is the coefficient of heat conduction. For the stress tensor the Stokes hypothesis is typically applied where the dissipation caused by expansion or compression only via normal stresses is neglected and the remaining stresses are proportional to the macroscopic velocity gradient:

$$\boldsymbol{\tau} = \mu \left(\boldsymbol{\nabla} \boldsymbol{u} + (\boldsymbol{\nabla} \boldsymbol{u})^T - \frac{2}{3} (\boldsymbol{\nabla} \cdot \boldsymbol{u}) \right) \tag{3.101}$$

Due to balance of angular momentum the stress tensor is symmetric.[66] Thermal stresses due to large temperature gradients derived by Maxwell[161] are typically neglected. Navier was the first who described the whole system of equations needed to solve the continuum equation for fluids with the Stokes hypothesis and Fourier's law applied. Therefore, the set of equations is also called Navier-Stokes equations or Navier-Stokes-Fourier equations including Fourier's law.[71]

3.6.2 Velocity Slip and Temperature Jump

The gas-surface interactions have been described on a molecular level with respect to equilibrium conditions in Sec. 3.5.5. It is convenient to describe this for the continuum model, too. Maxwell analysed that a macroscopic velocity slip $u_\mathrm{t} - U_\mathrm{t}$ occurs between tangential flow velocity u_t and the wall velocity U_t in tangential flow direction which is proportional to the mean free path $\bar{\mathfrak{l}}$. This arises from the fact that the incident molecules and the reflected molecules are not in an equilibrium and on average collide after the distance of the mean free path $\bar{\mathfrak{l}}$. Furthermore, the non-equilibrium increases with the macroscopic velocity gradient of the tangential flow velocity normal to the wall $\frac{\partial u_\mathrm{t}}{\partial n}|_\mathrm{w}$. Additionally, a macroscopic velocity at the wall arises from a temperature gradient in tangential wall direction causing a flow from cold regions to warm regions. This effect was first named thermal transpiration by Reynolds[102] and later moreover called thermal creep[78]. Neglecting higher order temperature gradients with a wall velocity vector $\boldsymbol{U}$ in tangential flow direction, this can be written as

$$\boldsymbol{u} - \boldsymbol{U} = \frac{\sigma \ell}{\mu} \boldsymbol{S} \cdot (\boldsymbol{n} \cdot \boldsymbol{\tau}) + \frac{\sigma_\mathrm{th} \mu}{\rho T} \boldsymbol{S} \cdot \boldsymbol{\nabla} T \tag{3.102}$$

where

$$\ell = \frac{\mu c_\mathrm{m}}{p} \tag{3.103}$$

is called the equivalent free path, which is often used as it does not depend on the molecular model[78]. The tangential surface tensor

$$\boldsymbol{S} = \boldsymbol{I} - \boldsymbol{n}\boldsymbol{n} \tag{3.104}$$

removes the normal components of a vector. The slip coefficient σ depends on the molecular model and contains the ratio of the mean free path to the equivalent free path and the TMAC. Using the simplification for the mean free path of hard-sphere molecules described in Sec. 3.5.1, the equivalent free path is related to the mean free path by

$$\ell \approx \frac{2}{\sqrt{\pi}} \bar{\mathfrak{l}} \tag{3.105}$$

and the slip coefficient reads

$$\sigma = \frac{\sqrt{\pi}}{2}\frac{2-\alpha_\mathrm{t}}{\alpha_\mathrm{t}} \,. \tag{3.106}$$

The thermal slip coefficient derived by Maxwell is $\sigma_\mathrm{th} = 3/4$. Slightly different definitions for the slip coefficients based on comparisons to numerical solutions of the Boltzmann equation are provided by Sharipov[78]:

$$\sigma = \frac{1.772}{\alpha_\mathrm{t}} - 0.754 \qquad \sigma_\mathrm{th} = 1.175 \tag{3.107}$$

In analogy to the velocity slip, Smoluchowski[117] derived a temperature jump between gas temperature T and wall temperature T_w to describe the heat flow in slightly rarefied gases which can be expressed as follows:[52,162]

$$T - T_\mathrm{w} = -\zeta \ell \boldsymbol{n} \cdot \boldsymbol{\nabla} T \tag{3.108}$$

The temperature jump coefficient ζ can be defined as a function of the energy accommodation coefficient α_th as

$$\zeta = \frac{2-\alpha_\mathrm{th}}{\alpha_\mathrm{th}}\frac{\sqrt{\pi}\gamma}{(\gamma+1)Pr} \tag{3.109}$$

where

$$Pr = \frac{c_p \mu}{\lambda} \tag{3.110}$$

is the Prandtl number.

A problem already mentioned in Sec. 3.5.5 is that the macroscopic energy accommodation coefficient is not independent of the tangential momentum accommodation coefficient and rather results from a combination of those in the CL-model where an analytic formula to derive the coefficient is not found to completely close the link from the molecular model to the continuum model[2]. For complete accommodation Sharipov observed a value $\zeta = 1.954$ as best fit to numerical results of the Boltzmann equation using the CL model.[78]

3.6.3 Dimensional Analysis and Simplifications

The described models for the velocity slip and the temperature jump are valid as long as the mean free path of the molecules is much smaller than the characteristic length of a geometry. For internal flows the characteristic length is typically the closest distance between surrounding walls. In the literature this is often described by the gas rarefaction parameter that is inversely proportional to the Knudsen number Kn

$$\delta = \frac{L}{\ell} = \frac{Lp}{\mu c_\mathrm{m}} \propto \frac{1}{Kn} \tag{3.111}$$

with valid results of the continuum model for $\delta > 10$[140,141]. Nevertheless, this is a soft limit, as the accuracy also depends on the flow. For $\delta \to \infty$ the velocity slip and temperature jump tend to zero. Therefore, in most continuum applications it is assumed that the temperature and velocity of the gas at the wall equal the respective wall values. This is often assumed for $\delta > 100$ or $\delta > 1000$ depending on the tolerated error.

Further simplifications can be made on the basis of a stagnation point flow with an initial velocity u_∞ considering a spontaneous isentropic deceleration to $u_0 = 0$, which represents a physical limit

estimation. According to Truckenbrodt[163] the change in density due to such a flow can be calculated using the continuum equations and integrating in flow direction:

$$\frac{\rho_0}{\rho_\infty} = \left(1 + \frac{\gamma - 1}{2} M_\infty^2\right)^{\frac{1}{\gamma - 1}} \tag{3.112}$$

Therefore, the ideal gas law and the equation for isentropic compression is applied, where

$$M = \frac{u}{c_\mathrm{s}} = \frac{u}{\sqrt{\gamma R T}} \tag{3.113}$$

is the isentropic Mach number which represents the ratio of the macroscopic stream velocity to the isentropic speed of sound. The index ∞ refers to the initial state and 0 to the state in the stagnation point. Due to this estimation it is obtained that a change of density due to a change of velocity is small when the Mach number is small and typically the density is assumed to be constant for $Ma < 0.3$[163]. In the same way the change of temperature can be derived:

$$\frac{T_0 - T_\infty}{T_\infty} = \frac{\gamma - 1}{2} M_\infty^2 \tag{3.114}$$

Therefore, for low Mach numbers only a small difference in temperature is obtained and typically the heat exchange with walls is fast enough that the flow can be considered to be isothermal as also observed in Refs [81, 118, 164–166]. Assuming an incompressible-like flow for low Mach numbers, it is possible to estimate the forces in the macroscopic momentum equation by means of dimensionless numbers. Therefore, the dimensioned variables are replaced by variables marked with an (*) and their respective magnitudes:

$$t = \frac{t^*}{f} \quad \boldsymbol{x} = L\boldsymbol{x}^* \quad \boldsymbol{u} = u\boldsymbol{u}^* \quad p = p_\infty + (p_0 - p_\infty)p^* \quad \boldsymbol{b} = b\boldsymbol{b}^* \quad \boldsymbol{\nabla} = \frac{\boldsymbol{\nabla}^*}{L} \tag{3.115}$$

f is a frequency, L is a length scale, u the velocity magnitude, b the magnitude of the external body force. The gradient is normalised by an inverse length scale and the pressure is replaced by a normalised pressure difference. Inserting this in Eq. (3.93) with the stress tensor according to Eq. (3.101) and assuming a constant density, the following normalised momentum equation is obtained:

$$\rho u f \frac{\partial \boldsymbol{u}^*}{\partial t^*} + \frac{\rho u^2}{L}(\boldsymbol{u}^* \cdot \boldsymbol{\nabla}^*)\boldsymbol{u}^* = -\frac{p_0 - p_\infty}{L}\boldsymbol{\nabla}^* p^* + \rho b \boldsymbol{b} + \frac{\mu u}{L^2}\boldsymbol{\nabla}^{*2}\boldsymbol{u}^* \tag{3.116}$$

$$\Leftrightarrow St\frac{\partial \boldsymbol{u}^*}{\partial t^*} + (\boldsymbol{u}^* \cdot \boldsymbol{\nabla}^*)\boldsymbol{u}^* = -Eu\boldsymbol{\nabla}^* p^* + \frac{1}{Fr^2}\boldsymbol{b}^* + \frac{1}{Re}\boldsymbol{\nabla}^{*2}\boldsymbol{u}^* \tag{3.117}$$

The dimensionless numbers represent the respective force related to the advective force:

$$\text{Strouhal: } St = \frac{\text{transient force (local change of momentum)}}{\text{advective force}} = \frac{fL}{u} \tag{3.118}$$

$$\text{Euler: } Eu = \frac{\text{force due to pressure difference}}{\text{advective force}} = \frac{p_0 - p_\infty}{\rho u^2} \tag{3.119}$$

$$\text{Froude: } Fr = \frac{\text{advective force}}{\text{external force}} = \frac{u}{\sqrt{bL}} \tag{3.120}$$

$$\text{Reynolds: } Re = \frac{\text{advective force}}{\text{fluid friction}} = \frac{\rho u L}{\mu} \tag{3.121}$$

A proposal for a different definition of the Strouhal number for the transient chamber filling process of SSVPs will be given in Sec. 5.4. The Reynolds number is probably the most famous number as it estimates the ratio of advective forces to fluid friction. If the Reynolds number is high, advective forces dominate. This can lead to instabilities in the flow called turbulence where the macroscopic fluid has a chaotic appearance leading to eddies. If the Reynolds number is low, the internal fluid friction is large enough to damp these eddies and the fluid flow appears in ordered stream lines. Comparing the orders of Eqs. (3.111), (3.113) and (3.121), the Reynolds number is related to the Mach number and the gas rarefaction parameter:

$$Re = \sqrt{2\gamma}\delta M \tag{3.122}$$

Therefore, the Reynolds number is small for rarefied gases and the advective forces can often be neglected. If the advective forces are small, it is convenient to take the ratio of the Reynolds number to the square of the Froude number, to discuss the impact of external forces:

$$\frac{Re}{Fr^2} = \frac{2bL\delta}{c_m u} \tag{3.123}$$

Taking the acceleration $b = \omega^2 r = 2\pi f u$ of the centrifugal pseudo force occurring in rotating systems, the following expression is obtained:

$$\frac{Re}{Fr^2} = \sqrt{8\gamma}\pi\delta M St \tag{3.124}$$

Therefore, the ratio of centrifugal pseudo force to friction is small for rarefied gases.

4 Numerical Methods

In this chapter the main ideas of the solvers used to simulate 3D flows on the basis of the continuum model and the kinetic gas theory are presented.

4.1 Computational Fluid Dynamics (CFD)

For slightly rarefied gases, 3D simulations can be performed on the basis of the continuum model. The solver used in this work is Ansys CFX[167] where the compressible Navier-Stokes equations are solved numerically using an element based finite volume method (FVM) using a pressure-velocity coupling method. Therefore, Eqs. (3.97) - (3.99) are solved in integral form for each element while the surface integrals change the state of the finite volume by exchanging mass, momentum or energy between the different cells or the boundaries. Therefore, the fluid domain must be discretised using a computational mesh. In this section the dissretization procedure is sketched at first. Furthermore, the implementation of the Maxwell slip boundary condition for rarefied gases is explained. Ansys CFX has already been successfully used for the calculation of screw compressors[62,63] and good results have also been achieved for the calculation of gap flows[22,43]. Furthermore, good agreement with experimental results was achieved for a rarefied Couette-Poiseuille flow[53] with the help of the implemented slip boundary condition described in Sec. 4.1.2, which makes the solver well suited.

4.1.1 Discretisation

At first the fluid domain is discretised with a 3D mesh which can consist of different elements (hexahedral, tetrahedral, wedge, or pyramid). As in this work only hexahedral elements are used, the explanation is limited to those elements. The principal spatial discretisation is sketched in 2D in Fig. 4.1. The physical properties are stored in the node points or vertices of each element. The control volumes (finite volumes) are created around the vertices connecting the surrounding element and face centres. Therefore, in the 2D sketch, one hexahedral volume consists of four sectors (I, II, III and IV) and eight sectors in the 3D case. The volume integral for a property ϕ is solved for each sector by evaluating the centroid value ϕ_i times the volume V_i of the sector and summation over all sectors:

$$\int_\Omega \phi \, \mathrm{dV} \approx \sum_{i=1}^{N_\mathrm{sec}} \phi_i V_i \tag{4.1}$$

The surface integrals are approximated evaluating the property ϕ_ip at the integration points times the respective surface normal vector $\boldsymbol{A}_\mathrm{n}$ which is the unit normal vector times the surface area:

$$\int_\mathcal{S} \phi \cdot \boldsymbol{n} \, \mathrm{d}\mathcal{S} \approx \phi_\mathrm{ip} \cdot \boldsymbol{A}_\mathrm{n} \tag{4.2}$$

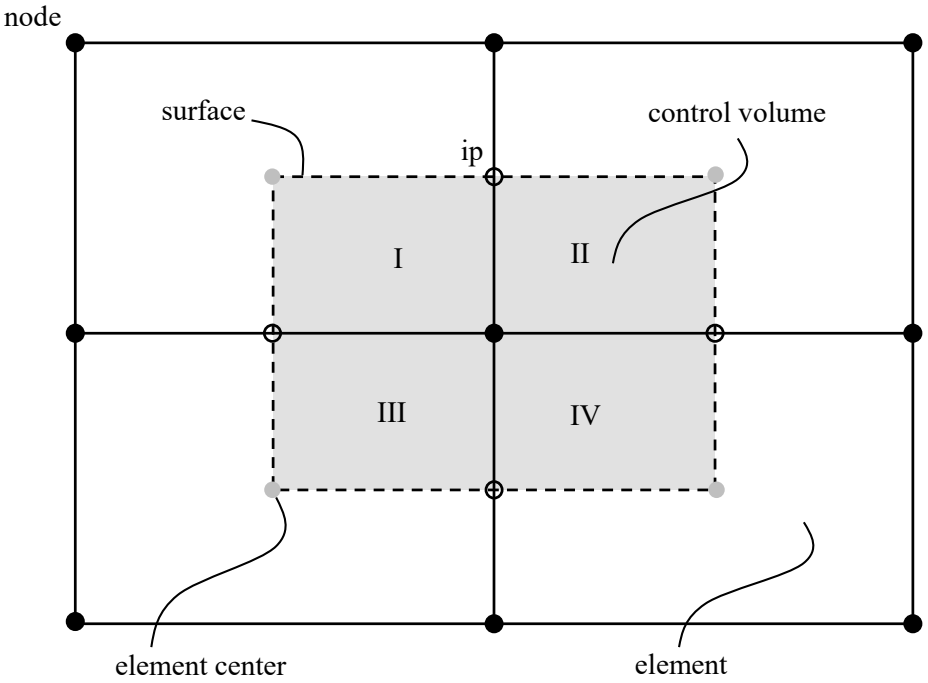

FIG. 4.1 Finite volume discretisation in Ansys CFX.

Physical and geometric properties at arbitrary positions are interpolated using shape functions, which are element specific, taking all nodal values of the element into account

$$\phi = \sum_{i=1}^{N_{\text{nodes}}} \mathcal{N}_i \phi_i \tag{4.3}$$

where $\mathcal{N}_i$ is the shape function of node i evaluated at the desired position and ϕ_i is the physical or geometric property at node point i. The local coordinates for a hexahedral element are shown in Fig. 4.2 and the corresponding shape functions read:

$$\mathcal{N}_1(\zeta,\eta,\theta) = (1-\zeta)(1-\eta)(1-\theta) \tag{4.4}$$
$$\mathcal{N}_2(\zeta,\eta,\theta) = \zeta(1-\eta)(1-\theta) \tag{4.5}$$
$$\mathcal{N}_3(\zeta,\eta,\theta) = \zeta\eta(1-\theta) \tag{4.6}$$
$$\mathcal{N}_4(\zeta,\eta,\theta) = (1-\zeta)\eta(1-\theta) \tag{4.7}$$
$$\mathcal{N}_5(\zeta,\eta,\theta) = (1-\zeta)(1-\eta)\theta \tag{4.8}$$
$$\mathcal{N}_6(\zeta,\eta,\theta) = \zeta(1-\eta)\theta \tag{4.9}$$
$$\mathcal{N}_7(\zeta,\eta,\theta) = \zeta\eta\theta \tag{4.10}$$
$$\mathcal{N}_8(\zeta,\eta,\theta) = (1-\zeta)\eta\theta \tag{4.11}$$
$$\zeta,\eta,\theta \in [0,1]$$

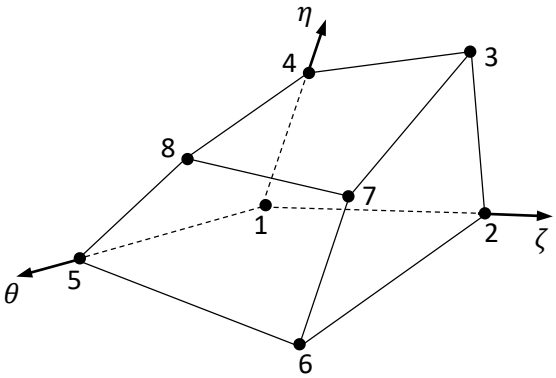

FIG. 4.2 Local coordinates of a hexahedral element.

Similarly, a surface gradient can be specified by

$$\frac{\partial \phi}{\partial \boldsymbol{x}} = \sum_{i=1}^{N_{\text{nodes}}} \frac{\partial \mathcal{N}_i}{\partial \boldsymbol{x}} \phi_i \tag{4.12}$$

using the Jacobian transformation matrix:

$$\begin{bmatrix} \frac{\partial \mathcal{N}}{\partial x} \\ \frac{\partial \mathcal{N}}{\partial y} \\ \frac{\partial \mathcal{N}}{\partial z} \end{bmatrix} = \begin{bmatrix} \frac{\partial x}{\partial \zeta} & \frac{\partial y}{\partial \zeta} & \frac{\partial z}{\partial \zeta} \\ \frac{\partial x}{\partial \eta} & \frac{\partial y}{\partial \eta} & \frac{\partial z}{\partial \eta} \\ \frac{\partial x}{\partial \theta} & \frac{\partial y}{\partial \theta} & \frac{\partial z}{\partial \theta} \end{bmatrix}^{-1} \cdot \begin{bmatrix} \frac{\partial \mathcal{N}}{\partial \zeta} \\ \frac{\partial \mathcal{N}}{\partial \eta} \\ \frac{\partial \mathcal{N}}{\partial \theta} \end{bmatrix} \tag{4.13}$$

For a gradient in a control volume the Gauss divergence theorem is used:

$$\boldsymbol{\nabla}\phi = \frac{1}{V}\sum_{\text{ip}}(\phi \cdot \boldsymbol{A}_n)_{\text{ip}} \tag{4.14}$$

Advection schemes are discretised as

$$\phi_{\text{ip}} = \phi_{\text{up}} + \beta \boldsymbol{\nabla}\phi \cdot \boldsymbol{r} \tag{4.15}$$

where ϕ_{up} is the upwind nodal value, $\boldsymbol{r}$ is the distance vector from the upwind node point to the integration point and $\beta \in [0, 1]$ is a blending factor that is solved to be as close to 1 as possible for each element without causing oscillations for high order discretisation.[167]

As time discretisation scheme for transient simulations, the 2nd order backward Euler implicit scheme is used in this work, which reads for a deformable mesh

$$\frac{\mathrm{d}}{\mathrm{d}t}\int_{\Omega}\rho\phi \ \mathrm{d}V(t) \approx \frac{1}{\Delta t}\left(\frac{3}{2}(\rho\phi V) - 2(\rho\phi V)^n + \frac{1}{2}(\rho\phi V)^{n-1}\right) \tag{4.16}$$

where n denotes the last time step. The values $(\rho\phi V)$ are evaluated using Eq. (4.1).

The conservation of mass in discretised form reads

$$\frac{1}{\Delta t}\left(\frac{3}{2}(\rho V) - 2(\rho V)^n + \frac{1}{2}(\rho V)^{n-1}\right) + \sum_{\text{ip}}\dot{m}_{\text{ip}} \tag{4.17}$$

and the surface mass flow rates in the integration points are discretised as follows using Eq. (4.2):

$$\dot{m}_{\text{ip}} = (\rho\,(\boldsymbol{u} - \boldsymbol{v}_{\mathcal{S}}) \cdot \boldsymbol{A}_n)_{\text{ip}} \tag{4.18}$$

For implicit treatment the density and the velocity vector are expanded using a Newton-Raphson linearisation within the conservation of mass

$$\rho\boldsymbol{u} \approx \rho\boldsymbol{u}^n + \rho^n\boldsymbol{u} - \rho^n\boldsymbol{u}^n \tag{4.19}$$

where the density at the current time step is replaced by the pressure using the ideal gas law:

$$\rho = \rho^n + \frac{p - p^n}{RT} \tag{4.20}$$

Similarly, the momentum and energy equation are discretised with a simplification done in the advective term of the momentum equation that reads

$$\sum_{\text{ip}}\dot{m}^n_{\text{ip}}\boldsymbol{u}_{\text{ip}} \tag{4.21}$$

and the mass flow rate here is treated explicitly to linearise the equation. Furthermore, the discretised momentum equation is rearranged, thus the implicit velocity is a function of the pressure gradient that is used to calculate the implicit treatment of the mass flow rate for the conservation of mass in Eq. (4.18) using a different discretisation on a staggered grid[167]. In Addition with Eqs. (4.19) and (4.20) the conservation of mass and the three momentum equations can be arranged as a system of fully implicit pressure-velocity coupling. The energy equation is treated decoupled and is calculated in the next step while the density is calculated using the ideal gas law. Due to the linearisation done in the momentum equation as well as the decoupled treatment of the energy equation the solution of one iteration does not fulfil the conservation laws and a loop repeating the steps described above needs to be established until the remaining error is negligible. For transient simulations the CFL number[159,160] needs to be observed with

$$\mathrm{CFL} = \frac{u\Delta t}{\Delta x} \tag{4.22}$$

where u is the magnitude of the velocity and Δx a length scale of the mesh. Although there is no hard limit as the implicit algorithm is stable for any CFL number, a large value ($\mathrm{CFL} \gg 1$) leads to a large amount of numerical diffusion and therefore to an overpredicted fluid friction. In a steady-state this effect vanishes. In Ansys CFX a steady state solution is also treated like a transient simulation using large pseudo time steps as *acceleration parameter*[167]. Therefore, both transient and steady-state simulations need to be initialised.

4.1.2 Boundary Conditions

The boundary conditions used in this work are briefly described here regarding the physical constraints.

Opening An opening allows the flow to cross the boundary in both directions. Therefore, a distinction is made. In case of an inflow the total pressure

$$p_\mathrm{t} = p\left(1 + \frac{\gamma - 1}{2} M^2\right)^{\frac{\gamma}{\gamma - 1}} \tag{4.23}$$

is prescribed, while for an outflow it is assumed to be the static pressure applying a zero gradient in normal direction for the flow velocity. The temperature is prescribed for inflow while a zero gradient condition normal to the opening is applied in case of an outflow.

Symmetry At a symmetry plane the normal velocity component is zero

$$u_n = 0 \tag{4.24}$$

as well as the gradients of scalar values in normal direction:

$$\frac{\partial \phi}{\partial \boldsymbol{n}} = \mathbf{0} \tag{4.25}$$

Wall The pressure gradient normal to the wall is set to zero:

$$\frac{\partial p}{\partial \boldsymbol{n}} = \mathbf{0} \tag{4.26}$$

For the flow velocity at the wall the Maxwell slip condition Eq. (3.102) is applied. As this boundary condition is not available in Ansys CFX, this is implemented using user defined expressions. Therefore, the predefined finite slip boundary condition is used which reads

$$\boldsymbol{u}_{\mathrm{FiniteSlip}} = U_{\mathrm{S}} \cdot \frac{\boldsymbol{\tau}_{\mathrm{t}}}{|\boldsymbol{\tau}_{\mathrm{t}}|} \left(\frac{|\boldsymbol{\tau}_{\mathrm{t}} - \tau_{\mathrm{c}}|}{\tau_{\mathrm{n}}} \right)^{m} \exp\left(\frac{-Bp}{\tau_{\mathrm{n}}} \right) \tag{4.27}$$

where U_{S} is the slip speed, $\boldsymbol{\tau}_{\mathrm{t}} = \boldsymbol{S} \cdot (\boldsymbol{n} \cdot \boldsymbol{\tau})$ is the tangential shear stress vector. $\tau_{\mathrm{n}} = 1$ Pa by default is a normalising stress, τ_{c} is a critical stress and B is a pressure coefficient. Therefore, the boundary condition is designed in generous manner. The Maxwell velocity slip boundary condition for isothermal conditions can be reproduced by setting the slip speed to

$$U_{\mathrm{S}} = \frac{\sigma \ell}{\mu} \cdot 1[\mathrm{Pa}] \tag{4.28}$$

with an exponent $m = 1$. There is no critical shear stress thus $\tau_{\mathrm{c}} = 0$ and with $B = 0$ the exponential function reduces to one. As the finite slip boundary condition depends on the shear stress, it also works for applied wall velocities.[53] As an isothermal flow is considered, the thermal slip and temperature jump conditions are omitted and the wall temperature is prescribed.

4.2 Direct Simulation Monte Carlo (DSMC) Method

For the simulation of rarefied gases in the transitional and free molecular regime the direct simulation Monte Carlo (DSMC) method is used. This method was invented by Bird[9] and is based on the kinetic theory of gases. In contradiction to deterministic methods that numerically solve the Boltzmann equation, the movement and collisions of molecules are simulated directly in a probabilistic manner. Originally he showed that he can simulate the relaxation of rigid sphere molecules towards an equilibrium state this way with good agreement to molecular dynamics (MD) methods where the collisions are calculated analytically[168]. Based on this idea, a method for the direct simulation of molecules is established that is suitable to simulate systems of rarefied gases for engineering purposes. Many problems refer to atmospheric re-entry problems of spacecraft[147,169], but internal flows in micro channels[78,165,170] or vacuum applications[12,48,171] are also widely simulated with this method. A proof that the method is not limited to rarefied gases is given by Gallis et al.[172] who simulated a turbulent flow with both the DSMC method and direct numerical simulation (DNS) based on the Navier-Stokes equations that are in good agreement.

The DSMC solver used in this work is *dsmcFoamPlus*[173], which is an extension of the open source software package *OpenFOAM*. The solver is benchmarked with several standard cases for both internal and external flows and is in good agreement with measurement results[12,169,173–177]. Due to the probabilistic approach, methods to generate random numbers are needed. There exist pseudo random number generators for equally distributed random numbers[178]. Based on this, it is possible to generate random numbers for normal distributed random numbers using the polar method[178] and random numbers for any distribution function with the acceptance-rejection method[9] which are used in the implementation.

4.2.1 Algorithm

The flow chart of the DSMC method is shown in Fig. 4.3 and shows the main steps of the algorithm. Detailed steps are explained in the following sections. The DSMC method simulates the movement of particular molecules in a physical space, but due to the probabilistic approach it is possible to reduce the number of simulated molecules significantly by introducing the factor

$$F_N = \frac{\text{number of identical molecules}}{\text{simulated particle}} \tag{4.29}$$

that assumes that there is a number of F_N real identical molecules, that perform the same action at the same time. This factor is constant for all simulated particles for the whole simulation. For the calculation of the intermolecular collisions as well as for the calculation of the macroscopic quantities, a computational mesh is required, which is generated at the beginning of the simulation depending on the geometry of the domain.

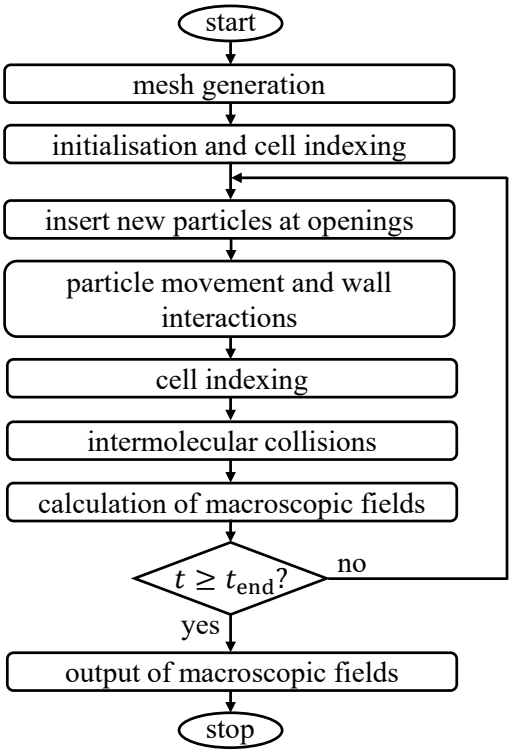

FIG. 4.3 Flow chart of the DSMC method.

The computational mesh is three dimensional and consists of discrete cells with a volume V_{cell}. For the initialisation, the gas type, pressure, temperature and stream velocity need to be specified. The number of particles per cell is then calculated using the ideal gas law by

$$N = \frac{pV_{\text{cell}}}{F_N kT} \tag{4.30}$$

and are distributed with a random 3D position within the cell. The velocity vector is calculated with random numbers according to the Maxwell-Boltzmann equilibrium condition in Eq. (3.78) using the prescribed temperature and stream velocity. Each particle is indexed to the respective cell where it is initialised. The following steps describe the repeated algorithm of the DSMC method for each discrete time step Δt. A key feature is the decoupled consideration of particle movement and intermolecular collisions. At first, new particles are inserted at the openings according to the prescribed boundary conditions. Then, the particles are moved according to their respective velocity. During this step, a particle can leave the cell that it was originally assigned to. If it enters a new cell within the domain, the new cell index is assigned. If it leaves the domain through an opening, the particle is deleted and if its trajectory intersects a wall, it receives a new velocity vector according to the respective wall interaction model. If a cyclic boundary condition is intersected, the movement is handled as a movement within the domain, but the absolute position is transferred to the connected cell. When all particles are moved, intermolecular binary collisions are performed. The collision partners are chosen in a probabilistic manner taking only particles into account that are within the respective cell which significantly reduces the computation time. This is further improved as the original cell is divided into eight sub cells where the collision partners are searched. If too few

particles are in this space the whole cell is taken into account. If collision partners are found, the collision is performed according to the chosen model where the colliding particles receive a new velocity vector according to the conservation of momentum and energy while they keep their mass. When all collisions are performed the macroscopic fields are calculated from the particle properties. If the selected end time is reached, an output is generated and the simulation stops. Otherwise, new particles are inserted through the openings and the procedure repeats.

4.2.2 Particle Movement

As particle movement and intermolecular collisions are decoupled, linear trajectories within the time step Δt are considered by neglecting body forces:

$$\boldsymbol{x}_{\text{new}} = \boldsymbol{x}_{\text{old}} + \mathfrak{c} \cdot \Delta t \tag{4.31}$$

If during the time step a wall is intersected, only a partial time step is performed until the wall is hit and the remaining movement step is performed according to the post collision velocity vector starting at the respective wall.

4.2.3 Boundary Conditions

The collisions with walls are calculated according to the respective wall interaction model described in Sec. 3.5.5. The velocity vector in normal and both tangential directions is calculated by random numbers according to the respective distribution functions. Therefore, each wall has a normal vector, a fixed temperature and a velocity vector. Furthermore, the respective TMAC and EAC needs to be prescribed when the CLL-Model is used. A symmetry plane is handled according to the specular reflection wall model.

The outflow of particles is handled during the movement step if an opening is intersected and thus the particle is deleted. At each opening, new particles must be inserted. In order to calculate the inward number flux, a local coordinate system is chosen where the molecules have the following velocity components

$$\mathfrak{c}_{\text{n}} = \mathfrak{c}'_{\text{n}} + u_{\text{n}} \tag{4.32}$$

$$\mathfrak{c}_{\text{t},1} = \mathfrak{c}'_{\text{t},1} + u_{\text{t},1} \tag{4.33}$$

$$\mathfrak{c}_{\text{t},2} = \mathfrak{c}'_{\text{t},2} + u_{\text{t},2} \tag{4.34}$$

where $\mathfrak{c}_{\text{n}}$ is the normal component of the molecular velocity vector and $\mathfrak{c}_{\text{t},1}, \mathfrak{c}_{\text{t},2}$ are two perpendicular tangential components. $u_{\text{n}}, u_{\text{t},1}, u_{\text{t},2}$ are the respective values of the stream velocity. Using Eq. (3.62), the particle flux through a surface element can be calculated:

$$\dot{N}_{\text{in}} = \frac{nA}{F_N} \int_{-\infty}^{\infty} \int_{-\infty}^{\infty} \int_{0}^{\infty} \mathfrak{c}_{\text{n}} f \, \mathrm{d}\mathfrak{c}_n \mathrm{d}\mathfrak{c}_{t,1} \mathrm{d}\mathfrak{c}_{t,2} \tag{4.35}$$

Assuming a local equilibrium condition according to Eq. (3.78) this can be solved[9] to

$$\dot{N}_{\text{in}} = \frac{n_{\text{in}} A c_{\text{m}}}{2F_N\sqrt{\pi}} \left(\exp\left(-\frac{u_{\text{n}}^2}{c_{\text{m}}^2} \right) + \frac{\sqrt{\pi} u_{\text{n}}}{c_{\text{m}}} \left(1 + \operatorname{erf}\left(\frac{u_{\text{n}}}{c_{\text{m}}} \right) \right) \right) \tag{4.36}$$

where the error function is defined as

$$\mathrm{erf}(x) = \frac{2}{\sqrt{\pi}} \int_0^x \exp\left(-\xi^2\right) \, \mathrm{d}\xi \ . \tag{4.37}$$

For a pressure driven flow, a distinction is made between an inlet boundary condition and an outlet boundary condition while for both the pressure is prescribed. The inlet boundary condition is used according to Wang and Li[179] where the pressure p_{in}, gas type and temperature T_{in} at the inlet face f are prescribed. The inlet velocity is extrapolated according to the theory of characteristics which can be found for example in Ref. [180]:

$$n_{\mathrm{in}} = \frac{p_{\mathrm{in}}}{kT_{\mathrm{in}}} \tag{4.38}$$

$$u_{\mathrm{n},f} = u_j + \frac{p_{\mathrm{in}} - p_j}{\rho_j c_{\mathrm{s},j}} \tag{4.39}$$

$$u_{\mathrm{t},1,f} = u_{\mathrm{t},1,j} \tag{4.40}$$

$$u_{\mathrm{t},2,f} = u_{\mathrm{t},2,j} \tag{4.41}$$

The values with the subscript j refer to the average cell values of the corresponding inlet face f. $c_{\mathrm{s},j}$ is the isentropic speed of sound. The outlet boundary conditions are treated similarly, according to Nance et al.[181] and Liou and Fang,[182,183]. Therefore, only the gas type and the outlet pressure need to be prescribed, while the outlet density and stream velocity are extrapolated by the theory of characteristics and the temperature is calculated with the extrapolated upwind value according to the ideal gas law leading to a zero gradient in normal direction:

$$\rho_{\mathrm{out},f} = \rho_j + \frac{p_{\mathrm{out}} - p_j}{c_{s,j}^2} \tag{4.42}$$

$$u_{\mathrm{n},f} = u_j + \frac{p_j - p_{\mathrm{out}}}{\rho_j c_{\mathrm{s},j}} \tag{4.43}$$

$$u_{\mathrm{t},1,f} = u_{\mathrm{t},1,j} \tag{4.44}$$

$$u_{\mathrm{t},2,f} = u_{\mathrm{t},2,j} \tag{4.45}$$

$$T_{\mathrm{out},f} = \frac{p_{\mathrm{out}}}{R\rho_{\mathrm{out},f}} \tag{4.46}$$

$$n_{\mathrm{out}} = \frac{p_{\mathrm{out}}}{kT_{\mathrm{out},f}} \tag{4.47}$$

These values are now used to calculate the inward number flux at the outlet to insert new particles. The velocity components of the inserted molecules are calculated according to Eqs. (4.32) - (4.34) while the thermal velocity components are calculated via random numbers fulfilling the distribution functions of Eqs. (3.83) and (3.85).

For a gas at rest ($u_{\mathrm{n}} = 0$) the number of particles leaving the domain is the same as the number joining the domain and the resulting mass flow rate from Eq. (4.36) is

$$\dot{m}_{\mathrm{eff}} = \frac{p_{\mathrm{in}} A}{c_{\mathrm{m}}\sqrt{\pi}} \tag{4.48}$$

which is called the effusion mass flow rate.

4.2.4 Binary Collisions

The calculation of intermolecular collisions within the DSMC method is restricted to binary collisions (Sec. 3.4), which is a valid assumption in a dilute gas[9]. The collision partners are chosen in a probabilistic manner within the collision cells. The probability that a collision occurs is equal to the ratio of the volume swept by the total collision cross-section times the relative particle velocity in a time step according to Fig. 3.3 to the cell volume:

$$P = \frac{\sigma_\mathrm{t} \mathfrak{c}_\mathrm{r} \Delta t}{V_\mathrm{cell}} \tag{4.49}$$

Typically, the number of collision partners equals $N_\mathrm{c} = N^2/2$ where N is the number of particles within the cell. Nevertheless, choosing all partners is inefficient due to the small probability. Therefore, the no time counter (NTC) method developed by Bird[9] is applied where the maximum probability is calculated and stored for each collision cell according to

$$P_\mathrm{max} = \frac{(\sigma_\mathrm{t} \mathfrak{c}_\mathrm{r})_\mathrm{max} \Delta t}{V_\mathrm{cell}} \tag{4.50}$$

updating the maximum value with time in each cell. On average the same number of collisions is calculated when the number of collision partners is chosen to

$$N_\mathrm{c} = \frac{N \overline{N} F_N (\sigma_\mathrm{t} \mathfrak{c}_\mathrm{r})_\mathrm{max} \Delta t}{2 V_\mathrm{cell}} \tag{4.51}$$

with the probability

$$P = \frac{\sigma_\mathrm{t} \mathfrak{c}_\mathrm{r}}{(\sigma_\mathrm{t} \mathfrak{c}_\mathrm{r})_\mathrm{max}} \tag{4.52}$$

as the value $(\sigma_\mathrm{t} \mathfrak{c}_\mathrm{r})_\mathrm{max}$ cancels out in total. For more stability one time average value for N is chosen, as the number of molecules within the collision cell fluctuates with time. Furthermore, only an integer value of collisions can be calculated while Eq. (4.51) delivers a rational number. Therefore, the rest is stored in each time step and added to the next collision partner selection step. When collision partners are chosen, the collision is performed according to the equations in Sec. 3.4 with random numbers generated for the angles χ and ε in Eq. (3.13).

4.2.5 Macroscopic Properties

As described in Sec. 3.5.1 the macroscopic properties are the average values of all molecules. These are calculated in each cell as follows:

$$n = \frac{\sum_{i=1}^{N} F_N \cdot i}{V_\mathrm{cell}} \tag{4.53}$$

$$\rho = \frac{\sum_{i=1}^{N} F_N \mathfrak{m}_i}{V_\mathrm{cell}} \tag{4.54}$$

$$\boldsymbol{u} = \frac{\sum_{i=1}^{N} \mathfrak{m}_i \mathfrak{c}_i}{\sum_{i=1}^{N} \mathfrak{m}_i} \tag{4.55}$$

$$T = \frac{\rho}{3nk} \left(\frac{F_N \sum_{i=1}^{N} \mathfrak{m}_i \mathfrak{c}_i^2}{\rho V_\mathrm{cell}} - u^2 \right) \tag{4.56}$$

$$p = nkT \tag{4.57}$$

The mass flow rate through an arbitrary plane can be calculated by the number of particles crossing this plane in each time step, while the number of N^+ particles crossing the plane in positive normal direction deliver a positive fraction of the mass flow rate, the N^- particles crossing in opposite direction deliver a negative mass flow rate:

$$\dot{m} = \frac{F_N}{\Delta t} \left(\sum_{i=1}^{N^+} \mathfrak{m}_i - \sum_{i=j}^{N^-} \mathfrak{m}_j \right) \tag{4.58}$$

4.2.6 Error Estimation

Due to the probabilistic approach of the method, the results are subject to strong statistical scatter. To reduce this scatter, averaging methods need to be applied. If transient simulations are performed, principally each time step needs to be repeated while the average state is used for the next time step, which is called ensemble averaging[9]. For stationary simulations as performed in this work a time average is established, where the macroscopic properties are calculated as an average state of many time steps. In order to estimate the error the empirical standard deviation[184,185]

$$s = \sqrt{\frac{1}{N-1} \sum_{i=1}^{N} (x_i - \bar{x})} \tag{4.59}$$

is calculated where N is the number of samples, x_i is the respective property and $\overline{x}$ is its time averaged value. Therefore, the accuracy depends on the number of time steps taken into account which can be adjusted to reach a desired accuracy. The result for the expected value can be given as

$$\hat{x} \approx \overline{x} \pm \frac{\xi s}{\sqrt{N}} \tag{4.60}$$

where the value ξ is related to the probability that the expected value lies within the interval $[\overline{x} - \xi s/\sqrt{N}, \overline{x} + \xi s/\sqrt{N}]$ and the number of samples can be used to adjust the absolute size of the interval, which decreases with the number of samples. The accuracy of the results is given as the relative deviation $((\xi s)/\sqrt{N}\overline{x})$ and ξ is chosen in such a way that the probability that the expected value does not lie within the interval is much smaller than the given accuracy of the results.

5 Working Chambers in Vacuum Spindle Pumps

In this chapter the working chambers in vacuum spindle pumps are analysed in order to derive suitable models for thermodynamic simulation. In the first section the geometry and the kinematics are discussed in order to define the system with the corresponding boundary conditions. Then, a dimensional analysis is performed regarding the influence parameters of an inhomogeneous chamber state. Finally, a one dimensional modelling approach is presented in order to calculate the inhomogeneous chamber states by means of a pressure distribution within the working chamber.[I]

5.1 Kinematics and Geometric Abstraction

In order to show why the pressure gradient occurs within the chambers it is necessary to take the kinematics into account. Fig. 5.1 shows the sketch of an unwound cylinder cut of one rotor of an SSVP, where the chamber and the profile are alternately placed along the rotor axis. The rotor lead and the piston's rotation cause a chamber to move from low pressure port to high pressure port along the rotor axis with a velocity

$$U_{\mathrm{ax}} = s \cdot f \qquad \text{with} \qquad s = 2\pi \frac{\mathrm{d}z}{\mathrm{d}\psi} \tag{5.1}$$

where f is the rotational speed and s is the rotor lead with z being the axial coordinate of the rotor and ψ the rotor's wrap angle. U_{ax} is the axial velocity of an encapsulated mass package that is carried in axial direction. Furthermore, each point on the rotor has a movement in circumferential direction

$$U_{\mathrm{circ}} = \pi \cdot D \cdot f \tag{5.2}$$

which is the absolute velocity, where D is twice the distance from the rotor axis to the considered rotor point. The relation between the absolute velocities of the rotor points due to the rotation and the movement of the mass package in axial direction can be obtained by the angle φ. Therefore, the magnitude of the relative movement U_{r} of rotor points within the chamber's fixed coordinate system can be obtained by

[I] Parts of this chapter are reproduced from "H. Pleskun, T. Jünemann, T. Bode and A. Brümmer, "Modelling of inhomogeneous chamber states in rotary positive displacement vacuum pumps," IOP Conf. Ser.: Mater. Sci. Eng. **1180**, 012009 (2021)" and "H. Pleskun, T. Jünemann and A. Brümmer, "Validation of inhomogeneous chamber states in rotary positive displacement vacuum pumps," IOP Conf. Ser.: Mater. Sci. Eng. **1267**, 012010 (2022)" and "H. Pleskun, A. Syring and A. Brümmer, "Transient chamber filling in rotary positive displacement vacuum pumps," IOP Conf. Ser.: Mater. Sci. Eng. **1267**, 012016 (2022)", with permission of IOP Publishing published under the CC BY license.[186–188]

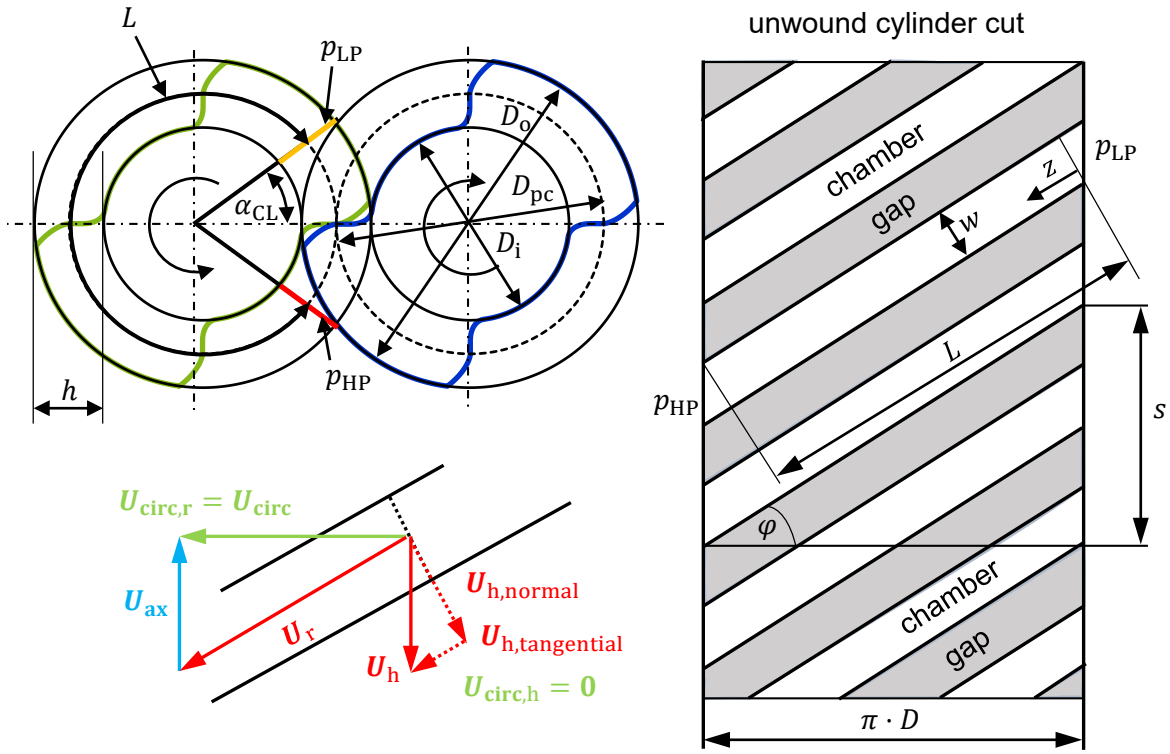

FIG. 5.1 Geometry of a two-lobed cycloid profile and boundary velocities in the relative system of screw vacuum pumps.[187]

$$U_r = \frac{\pi D \cdot f}{\cos(\varphi)} \qquad \varphi(D) = \tan^{-1}\left(\frac{s}{\pi D}\right) \qquad D_i \leq D \leq D_o \tag{5.3}$$

where D_o is the vacuum pump's outer diameter and D_i the inner diameter respectively.

The housing (h) does not move, so the housing's relative velocity $U_h = -U_{ax}$ is negative to the movement of the relative system. This can be divided into a part tangential and normal to the rotor lobe:

$$U_{h,tangential} = s \cdot f \cdot \sin(\varphi(D_o)) \tag{5.4}$$

$$U_{h,normal} = s \cdot f \cdot \cos(\varphi(D_o)) \tag{5.5}$$

In each cross section within the chamber's fixed coordinate system there are four bounding surfaces causing a Couette flow in the same direction tangential to the rotor lobe and the housing which additionally causes a flow in direction normal to the rotor lobe. Because of the chamber's encapsulation due to the other rotor and the surrounding housing, this flow is dammed up. This leads to a pressure gradient which results in a Poiseuille flow in opposite direction of the Couette flow caused by the moving boundaries.

Geometrically the chamber can be abstracted as a channel with rectangular cross section with height

$$h = \frac{D_o - D_i}{2} \tag{5.6}$$

and the mean channel width

$$w = \frac{s}{2Z} \cos\left(\varphi(D_{pc})\right) \tag{5.7}$$

which represents the linearised mean distance between two lobes where Z is the number of starts per rotor.

$$D_{\mathrm{pc}} = \frac{D_{\mathrm{o}} + D_{\mathrm{i}}}{2} \tag{5.8}$$

is the pitch circle diameter and mean value of inner and outer diameter. The chamber length is defined as

$$L = (\pi - \alpha_{\mathrm{CL}}) \cdot D_{\mathrm{pc}} \cdot \sqrt{1 + \left(\frac{s}{\pi D_{\mathrm{pc}}}\right)^2} \tag{5.9}$$

with the angle of the cut lens

$$\alpha_{\mathrm{CL}} = \tan^{-1}\left(\frac{\sqrt{D_{\mathrm{o}}^2 - D_{\mathrm{pc}}^2}}{D_{\mathrm{pc}}}\right) \quad \text{(see Fig. 5.1)} \tag{5.10}$$

This is the length of the helix at the pitch circle. The end chamber geometry is defined between the intersection lines of rotor axis and the cusps of the cut lens which is the intersection area of the outer diameters of both rotors (see the yellow and red lines in Fig. 5.1). The mean pressure in each of these intersection lines is defined as the chamber's high pressure p_{HP} and low pressure p_{LP} respectively, which is used as inlet and outlet boundary values of adjacent clearances. Thus the chamber is defined with constant cross section area for constant rotor lead s. The impact of a non-constant rotor lead on the pressure distribution within the chamber is neglected in this work.

5.2 Dimensional Analysis

The dimensional analysis is derived for the more general case of the open chamber where the chamber volume is a function of time and therefore a transient behaviour of the inhomogeneity is considered. Assuming isothermal conditions and a constant gas mixture that can be related to single gas parameters of a perfect gas, the following fourteen parameters influence the pressure distribution within an SSVP's chamber with the above geometric constraints: The specific gas constant R, the mean temperature within the chamber T, the dynamic viscosity μ, the chamber's mass averaged pressure at time t

$$p_{\mathrm{ch}}(t) = \frac{m_{\mathrm{t}}(t) \cdot R \cdot T}{V(t)} \tag{5.11}$$

where $m_{\mathrm{t}}(t)$ is the total mass of the gas within the chamber and $V(t) = A \cdot L(t)$ is the chamber's total volume at time t. Alternatively, the chamber's mid point pressure p_{ch}^* is defined, which is used for the experimental setup and for CFD simulations where the pressure in the middle of the chamber is prescribed. Furthermore, a mass flow rate $\dot{m}_{\mathrm{cl,t}}$ within the chamber due to adjacent clearances tangential to the lobe is considered. Further parameters are the rotational speed f and the geometric constraints: The rotor lead s, the outer and inner rotor diameter D_{o} and D_{i} and the number of starts Z. Two more parameters are the tangential momentum accommodation coefficients (TMAC) of the housing α_{h} and the rotor α_{r}. As these parameters describe the gas surface interaction in rarefied gases, they depend on the wall material and the gas properties and can be obtained by measurements. If the rotor is made of a different material than the housing (for example due to coating), different TMACs are needed for the respective walls in the model. This also changes if the gas is exchanged, for example if instead of air, helium or hydrogen is evacuated. The TMACs used in this work are summarized in Tab. 5.1.

TAB. 5.1 Tangential Momentum Accommodation Coefficients (TMACs) for different surface material - gas combinations used in this work. The values are taken from Refs. [116, 125, 189]

materials	H_2	N_2	air
steel	0.83	$[0.86, ..., 1.01] \approx 0.92$[II]	
brass			0.71
aluminium			0.72

According to Buckingham's theorem[190] this set of fourteen parameters leads to the following set of ten dimensionless parameters:

The pressure ratio

$$\Pi = \frac{p(z,t)}{p_{\mathrm{ch}}(t)} \quad \text{or} \quad \Pi^* = \frac{p(z,t)}{p^*_{\mathrm{ch}}(t)} \tag{5.12}$$

for an arbitrary streamwise position z within the chamber (see coordinate system in Fig. 5.1), the gas rarefaction parameter δ with the shortest channel approach as characteristic length

$$\delta = \frac{\min(h,w) \cdot p_{\mathrm{ch}}(t)}{\mu \cdot c_{\mathrm{m}}} \quad \text{or} \quad \delta^* = \frac{\min(h,w) \cdot p^*_{\mathrm{ch}}(t)}{\mu \cdot c_{\mathrm{m}}} \tag{5.13}$$

with c_{m} the molecule's most probable speed derived in Sec. 3.5.4, the speed ratio

$$u_0 = \frac{U_{\mathrm{circ,o}}}{c_{\mathrm{m}}} = \frac{\pi D_{\mathrm{o}} \cdot f}{\sqrt{2RT}} \tag{5.14}$$

the dimensionless mass flow rate

$$C_0 = \frac{\dot{m}_{\mathrm{cl,t}}}{\dot{m}_{\mathrm{eff}}} = \frac{\dot{m}_{\mathrm{cl,t}} \cdot \sqrt{\pi} c_{\mathrm{m}}}{p_{\mathrm{ch}}(t) \cdot hw} \quad \text{or} \quad C_0^* = \frac{\dot{m}_{\mathrm{cl,t}} \cdot \sqrt{\pi} c_{\mathrm{m}}}{p^*_{\mathrm{ch}}(t) \cdot hw} \tag{5.15}$$

with $\dot{m}_{\mathrm{eff}}$ the chamber's effusion mass flow rate according to Eq. (4.48) and the geometric relations

$$g_1 = \frac{D_{\mathrm{o}}}{D_{\mathrm{i}}} \quad g_2 = \frac{D_{\mathrm{o}}}{s} \quad g_3 = \frac{L(t)}{L_{\max}} \tag{5.16}$$

where $L(t)$ is the length at time t and $L_{\max}$ is the length calculated with Eq. (5.9). The last numbers are the already dimensionless number of starts Z which scales the channel width and the two TMACs α_{h} and α_{r}. For closed chambers a quasi-static assumption is made, so that the relations with respect to time vanish and therefore $g_3 = 1$ becomes a constant.

5.3 Thermodynamic Model for Closed Chambers

In order to calculate the pressure distribution within the chamber the approach of an isothermal channel flow model is adapted from the gap flow modelling in Ref. [47]. Thus, in steady state the mass flow rate $\dot{m}_{\mathrm{cl,t}}$ in a certain direction can be expressed as the sum of the mass flow rate $\dot{m}_{\mathrm{C}}$ caused by a Couette flow and the mass flow rate $\dot{m}_{\mathrm{P}}$ caused by a Poiseuille flow:

$$\dot{m}_{\mathrm{cl,t}} = \dot{m}_{\mathrm{C}} + \dot{m}_{\mathrm{P}} \tag{5.17}$$

[II] There are different values listed throughout the literature, thus, there is an uncertainty of the taken values. Therefore, an average value is taken. As no value was found for the pair steel - air, it is assumed that N_2 is similar to air.

The mass flow rate caused by a Couette flow in a rectangular channel is the sum of the mass flow rate caused by each moving wall:

$$\dot{m}_{\mathrm{C}} = \rho A \cdot \sum_{i=1}^{4} G_{\mathrm{C},i}(\delta, \eta, \alpha_{\mathrm{h}}, \alpha_{\mathrm{r}}) \cdot U_i \tag{5.18}$$

ρ is the density, $A = hw$ the cross section area, U_i is the mean velocity of the respective wall and $G_{\mathrm{C},i}$ is the reduced flow rate of the Couette flow depending on the geometric ratio $\eta = \tilde{w}^2/A$, with $\tilde{w}$ the width of the respective moving wall within the cross section.

The mass flow rate of the Poiseuille flow reads as follows

$$\dot{m}_{\mathrm{P}} = -\frac{\min(h, w) \cdot A}{c_{\mathrm{m}}} \cdot G_{\mathrm{P}}(\delta, \eta, \alpha_{\mathrm{h}}, \alpha_{\mathrm{r}}) \cdot \frac{\partial p}{\partial z} \tag{5.19}$$

and is related to the pressure gradient in flow direction (in this case the tangential lobe direction, see the local coordinate system in Fig. 5.1). The dimensionless flow rates G_{C} and G_{P} for the Couette and Poiseuille flow respectively form a closure problem, which is solved in Chap. 6. A pressure gradient in radial direction is not expected, as centrifugal forces are negligible in rarefied gases as shown in Sec. 3.6.3. This is validated in Chap. 7.

Inserting Eqs. (5.18) and (5.19) in Eq. (5.17) leads to a differential equation in tangential lobe direction which is solved by a 5th order Dormand-Prince-Method with adaptive step size with an accuracy of 10^{-9} from the boost library[191]:

$$\frac{\partial p}{\partial z} = \frac{2}{G_{\mathrm{P}} \min(h, w) c_{\mathrm{m}}} \left(p \sum_{i=1}^{4} G_{\mathrm{C},i} \cdot U_i - \frac{\dot{m}_{\mathrm{cl,t}} RT}{hw} \right) \tag{5.20}$$

Using the dimensionless numbers of Sec. 5.2 Eq. (5.20) can be normalised as follows:

$$\mathcal{P} = \frac{L}{p}\frac{\partial p}{\partial z} = \frac{L}{\min(h, w) G_{\mathrm{P}}} \left(\frac{2 \sum_{i=1}^{4} G_{\mathrm{C},i} U_i}{c_{\mathrm{m}}} - \frac{C_0}{\sqrt{\pi}} \right) \tag{5.21}$$

If the mass averaged pressure within the chamber is known, a bisection method is used to find the low pressure in a way that the resulting pressure distribution conserves the mass within the chamber under isothermal conditions

$$m_{\mathrm{1D}} = \frac{A}{RT} \int_0^L p \, \mathrm{d}z \approx \frac{A}{RT} \sum_{j=1}^{N} \bar{p}_j \Delta z_j \tag{5.22}$$

where the trapezoidal rule is used. Δz_j is the step size between two pressure values p_j and p_{j+1} of the discretized differential Eq. (5.20) with variable step size and $\bar{p}_j = (p_j + p_{j+1})/2$ is the average pressure value in this increment. As the trapezoidal method is exact for linear curves and the step size is calculated adaptively to provide small step sizes in case of non linear curves, the error provided by this method is negligible. If the pressure p^*_{ch} in the middle of the chamber is known, Eq. (5.20) can be solved starting in the middle of the chamber once with a positive sign to find the high pressure and once with a negative sign to find the low pressure. Therefore, no bisection method is needed.

For a further simplified model where the differential equation is not solved, one can consider that the pressure ratio $\Pi(z,t)$ at a certain time and position in Eq. (5.12) is a function of the normalised pressure gradient of Eq. (5.21):

$$\Pi = f(\mathcal{P}) \tag{5.23}$$

This will be shown in Sec. 7.3.

5.4 Strouhal Number for Open Chambers

In order to characterise the transient states within the chamber filling process, it is useful to estimate the inertial forces within the chamber:

$$F = \frac{\mathrm{d}(m \cdot v)}{\mathrm{d}t} \approx \pi D_{\mathrm{pc}} f \left(V \frac{\partial \rho}{\partial t} + \rho \frac{\partial V}{\partial t} \right) = \pi D_{\mathrm{pc}} f A \rho \left(\frac{L}{\rho} \frac{\partial \rho}{\partial t} + \frac{\partial L}{\partial t} \right) \tag{5.24}$$

As the chamber grows with an average constant velocity

$$v = \pi D_{\mathrm{pc}} f \tag{5.25}$$

the derivative $\partial v / \partial t \approx 0$. The mass $m = \rho V$ within the chamber is the mean density times the chamber volume with a constant cross section area $A = hw$. Neglecting the rotor lead, the length of the chamber grows with a linear function and therefore

$$\frac{\partial L}{\partial t} = \pi D_{\mathrm{pc}} f = v \tag{5.26}$$

is a constant and the second term in Eq. (5.24) becomes

$$F_{\mathrm{advective}} = \rho A v^2 \tag{5.27}$$

which resembles the estimation of advective forces, while the first term is the transient part which can be extended as follows under isothermal conditions:

$$F_{\mathrm{transient}} = \rho v A \frac{L}{\rho} \frac{\partial \rho}{\partial t} = \rho v A \frac{L}{p} \frac{\partial p}{\partial t} = \rho v A \frac{L}{p} \left(\frac{\partial p}{\cancel{\partial x}} \underbrace{\frac{\cancel{\partial x}}{\partial t}}_{\approx 0} + \frac{\partial p}{\cancel{\partial y}} \underbrace{\frac{\cancel{\partial y}}{\partial t}}_{\approx 0} + \frac{\partial p}{\partial z} \frac{\partial z}{\partial t} \right) = \rho A v^2 \frac{L}{p} \frac{\partial p}{\partial z} \tag{5.28}$$

This is justified by the estimation of negligible centrifugal force. Therefore, a parameter resembling a compressible Strouhal number St is obtained through the relation of the first term to the second term

$$St = \frac{F_{\mathrm{transient}}}{F_{\mathrm{advective}}} = \frac{L}{p} \frac{\partial p}{\partial z} = \mathcal{P} \tag{5.29}$$

which can be expressed by a normalised pressure gradient at the chamber's center of mass. In Chap. 9 it will be shown that if the Strouhal number Eq. (5.29) is evaluated with the chamber's average pressure p_{ch} using Eq. (5.21), an expression for Eq. (5.23) can be found without solving a differential equation.

6 Reduced Flow Rates

In order to solve the differential equation formulated in Eq. (5.20) in Chap. 5, the reduced flow rates of the Couette flow and the Poiseuille flow need to be known as a function of the channel shape, the gas rarefaction parameter and TMACs of the surrounding walls. This closure problem is solved in this chapter by means of analytical solutions while simplifying modelling approaches are validated with numerical simulations by means of the DSMC method. The results are provided in a general dimensionless form so that they can be adapted for different flow problems. Therefore the application limits are discussed at the end of the chapter. The TMACs in this chapter are only represented as α and further indices refer to the position of the walls.[I]

6.1 Poiseuille Flow

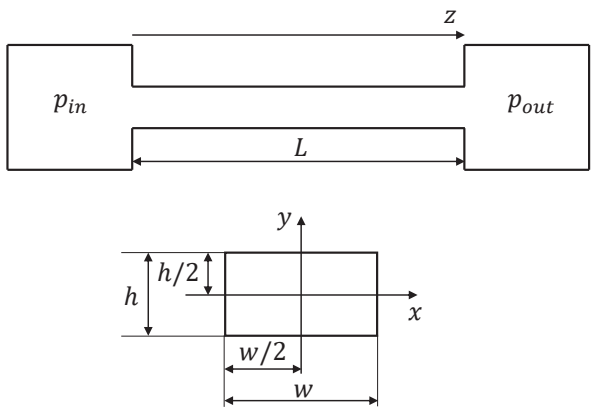

FIG. 6.1 Sketch of the channel between two constant pressure tanks and cross sectional view.[193]

At first the flow rate for the Poiseuille flow is calculated. According to Fig. 6.1 a channel between two tanks of constant pressure $p_{\text{in}} > p_{\text{out}}$ is considered. The cross section in flow direction is constant with

$$\eta = \frac{w}{h} \geq 1 \tag{6.1}$$

and $w \ll L$ so that channel end effects can be neglected. L is the channel length. The flow is considered to be isothermal and the opposite walls are restricted to have the same TMAC thus symmetry planes normal to the x and y direction in the middle of the cross section can be applied. Arkilic[118] showed that a small component of the velocity transverse to the cross section can occur which can be explained by the change of the shape of the velocity profile due to the change of the local density and gas rarefaction. He also showed that this transversal velocity component is about five decades lower than the velocity in flow direction and is therefore neglected in this work. Furthermore, a temperature drop due to flow acceleration as shown in Refs. [166, 194, 195] is neglected as low Mach numbers and low Reynolds numbers are assumed, which leads to a constant pressure within a cross section ($\partial p/\partial x = \partial p/\partial y \approx 0$).

[I] Parts of this chapter are reproduced from "H. Pleskun and A. Brümmer, "Gas-surface interactions of a Couette-Poiseuille flow in a rectangular channel," Phys. Fluids 34(8), 082009 (2022)" and "H. Pleskun, T. Bode, and A. Brümmer, "Couette flow in a rectangular channel in the whole range of the gas rarefaction," Phys. Fluids 34(3), 032004 (2022)", with the permission of AIP Publishing.[192,193]

6.1.1 Slip Regime

Rectangular Channel In this section the reduced mass flow rate for the slip regime is calculated for opposite walls having the same TMAC in a steady-state.[II]

In the continuum regime such a flow can be formulated with the help of the Navier-Stokes equations explained in Sec. 3.6.1, which are with the above made restrictions at low Reynolds numbers reduced to the Poisson equation where u is the macroscopic velocity component in flow direction:

$$\frac{\partial^2 u}{\partial x^2} + \frac{\partial^2 u}{\partial y^2} = \frac{1}{\mu}\frac{\partial p}{\partial z} = P(z) \tag{6.2}$$

With the help of the symmetry planes and the definition of the velocity slip defined in Eq. (3.102) and the slip coefficient in Eq. (3.106) the boundary conditions for such a flow under isothermal conditions read (upper right quadrant of Fig. 6.1):

$$\frac{\partial u}{\partial x}(0, y) = 0 \tag{6.3}$$

$$u(w/2, y) = -\sigma_{\mathrm{v}}\ell\frac{\partial u}{\partial x}(w/2, y) \tag{6.4}$$

$$\frac{\partial u}{\partial y}(x, 0) = 0 \tag{6.5}$$

$$u(x, h/2) = -\sigma_{\mathrm{h}}\ell\frac{\partial u}{\partial y}(x, h/2) \tag{6.6}$$

The index v refers to vertical walls and h to horizontal walls. The boundary value problem for the velocity field in flow direction can be solved with separating the variables and therefore the shape of the solution looks as follows:

$$u(x, y) = \sum_{n=0}^{\infty} g_n(x) f_n(y) \tag{6.7}$$

Furthermore, the right hand side of Eq. (6.2) can be expanded by a series

$$P(z) = \sum_{n=0}^{\infty} s_n f_n(y) \tag{6.8}$$

and therefore the separated Poisson equation looks as follows

$$\frac{\partial^2 g_n(x)}{\partial x^2} f_n(y) + \frac{\partial^2 f_n(y)}{\partial y^2} g_n(x) = s_n f_n(y) \tag{6.9}$$

$$\Leftrightarrow \quad \frac{1}{g_n(x)}\left(\frac{\partial^2 g_n(x)}{\partial x^2} - s_n\right) = -\frac{1}{f_n(y)}\frac{\partial^2 f_n(y)}{\partial y^2} = \nu_n^2$$

where ν_n^2 are separation constants and define the equation's eigenvalues.

A non trivial homogeneous solution of $f_n(y)$ is found by

$$f_n(y) = a_n \cos(\nu_n y) + b_n \sin(\nu_n y)\,. \tag{6.10}$$

[II] The procedure is quite similar to a combination presented in Refs. [85, 89], but they refer to equal TMACs of all walls.

Using boundary conditions of Eq. (6.5) this reduces to:

$$f_n(y) = a_n \cos(\nu_n y) \tag{6.11}$$

With Eq. (6.6) an implicit expression to calculate the eigenvalues is found

$$\cot(\beta_n) = \varepsilon_\mathrm{h} \beta_n \tag{6.12}$$

with the definitions:

$$\beta_n = \nu_n h/2 \tag{6.13}$$

$$\varepsilon_\mathrm{h} = \frac{2\sigma_\mathrm{h}}{\delta} \tag{6.14}$$

Now the coefficients s_n of the series Eq. (6.8) can be calculated according to Ref. [196]:

$$s_n = \int_0^{h/2} P(z) f_n(y)\,\mathrm{d}y = \frac{2P(z)a_n \sin(\beta_n)}{\beta_n} \tag{6.15}$$

The differential equation for $g_n(x)$ can be derived from Eq. (6.9)

$$\frac{\partial^2 g_n(x)}{\partial x^2} - \nu_n^2 g_n(x) - s_n = 0 \tag{6.16}$$

where the homogeneous solution is the sum of two exponential functions and the inhomogeneous term includes a constant trivial solution which leads to

$$g_n(x) = A_n \mathrm{e}^{\nu_n x} + B_n \mathrm{e}^{-\nu_n x} - s_n/\nu_n^2\,. \tag{6.17}$$

Using boundary conditions of Eqs. (6.3) and (6.4), it is found that $A_n = B_n$ and

$$A_n = \frac{s_n h^2}{8\beta_n^2}\left[\cosh\left(\beta_n \frac{w}{h}\right) + \frac{2\sigma_\mathrm{v}\beta_n}{\delta}\sinh\left(\beta_n \frac{w}{h}\right)\right]^{-1}. \tag{6.18}$$

Inserting Eqs. (6.11), (6.15) and (6.17) in Eq. (6.9), it is found that $f_n(y)$ needs to be normalised, thus

$$||f_n(y)|| = \sqrt{\int_0^{h/2} \left(f_n(y)\right)^2\,\mathrm{d}y} = 1 \tag{6.19}$$

holds. By doing this, the coefficients a_n are found:

$$a_n = \frac{2\sqrt{2\beta_n/h}}{\sqrt{2\beta_n + 2\sin(2\beta_n)}} \tag{6.20}$$

Then putting Eqs. (6.11), (6.15), (6.17) and (6.20) in Eq. (6.7) delivers

$$u(x,y) = \frac{h^2}{\mu}\frac{\partial p}{\partial z}\sum_{n=0}^{\infty}\phi_n(x,y) \tag{6.21}$$

with

$$\phi_n(x,y) = \frac{\sin(\beta_n)\cos(2\beta_n y/h)}{\beta_n^2(2\beta_n + \sin(2\beta_n))} \times \left(\frac{\cosh(2\beta_n x/h)}{\cosh(\beta_n w/h) + \beta_n \varepsilon_\mathrm{v}\sinh(\beta_n w/h)} - 1\right) \tag{6.22}$$

and the parameter

$$\varepsilon_\mathrm{v} = \frac{2\sigma_\mathrm{v}}{\delta}, \qquad \varepsilon_\mathrm{v} \ll 1 \tag{6.23}$$

which is assumed to be small.

The mass flow rate is calculated as

$$\dot{m} = 4\rho \int_0^{h/2} \int_0^{w/2} u(x,y)\,\mathrm{d}x\mathrm{d}y \tag{6.24}$$

with the normalisation

$$G_\mathrm{P} = -\frac{\dot{m} c_\mathrm{m}}{hA} \left(\frac{\partial p}{\partial z}\right)^{-1} \tag{6.25}$$

$$= -\frac{8\delta}{wh} \sum_{n=0}^{\infty} \int_0^{h/2} \int_0^{w/2} \phi_n \,\mathrm{d}x\mathrm{d}y\,. \tag{6.26}$$

Before the integral is solved, the slip coefficients are separated by a linear Taylor series expansion for the small parameters ε_h and ε_v with

$$(\phi_n) \approx (\phi_n)_0 + \varepsilon_\mathrm{h} \left(\frac{\partial \phi_n}{\partial \beta_n} \frac{\partial \beta_n}{\partial \varepsilon_\mathrm{h}}\right)_0 + \varepsilon_\mathrm{v} \left(\frac{\partial \phi_n}{\partial \varepsilon_\mathrm{v}}\right)_0 \tag{6.27}$$

where the index 0 stands for the evaluation of the term at $\varepsilon_\mathrm{h} = \varepsilon_\mathrm{v} = 0$. Using the expressions

$$(\beta_n)_0 = \frac{\pi}{2}(2n+1) \tag{6.28}$$

$$\left(\frac{\partial \beta_n}{\partial \varepsilon_\mathrm{h}}\right)_0 = -\frac{\pi}{2}(2n+1) \tag{6.29}$$

$$k_n = \pi(2n+1)\,, \quad \omega_n = \frac{\pi w}{2h}(2n+1) \tag{6.30}$$

$$(\varphi_n)_0 = \left(\frac{\partial \phi_n}{\partial \beta_n} \frac{\partial \beta_n}{\partial \varepsilon_\mathrm{h}}\right)_0 \tag{6.31}$$

$$(\psi_n)_0 = \left(\frac{\partial \phi_n}{\partial \varepsilon_\mathrm{v}}\right)_0 \tag{6.32}$$

$$\sin(\beta_n)_0 = (-1)^{n+1}\,, \quad \cos(\beta_n)_0 = 0 \tag{6.33}$$

$$\sin(2\beta_n)_0 = 0\,, \quad \cos(2\beta_n)_0 = -1 \tag{6.34}$$

one obtains

$$(\phi_n)_0 = \frac{4(-1)^{n+1}\cos(k_n y/h)}{k_n^3} \left(\frac{\cosh(k_n x/h)}{\cosh(\omega_n)} - 1\right) \tag{6.35}$$

$$(\varphi_n)_0 = \frac{4(-1)^{n+1}}{k_n^2 \cosh(\omega_n)} \left(\cosh\left(\frac{k_n x}{h}\right) - \cosh(\omega_n)\right)$$
$$\times \left(\frac{y}{h}\sin\left(\frac{k_n y}{h}\right) + \frac{2\cos\left(\frac{k_n y}{h}\right)}{k_n}\right) - \frac{2(-1)^{n+1}\cos(k_n y/h)}{h k_n^2 \cosh(\omega_n)} \tag{6.36}$$
$$\times \left(2x\sinh(k_n x/h) - w\cosh(k_n x/h)\tanh(\omega_n)\right)$$

$$(\psi_n)_0 = -\frac{2(-1)^{n+1}\tanh(\omega_n)}{\cosh(\omega_n)} \cos\left(\frac{k_n y}{h}\right) \cosh\left(\frac{k_n x}{h}\right) \tag{6.37}$$

and the integrals

$$\int_0^{h/2}\int_0^{w/2} (\phi_n)_0 \,\mathrm{d}x\mathrm{d}y = \frac{4h^2\tanh(\omega_n)}{k_n^5} - \frac{2hw}{k_n^4} \tag{6.38}$$

$$\int_0^{h/2}\int_0^{w/2} (\varphi_n)_0 \,\mathrm{d}x\mathrm{d}y = \frac{16h^2\tanh(\omega_n)}{k_n^5} - \frac{8hw}{k_n^4} + \frac{2hw\tanh^2(\omega_n)}{k_n^4} \tag{6.39}$$

$$\int_0^{h/2}\int_0^{w/2} (\psi_n)_0 \,\mathrm{d}x\mathrm{d}y = -\frac{2h^2}{k_n^4}\tanh^2(\omega_n) \tag{6.40}$$

with the exact solution

$$\sum_{n=0}^{\infty}\frac{1}{k_n^4} = \frac{1}{96}\,. \tag{6.41}$$

Now inserting Eqs. (6.38) - (6.40) in Eqs. (6.27) and (6.26) with the use of Eqs. (6.14), (6.23) and (6.41) one obtains the slip solution of the Poiseuille flow in a rectangular channel where the wall material of the opposite walls is equal:

$$G_\mathrm{P} = \frac{\delta}{6}H + \sigma_\mathrm{h}S + \sigma_\mathrm{v}T \tag{6.42}$$

The shape factors are:

$$H = 1 - 192\frac{h}{w}\sum_{n=0}^{\infty}\frac{\tanh(\omega_n)}{k_n^5} \tag{6.43}$$

$$S = \frac{4}{3}H - 32J \tag{6.44}$$

$$T = 32\frac{h}{w}J \tag{6.45}$$

$$J = \sum_{n=0}^{\infty}\frac{\tanh^2(\omega_n)}{k_n^4} \tag{6.46}$$

Eq. (6.43) is the well-known solution for the hydrodynamic regime, which can be found in similar form for example in Refs. [72, 87, 89][III]. The coefficient S is the shape factor for the Poiseuille flow of the longer walls, while the coefficient T is the shape factor of the Poiseuille flow of the shorter walls in the rectangular channel. If all wall materials are equal, $\sigma_\mathrm{h} = \sigma_\mathrm{v} = \sigma$ holds and $\sigma(S+T)$ should be the same result as the slip solution of equation 12 in Ref. [89][IV].

As Eq. (6.42) is already linearised due to the Taylor expansion, the superposition principle applies. Therefore, the symmetry of the channel implies that the shape factor S for the slip of the horizontal walls is affected by half of the slip of the top wall (t) and half of the bottom wall (b). The same applies for the shape factor T for the slip of the vertical walls which is affected by half of the left

[III] There is a mistake in Fig. 3-9 of Ref. [72], as width and height are exchanged.

[IV] They forgot the square of the last tangens hyperbolicus term. However, the square was present in their previous paper in Ref. [85] and can similarly be found in Ref. [197].

wall (l) and half of the right wall (r). Therefore, the reduced mass flow rate G_P in the slip regime for each wall having a different TMAC α can be calculated by

$$G_\mathrm{P} = \frac{\delta}{6}H + \frac{\sigma_\mathrm{t}+\sigma_\mathrm{b}}{2}S + \frac{\sigma_\mathrm{l}+\sigma_\mathrm{r}}{2}T \tag{6.47}$$

where σ_i with $i \in [\mathrm{t}, \mathrm{b}, \mathrm{l}, \mathrm{r}]$ is the slip coefficient of the certain wall.

Plane Channel The flow between two parallel plates made of different materials can be considered without linearisation. Therefore, the Poisson equation reduces to

$$\frac{\partial^2 u}{\partial y^2} = \frac{1}{\mu}\frac{\partial p}{\partial z} \tag{6.48}$$

and the boundary conditions

$$u(-h/2) = \sigma_\mathrm{b}\ell\frac{\partial u}{\partial y}(-h/2) \tag{6.49}$$

$$u(h/2) = \sigma_\mathrm{t}\ell\frac{\partial u}{\partial y}(h/2) \tag{6.50}$$

can be applied with σ_b and σ_t being the slip coefficient of the bottom (b) and top (t) plate.

The corresponding velocity profile reads

$$u(y) = -\frac{h^2}{2\mu}\frac{\partial p}{\partial z}\left[\frac{1}{4} - \left(\frac{y}{h}\right)^2 + \frac{\sigma_\mathrm{b}}{\delta} + \frac{\sigma_\mathrm{b}+\sigma_\mathrm{t}}{\sigma_\mathrm{b}+\sigma_\mathrm{t}+\delta}\left(\frac{y}{h} + \frac{\sigma_b h}{\delta} + \frac{h}{2}\right)\right] \tag{6.51}$$

and the mass flow rate per channel width is calculated by

$$\frac{\dot{m}}{w} = \rho \int_{-h/2}^{h/2} u(y)\,\mathrm{d}y\,. \tag{6.52}$$

Applying the normalisation of Eq. (6.25), the reduced flow rate for the flow between parallel plates of different wall materials in the slip regime is obtained:

$$G_\mathrm{P} = \frac{\delta}{6} + \frac{2\sigma_\mathrm{b}\sigma_\mathrm{t}}{\sigma_\mathrm{b}+\sigma_\mathrm{t}} + \frac{\delta(\sigma_\mathrm{b}-\sigma_\mathrm{t})^2}{2(\sigma_\mathrm{b}+\sigma_\mathrm{t})(\sigma_\mathrm{b}+\sigma_\mathrm{t}+\delta)} \tag{6.53}$$

For small differences of the slip coefficients, the last term in Eq. (6.53) can be neglected.

In case that the top and bottom plate have equal slip coefficients ($\sigma_\mathrm{b} = \sigma_\mathrm{t} = \sigma$), Eq. (6.53) reduces to the well-known solution

$$G_\mathrm{P} = \frac{\delta}{6} + \sigma \tag{6.54}$$

which can be found for example in Ref. [78].

Pipe Flow For later validations, the flow through a pipe of radius R is derived, too. Therefore, the Poisson equation can be solved with cylindrical coordinates using $r = \sqrt{x^2+y^2}$:

$$\frac{1}{r}\frac{\partial}{\partial r}\left(r\frac{\partial u}{\partial r}\right) = \frac{1}{\mu}\frac{\partial p}{\partial z} \tag{6.55}$$

With the boundary conditions

$$\frac{\partial u}{\partial r}(0) = 0 \tag{6.56}$$

$$u(R) = -\sigma\ell\frac{\partial u}{\partial r}(R) \tag{6.57}$$

the velocity field is found to be

$$u(r) = -\frac{R^2}{4\mu}\frac{\partial p}{\partial z}\left(1 + \frac{2\sigma}{\delta} - \frac{r^2}{R^2}\right) \tag{6.58}$$

and the mass flow rate reads

$$\dot{m} = \rho\int_0^R\int_0^{2\pi} ru(r)\,\mathrm{d}\varphi\mathrm{d}r = -\frac{\rho\pi R^4}{2\mu}\frac{\partial p}{\partial z}\left(\frac{1}{4} + \frac{\sigma}{\delta}\right). \tag{6.59}$$

Using Eq. (6.25) the reduced flow rate can be calculated

$$G_\mathrm{P} = \frac{\delta}{4} + \sigma \tag{6.60}$$

and is similarly found in Refs. [67, 127, 153]. In Eq. (6.60) the gas rarefaction parameter is calculated by $\delta = R/\ell$.

6.1.2 Transitional Regime

Rectangular Channel The slip solution is not valid for small gas rarefaction parameters, so typically numerical solutions of the Boltzmann equation or DSMC simulations are used to create tabulated data for different cross section ratios and gas rarefaction parameters. In the past this was done for fully diffuse scattered molecules in a rectangular channel, for example in Refs. [87, 88] or for the plane Poiseuille flow with different TMACs in Refs. [198, 199]. However, any variation of the TMAC would require a completely new set of simulations even if all walls had equal TMACs. This is an immense cost of computation time. Now a different approach is proposed in order to reuse the currently available data of the fully diffuse channel. To achieve this, the assumption is made that the wall slip caused by the TMAC is independent of the gas rarefaction and therefore causes a constant offset from the given diffuse solution. So if we consider the reduced flow rate as a function of the gas rarefaction δ, the cross section ratio η and the four TMACs α_t, α_b, α_l and α_r of the four walls similar to the slip solution in Eq. (6.47) we obtain

$$G_\mathrm{P} = G_\mathrm{P,U}(\delta,\eta) + \frac{\sigma_\mathrm{t}+\sigma_\mathrm{b}}{2}S(\eta) + \frac{\sigma_\mathrm{l}+\sigma_\mathrm{r}}{2}T(\eta) \tag{6.61}$$

where the coefficient $G_\mathrm{P,U}$ is an unknown. If now the reduced flow rate of the well-known fully diffuse walls is evaluated, Eq. (6.61) reads

$$G_\mathrm{P,d}(\delta,\eta) = G_\mathrm{P,U}(\delta,\eta) + \sigma_\mathrm{d}S(\eta) + \sigma_\mathrm{d}T(\eta) \tag{6.62}$$

$$\Leftrightarrow G_\mathrm{P,U}(\delta,\eta) = G_\mathrm{P,d}(\delta,\eta) - \sigma_\mathrm{d}S(\eta) - \sigma_\mathrm{d}T(\eta) \tag{6.63}$$

where $\sigma_\mathrm{d} = \sigma(1)$ is the slip coefficient for a diffuse wall scattering and the reduced flow rates $G_\mathrm{P,d}(\delta, \eta)$ for the diffuse wall scattering can be taken from the above mentioned papers as tabulated data. Inserting Eq. (6.63) in Eq. (6.61) the approximation

$$G_\mathrm{P} \approx G_\mathrm{P,d} + \left(\frac{\sigma_\mathrm{t} + \sigma_\mathrm{b}}{2} - \sigma_\mathrm{d}\right) S + \left(\frac{\sigma_\mathrm{l} + \sigma_\mathrm{r}}{2} - \sigma_\mathrm{d}\right) T \tag{6.64}$$

is obtained, which can be used for any TMAC combination and any gas rarefaction parameter δ and cross section ratio η, where the diffuse solution is known and where the slip solution provides valid results. This might not be true for very small TMACs as due to the linear Taylor series expansion in Eq. (6.27) the parameter ε cannot be considered small when α tends to zero.

Plane Channel and Pipe Flow For the flow between parallel plates with different TMACs of the top and bottom wall using Eq. (6.53), an approximation for the transitional regime is obtained by

$$G_\mathrm{P} \approx G_\mathrm{P,d} - \sigma_\mathrm{d} + \frac{2\sigma_\mathrm{b}\sigma_\mathrm{t}}{\sigma_\mathrm{b} + \sigma_\mathrm{t}} + \frac{\delta(\sigma_\mathrm{b} - \sigma_\mathrm{t})^2}{2(\sigma_\mathrm{b} + \sigma_\mathrm{t})(\sigma_\mathrm{b} + \sigma_\mathrm{t} + \delta)} \,. \tag{6.65}$$

If both walls have the same TMAC this reduces to

$$G_\mathrm{P} \approx G_\mathrm{P,d} - \sigma_\mathrm{d} + \sigma \tag{6.66}$$

which is also valid for the pipe flow.

6.1.3 DSMC Model

In order to validate the model for the transitional regime ($0 < \delta \leq 10$), numerical simulations are performed by means of the DSMC method using the extended OpenFOAM solver dsmcFoam+[173]. The simulations are performed using the VHS model for monatomic gases and the no time-counter (NTC) method is applied.[9] The gas properties for the DSMC simulations used in this work are provided in Tab. 6.1. For the case $\delta = 0$ no collision is performed. The macroscopic cells are designed to be cubic and are divided in eight sub cells where intermolecular collisions are performed with a maximum collision cell size being smaller than a third of the molecules' mean free path $\bar{\mathrm{l}} = \sqrt{\pi}/2\ell$. The time step is smaller than a third of the mean collision time

$$\nu = \frac{\pi\ell}{4c_\mathrm{m}} \tag{6.67}$$

and the number of equivalent particles F_N is adjusted in a way that the number of particles per collision cell is equal to seven. These conditions are recommended by Bird[200]. For the surrounding walls the Cercignani-Lampis-Lord (CLL) wall reflection model is chosen, with the TMAC smaller than one and the other accommodation coefficients equal to one[V].

A channel with prescribed pressure boundary conditions p_in and p_out at inlet and outlet is simulated. The channel length L in flow direction is chosen to be ten times larger than the channel width ($L = 10 \cdot w$). The gas rarefaction parameter δ is prescribed by the mean value of inlet and outlet

[V] There is a mistake in the dsmcFoam+ source code that has been corrected in this work. The tangential wall velocity must be multiplied by the TMAC when added to the molecules' velocity vector. In the source code it is multiplied by TMAC $\cdot$ (2 − TMAC). This violates Eq. (6.73) as values greater than one are obtained and an effective higher wall velocity is simulated. With the correction, equal results are obtained with the Maxwell model and the CLL model and Eq. (6.73) is fulfilled and the integral momentum conserved.

TAB. 6.1 VHS properties of Argon[9]

property	value	unit
internal degrees of freedom	0	–
mass	$6.63 \cdot 10^{-26}$	kg
diameter	$4.17 \cdot 10^{-10}$	m
viscosity index	0.81	–
reference temperature	273	K

pressure $p(\delta) = (p_{\text{in}} + p_{\text{out}})/2$. In order to calculate the reduced flow rate, the pressure gradient must be evaluated and is therefore linearised by

$$\frac{\partial p}{\partial z}(\delta) \approx \frac{p_{\text{out}} - p_{\text{in}}}{L} \tag{6.68}$$

with the condition that the normalised pressure gradient is small:

$$\left| \frac{h}{p(\delta)} \frac{\partial p}{\partial z} \right| \approx \left| \frac{p_{\text{out}} - p_{\text{in}}}{p(\delta)} \right| \frac{h}{L} = 0.01 \tag{6.69}$$

The mass flow rate is evaluated at the inlet and at the outlet of the channel. It is demanded that the relative difference of both time averaged mass flow rates is smaller than 0.5 %. As a result the mean value of inlet and outlet mass flow rate is evaluated and normalised by Eq. (6.25). The results are given as tabulated data in Tab. B.1 - Tab. B.4.

6.1.4 Validation

In this section the results of the Poiseuille flow are shown. An overview of the derived equations for G_{P} and u and the corresponding figures and data is given in Tab. 6.2. At first, simulation results from the literature are taken to verify the hypothesis that the impact of the TMAC itself only

TAB. 6.2 Overview of Poiseuille flow: rectangular channel is marked as 2D, plane flow is marked as 1D. The equations used for the transitional and slip flow for the results in the figures as well as the used or referenced data is summarized with the remarks on the TMACs.

	Eq. for				
flow	G_{P}	u	figure	data	remark
2D slip	(6.42)	(6.21)	6.10	–	$u(\delta \to \infty)$
			6.11	–	$\alpha_{\text{t}} = \alpha_{\text{b}} = \alpha_{\text{l}} = \alpha_{\text{r}}$
			6.12	–	$\alpha_{\text{t}} = \alpha_{\text{b}},\ \alpha_{\text{l}} = \alpha_{\text{r}}$
	(6.47)	–	–	–	All α differently
2D trans.	(6.64)	–	6.6	Tab. B.1	$\alpha_{\text{t}} = \alpha_{\text{b}} = \alpha_{\text{l}} = \alpha_{\text{r}}$
			6.7	Tab. B.2	$\alpha_{\text{t}} = \alpha_{\text{b}},\ \alpha_{\text{l}} = \alpha_{\text{r}}$
			6.8	Tab. B.3	$\alpha_{\text{t}} = \alpha_{\text{b}},\ \alpha_{\text{l}} = \alpha_{\text{r}}$
			6.9	Tab. B.4	All α differently
1D slip	(6.53)	(6.51)	–	–	$\alpha_{\text{t}} \neq \alpha_{\text{b}}$
	(6.54)	–	–	–	$\alpha_{\text{t}} = \alpha_{\text{b}}$
1D trans.	(6.65)	–	6.3	Ref. [129]	$\alpha_{\text{t}} \neq \alpha_{\text{b}}$
			6.4	Ref. [129]	$\alpha_{\text{t}} \neq \alpha_{\text{b}}$
	(6.66)	–	6.2	Refs. [153, 198, 199]	$\alpha_{\text{t}} = \alpha_{\text{b}}$
pipe slip	(6.60)	(6.58)	–	–	–
pipe trans.	(6.66)	–	6.5	Ref. [127]	–

weakly depends on the gas rarefaction parameter. Therefore, available simulations for the plane Poiseuille flow with equal TMACs α_h for both plates are compared to model Eq. (6.66). The simulation results for $\alpha_\mathrm{h} = 0.92$ and $\alpha_\mathrm{h} = 0.84$ are provided by Ref. [198] based on a direct numerical method and the simulation results for $\alpha_\mathrm{h} = 0.75$ and $\alpha_\mathrm{h} = 0.5$ are provided by Ref. [199] with the help of the discrete velocity method. Both are summarized in Ref. [153]. The results are shown in Fig. 6.2. For $\delta > 1$ a good agreement between the model and simulation results is obtained. For $\delta < 1$ the model equation slightly underrates the impact of the TMAC with larger deviations for small values of the TMAC. But overall the model can depict the qualitative behaviour of the TMAC for different gas rarefaction parameters.

Figure 6.3 shows a comparison of simulation results taken from Ref. [129] to model Eq. (6.53) for the plane Poiseuille flow. In this case the TMAC of the bottom wall is fixed to $\alpha_\mathrm{b} = 1$ while the TMAC of the top wall varies. It is obtained that even for very small TMACs a good agreement to simulation results is achieved for $\delta > 1$. Again for $\delta < 1$ the deviation between both approaches is higher for very small values of the TMAC. This is highlighted in Fig. 6.4, which shows the same comparison for a fixed TMAC of the bottom wall $\alpha_\mathrm{b} = 0.5$.

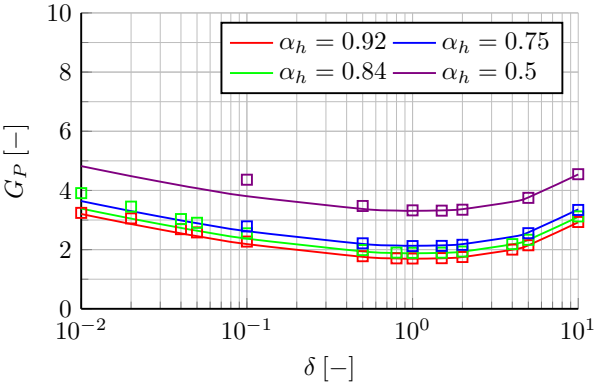

FIG. 6.2 Comparison of simulation results (symbols) and model Eq. (6.66) (solid lines) for the plane Poiseuille flow: $G_\mathrm{P}(\delta)$ for different TMACs α_h. Both plates have equal TMACs. Simulation results are taken from Refs. [153, 198, 199].[193]

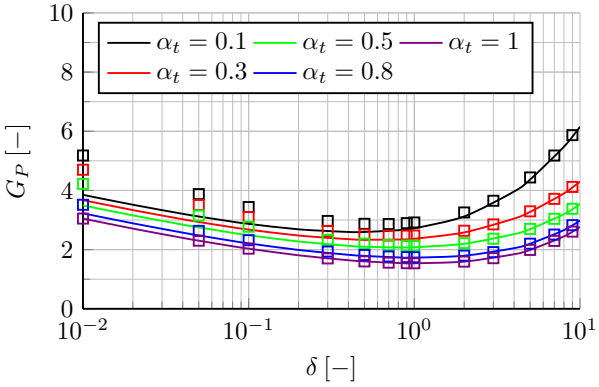

FIG. 6.3 Comparison of simulation results (symbols) and model Eq. (6.66) (solid lines) for the plane Poiseuille flow: $G_\mathrm{P}(\delta)$ for different TMACs α_t of the top wall for a fixed TMAC of the bottom wall $\alpha_\mathrm{b} = 1$. Simulation results are taken from Ref. [129].[193]

It needs to be noted that even for a fully diffuse wall scattering the theoretical value of the reduced flow rate for the Poiseuille flow between two plates of infinite width tends to infinity if the gas rarefaction parameter δ tends to zero. Although this is a theoretical result due to the fact, that a channel of infinite width and infinite length is calculated, in practical applications this is not very useful. Therefore, in a channel of infinite width and $\delta \to 0$ the reduced flow rate is a function of the channel length, which is studied for example in Ref. [78]. This is not the case if the channel width is finite or in a pipe flow.

The latter is shown in Fig. 6.5 where a comparison of simulation results to model Eq. (6.66) for a Poiseuille flow though a pipe with different TMACs α_t is made. The values for a TMAC $\alpha_\mathrm{t} > 1$ are referred to back scattering where a part of the tangential velocity is not kept, but inverted. There

is an overall good agreement between the model equation and the simulation results even in case of $\alpha > 1$.

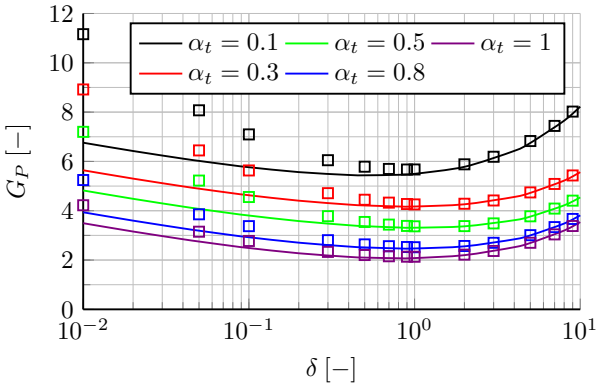

FIG. 6.4 Comparison of simulation results (symbols) and model Eq. (6.66) (solid lines) for the plane Poiseuille flow: $G_\mathrm{P}(\delta)$ for different TMACs α_t of the top wall for a fixed TMAC of the bottom wall $\alpha_\mathrm{b} = 0.5$. Simulation results are taken from Ref. [129]. [193]

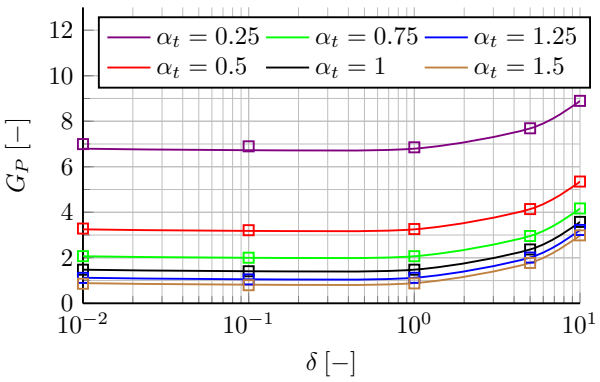

FIG. 6.5 Comparison of simulation results (symbols) and model Eq. (6.66) (solid lines) for pipe flow: $G_\mathrm{P}(\delta)$ for different TMACs α_t in a pipe. $\alpha_\mathrm{t} > 1$ is referred to back scattering. Simulation results are taken from Ref. [127]. [193]

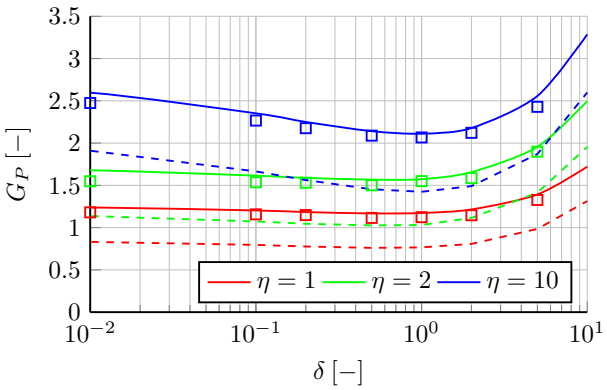

FIG. 6.6 Comparison of DSMC results (symbols) and model Eq. (6.64) (solid lines) and the values of the fully diffuse channel of Ref. [87] (dashed lines) for different cross section ratios η of a Poiseuille flow in a rectangular channel: $\alpha_\mathrm{h} = \alpha_\mathrm{v} = 0.71$. [193]

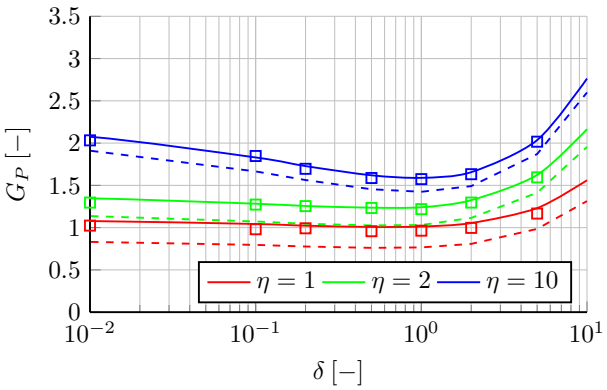

FIG. 6.7 Comparison of DSMC results (symbols) and model Eq. (6.64) (solid lines) and the values of the fully diffuse channel of Ref. [87] (dashed lines) for different cross section ratios η of a Poiseuille flow in a rectangular channel: $\alpha_\mathrm{h} = 0.92$, $\alpha_\mathrm{v} = 0.71$. [193]

In Fig. 6.6 a comparison of DSMC results according to Sec. 6.1.3 to model Eq. (6.64) for different cross section ratios is shown, when all walls have a TMAC $\alpha_\mathrm{h} = \alpha_\mathrm{v} = 0.71$. Furthermore, the fully diffuse values are added to show the impact of the TMAC. Overall a good agreement of the model and the DSMC simulations is achieved. In Fig. 6.7 the same comparison is done for the case that the horizontal walls have a TMAC $\alpha_\mathrm{h} = 0.92$ and the vertical walls have a TMAC $\alpha_\mathrm{v} = 0.71$, so the walls with higher TMAC are larger for $\eta > 1$. The difference to the diffuse values shrinks with a rising cross section ratio. Again the model is in good agreement with the DSMC results.

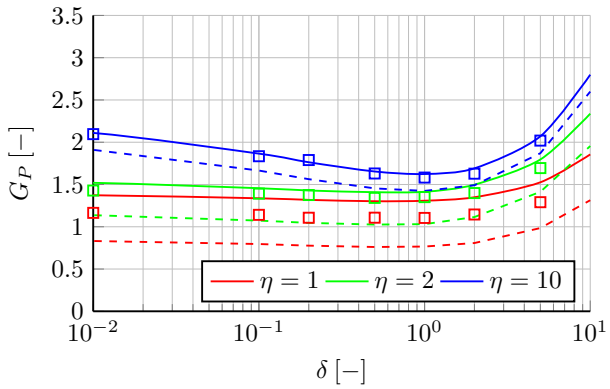

FIG. 6.8 Comparison of DSMC results (symbols) and model Eq. (6.64) (solid lines) and the values of the fully diffuse channel of Ref. [87] (dashed lines) for different cross section ratios η of a Poiseuille flow in a rectangular channel: $\alpha_\mathrm{h} = 0.92$, $\alpha_\mathrm{v} = 0.5$.[193]

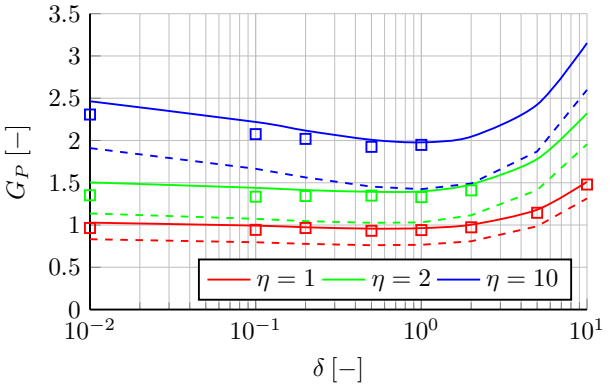

FIG. 6.9 Comparison of DSMC results (symbols) and model Eq. (6.64) (solid lines) and the values of the fully diffuse channel of Ref. [87] (dashed lines) for different cross section ratios η of a Poiseuille flow in a rectangular channel: $\alpha_\mathrm{t} = 0.7$, $\alpha_\mathrm{b} = 0.8$, $\alpha_\mathrm{r} = 0.9$, $\alpha_\mathrm{l} = 1$.[193]

In Fig. 6.8 the same comparison is done with a TMAC of the horizontal walls $\alpha_\mathrm{h} = 0.92$ and a TMAC of the vertical walls $\alpha_\mathrm{v} = 0.5$. This figure shows that the model overrates the flow rates compared to the DSMC results especially for the case that the cross section ratio is $\eta = 1$. So the vertical walls with a small TMAC have the same impact as the horizontal walls with a high TMAC. The results can be interpreted in a way that the model becomes worse when the TMAC has small values because the difference between model and DSMC results shrinks when the cross section ratio rises and the vertical walls with a small TMAC have a decreasing impact on the flow rate. This might be referred to the fact that a linear Taylor series expansion is performed in Eq. (6.27) and for small values of α the parameter ε, which is linearised, cannot be considered small any more. Such a linearisation is not done for Eq. (6.60). Therefore, the slip solution is valid even for very small values of α which explains the good agreement in Fig. 6.5. Therefore, a possible interpretation is that the higher deviations between DSMC and the model equation in Fig. 6.8 are related to the fact that the slip solution is only accurate for $\alpha \gtrsim 0.7$. A more accurate slip solution for smaller TMACs would also lead to better results in the transitional regime.

Figure 6.9 shows the same comparison as before, but now every wall has a different TMAC with $\alpha_\mathrm{t} = 0.7$, $\alpha_\mathrm{b} = 0.8$, $\alpha_\mathrm{r} = 0.9$ and $\alpha_\mathrm{l} = 1$. Overall, a good agreement between model Eq. (6.64) and the DSMC results is obtained. Therefore, in the most general case the model equation can be used as long as the TMACs are not too small.

6.1.5 Contour Plots

In this section, the impact of the TMACs on the resulting velocity field is shown for the Poiseuille flow. Therefore, the dimensionless velocity

$$\phi(x,y) = u(x,y) \cdot \left(\frac{h^2}{\mu}\frac{\partial p}{\partial z}\right)^{-1} = \sum_{n=0}^{\infty} \phi_n(x,y) \tag{6.70}$$

is introduced with ϕ_n being defined in Eq. (6.27).

At first in Fig. 6.10 the reduced velocity field of the continuum regime is shown, which looks like a paraboloid profile which is extended to the channel edges with the highest flow velocity in the middle of the channel and the no slip condition at the walls. As a comparison in Fig. 6.11 the velocity field in the slip regime is shown for $\delta = 10$. All surrounding walls have the same TMAC $\alpha = 0.71$. Therefore, a higher overall flow velocity is obtained, but the principal shape still looks similar. Fig. 6.12 also shows the reduced velocity field in the slip regime for $\delta = 10$.

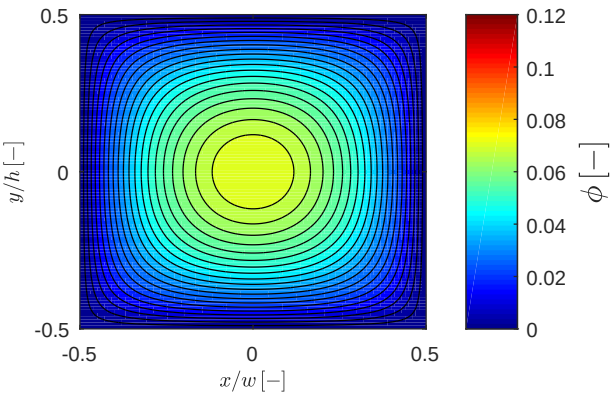

FIG. 6.10 Dimensionless velocity field ϕ of the Poiseuille flow using Eq. (6.70) in a channel of quadratic cross section $\eta = 1$ for $\delta = 10$ for $\delta \to \infty$.[193]

Now the horizontal walls have a TMAC $\alpha_\mathrm{h} = 0.92$ while the vertical walls still have a TMAC of $\alpha_\mathrm{v} = 0.71$. As a result the shape of the reduced velocity field slightly shifts into an ellipsoid which is still extended to the channel edges. Although the cross section is still quadratic the flow velocity along the x-axis is lower than along the y-axis due to a higher friction.

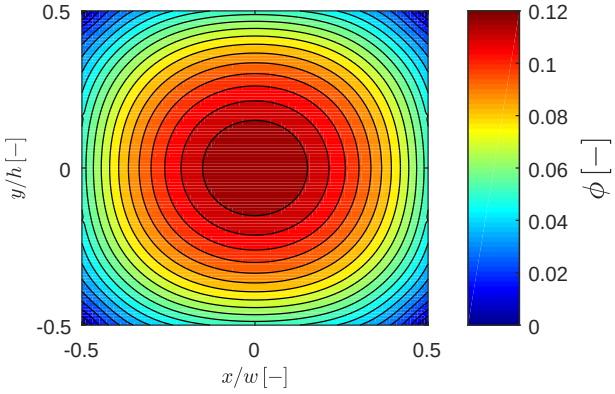

FIG. 6.11 Dimensionless velocity field ϕ of the Poiseuille flow using Eq. (6.70) in a channel of quadratic cross section $\eta = 1$ for $\delta = 10$, $\alpha_\mathrm{h} = \alpha_\mathrm{v} = 0.71$.[193]

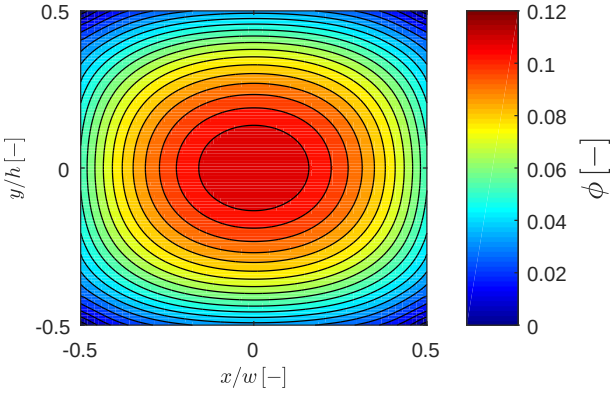

FIG. 6.12 Dimensionless velocity field ϕ of the Poiseuille flow using Eq. (6.70) in a channel of quadratic cross section $\eta = 1$ for $\delta = 10$, $\alpha_\mathrm{h} = 0.92$ and $\alpha_\mathrm{v} = 0.71$.[193]

6.2 Couette Flow

In this section the reduced flow rates for the pure Couette flow in a rectangular channel of infinite length are derived in order to solve the closure problem in Eq. (5.20). Figure 6.13 shows a sketch of the most general case of a rectangular channel with all walls moving with a different wall velocity in flow direction.

Each wall may have a linear velocity profile within the cross section, which does not change along the channel in z-direction. Furthermore, each wall may have a different TMAC. Therefore, the kinematics shown in Fig. 5.1 can be depicted even in the case, that the rotor is made of a different material than the housing. The flow is considered to be in steady state and isothermal. There are no gradients in the flow direction, and the pressure in each cross section is considered to be constant.

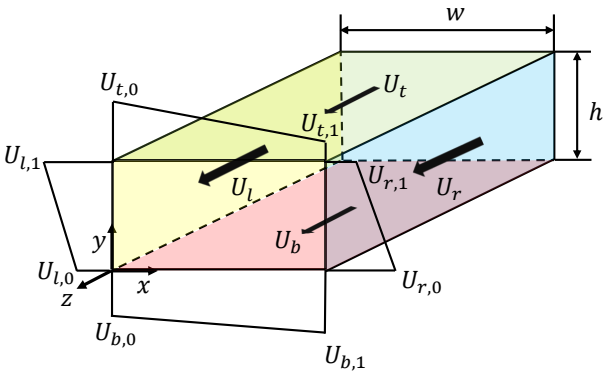

FIG. 6.13 Sketch of the rectangular channel with all walls moved with different linear velocity profiles. Each wall may have a different TMAC.[192]

6.2.1 Properties of the Couette Flow

The reduced mass flow rate G_C of the Couette flow for each moving wall i is defined as

$$G_{\mathrm{C},i}(\delta, \tilde{\eta}, \tilde{\alpha}_\mathrm{l}, \tilde{\alpha}_\mathrm{t}, \tilde{\alpha}_\mathrm{r}, \tilde{\alpha}_\mathrm{b}) = \frac{\dot{m}_i}{\rho h w U_i}\,. \tag{6.71}$$

In the following, the variables and indices with $\tilde{}$ are related to a local coordinate system in which the current moving wall is always considered to be the top wall in order to generalise the solution. Therefore, the cross section's coordinates $\tilde{x}$ in tangential direction of the moving wall i with width $\tilde{w}$ and $\tilde{y}$ the direction normal to the moving wall i with the height $\tilde{h}$ are introduced with $hw = \tilde{h}\tilde{w}$ and $\tilde{\eta} = \tilde{w}/\tilde{h}$. The velocity U_i is the average wall velocity of moving wall i. The total mass flow rate for more than one moving wall can be calculated by superposition of the partial mass flow rates of each moving wall:

$$\dot{m} = \rho h w \sum_i U_i G_{\mathrm{C},i}(\delta, \tilde{\eta}, \tilde{\alpha}_\mathrm{l}, \tilde{\alpha}_\mathrm{t}, \tilde{\alpha}_\mathrm{r}, \tilde{\alpha}_\mathrm{b})\,, \quad i = \mathrm{l}, \mathrm{t}, \mathrm{r}, \mathrm{b} \tag{6.72}$$

For the definition of the TMACs in the local coordinate system one can consider the following example: If the movement of the left wall is regarded, the index is $i = \mathrm{l}$. In this case the left wall is considered as local top wall. Therefore, the assignment of the TMACs between both coordinate systems are as follows: $\alpha_{\tilde{\mathrm{l}}} = \alpha_\mathrm{b} \quad \alpha_{\tilde{\mathrm{t}}} = \alpha_\mathrm{l} \quad \alpha_{\tilde{\mathrm{r}}} = \alpha_\mathrm{t} \quad \alpha_{\tilde{\mathrm{b}}} = \alpha_\mathrm{r}$.

The reduced mass flow rates $G_{\mathrm{C},i}$ will be shown to be a function of the gas rarefaction δ, the cross section ratio $\tilde{\eta}_i$ and the TMACs of each wall, but regardless of how the TMACs are distributed on the four walls, the following expressions hold:

$$\sum_i G_{\mathrm{C},i} = 1 \quad \exists \alpha_i \neq 0 \tag{6.73}$$

$$\sum_i G_{\mathrm{C},i} = 0 \quad \forall \alpha_i \equiv 0 \tag{6.74}$$

The proof of Eq. (6.74) is trivial. If there is no friction at any wall, a moving wall will not cause a mass flow rate and thus the reduced flow rate must be zero. For the proof of Eq. (6.73) consider

that every wall has the same constant velocity. As in a time averaged equilibrium state no gradient occurs in any direction this could be seen as a change of the reference frame as due to balance of momentum the flow moves with velocity of the surrounding walls. A further proof is given in App. A using the analytical solutions for the different flow regimes. Numerical validations for the superposition principle are given by means of the DSMC method and the impact of large wall velocities is studied.

6.2.2 Hydrodynamic Regime

Rectangular Channel As before for the Poiseuille flow, the governing equations in the hydrodynamic regime are the Navier-Stokes equations. Additionally, it is obtained that the pressure gradients transverse to the flow direction are zero and therefore, the pressure within the cross section is constant. Therefore, in a purely shear-driven flow in a rectangular channel the remaining part of the Navier-Stokes equations is reduced to Laplace's equation

$$\frac{\partial^2 u}{\partial x^2} + \frac{\partial^2 u}{\partial y^2} = 0 \tag{6.75}$$

Due to the linear behaviour of Laplace's equation, the solution $u(x, y)$ for more than one moving wall may be obtained by superposition

$$u(x, y) = \sum_i u_i(x, y)\,, \quad i = \mathrm{l, t, r, b} \tag{6.76}$$

where $u_i(x, y)$ are the velocity fields caused by a moving wall i. Thus the solution of the boundary value problem can be separated. Now the boundary conditions of moving wall i with no slip conditions read

$$u_i(0, \tilde{y}) = 0\,,\ u_i(\tilde{w}, \tilde{y}) = 0\,,\ u_i(\tilde{x}, 0) = 0\,,\ u_i(\tilde{x}, \tilde{h}) = f(\tilde{x}) \tag{6.77}$$

with

$$f(\tilde{x}) = \frac{U_{i,1} - U_{i,0}}{\tilde{w}}\tilde{x} + U_{i,0} \tag{6.78}$$

being a linear velocity profile along the wall as sketched in Fig. 6.13. Separation of variables leads to

$$u_i(\tilde{x}, \tilde{y}) = \sum_{n=1}^{\infty} B_n \sinh\left(\frac{n\pi\tilde{y}}{\tilde{w}}\right) \sin\left(\frac{n\pi\tilde{x}}{\tilde{w}}\right) \tag{6.79}$$

with the coefficients:

$$B_n = \frac{2}{\tilde{w}\sinh\left(\frac{n\pi\tilde{h}}{w}\right)} \int_0^{\tilde{w}} f(\tilde{x}) \sin\left(\frac{n\pi\tilde{x}}{\tilde{w}}\right) = \frac{2(U_{i,0} - U_{i,1}\cos(n\pi))}{n\pi\sinh\left(\frac{n\pi\tilde{h}}{\tilde{w}}\right)} \tag{6.80}$$

The boundary conditions for the movement of the other walls are analogous. Integration over the cross section area provides the volumetric flow rate

$$\dot{V}_i = \int_0^{\tilde{h}} \int_0^{\tilde{w}} u_i(\tilde{x}, \tilde{y})\ \mathrm{d}\tilde{x}\mathrm{d}\tilde{y} = 8\tilde{w}^2 U_i \sum_{n=0}^{\infty} \frac{1}{k_n^3} \left(\frac{1}{\tanh\left(k_n\tilde{h}/\tilde{w}\right)} - \frac{1}{\sinh\left(k_n\tilde{h}/\tilde{w}\right)} \right) \tag{6.81}$$

with

$$U_i = \frac{U_{i,0} + U_{i,1}}{2} \tag{6.82}$$

being the mean value of the moving wall velocity and k_n defined in Eq. (6.30).

Finally the reduced flow rate is obtained by dividing by the cross section area and the wall velocity:

$$G_{\mathrm{C}} = \frac{8\tilde{w}}{\tilde{h}} \sum_{n=0}^{\infty} \frac{1}{k_n^3} \left(\frac{1}{\tanh\left(k_n \tilde{h}/\tilde{w}\right)} - \frac{1}{\sinh\left(k_n \tilde{h}/\tilde{w}\right)} \right) \tag{6.83}$$

Plane Channel In case of a channel of infinite width Laplace's equation is further reduced to

$$\frac{\partial^2 u_i}{\partial \tilde{y}^2} = 0 \Leftrightarrow u_i(\tilde{y}) = C_1 \tilde{y} + C_2 \tag{6.84}$$

with the boundary conditions

$$u_i(0) = 0 \quad u_i(h) = U_i \tag{6.85}$$

the boundary value problem's solution is

$$u_i(\tilde{y}) = \frac{\tilde{y}}{h} U_i \tag{6.86}$$

with the reduced flow Rate

$$G_{\mathrm{C},i} = \frac{\dot{V}}{U_i h w} = \frac{1}{U_i h} \int_0^h u_i(\tilde{y}) \, \mathrm{d}\tilde{y} = \frac{1}{2} \,. \tag{6.87}$$

which can be adapted from many text books like Ref. [71].

6.2.3 Slip Regime

Rectangular Channel In order to derive a solution of the Couette flow for the rectangular channel in the slip regime, the velocity gradient at the wall is linearised. Therefore, at the length $\sigma_i \ell$ behind the wall the no slip condition applies and a channel is defined which has the virtual width

$$\tilde{w}^* = \tilde{w} + (\sigma_{\tilde{\mathrm{l}}} + \sigma_{\tilde{\mathrm{r}}})\ell \tag{6.88}$$

and the virtual height

$$\tilde{h}^* = \tilde{h} + (\sigma_{\tilde{\mathrm{b}}} + \sigma_{\tilde{\mathrm{t}}})\ell \tag{6.89}$$

where mathematically no velocity slip occurs. This procedure is similarly done in Ref. [86].

The boundary conditions read as follows:

$$u_i(-\sigma_{\tilde{\mathrm{l}}}\ell, \tilde{y}) = 0 \,, \quad u_i(\tilde{w} + \sigma_{\tilde{\mathrm{r}}}\ell, \tilde{y}) = 0 \tag{6.90}$$

$$u_i(\tilde{x}, -\sigma_{\tilde{\mathrm{b}}}\ell) = 0 \,, \quad u_i(\tilde{x}, \tilde{h} + \sigma_{\tilde{\mathrm{t}}}\ell) = f(\tilde{x}) \tag{6.91}$$

This leads to the velocity field

$$u_i(\tilde{x}, \tilde{y}) = \sum_{n=1}^{\infty} \frac{2(U_{i,0} - U_{i,1}\cos(n\pi))}{n\pi \sinh\left(\frac{n\pi \tilde{h}^*}{\tilde{w}^*}\right)} \times \sinh\left(\frac{n\pi(\tilde{y} + \sigma_{\tilde{\mathrm{b}}}\ell)}{\tilde{w}^*}\right) \sin\left(\frac{n\pi(\tilde{x} + \sigma_{\tilde{\mathrm{l}}}\ell)}{\tilde{w}^*}\right) \tag{6.92}$$

$$\tilde{x} \in [0, \tilde{w}] \quad \tilde{y} \in [0, \tilde{h}]$$

and with integration and normalisation to the reduced flow rate of the Couette flow in the slip regime for any TMAC combination α_i is obtained:

$$G_{\mathrm{C,S}} = \frac{8(\tilde{w}^*)^2}{hw} \sum_{n=0}^{\infty} \frac{(-1)^n \sin\left(\frac{k_n \tilde{w}}{2\tilde{w}^*}\right)}{k_n^3} \times \left[\frac{\cosh\left(\frac{k_n(\tilde{h}+\sigma_{\tilde{\mathrm{b}}}\ell)}{\tilde{w}^*}\right) - \cosh\left(\frac{k_n \sigma_{\tilde{\mathrm{b}}}\ell}{\tilde{w}^*}\right)}{\sinh\left(\frac{k_n \tilde{h}^*}{\tilde{w}^*}\right)} \right] \tag{6.93}$$

The gas rarefaction parameter is implicitly used in the equivalent free path ℓ.

Plane Channel In case of a channel of infinite width no linearisation is needed. Again Laplace's equation is used:

$$\frac{\partial^2 u_i}{\partial \tilde{y}^2} = 0 \Leftrightarrow u_i(\tilde{y}) = C_1 \tilde{y} + C_2 \tag{6.94}$$

But now the boundary conditions read

$$u_i(0) = \sigma_{\tilde{\mathrm{b}}} \ell \frac{\partial u}{\partial \tilde{y}} \quad u_i(h) = U_i - \sigma_{\tilde{\mathrm{t}}} \ell \frac{\partial u}{\partial \tilde{y}} \tag{6.95}$$

and the boundary value problem's solution is

$$u_i(\tilde{y}) = \frac{U_i}{h + (\sigma_{\tilde{\mathrm{b}}} + \sigma_{\tilde{\mathrm{t}}})\ell} (\tilde{y} + \sigma_{\tilde{\mathrm{b}}} \ell) \tag{6.96}$$

with the reduced flow Rate

$$G_{\mathrm{C},i} = \frac{\dot{V}}{U_i h w} = \frac{1}{U_i h} \int_0^h u_i(\tilde{y}) \, \mathrm{d}\tilde{y} = \frac{\delta/2 + \sigma_{\tilde{\mathrm{b}}}}{\delta + \sigma_{\tilde{\mathrm{b}}} + \sigma_{\tilde{\mathrm{t}}}} \,. \tag{6.97}$$

For $\delta \to \infty$ Eq. (6.97) tends to Eq. (6.87) and Eq. (6.93) tends to Eq. (6.83). Therefore, the hydrodynamic limit is an asymptotic result of the slip solution.

6.2.4 Free Molecular Regime

Rectangular Channel For more rarefied gases the Boltzmann equation Eq. (3.68) has to be solved. For the free molecular flow ($\delta \to 0$) no intermolecular collisions occur, thus, under stationary conditions without external forces the equation reduces to

$$\boldsymbol{c} \cdot \frac{\partial f}{\partial \boldsymbol{x}} = c_1 \frac{\partial f}{\partial x} + c_2 \frac{\partial f}{\partial y} = 0 \tag{6.98}$$

with the assumption that there is no change in flow direction (z-direction). The temperature of the walls is considered to be equal and constant. The free molecular solution derived here is only valid for diffuse wall scattering with all TMACs equal to one. The number density

$$n = \int_{-\infty}^{\infty} f \, \mathrm{d}\boldsymbol{c} \tag{6.99}$$

is supposed to be constant and the macroscopic flow velocity can be obtained by the integral of all molecule velocities

$$\boldsymbol{u} = \frac{1}{n} \int_{-\infty}^{\infty} \boldsymbol{c} f \, \mathrm{d}\boldsymbol{c} \,. \tag{6.100}$$

Assuming full wall accommodation, the solution of Eq. (6.100) is known to be the velocity vector $\boldsymbol{U}$ of the moving wall for those molecules that collided with the wall, which can be derived from Sec. 3.5.5.[78] Thus, different velocity distribution functions for local equilibrium states can be obtained for molecules colliding with different walls. Due to the vanishing of the collision integral in Eq. (6.98), molecules do not interact with each other and the velocity distribution function can be build by superposition:

$$f = f_{\varphi} + f_{2\pi-\varphi} \tag{6.101}$$

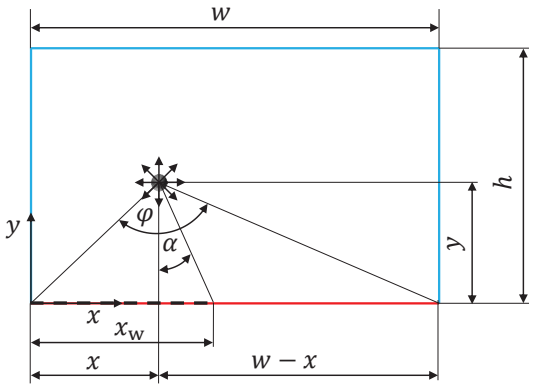

FIG. 6.14 Sketch of the rectangular channel for the free molecular flow with bottom wall moving in z direction.[192]

With linear molecular trajectories a macroscopic velocity field can be obtained by geometric consideration. Regarding Fig. 6.14 it can be shown that a partial of molecules $\frac{2\pi-\varphi}{2\pi}$ at point x, y is scattered from the static walls and a partial $\frac{\varphi}{2\pi}$ from the moving wall considering a constant wall velocity vector $\boldsymbol{U}$. Therefore, two different velocity distribution functions f_{φ} and $f_{2\pi-\varphi}$ can be formulated, with

$$n_{\varphi(x,y)} = \int_{-\infty}^{\infty} f_{\varphi}(x,y)\mathrm{d}\boldsymbol{c} = \frac{\varphi(x,y)}{2\pi} n \tag{6.102}$$

being the partial number density of the molecules with macroscopic velocity $\boldsymbol{U}$ and

$$n_{2\pi-\varphi} = \int_{-\infty}^{\infty} f_{2\pi-\varphi}(x,y)\mathrm{d}\boldsymbol{c} = \frac{2\pi-\varphi(x,y)}{2\pi} n \tag{6.103}$$

being the partial number density of the molecules with macroscopic velocity zero. Similarly this is shown in Ref. [78] for the plane Couette flow.

Using Eq. (6.100) the resulting velocity field reads as follows

$$\boldsymbol{u}(x,y) = \frac{1}{n}\left[\int_{-\infty}^{\infty} \boldsymbol{c} f_{\varphi}\mathrm{d}\boldsymbol{c} + \int_{-\infty}^{\infty} \boldsymbol{c} f_{2\pi-\varphi}\mathrm{d}\boldsymbol{c}\right] = \frac{\varphi(x,y)}{2\pi}\boldsymbol{U} \tag{6.104}$$

and is only a function of the wall velocity $\boldsymbol{U}$ and the angle

$$\varphi = \arctan\left(\frac{x}{y}\right) + \arctan\left(\frac{w-x}{y}\right) . \tag{6.105}$$

The same procedure can be performed for a non constant wall velocity profile. Therefore, Eqs. (6.102)-(6.104) must be performed for an integral over the angle increment α depending on the wall coordinate

$$x_w = x + y \cdot \tan(\alpha) \tag{6.106}$$

as shown in Fig. 6.14 which leads to

$$\alpha = \arctan\left(\frac{x_w - x}{y}\right) . \tag{6.107}$$

Thus Eq. (6.104) must be expanded by

$$\boldsymbol{u}(x,y) = \frac{1}{2\pi}\int_{\alpha(x_\mathrm{w}=0)}^{\alpha(x_\mathrm{w}=w)} \boldsymbol{U}(x_\mathrm{w}(\alpha))\ \mathrm{d}\alpha \tag{6.108}$$

Considering only the z-component of the bottom wall velocity to be non zero and linear

$$U(x_\mathrm{w}(\alpha)) = \frac{U_{\mathrm{b},1} - U_{\mathrm{b},0}}{w}\cdot x_\mathrm{w}(\alpha) + U_{\mathrm{b},0} \tag{6.109}$$

and inserting the integral limits

$$\alpha(x_\mathrm{w}=0) = -\arctan\left(\frac{x}{y}\right) \tag{6.110}$$

and

$$\alpha(x_\mathrm{w}=w) = \arctan\left(\frac{w-x}{y}\right) \tag{6.111}$$

in Eq. (6.108) one obtains

$$\begin{aligned} u_\mathrm{b}(x,y) \quad &= \frac{U_{\mathrm{b},1}-U_{\mathrm{b},0}}{2\pi w}\cdot\left[\frac{y}{2}\cdot\ln\left(\frac{(w-x)^2+y^2}{x^2+y^2}\right)\right. \\ &\left. + x\cdot\arctan\left(\frac{w-x}{y}\right) + x\cdot\arctan\left(\frac{x}{y}\right)\right] \\ &+\frac{U_{\mathrm{b},0}}{2\pi}\cdot\left[\arctan\left(\frac{x}{y}\right)+\arctan\left(\frac{w-x}{y}\right)\right] \end{aligned} \tag{6.112}$$

which is a superposition of the constant wall velocity of Eq. (6.104) and a linear velocity without offset. In the same manner the velocity fields for the movement of left, top or right wall can be obtained as shown in Ref. [192] or by coordinate transformation.

The volumetric flow rate is calculated according to Eq. (6.81) which can be written for the ith wall after integration as:

$$\dot{V}_i = \frac{(U_{i,1}+U_{i,0})\cdot wh}{8\pi}\cdot\left[\left(\tilde{\eta}-\frac{1}{\tilde{\eta}}\right)\cdot\ln\left(\tilde{\eta}^2+1\right) - 2\cdot\tilde{\eta}\cdot\ln\left(\tilde{\eta}\right) + 4\cdot\arctan\left(\tilde{\eta}\right)\right] \tag{6.113}$$

Again the volumetric flow rate only depends on the average wall velocity of Eq. (6.82) and with Eq. (6.71) the dimensionless reduced mass flow rate reads as follows:

$$G_\mathrm{C}(\delta=0,\tilde{\eta}) = \frac{1}{4\pi}\cdot\left[\left(\tilde{\eta}-\frac{1}{\tilde{\eta}}\right)\cdot\ln\left(\tilde{\eta}^2+1\right) - 2\cdot\tilde{\eta}\cdot\ln\left(\tilde{\eta}\right) + 4\cdot\arctan\left(\tilde{\eta}\right)\right] \tag{6.114}$$

Plane Channel For the flow between parallel plates a series solution can be derived for arbitrary TMACs of the top and bottom plate. In a steady state, due to symmetry, half of the molecules will collide with the top wall and half of the molecules will collide with the bottom wall in each cross section as according to Eq. (6.102) $\varphi(x,y) \to \pi$ for $h/w \to 0$. Afterwards each molecule that collided with the top wall collides with the bottom wall and the other way round. The fraction of molecules that are scattered diffusely will have a mean velocity equal to the wall velocity. The others will keep their tangential velocity and will collide with the other wall next. Again, a part of

the reflected molecules will be reflected diffusely and the other part specularly, just with another probability. As this happens in any cross section of an infinite channel, this can be calculated as an infinite series where the part of the molecules within the cross section travelling with the mean velocity of the top or of the bottom wall can be calculated as follows and is equal to the reduced flow rate of the certain moving wall:

$$G_{\mathrm{C},i} = \frac{1}{2}\sum_{n=0}^{\infty} \alpha_{\tilde{\mathrm{t}}}(1-\alpha_{\tilde{\mathrm{t}}})^n(1-\alpha_{\tilde{\mathrm{b}}})^n + \alpha_{\tilde{\mathrm{t}}}(1-\alpha_{\tilde{\mathrm{t}}})^n(1-\alpha_{\tilde{\mathrm{b}}})^{n+1} \tag{6.115}$$

The left term within the sum results from half of the molecules that at first collide with the top wall and the right term results from the other half of the molecules that first collide with the bottom wall. Only the fraction of molecules that receive the momentum of the local top wall is regarded. The resulting time averaged velocity profile is constant with

$$u_i = G_{\mathrm{C},i} U_i \ , \tag{6.116}$$

as the amount of molecules coming from the moving wall equals the amount of particles coming from the static wall at any space coordinate. For equal TMACs of the top and bottom plate the value $G_{\mathrm{C},i} = 1/2$ is obtained. Furthermore, while $n \to \infty$ Eq. (6.115) tends to the same limiting value as the slip solution Eq. (6.97) for $\delta = 0$ if the TMAC is calculated by Eq. (3.106) according to Maxwell. For other formulas available in the literature, this is not necessarily true. For example, the definition of Sharipov in Eq. (3.107).

6.2.5 Transitional Regime

For the transitional regime no such analytical solution is known and numerical simulations by means of the DSMC method are needed. The conditions for the cell sizes, time steps and used models are the same as in Sec. 6.1.3. For the case $\tilde{\eta} \to \infty$ symmetry planes on left and right wall are chosen with only one macroscopic cell in between. In flow direction, the mesh has only two macroscopic cells with cyclic boundaries applied. Thus, an endless channel is simulated according to Fig. 6.13. A wall movement is only performed in z-direction. The mass flow rate is detected due to the mass of the molecules crossing the plane between the two macroscopic cells in flow direction during a time step. As there is no inlet or outlet boundary, the mass in the system stays constant after the initialization step. The statistical uncertainty of the mass flow rate is calculated according to Sec. 4.2.6 with a total uncertainty < 0.1 % for fully diffuse walls and an uncertainty < 0.5 % for simulations including different TMACs.

Diffuse Wall Scattering At first, simulations for a rectangular channel with fully diffuse walls are performed. The results of the DSMC method and of Eqs. (6.114) and (6.83) are listed in Tab. B.5 in a wide range of δ and $\tilde{\eta}$. Only results for $\tilde{\eta} \geq 1$ are listed, due to the symmetry obtained by Eq. (6.72). If all walls are diffuse, the reduced flow rates caused by movements of opposite walls are equal and the following relation holds:

$$G_{\mathrm{C}}(\delta, \tilde{\eta}^{-1}) = \frac{1}{2} - G_{\mathrm{C}}(\delta, \tilde{\eta}) \tag{6.117}$$

Figure 6.15 shows the reduced flow rate G_{C} as a function of $\tilde{\eta}$ for the free molecular regime ($\delta = 0$), the continuum regime ($\delta \to \infty$) and two intermediate states ($\delta = 0.1$ and $\delta = 1$). Independently of

δ, the value of G_C is equal to 0.25 for $\tilde{\eta} = 1$. For $\tilde{\eta} \to \infty$ the value $G_C = 0.5$ for the well-known plane Couette flow is obtained.

On the other hand, when the width of the moving wall tends to zero, the resulting reduced flow rate tends to zero for all δ. For the analytical solutions, the limits can be shown using l'Hôspitals rule[201]. A different result related to δ is only shown between these points. With the highest deviations for $2 < \tilde{\eta} < 20$ and $0.05 < \tilde{\eta} < 0.5$ respectively. There is an infliction point at $\tilde{\eta} = 1$ for all δ, where for $\tilde{\eta} > 1$ the course of $G_C(\delta \to \infty)$ marks an upper and $G_C(\delta = 0)$ a lower boundary where all $G_C(0 < \delta < \infty)$ lie in between. For $\tilde{\eta} < 1$ $G_C(\delta \to \infty)$ marks the lower and $G_C(\delta = 0)$ the upper boundary respectively.

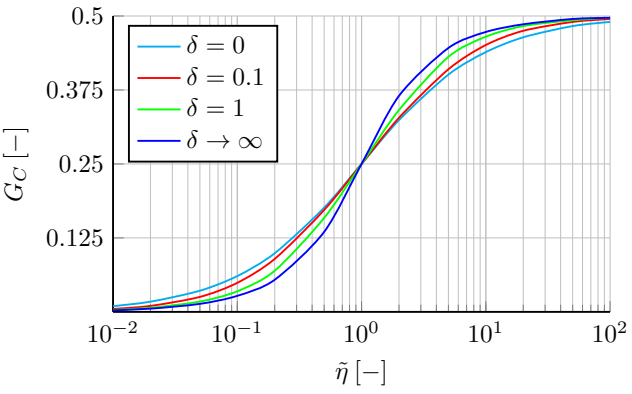

FIG. 6.15 Reduced flow rates G_C of the Couette flow with diffuse walls as a function of the cross section ratio $\tilde{\eta}$ for different gas rarefaction parameters δ.[192]

Nonlinear Regression To avoid any bilinear interpolation or calculating series expansions for simple practical application, an overall two dimensional nonlinear regression of Tab. B.5 has been performed resulting in Eq. (6.118). The parameters $k_1 - k_5$ are found via least square method solved with the Levenberg-Marquardt[202,203] algorithm using MATLAB[204]:

$$G_C(\delta, \tilde{\eta}) = G_C(\delta = 0, \tilde{\eta}) + k_1 \cdot \ln(\tilde{\eta}) \cdot \arctan\left(k_2 \cdot \delta \cdot \ln(\tilde{\eta}) - k_3 \cdot \delta\right) \cdot \exp\left(-k_4 \cdot \ln^2(k_5 \cdot \tilde{\eta})\right) \quad (6.118)$$

$$k_1 = 86.74 \quad k_2 = 2.66 \quad k_3 = 1.07 \quad k_4 = 23.08 \cdot 10^{-3} \quad k_5 = 46.08 \cdot 10^{6}$$

Eq. (6.118) is designed in a way that it tends to Eq. (6.114) as $\delta \to 0$. For $\tilde{\eta} = 1$ $G_C = 0.25$ and for $\tilde{\eta} \to \infty$ $G_C \to 0.5$ is obtained for all δ. Due to the asymptotic behaviour for $\delta \to \infty$ there is no remarkable change in the continuum regime. Thus, the equation can be used in the whole range of gas rarefaction for $\tilde{\eta} \geq 1$ and holds a maximum deviation to the tabulated data of 0.96 % with a mean error of 0.29 % using all data values. For $\tilde{\eta} < 1$ Eq. (6.117) has to be applied.

For a more simplified approach the reduced flow rate can be approximated by the ratio of the width of the moving wall to the cross section's perimeter which can be normalised as follows:

$$G_C(\tilde{\eta}) = \frac{\tilde{\eta}}{2\tilde{\eta} + 2} \quad (6.119)$$

As this approach is not a function of the gas rarefaction parameter, neither the free molecular solution nor the continuum solution is depicted exactly with this formula, but the limits for $\tilde{\eta} \to 0$, $\tilde{\eta} = 1$ and $\tilde{\eta} \to \infty$ are correct. For all other values of $\tilde{\eta}$ the value of Eq. (6.119) lies in between the values of the free molecular solution and the hydrodynamic solution. Therefore, the maximum deviation of Eq. (6.119) to the tabulated data of Tab. B.5 is smaller then 10 % and the average deviation is smaller than 2 %.

TAB. 6.3 Overview of Couette flow: rectangular channel is marked as 2D, plane flow is marked as 1D. The equations used for the hydrodynamic, transitional, slip and molecular flow used for the results in the figures as well as the used or referenced data are summarized with the remarks on the TMACs.

	Eq. for				
flow	G_C	u	figure	data	remark
2D hydro	(6.83)	(6.76)	6.24	Tab. B.5	–
2D slip	(6.93)	(6.92)	6.25	–	$\alpha_t = \alpha_b = \alpha_l = \alpha_r$
			6.26	–	$\alpha_t = \alpha_b,\ \alpha_l = \alpha_r$
			6.27	–	All α differently
2D trans.	(6.120)	–	6.17	Tab. B.6	$\alpha_t = \alpha_b = \alpha_l = \alpha_r$
			6.18	Tab. B.7	$\alpha_t = \alpha_b,\ \alpha_l = \alpha_r$
			6.19	Tab. B.8	$\alpha_t = \alpha_b,\ \alpha_l = \alpha_r$
			6.20	Tab. B.6-B.8	$\alpha_t = \alpha_b,\ \alpha_l = \alpha_r$
	(6.118)	–	–	–	diffuse
2D mol.	(6.114)	(6.112)	–	–	diffuse
1D slip	(6.97)	(6.96)	–	–	$\alpha_t \neq \alpha_b$
1D trans.	(6.97)	–	6.16	Ref. [95]	$\alpha_t \neq \alpha_b$
1D mol.	(6.115)	(6.116)	–	–	$\alpha_t \neq \alpha_b$

Model for Different TMACs In order to reduce the effort for the different TMACs as for the Poiseuille flow, a modelling assumption is desired. Nevertheless, a Taylor series expansion as performed in Eq. (6.27) is not convenient. A result would be that the slip term would rise linearly with the equivalent free path which would violate the condition in Eq. (6.73). Due to this limitation, the reduced flow rate of the Couette flow can only weakly depend on the gas rarefaction parameter. So in order to generalise a functional for different TMACs in the whole range of the gas rarefaction, the assumption is made that the impact of the TMAC on the reduced flow rate for the transitional regime is independent of the gas rarefaction parameter. Therefore, using Eq. (6.93) the difference of the slip solution $G_{C,S}(\delta = 10)$ to the fully diffuse solution $G_{C,d}(\delta = 10)$ is evaluated at $\delta = 10$, which is the lowest value of the defined slip regime and the transitional regime begins. For equal channel shapes this difference is added to the diffuse solution at any rarefaction parameter to obtain the superposed value for different TMACs α_i:

$$G_C(\delta) = G_{C,d}(\delta) + G_{C,S}(\delta = 10) - G_{C,d}(\delta = 10) \tag{6.120}$$

For the quadratic case ($h = w$) the reduced flow rate of the fully diffuse channel is not a function of the gas rarefaction. For the flow between parallel plates it will be shown in Sec. 6.2.6 that the slip solution of Eq. (6.97) can depict the whole range of the gas rarefaction due to the linear behaviour of the plane Couette flow.

6.2.6 Validation

In this section the results of the Couette flow are shown. An overview of the derived equations for G_C and u and the corresponding figures and data is given in Tab. 6.3. The G_C values in the figures of this section are all related the top wall which is moving and all the other walls being static.

At first, the Couette flow between two parallel plates of infinite width is reviewed. Therefore, Eq. (6.97) is compared to numerical results found in Ref. [95] which are shown in Fig. 6.16. The moving wall has a fixed TMAC $\alpha_t = 0.5$ while three different TMACs for the static walls are investigated. It is obtained that for the Couette flow between parallel plates the slip solution fits perfectly in the whole range of the gas rarefaction under isothermal conditions. Furthermore, it tends asymptotically to the free molecular solution of Eq. (6.115).

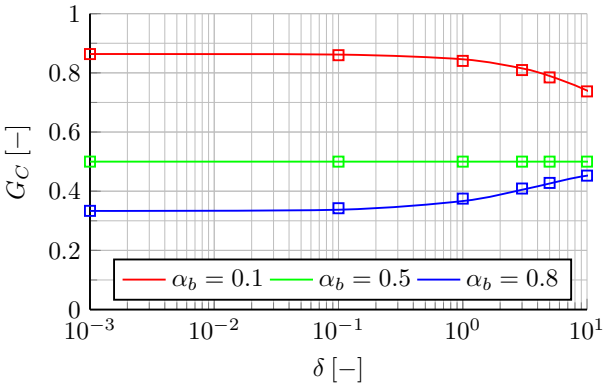

FIG. 6.16 Comparison of simulation results (symbols) and model Eq. (6.97) (solid lines) for plane Couette flow: $G_C(\delta)$ for different TMACs α_b of the static bottom wall for a fixed TMAC of the moving top wall $\alpha_t = 0.5$. Simulation results are taken from Ref. [95] and normalised with Eq. (6.71).[193]

For the Couette flow in a rectangular channel one horizontal wall with wall velocity in flow direction is considered. Fig. 6.17 shows the reduced flow rate G_C as a function of δ for different cross section ratios η when all walls have a TMAC $\alpha_h = \alpha_v = 0.71$. The symbols show DSMC results while the lines are results of model Eq. (6.120). For $\eta = 1$ no gas rarefaction effect is notable and the reduced flow rate is equal to 0.25, which is identical to the result of the fully diffuse channel. For higher cross section ratios the reduced flow rates rise and furthermore the reduced flow rate rises asymptotically with δ.

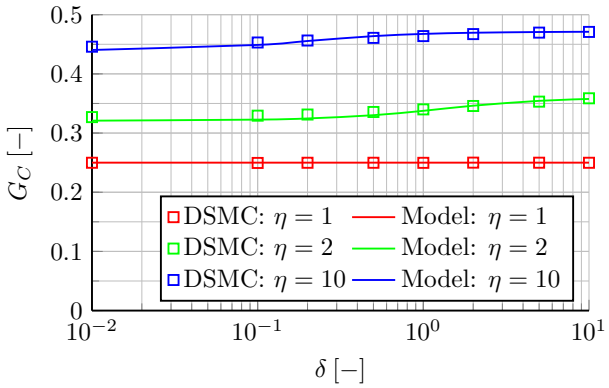

FIG. 6.17 Comparison of DSMC results and model Eq. (6.120): $G_C(\delta)$ for different cross section ratios η with $\alpha_h = \alpha_v = 0.71$.[193]

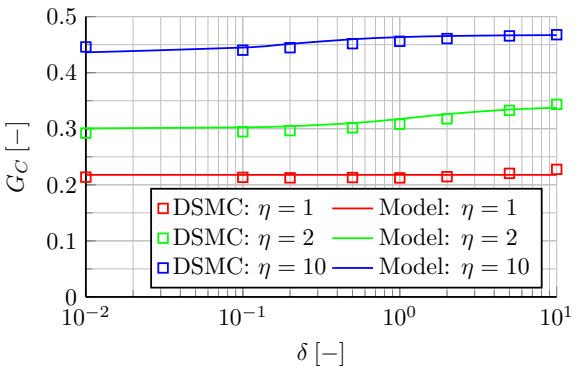

FIG. 6.18 Comparison of DSMC results and model Eq. (6.120) for Couette flow in a rectangular channel: $G_C(\delta)$ for different cross section ratios η with $\alpha_h = 0.71$ and $\alpha_v = 0.92$.[193]

Figure 6.18 shows a similar chart, but now the vertical walls have a TMAC $\alpha_v = 0.92$ while the horizontal walls still have a TMAC $\alpha_h = 0.71$. The qualitative behaviour is the same, but due to the higher friction of the vertical walls the flow rate at each point is reduced. This effect is the strongest at $\eta = 1$ due to the larger fraction of the vertical walls in the cross section area. Already

for $\eta = 10$ only marginal differences are seen, as the impact of the friction of the vertical walls is small.

In Fig. 6.19 the TMACs of horizontal and vertical walls are swapped, thus the horizontal walls cause a relative higher friction. The results still show the same qualitative behaviour but this time at a higher value of the reduced flow rate. This is highlighted in Fig. 6.20, where the results of the different combinations of the TMAC for $\eta = 1$ are compared. This shows that the reduced flow rate rises when the TMAC of the moving wall rises in comparison to the static walls.

Overall, the model equation is in good agreement with the DSMC results and can depict the qualitative and quantitative behaviour of reduced flow rates depending on the TMACs, the gas rarefaction and the cross section ratio. The maximum relative deviation of both approaches is 4.5 % for $\eta = 2$ and $\delta = 0.1$, which for engineering purposes is still an acceptable result. Nevertheless, if only the diffuse solution would be applied, a deviation of about 10 % would occur.

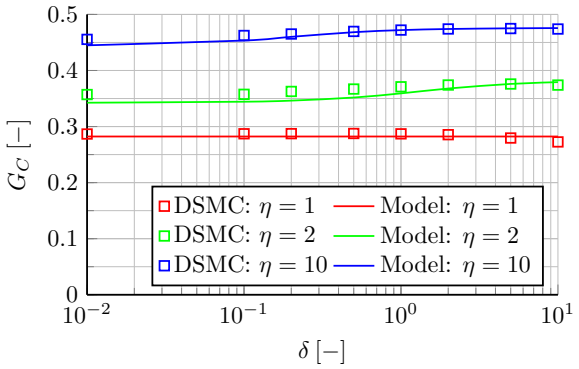

FIG. 6.19 Comparison of DSMC results and model Eq. (6.120) for Couette flow in a rectangular channel: $G_C(\delta)$ for different cross section ratios η with $\alpha_h = 0.92$ and $\alpha_v = 0.71$.[193]

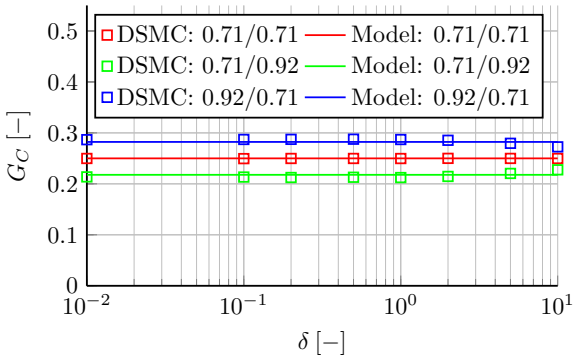

FIG. 6.20 Comparison of DSMC results and model Eq. (6.120) for Couette flow in a rectangular channel: $G_C(\delta)$ for cross section ratio $\eta = 1$. The first number in the legend is α_h, the second number is α_v.[193]

6.2.7 Contour Plots

First of all, in order to validate the velocity field of Eqs. (6.76) and (6.112), a comparison between the analytical and DSMC solution is made with a quadratic cross section $\eta = 1$ for a free molecular flow $\delta = 0$ with diffuse wall scattering, thus the absolute dimensions do not matter. The boundary conditions according to Fig. 6.13 are chosen as follows:

$$\begin{aligned} U_{b,0} = U_{b,1} = U_{l,0} = U_{r,0} &= 35\,\mathrm{m/s} \\ U_{l,1} = U_{r,1} &= 70\,\mathrm{m/s} \\ U_{t,0} = U_{t,1} &= 0\,\mathrm{m/s} \end{aligned} \tag{6.121}$$

The bottom wall moves with a constant wall velocity, the left and right wall velocities increase linearly and the top wall is static. This is a typical case in a working chamber of a positive displacement vacuum pump according to Fig. 5.1. The boundary conditions are applied for the DSMC method with the same settings described in Sec. 6.1.3 with $100 \times 100 \times 2$ macroscopic cells.

As no collisions have to be performed, the collision cell size has no impact on the accuracy of the simulation. Independent of this, the same number of molecules per collision cell have still been used in order to reduce the statistical scatter of the macroscopic velocity field. The same boundary conditions have been used for the analytical solution and a value is calculated for every cell centre. The results of the flow field of the DSMC simulation and the analytical solution are shown in Fig. 6.21. The mean deviation of the macroscopic velocities over all cells in both plots is smaller than 0.1 %, thus the simulation of the flow field is in good agreement with the analytical solution.

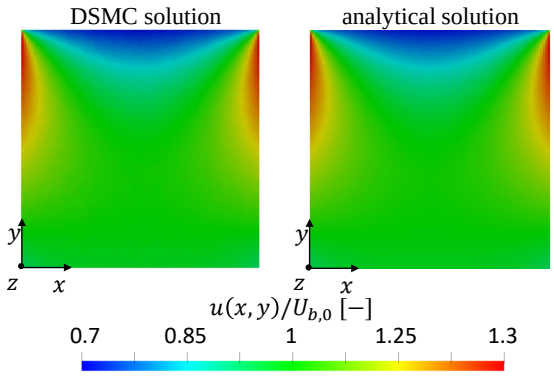

FIG. 6.21 Comparison of the velocity field of DSMC results and the analytical solution (Eq. (6.112)) with $\eta = 1$, $\delta = 0$ and $\alpha = 1$ following the boundary conditions of Eq. (6.121).[192]

Figure 6.22 shows the contour plot of the DSMC results for $\delta = 10$ with diffuse wall scattering while Fig. 6.23 shows the analytical solution of the slip regime using Eq. (6.92) for the same boundary conditions of Eq. (6.121). The channel height, temperature and viscosity are equal to those in Sec. A.3 and the number of molecules and cells is identical to that of the free molecular solution. The resulting velocity fields are symmetric at $x/w = 0.5$ along the y-axis. Comparing the cell centre values of the velocity components between analytical solution and DSMC results, the maximum deviation is about 30 % in the four corners of the cross section. While the root mean square deviation of all cells is about 3 %. This deviation can be explained by the linearisation which has been performed in the analytical solution when the virtually larger channel is calculated. It needs to be noted that this deviation becomes smaller with higher gas rarefaction parameter δ, as the error caused by the linearisation shrinks. Furthermore, the deviation becomes smaller when higher cross section ratios are considered, as the values in the edges have a smaller impact on the whole cross section. Therefore, this can be considered as a worst case. Additionally, it is seen that the contour lines of the DSMC simulations are not as smooth as the analytical values. The cell center values have a larger statistical error than the mass flow rate, which is determined by the particles in all 200000 cells. But the statistical error in each cell is not determined separately. The mass flow rate calculated with the DSMC method is $\dot{m}_{\mathrm{DSMC}} = 4.5122 \cdot 10^{-7}\,\mathrm{kg/s}$ while that of the superposition approach of Eq. (6.72) using the tabulated data of Tab. B.5 is $\dot{m} = 4.5095 \cdot 10^{-7}\,\mathrm{kg/s}$. This is a deviation smaller than 0.06 %. A further simulation has been performed for $\delta = 1$ with the same settings. Therefore, the DSMC mass flow rate is $\dot{m}_{\mathrm{DSMC}} = 4.5117 \cdot 10^{-8}\,\mathrm{kg/s}$ and the superposition approach delivers $\dot{m} = 4.509 \cdot 10^{-8}\,\mathrm{kg/s}$ with a deviation smaller 0.05 %.

Figure 6.24 shows the contour plots of the analytical solutions in the continuum flow regime ($\delta \to \infty$) using Eq. (6.79) for the same boundary conditions of Eq. (6.121). The comparison of the three cases shows that although the same reduced flow rate G_{C} is obtained, the velocity profiles are different. Due to the no slip condition in the continuum case, the velocity range within the cross section is between zero at the top wall which is not moving and the maximum value $U_{\mathrm{l},1} = U_{\mathrm{r},1}$, while with decreasing gas rarefaction parameter the differences between maximum and minimum velocity decrease, holding the same integral value. Note that for better comparison to the DSMC values the color scheme in Fig. 6.21 has a different range than in Figs. 6.22-6.27.

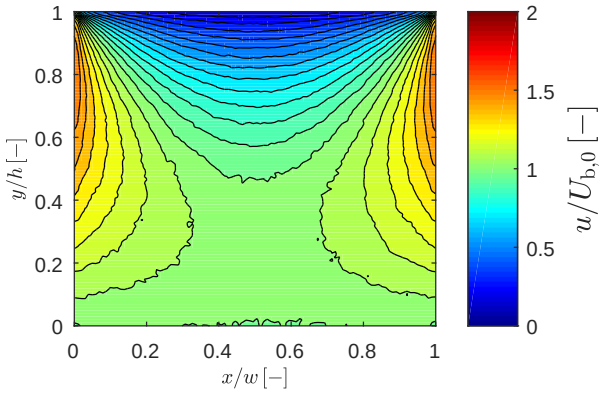

FIG. 6.22 Velocity field of the DSMC results with $\eta = 1$, $\delta = 10$ and $\alpha = 1$ following the boundary conditions of Eq. (6.121).[192]

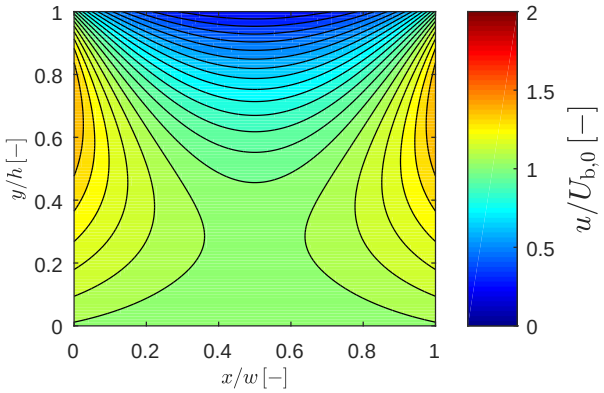

FIG. 6.23 Velocity field of the analytical solution (Eq. (6.92)) with $\eta = 1$, $\delta = 10$ and $\alpha = 1$ following the boundary conditions of Eq. (6.121).[192]

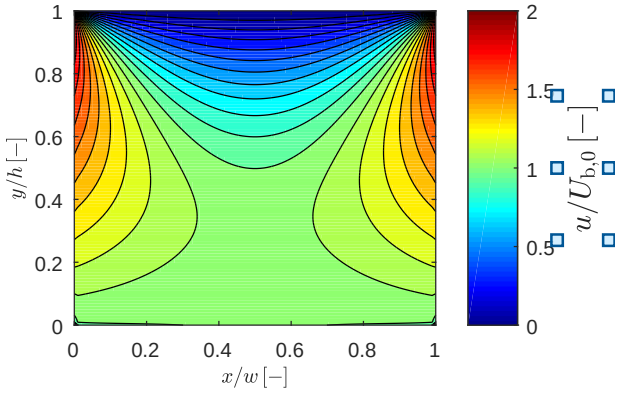

FIG. 6.24 Velocity field of the Couette flow (Eq. (6.79)) with $\eta = 1$ and $\delta \to \infty$ following the boundary conditions of Eq. (6.121).[192]

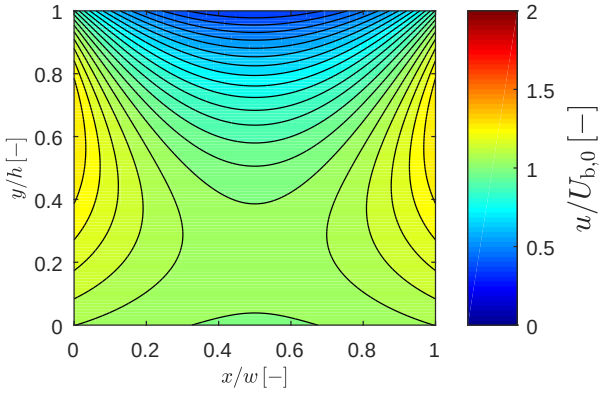

FIG. 6.25 Velocity field of the Couette flow (Eq. (6.92)) with $\eta = 1$ and $\delta = 10$ with $\alpha_\mathrm{h} = \alpha_\mathrm{v} = 0.71$ following the boundary conditions of Eq. (6.121).[193]

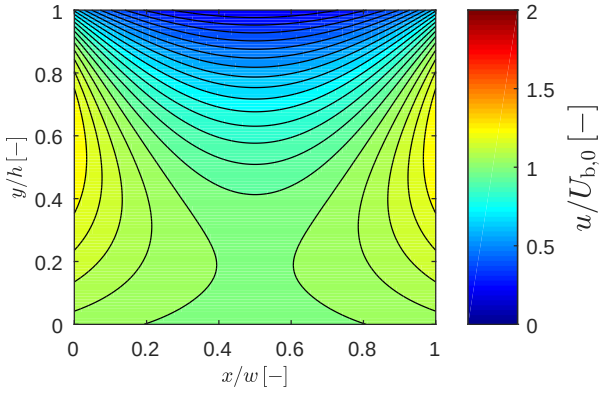

FIG. 6.26 Velocity field of the Couette flow (Eq. (6.92)) with $\eta = 1$ and $\delta = 10$ with $\alpha_\mathrm{h} = 0.92$ and $\alpha_\mathrm{v} = 0.71$ following the boundary conditions of Eq. (6.121).[193]

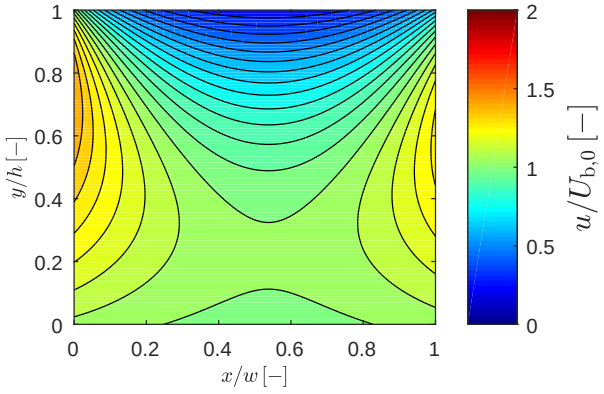

FIG. 6.27 Velocity field of the Couette flow (Eq. (6.92)) with $\eta = 1$ and $\delta = 10$ following the boundary conditions of Eq. (6.121). TMACs of the walls are $\alpha_\mathrm{r} = 0.7$, $\alpha_\mathrm{b} = 0.8$, $\alpha_\mathrm{t} = 0.9$, $\alpha_\mathrm{l} = 1$.[193]

In Fig. 6.25, all walls have a TMAC $\alpha_\mathrm{h} = \alpha_\mathrm{v} = 0.71$ for $\delta = 10$ and $\eta = 1$. It is obtained that due to the reduced friction compared to the diffuse wall scattering in Fig. 6.23 the difference between maximum and minimum velocity is even lower. Therefore, the fluid velocity at the static wall is slightly larger and at the moving walls slightly lower. Nevertheless, the same integral mass flow rate is obtained. In Fig. 6.26, the horizontal walls have a TMAC $\alpha_\mathrm{h} = 0.92$. Therefore, the walls with lower wall velocities cause a relatively higher friction, which leads to lower flow velocities and, therefore, a reduced mass flow rate. The resulting velocity field is still symmetric. Figure 6.27 shows the contour plot of the velocity field with all walls having different TMACs which is not symmetric any more and the highest flow velocity occurs on the left wall with $\alpha_\mathrm{l} = 1$. The right wall has the same wall velocity as the left wall, but a lower TMAC $\alpha_\mathrm{r} = 0.7$. Therefore, the flow velocity at this wall is much lower.

6.3 Applications and Application Limits

In this section further applications and their limits of the derived flow rates are discussed. Therefore, a dimensional analysis is performed in order to obtain the number of dimensionless parameters needed to fully describe the Couette and the Poiseuille flow in a rectangular channel in the absence of turbulence under isothermal conditions. The ideal gas law

$$\rho = \frac{p}{R \cdot T} \tag{6.122}$$

is applied and a low Reynolds number

$$Re = \frac{\rho D_\mathrm{h} \bar{u}}{\mu} \tag{6.123}$$

and a low Mach number

$$M^2 = \frac{\bar{u}^2}{\gamma R T} \ll 1 \tag{6.124}$$

are assumed as turbulence effects and inertial forces are neglected and to ensure the isothermal conditions[81,118,163–166]. In this representation

$$\bar{u} = \frac{\dot{m}}{\rho A} \tag{6.125}$$

is the average velocity in a cross section, $D_\mathrm{h} = 4A/P$ is the hydraulic diameter, while P is the cross section's perimeter and γ is the heat capacity ratio. Furthermore, it is assumed that the channel height is significantly larger than the molecular diameter.

6.3.1 Poiseuille Flow

For the Poiseuille flow the mass flow rate is a function of the channel shape with the height h and the width w. The thermodynamic state is prescribed by the pressure p and the pressure gradient $\partial p/\partial z$ and the isothermal temperature T. Further influence parameters are the gas properties dynamic viscosity μ and the specific gas constant R and the wall TMACs α_i of each wall. Therefore, the mass flow rate $\dot{m}$ is influenced by seven dimensioned parameters with four SI units kg, m, s and K and the up to four already dimensionless TMACs of the walls. According to Buckingham's theorem[190], this leads to the following dimensionless parameters, which describe the problem completely: G_P,

δ,η, $\frac{h}{p}\frac{\partial p}{\partial z}$ and the TMACs. For the plane or pipe flow η vanishes. As stated in Refs. [78, 85, 87] the dimensionless pressure gradient in any cross section needs to be small:

$$\left|\frac{h}{p}\frac{\partial p}{\partial z}\right| \ll 1 \tag{6.126}$$

For the slip regime the mass flow rate can be calculated for any pressure difference from inlet pressure p_{in} to outlet pressure p_{out}. Therefore, the definition of the reduced flow rate of Eq. (6.25) is used and integrated along the channel length:

$$\int_{p_{\mathrm{in}}}^{p_{\mathrm{out}}} G_P \, \mathrm{d}p = -\int_0^L \frac{\dot{m} c_{\mathrm{m}}}{hA} \, \mathrm{d}z \tag{6.127}$$

Using for G_{P} the definition of Eq. (6.47) for the slip regime of a rectangular channel with the implicit treatment of $\delta(p)$, this is solved by

$$\dot{m} = -\frac{hA\Delta p}{c_{\mathrm{m}} L} G_P(\bar{\delta}) \tag{6.128}$$

with

$$\Delta p = p_{\mathrm{out}} - p_{\mathrm{in}} \tag{6.129}$$

and G_{P} evaluated with the average gas rarefaction parameter

$$\bar{\delta} = \frac{h(p_{\mathrm{in}} + p_{\mathrm{out}})}{2\mu c_{\mathrm{m}}} \, . \tag{6.130}$$

This is also valid for the plane flow and the pipe flow using Eqs. (6.54) and (6.60). Although the representation is a bit different from the mass flow rate of a plane Poiseuille flow found in Refs. [79, 118], it can be shown that the expressions are equivalent.

For the transitional regime Eq. (6.128) is only valid if the pressure difference is small

$$\frac{|p_{\mathrm{in}} - p_{\mathrm{out}}|}{p_{\mathrm{in}}} \ll 1 \, . \tag{6.131}$$

Otherwise a numerical integration is needed using local values for G_{P} depending on the pressure at each location. The mass flow rate for prescribed inlet and outlet pressure can be found with a shooting method, for example, using a bisection method that fits the mass flow rate in a way that the boundary conditions are preserved (see for example section 18.1 in Ref. [202]). The impact of the cross section ratio η, the gas rarefaction parameter δ and the different TMACs α on the Poiseuille flow is studied in Sec. 6.1.4.

6.3.2 Couette Flow

The dimensional analysis for the pure Couette flow in a rectangular channel with diffuse walls under isothermal conditions has been discussed in Ref. [192] where the dimensioned influence parameters for the mass flow rate caused by the movement of each wall are the channel height h, channel width w, pressure p, temperature T, specific gas constant R and the dynamic viscosity μ as well as the wall velocity of the ith wall U_i. Furthermore, as stated before, for the Poiseuille flow, the TMACs

α_i of each wall are dimensionless influence parameters. This again leads to a set of dimensionless parameters G_C, δ, η and $u_0 = U_i/c_\mathrm{m}$ as well as the up to four TMACs α_i.

As the pure Couette flow has no gradient in flow direction, the mass flow rate can directly be calculated if G_C is known and no further integration is needed. Although low Mach numbers are assumed for the Poiseuille flow, this is a non-necessary assumption for the Couette flow as results of the DSMC method in App. A.2 show that for similar setups there is no significant change of the G_C value for wall velocities up to $U_i = c_\mathrm{m}$. Just wall velocities much higher than the most probable molecular speed ($u_0 = 3$) show a slight change of about 2 % in the flow rate. The impact of η and δ as well as the different TMACs α is studied in Sec. 6.2.6.

6.3.3 Couette-Poiseuille Flow

The mass flow rate under the above made assumptions can be calculated by superposition of the mass flow rates of the Couette flow $\dot{m}_\mathrm{C}$ and the Poiseuille flow $\dot{m}_\mathrm{P}$ as shown in Sec. 5.3 to calculate the pressure distribution within the vacuum chamber and is also applied to calculate the mass flow rate in gaps in Refs. [47, 48]:

$$\dot{m} = \dot{m}_\mathrm{C} + \dot{m}_\mathrm{P} = \rho A \sum_{i=1}^{4} G_{\mathrm{C},i} U_i - \frac{hA}{c_\mathrm{m}} G_\mathrm{P} \frac{\partial p}{\partial z} \tag{6.132}$$

which is constant in any cross section due to conservation of mass. Rearranging the equation as done in Eq. (6.132) together with Eq. (6.126), this leads to an applicability condition for the resulting differential equation

$$\left| \frac{h}{p} \frac{\partial p}{\partial z} \right| = \left| \frac{1}{G_\mathrm{P}} \left(\frac{2 \sum_{i=1}^{4} G_{\mathrm{C},i} U_i}{c_\mathrm{m}} - \frac{C_0}{\sqrt{\pi}} \right) \right| \ll 1 \tag{6.133}$$

with

$$C_0 = \frac{\dot{m} \sqrt{\pi} c_\mathrm{m}}{pA} \tag{6.134}$$

being the mass flow rate related to the effusion mass flow rate of the channel. With this normalisation one can observe the applicability of the procedure for a Couette-Poiseuille flow in the whole range of the gas rarefaction.

This procedure can also be applied to channels with variable cross section with $h(z)$ in case the inertial forces are small, which is obtained if

$$\left| \frac{\partial h}{\partial z} \right| Re \ll 1 \,. \tag{6.135}$$

This condition can be derived from Ref. [71] and a validation for the plane rarefied Couette-Poiseuille flow with variable cross section is given in Ref. [47] with measurements and a comparison to DSMC simulations is done in Ref. [48]. For higher Reynolds or Mach numbers, inertial forces cannot be neglected and an isothermal assumption in the whole channel is not valid. In this case the differential equation derived by Shapiro[113] should be solved, which is applied to rarefied gases for a plane Poiseuille flow by Müller[46] and to a rarefied Couette-Poiseuille flow with variable cross

section by Jünemann[49]. Following the procedure of Jünemann[49] and neglecting thermal creep flow, a friction factor f_z is defined as follows:

$$\mathrm{d}p = -f_z \frac{\rho \bar{u}^2}{2} \frac{\mathrm{d}z}{D_\mathrm{h}} \tag{6.136}$$

Using Eq. (6.132) with Eq. (6.125) one obtains the following expression:

$$\mathrm{d}p = -\underbrace{\frac{4\left(\frac{D_\mathrm{h}}{h}\right)^2 \delta}{G_\mathrm{P} Re}\left(1 - \frac{\sum_{i=1}^{4} G_{\mathrm{C},i} U_i}{\bar{u}}\right)}_{f_z} \frac{\rho \bar{u}^2}{2} \frac{\mathrm{d}z}{D_\mathrm{h}} \tag{6.137}$$

The friction factor can be expressed as a function of the Poiseuille number

$$Po = 4\left(\frac{D_\mathrm{h}}{h}\right)^2 \frac{\delta}{G_\mathrm{P}}, \quad Re < 3000 \tag{6.138}$$

as follows:

$$f_z = \frac{Po}{Re}\left(1 - \frac{\sum_{i=1}^{4} G_{\mathrm{C},i} U_i}{\bar{u}}\right) \tag{6.139}$$

Using this expression for the friction factor the differential equation in Ref. [49] can be solved for a rectangular channel with any TMAC combination and different wall velocities for each surrounding wall. For a plane flow with diffuse walls Eq. (6.139) is reduced to

$$f_z = \frac{Po}{Re}\left(1 - G_\mathrm{C} \frac{U_1 + U_2}{\bar{u}}\right) \tag{6.140}$$

which is equal to equation 47 in Ref. [49].

7 Inhomogeneous Chamber States

Once the closure problem of the 1D model for calculating the inhomogeneous chamber states has been solved, the question arises as to whether the flow in the chamber has a 1D character. Therefore, a validation of the geometric abstraction is given in this chapter by means of 3D Computational Fluid Dynamics simulations (CFD) using ANSYS CFX 2021 R2[167] where the Navier-Stokes-Fourier equations (NSF) are solved numerically as explained in Sec. 4.1. For this study the midpoint pressure p^*_{ch} is prescribed. Afterwards a detailed parameter study taking all the influence parameters identified in Sec. 5.2 is performed with the 1D model. It will be shown, that the main results of the study can be reproduced by means of an approximative analytical function depending on the dimensionless pressure gradient which is only evaluated using the mass averaged pressure p_{ch}. The dimensionless numbers used in this chapter are explained in Sec. 5.2, where the values marked with an * are related to the midpoint pressure p^*_{ch} and the ones without to the mass averaged pressure p_{ch}.[I]

7.1 CFD Model

In this section the CFD model for the 3D simulations is explained. The used mesh including the boundaries are shown in Fig. 7.1. The setup is designed to be similar to the experimental test rig shown in Chap. 8. Therefore, one vacuum chamber with zero rotor lead but a constant width of $w = 15$ mm is simulated. Similar to the real machine, the chamber is encapsulated due to the other rotor which forms a radial clearance. In order to vary the clearance mass flow rate $\dot{m}_{\mathrm{cl,t}}$ this radial clearance is replaced by an inlet and an outlet where the same mass flow rate is prescribed with a uniform velocity profile. The distance between inlet and outlet is 20 mm. The system pressure p^*_{ch} is prescribed with a pressure opening in the middle of the chamber. The inner diameter and the side wall are rotating around the rotation axis. The opposite boundary of the side wall is a symmetry plane. The other walls are static. For all walls Maxwell slip boundary conditions with accommodation coefficients $\alpha = 1$ according to Eqs. (3.102), (3.106) and (4.27) are used in order to improve the results for the slip regime $\delta^* \geq 10$. For lower gas rarefaction parameters the first order slip boundary condition models too much friction with an increasing discrepancy to the kinetic theory of gases with decreasing gas rarefaction parameter[9,87]. This is shown and discussed in the next section. In order to compare the results to the 1D model the chamber's high pressure p_{HP} and low pressure p_{LP} are evaluated as an area average as shown in Fig. 7.1.

[I] Parts of this chapter are reproduced from "H. Pleskun, T. Jünemann and A. Brümmer, "Validation of inhomogeneous chamber states in rotary positive displacement vacuum pumps," IOP Conf. Ser.: Mater. Sci. Eng. **1267**, 012010 (2022)", with permission of IOP Publishing published under the CC BY license.[187]

The domain's outer diameter D_o is 170 mm and the inner diameter D_i is 100 mm. The opening size is $20 \times 20 \times 7.5$ mm and is placed in the middle of the chamber on the opposite side of the radial clearance. Due to the symmetry plane the actual domain width is half the chamber width. The mass flow rate through the opening in steady state is numerically zero. The temperature at the walls is fixed to $T = 298.15$ K and is equal to the temperature at the opening and the inlet.

A Richardson extrapolation according to references [205] and [206] with two finer meshes and a constant refinement factor of $r_f = 1.5$ in all directions for the case $\delta^* = 10$ and $\delta^* = 100$, $u_0 = 0.12$ and $C_0^* = 0.01$ has been performed. For $\delta^* = 10$ the numerical error of the used mesh to the theoretically exact value for the pressure ratio is $\frac{\Delta(p_{HP}/p_{ch}^*)}{p_{HP}/p_{ch}^*} \approx 1$ % and $\frac{\Delta(p_{HP}/p_{LP})}{p_{HP}/p_{LP}} \approx 2.8$ %. For $\delta^* = 100$ the numerical errors for the pressure ratio are $\frac{\Delta(p_{HP}/p_{ch}^*)}{p_{HP}/p_{ch}} \approx 0.3$ % and $\frac{\Delta(p_{HP}/p_{LP})}{p_{HP}/p_{LP}} \approx 0.8$ %.

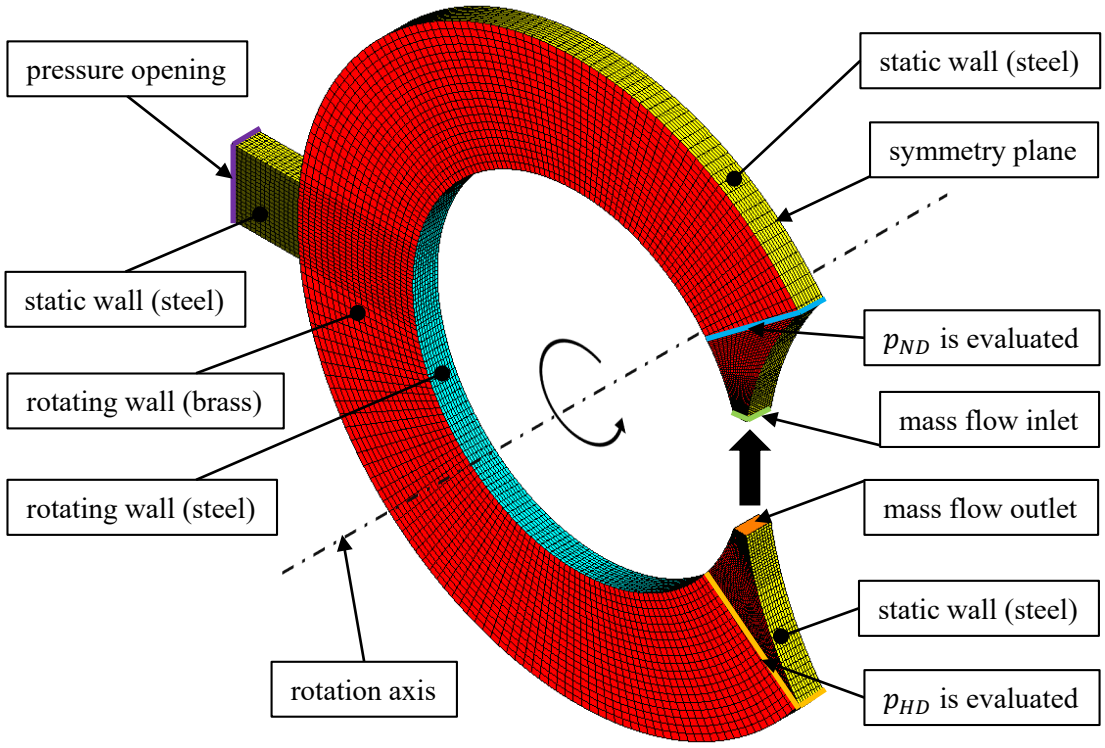

FIG. 7.1 3D domain of the vacuum chamber for CFD simulations with Ansys CFX.

7.2 Validation of the 1D Model

In order to compare the results of the 1D model to those of the CFD simulations for equal boundary conditions the pressure is prescribed in the middle of the chamber at $z = L/2$ with the opening pressure p_{ch}^* and Eq. (5.20) defines an initial value problem in positive and negative direction as explained in Sec. 5.3 to get the high pressure p_{HP} at $z = L$ and the low pressure p_{LP} at $z = 0$ respectively. Figure 7.2 shows the pressure ratio p_{HP}/p_{ch}^* as a function of the gas rarefaction parameter δ^* for different speed ratios, with p_{ch}^* the opening pressure (CFD) or midpoint pressure (1D). The normalised mass flow rate is $C_0^* = 0$. For this purpose in CFD the inlet and outlet are replaced by static walls. The results of the 1D model show a maximum of the pressure ratio at $\delta^* \approx 0.5$. For $\delta^* < 0.5$ the pressure ratio tends to an asymptotic value for the free molecular flow. For $\delta^* > 0.5$ the pressure ratio tends to unity, thus for the hydrodynamic regime $\delta^* > 1000$ a homogeneous chamber state is obtained.

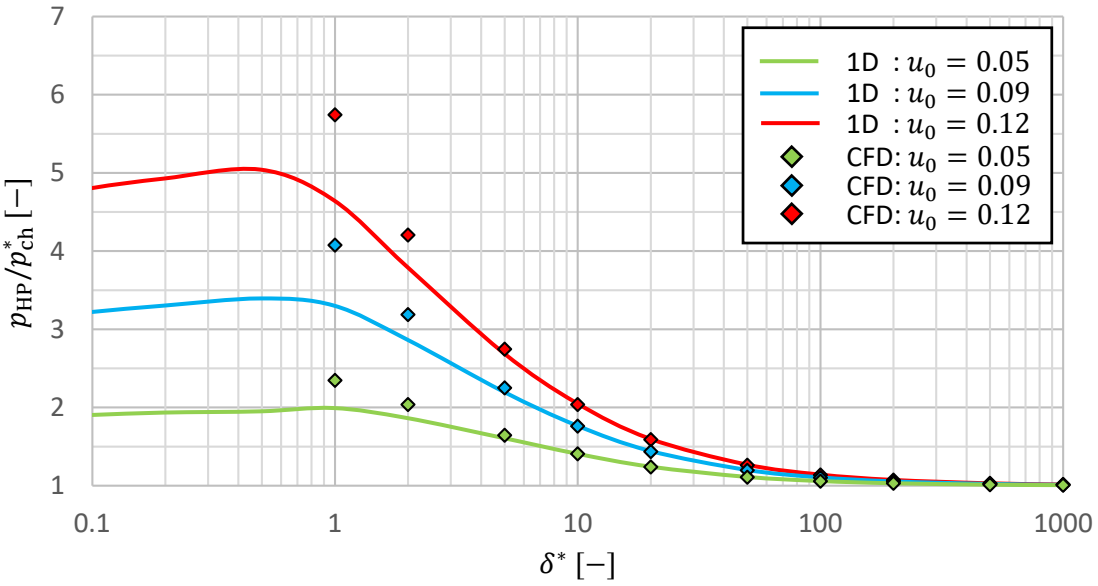

FIG. 7.2 Comparison of the pressure ratio p_{HP}/p^*_{ch} between 1D model and CFD for different speed ratios u_0 for $C^*_0 = 0$.

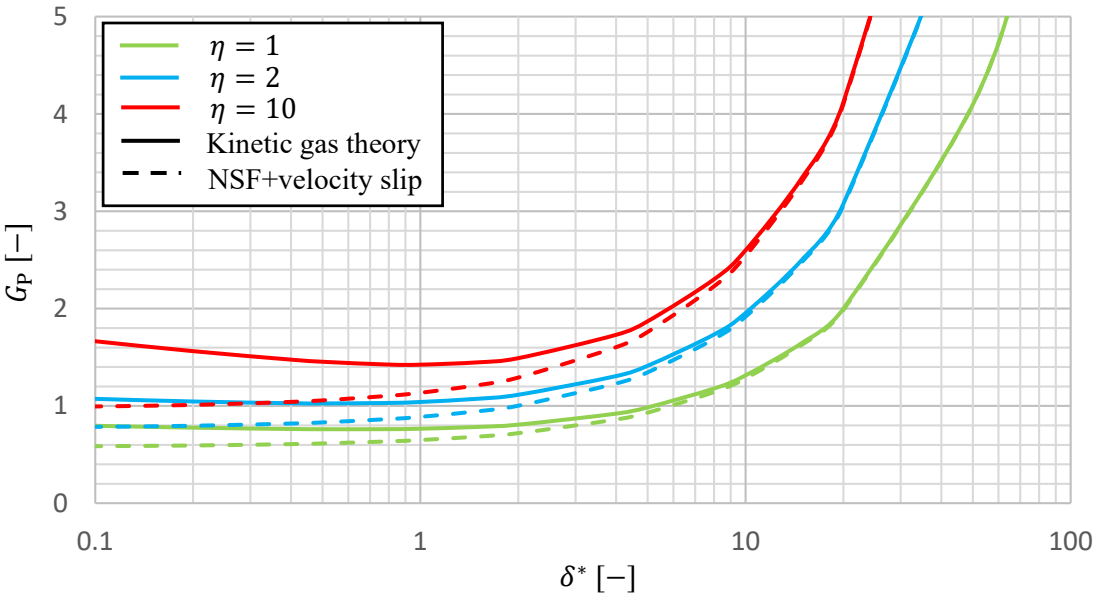

FIG. 7.3 Comparison of the reduced Poiseuille flow rate as a function of the gas rarefaction parameter δ for different width to heigh ratios η according to Tab. II in Ref. [87] and Eq. (6.42).

Generally the pressure ratio increases with a higher speed ratio u_0. The results of the 1D model and of the CFD simulations are in good agreement for $\delta^* > 10$ as the velocity slip boundary condition is applicable there. For $\delta^* < 10$ the Boltzmann equation based on the kinetic theory of gases has to be solved. In this regime the pressure ratio obtained by CFD is higher than that of the 1D model. This can be explained with the behaviour of the reduced Poiseuille flow rate G_P shown in Fig. 7.3 for different width to height ratios η. The values for the diagram can be derived from the data given by Sharipov[87]. The results of the kinetic gas theory deliver the well-known Knudsen minimum[8] whereas the NSF equations with velocity slip boundary conditions do not show this minimum but tend monotonically to an asymptotic value lower than that of the kinetic theory. This behaviour is

seen in the results of the pressure ratio. As the Couette flow is not as sensitive to the gas rarefaction as the Poiseuille flow, the pressure ratio has its maximum at a similar rarefaction parameter where the reduced Poiseuille flow rate has its minimum. For the CFD simulations a too large amount of friction is modelled which leads to a lower reduced Poiseuille flow rate. This means an increasing pressure gradient is needed to compensate the Couette flow resulting in higher calculated pressure ratios.

On the other side for large values of δ^* a very small pressure gradient is sufficient to compensate the mass flow rate caused by the Couette flow. As the Knudsen minimum is not depicted by the NSF equations, the pressure ratio for small values of δ^* is higher than that depicted by the 1D model. And thus the 1D model provides even more physically reasonable results. The same behaviour is obtained for the pressure ratio $p_{\mathrm{HP}}/p_{\mathrm{LP}}$ shown in Fig. 7.4 but on a much higher level. Note that a higher temperature level has the same effect on the pressure distribution as a lower rotational speed.

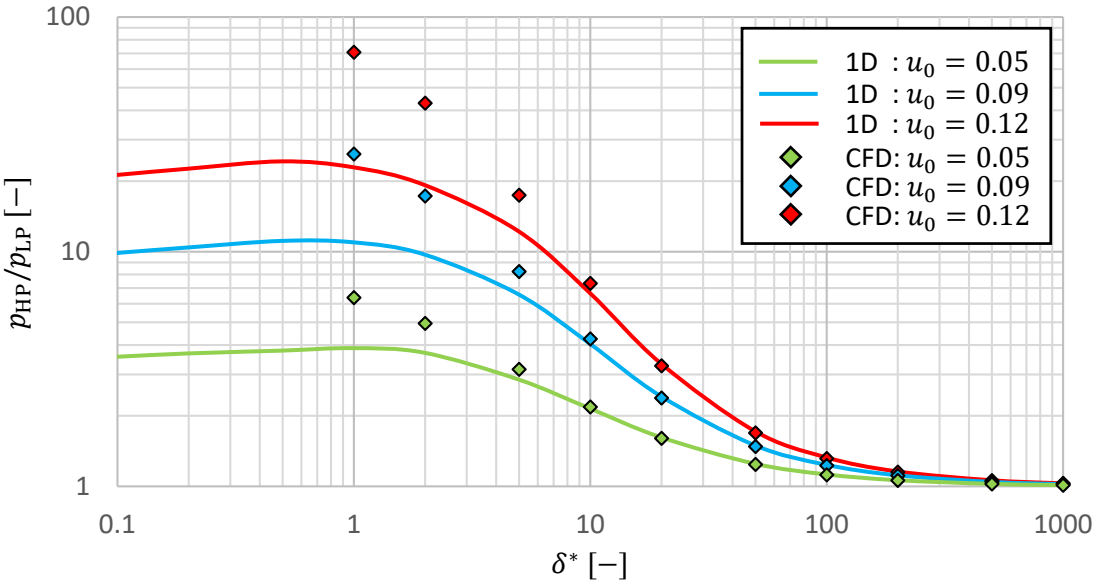

FIG. 7.4 Comparison of the pressure ratio $p_{\mathrm{HP}}/p_{\mathrm{LP}}$ between 1D model and CFD for different speed ratios u_0 for $C_0^* = 0$.

Figure 7.5 shows the normalised pressure distribution as a function of the normalised chamber length for a speed ratio $u_0 = 0.12$ and a mass flow ratio $C_0^* = 0$. The plot for the CFD results is the pressure distribution along the pitch circle between the planes where high and low pressure are evaluated. Within the slip regime for $\delta^* = 20$ the pressure distributions of 1D and CFD results match perfectly and the pressure distribution is nearly linear. In the transition regime $\delta^* = 2$ the pressure distribution is not linear any more and according to the deviations in the previous plots the CFD simulation shows a higher gradient than the 1D model. The non-linearity in the pressure distribution implies that there is a deviation between the midpoint pressure p_{ch}^* and the mass averaged pressure p_{ch}. Thus, in order to assure conservation of mass in chamber model simulation the mass averaged pressure p_{ch} has to fulfil the total mass within the chamber and it is not sufficient to take the midpoint pressure p_{ch}^*.

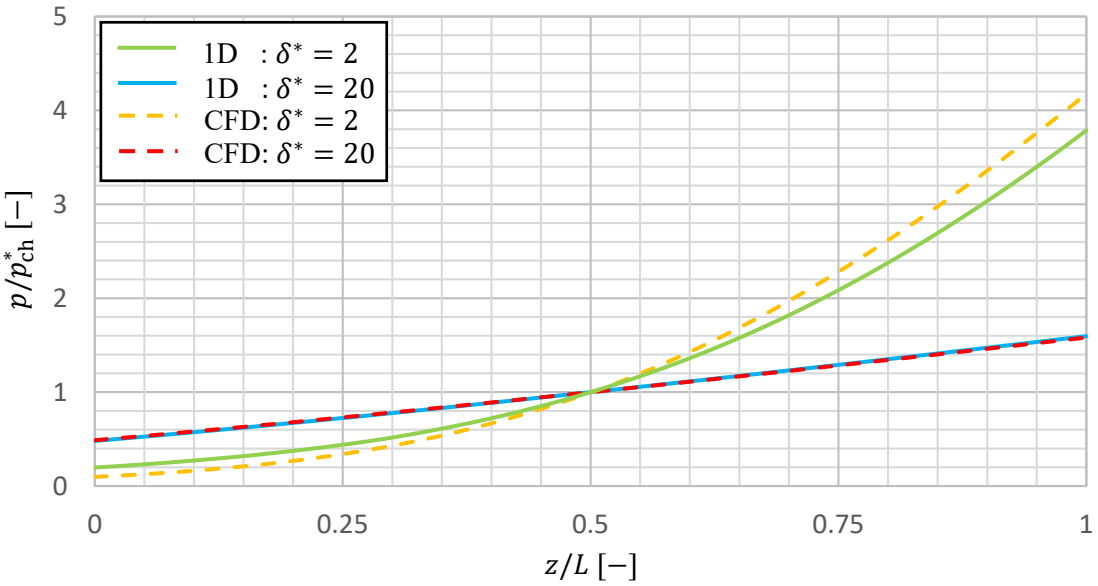

FIG. 7.5 Comparison of the normalised pressure distribution between 1D model and CFD for $u_0 = 0.12$ and $C_0^* = 0$

Figures 7.6 and 7.7 show the impact of a steady clearance mass flow rate carried along the chamber. Such a mass flow rate slightly reduces the impact of the Couette flow within the chamber and as a result the pressure ratio shrinks. Again CFD and 1D model are in good agreement for $\delta^* > 10$. Although the NSF equations are not exact in the transition regime $\delta^* < 10$ the qualitative behaviour of both models is the same. Note that quite a high normalised mass flow rate is needed to have a significant impact on the pressure distribution. Huck's[12,47] measurements show that the typical mass flow rates for rarefied gap flows including positive wall movement in this regime are $0.01 < C_0^{\mathrm{cl}} < 0.4$ with C_0^{cl} related to the minimum clearance cross section area which is typically more than factor 100 smaller than the chamber's cross section area. So there might only be a small impact if the gap heights and pressure ratios are large.

Figures 7.8 and 7.9 show the impact of a steady normalised housing gap mass flow rate $C_{0,\mathrm{h}}^*$ carried along the chamber with an additional constant tangential mass flow rate $C_0^* = 0.01$ for $u_0 = 0.12$. The housing gap mass flow rate $\dot{m}_{\mathrm{h}}$ is modelled as mass source coming from the housing with the assumption that it is equally distributed along the chamber length. The normalisation to $C_{0,\mathrm{h}}^*$ is still performed with the chamber cross section area and midpoint pressure equal to C_0^*. To reach a steady state, the sum of $C_0^* + C_{0,\mathrm{h}}^*$ is modelled as the mass flow outlet. Therefore, the mass flow rate increases with a linear function from p_{LP} to p_{HP}. This procedure is adapted for the 1D model and therefore the mass flow rate $\dot{m}_{\mathrm{cl,t}}$ is not a constant, but a linear function of the length coordinate z, if the housing gap mass flow rate is taken into account. Again a good agreement between CFD and 1D model is achieved for $\delta^* \geq 10$ with the increasing deviation for $\delta^* < 10$. It needs to be noted that typically there is an incoming housing clearance mass flow rate and an outflowing housing clearance mass flow rate within a chamber, so this mass source model only takes the difference of both mass flow rates into account.

Finally, the impact of the rotor material is investigated and shown in Figs. 7.10 and 7.11. In technical applications is is mostly air that collides with steel walls. In the literature, TMACs for

this configuration are obtained by measurements in the range of $0.86 \leq \alpha \leq 1.01$ (see Ref. [116]). This effect is often neglected and mostly the assumption of diffuse wall scattering is made for the sake of simplicity. Now the case is investigated, that the rotor has a TMAC $\alpha_\mathrm{r} = 0.9$. For air molecules colliding with aluminium walls a TMAC $\alpha_\mathrm{r} = 0.72$ is obtained[116]. It is assumed that the housing has a TMAC $\alpha_\mathrm{h} = 1$ and the rotor material is exchanged by varying α_r. It can be seen that the gas surface interaction has a much higher impact on the pressure distribution within the chamber than a clearance mass flow rate and the pressure ratio within the chamber significantly shrinks with a decreasing TMAC. Both the 1D model and the CFD simulations are in perfect agreement for $\delta^* > 10$ with the previously mentioned higher deviation in the transitional regime.

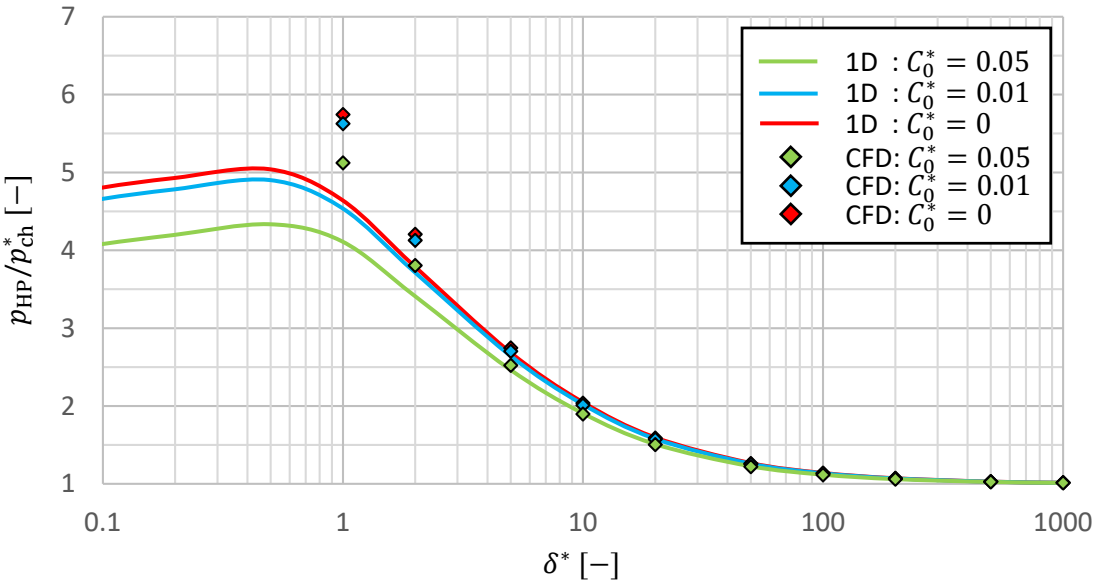

FIG. 7.6 Comparison of the pressure ratio $p_\mathrm{HP}/p^*_\mathrm{ch}$ between 1D model and CFD for different mass flow ratios C_0^* for $u_0 = 0.12$.

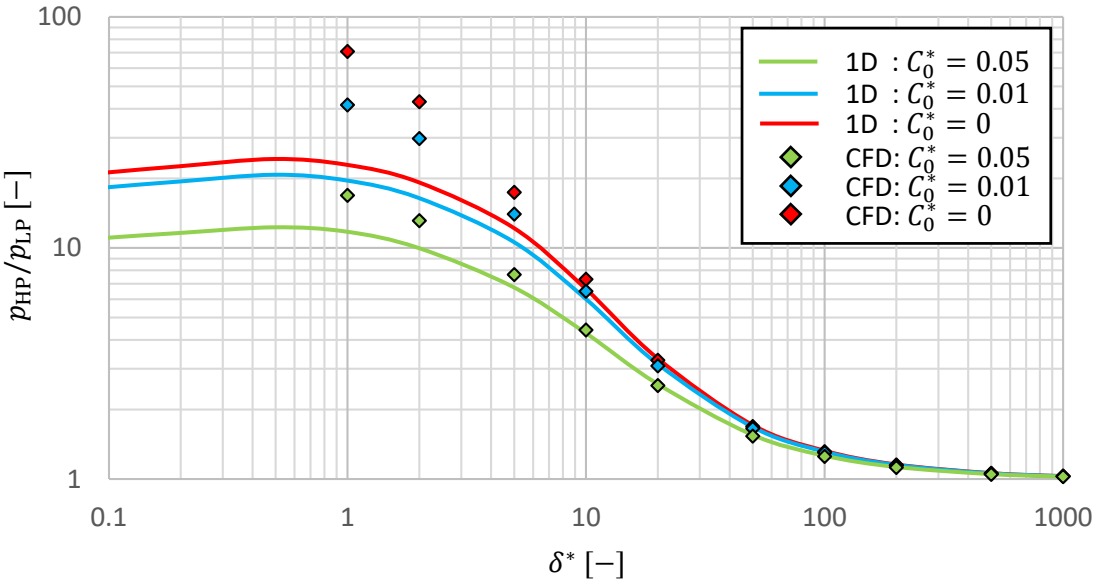

FIG. 7.7 Comparison of the pressure ratio $p_\mathrm{HP}/p_\mathrm{LP}$ between 1D model and CFD for different mass flow ratios C_0^* for $u_0 = 0.12$.

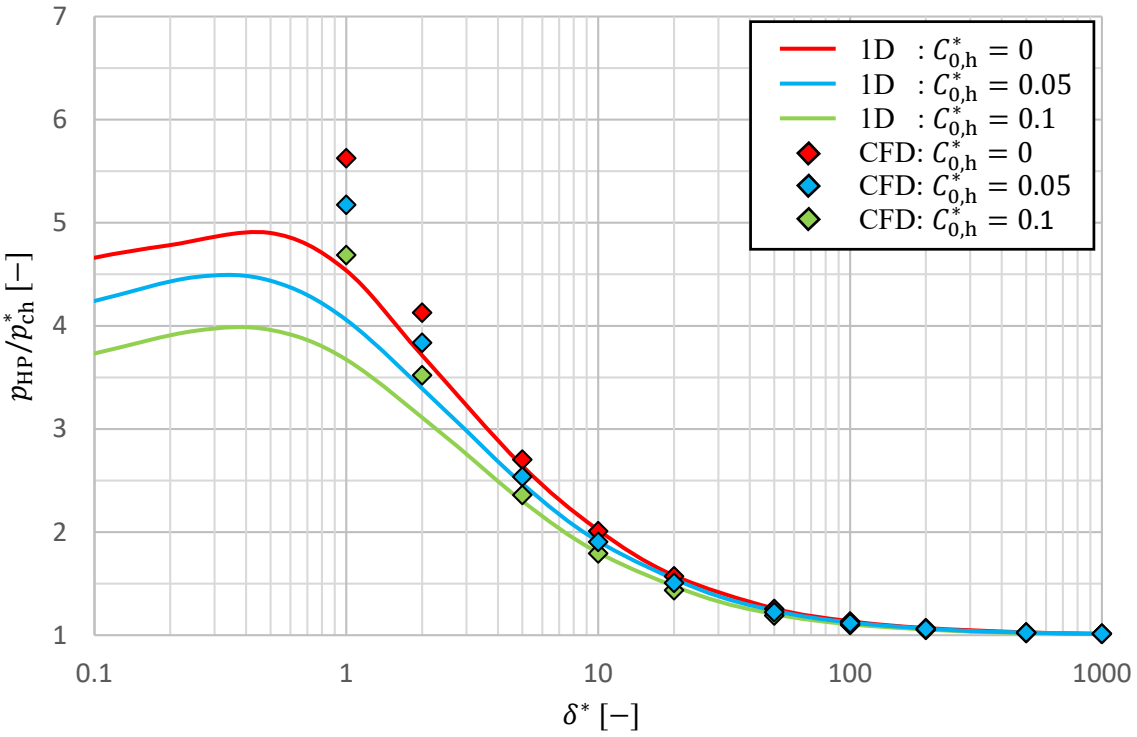

FIG. 7.8 Comparison of the pressure ratio p_{HP}/p^*_{ch} between 1D model and CFD for different mass flow ratios of the housing clearance $C^*_{0,h}$ for $u_0 = 0.12$ and $C^*_0 = 0.01$.

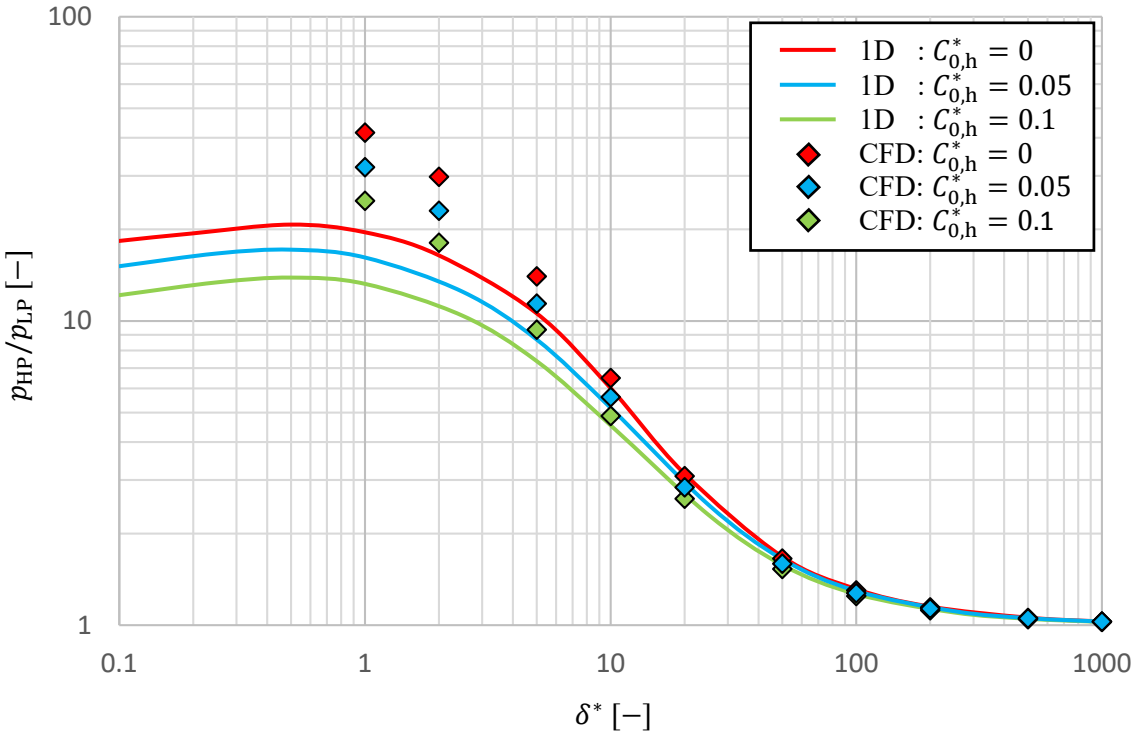

FIG. 7.9 Comparison of the pressure ratio p_{HP}/p_{LP} between 1D model and CFD for different mass flow ratios of the housing clearance $C^*_{0,h}$ for $u_0 = 0.12$ and $C^*_0 = 0.01$.

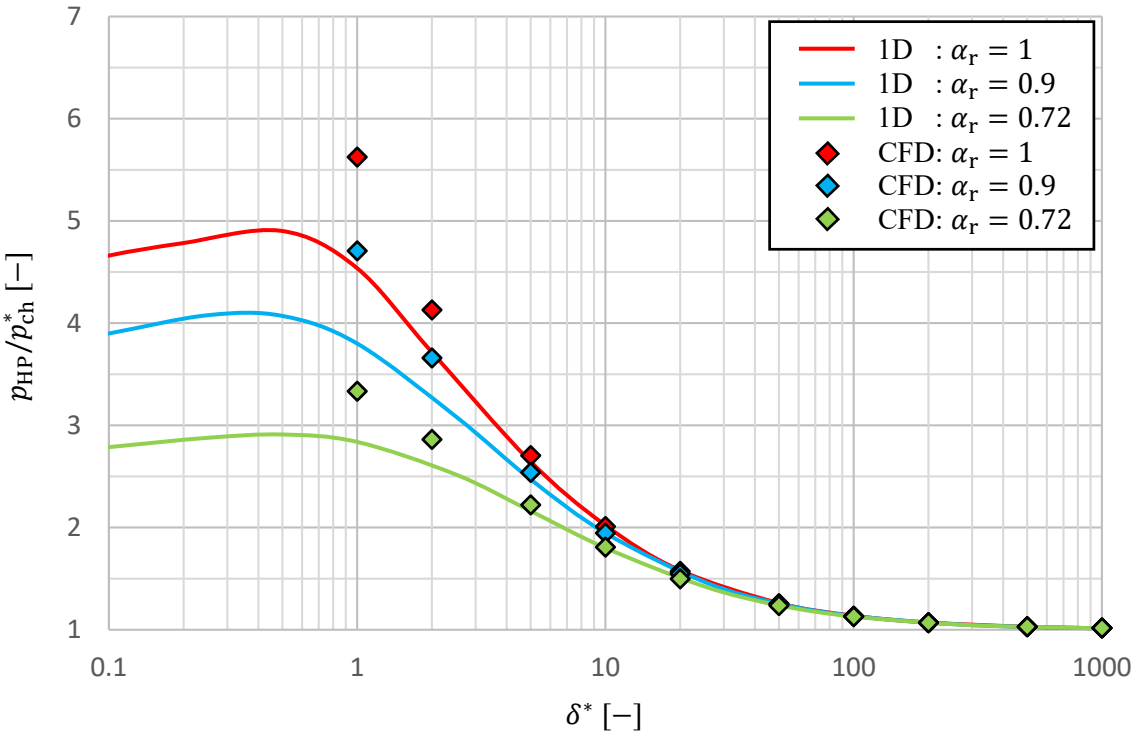

FIG. 7.10 Comparison of the pressure ratio p_{HP}/p^*_{ch} between 1D model and CFD for different α_r with $\alpha_h = 1$, $C^*_0 = 0.01$ and $u_0 = 0.12$.

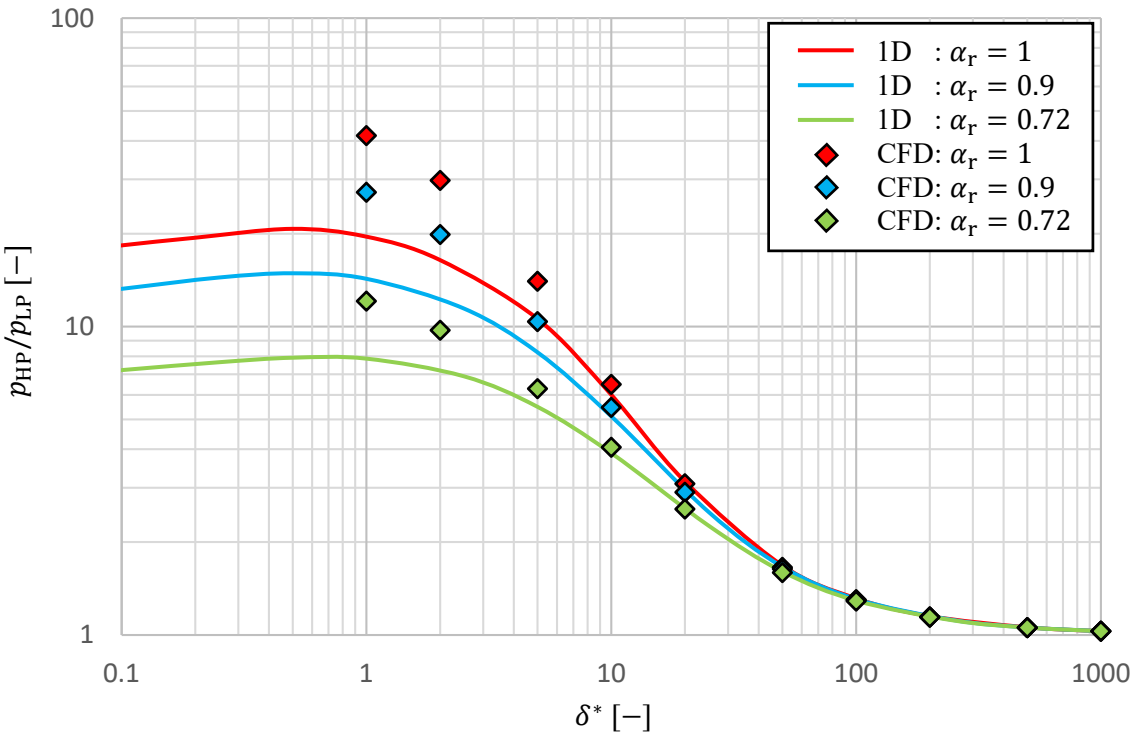

FIG. 7.11 Comparison of the pressure ratio p_{HP}/p_{LP} between 1D model and CFD for different α_r with $\alpha_h = 1$, $C^*_0 = 0.01$ and $u_0 = 0.12$.

TAB. 7.1 Different simulation configurations for the empirical study

D_o/D_i	D_o/s	u_0	C_0^*	Z	α_h	α_r	gas
1.7	2	0.12	0	1	1	1	air
1.7	2	0.12	0	2	1	1	air
1.7	2.8	0.12	0	1	1	1	air
1.7	2.8	0.12	0	2	1	1	air
1.7	2.8	0.12	0.05	2	1	1	air
1.7	2.8	0.12	0.1	2	1	1	air
1.7	2.8	0.155	0.01	2	1	1	air
1.7	2.8	0.09	0.01	2	1	1	air
1.5	2.8	0.12	0.01	2	1	1	air
1.9	2.8	0.12	0.01	1	1	1	air
1.7	2.8	0.12	0.01	2	1	0.72	air
1.7	2.8	0.12	0.01	2	1	0.9	air
1.7	2.8	0.06	0.01	2	0.83	0.83	H_2
1.7	2.8	0.034	0.01	2	0.83	0.83	H_2
1.7	2.8	0.155	0.05	2	1	1	air
1.571	5.641	0.14	0.05	2	1	1	air
1.571	5.641	0.14	0.1	2	1	1	air
1.571	5.641	0.14	0.2	2	1	1	air

7.3 Approximative Functions Depending on the Dimensionless Pressure Gradient

After the geometrical abstraction of the 1D model is validated, it is ready to use for chamber model simulation, but the computational cost of solving differential equations every time the mass within a chamber changes is non-negligible. Therefore, the pressure distribution is analysed. Following Fig. 2.1, in the context of chamber model simulation the mass averaged pressure p_{ch}, the low pressure p_{LP} and the high pressure p_{HP} of a chamber is needed to correct the boundary conditions, while only the mass averaged pressure p_{ch} is known. In the following cases the dimensionless numbers of Sec. 5.2 are varied related to the mass averaged pressure p_{ch} as summarized in Tab. 7.1. Therefore, the geometrical ratios, the number of starts Z, the velocity ratio u_0 and the mass flow ratio C_0 are varied in common ranges. Both the housing gap and the other gaps are taken into account. Different TMACs α_r for the rotor are investigated in case the rotor surface material is exchanged. Furthermore, the gas is exchanged to hydrogen with housing and rotor made of steel, where the TMAC is changed to $\alpha_r \approx 0.83$ [189]. The 1D model is used for the simulation results and the pressure ratio p_{HP}/p_{ch} is given as a function of the dimensionless pressure gradient $\mathcal{P}$ given in Eq. (5.21). This function only depends on the geometric ratio $L/\min(h, w)$ where the chamber length is given in Eq. (5.9), the reduced flow rates of the Couette flow G_C and Poiseuille flow G_P (see Chap. 6), the normalised mass flow rate C_0 and the speed ratio U_i/c_m due to the relative wall movements described in Chap. 5. This pressure gradient can be evaluated explicitly without solving a differential equation using the known mass averaged pressure p_{ch} which is implicitly treated in the gas rarefaction parameter δ used to calculate the reduced flow rates G_C and G_P. A simplification is done regarding the reduced mass flow rate for the housing gap for the calculation of $\mathcal{P}$, due the fact that it is not constant along the channel but linearly increasing. Therefore, only half of the maximum value of $C_{0,h}$ is used to calculate the dimensionless pressure gradient for the mass

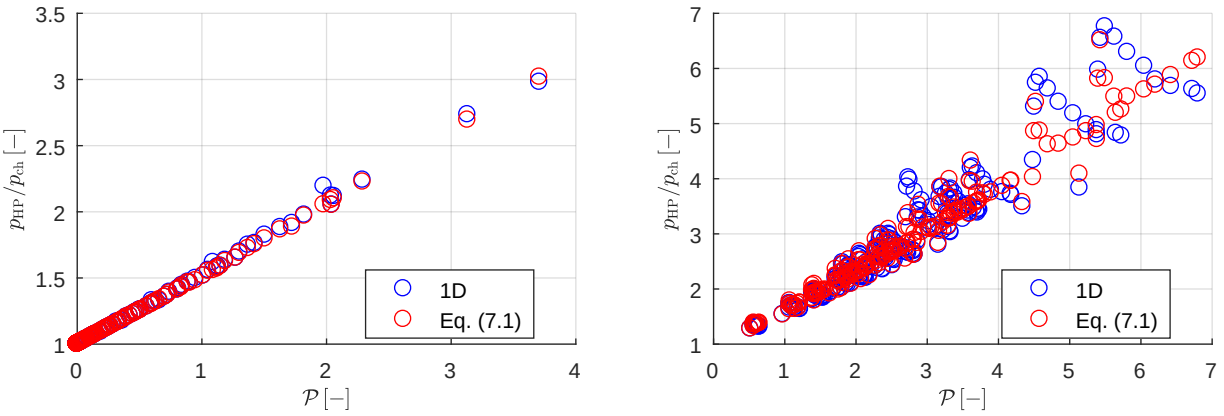

(a) $10 \leq \delta \leq 10^5$ **(b)** $0.001 \leq \delta < 10$

FIG. 7.12 Results of the 1D model compared to Eq. (7.1).

averaged pressure p_{ch}. This simplification is not done for the results of the 1D model as here the mass source model with a non-constant mass flow rate along the chamber is used.

The gas rarefaction parameter is varied in a range $0.001 \leq \delta \leq 100000$ with three values per decade. Regarding Fig. 7.12a, it is obtained that the pressure ratio p_{HP}/p_{ch} is a linear function of the dimensionless pressure gradient $\mathcal{P}$ as long as the gas rarefaction parameter is $\delta \geq 10$. For $\delta < 10$ the pressure ratio differs from the linear function with higher deviations for larger values of the dimensionless pressure gradient. This is taken into account to form the functional in Eq. (7.1) with two constants k_1 and k_2 that are found with a Levenberg-Marquardt[203] algorithm using MATLAB[207]. The overall agreement between the 1D model and Eq. (7.1) is very good for $\delta \geq 10$ with a mean deviation of 0.15 % and depicts the main behaviour in the whole range of the gas rarefaction with a mean deviation of 4.3 % for $\delta < 10$ (see Fig. 7.12b). Especially for a very large dimensionless pressure gradient there are some theoretical operation points that have a deviation between both models of about 20 %.[II]

$$\frac{p_{HP}}{p_{ch}} \approx 1 + \mathcal{P} \cdot \left(\frac{1}{2} + k_1 \cdot \sqrt{\mathcal{P}} \cdot \exp\left(- \left| \ln(\delta + k_2) \right| \right) \right) \tag{7.1}$$
$$k_1 = 0.238 \qquad k_2 = 0.4226$$

Figure 7.13a shows the pressure ratio p_{ch}/p_{LP} as a function of the dimensionless pressure gradient $\mathcal{P}$ for $\delta \geq 10$. It is obtained that this is already a non linear function which starts to spread at $\mathcal{P} > 2$. But a main trend can be seen. The pressure ratio even spreads more from the main trend for low values of the gas rarefaction parameter, which is highlighted in Fig. 7.13b. The main deviations occur on the right hand side of the diagram, which mark the large values of C_0 at $\delta < 10$. As explained before in Figs. 7.6 and 7.7, a mass flow rate within the chamber has a much larger impact on the low pressure than on the high pressure. Therefore, this relation has to be added to the functional in Eq. (7.2) which fits the pressure ratio p_{ch}/p_{LP} as a function of the dimensionless pressure gradient $\mathcal{P}$, δ and u_0/C_0 with seven constants $g_1 - g_7$ which are found with the Levenberg-

[II] The operation points with the largest deviation will not be reached in a fore vacuum pump as the calculated gas rarefaction parameters are too low.

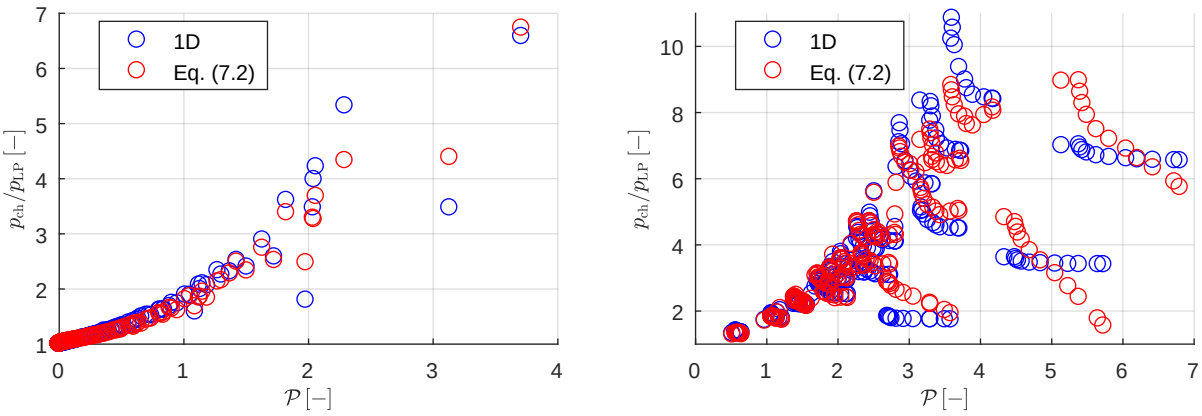

(a) $10 \leq \delta \leq 10^5$ **(b)** $0.001 \leq \delta < 10$

FIG. 7.13 Results of the 1D model compared to Eq. (7.2).

Marquardt algorithm. For $\delta \geq 10$ the mean deviation is about 1.9 %. For $\delta < 10$ the mean deviation is about 9.5 %. Although this deviation seems quite large, it needs to be noted, that the low pressure has a much smaller impact on the adjacent clearances than the high pressure. As the high pressure side typically marks the inlet pressure for the gaps, the resulting mass flow rate scales with this value. The low pressure side of the chamber typically has an impact on the pressure ratio of the certain gap. But this has only a small impact on the resulting mass flow rate which can be seen in Refs. [12, 47, 49]. Moreover, as before, most operation points are within the scope of smaller values of the dimensionless pressure gradient.

$$\frac{p_{ch}}{p_{LP}} \approx 1 + (g_1 \cdot \mathcal{P}^{g_2} + \mathcal{P}^{g_3}) \cdot \left(g_4 + g_5 \cdot \exp\left(-\frac{g_6 \cdot \sqrt{\delta}}{\mathcal{P}}\right)\right) \cdot \left(1 - g_7 \cdot \mathcal{P}\sqrt{\frac{C_0}{u_0}}\right) \tag{7.2}$$

$$g_1 = 1.923 \quad g_2 = 2.23 \quad g_3 = 0.66 \quad g_4 = 0.27 \quad g_5 = -0.095 \quad g_6 = 8.56 \quad g_7 = 0.2$$

8 Experimental Investigations

In this chapter experimental validations for inhomogeneous chambers states are given. Therefore, an experimental test rig is set up to measure the pressure at different positions in a vacuum chamber. At first, the test rig and the corresponding method of measurement is explained leading to the uncertainty estimation. The measurements are compared to results of the 1D model that rebuild the test rig's structure. The experiments have two major purposes. One is to verify the hypothesis that there exist non-negligible inhomogeneous chamber states. The other is to validate the 1D model which has the great advantage of being much more generic. Therefore, a validated model offers the opportunity to make predictions for cases that are not covered with the experimental setup.

8.1 Test Rig

The idea of the experimental setup is to separate the various effects of the whole machine and just focusing on the occurring inhomogeneity within one chamber at different operating points. Two principle sketches are shown in Figs. 8.1 and 8.2 and three photos are shown in Figs. C.1-C.3 to give an overview. A motor drives a rotating shaft on which two brass cylinders of equal size are placed and separated by a sleeve of smaller radius. The vacuum chamber of one rotor without lead is represented by the gap between the two brass cylinders, the sleeve and the housing. A static counter contour represents the gate rotor within the cut lens so that the chamber is encapsulated. The sleeve and the counter contour are exchangeable so that the chamber height h can be changed while the chamber width w is fixed. The counter contour's radial position can be adjusted in order to vary the radial clearance $h_{\mathrm{cl,r}}$ as smallest distance between the sleeve (machine's inner diameter) and the counter contour (gate rotor's outer diameter). There are two additional "inter-lobe" clearances placed between the faces of the counter contour and the two brass cylinders shaped by the cut lens of the two outer diameters. These gaps have an equal clearance $h_{\mathrm{cl,il}}$. The housing clearance between the brass cylinders and the housing is $h_{\mathrm{cl,h}} = 0.15$ mm with a length $L_{\mathrm{cl,h}} = 92.5$ mm on each brass cylinder. There are boreholes in the housing connecting the vacuum chamber at the two cusps with absolute pressure sensors to measure the static low pressure p_{LP} and the static high pressure p_{HP} on both sides of the counter contour. In order to adjust the pressure level within the vacuum chamber a supply line from a recipient is placed on the opposite side of the counter contour in the middle of the vacuum chamber. The recipient has a suction line to a vacuum pump[208] via a valve, thus, the system can be evacuated, and a supply line from the atmosphere via a throttle valve where the pressure level can be adjusted. Therefore, in steady state the pressure within the recipient should equal chamber's midpoint pressure p^*_{ch}.

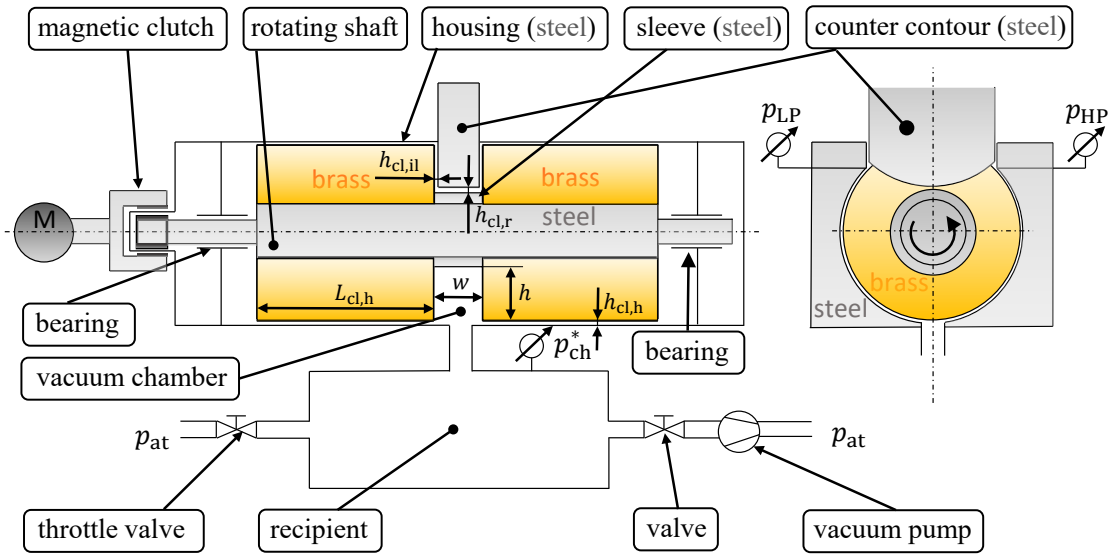

FIG. 8.1 Principle sketch of the test rig of a vacuum chamber without lead.

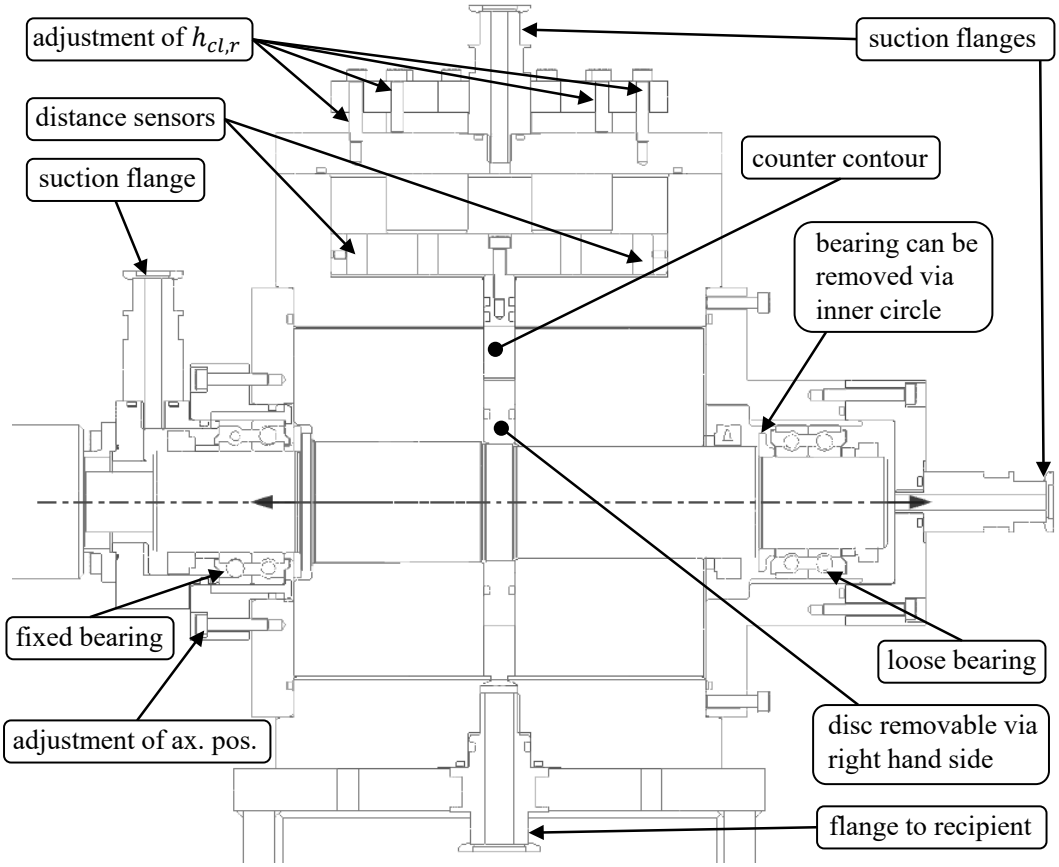

FIG. 8.2 Detail sketch of the vacuum chamber model without lead.

Figure 8.2 shows a detailed sketch of the vacuum chamber model in a sectional view. It is shown that the radial clearance height $h_{cl,r}$ can be adjusted by the radial movement of the counter contour via screws on the top of the housing. With two screws the counter contour can be pushed down and with two additional screws it can be pulled up with a symmetric arrangement on both sides. Two distance sensors are placed for an indirect measurement of the clearance. Although each

connection between different components is sealed with O-rings to minimise leakages from the atmosphere, there is an issue sealing the cables from the distance sensors where epoxy resin is used with additional silicone paste. To avoid large leakages directly into the vacuum chamber, the counter contour itself is sealed with two O-rings that separate the vacuum chamber from the counter contour's back room. Nevertheless, the counter contour's shape is not optimal for the use of O-rings, therefore another leakage minimizing step is established. As leakage scales with the high pressure, the counter contour's back room is evacuated via a suction flange with a rotary vane pump, which is decoupled from the vacuum chamber. Similar suction flanges are also set up in the back room of the two bearings in case there is a higher leakage. The fixed bearing on the driving side of the shaft is built using two angular contact bearings in O-arrangement. Similarly, the loose bearing is arranged on the opposite side of the shaft. The double O-arrangement was chosen in order to make use of the high accuracy of the angular contact bearings. In addition, a fixed-loose arrangement is set up for a simple adjustment of the axial position of the rotary shaft via screws and counter screws. This is necessary to adjust the axial clearances (inter-lobe clearances) between the counter contour and the brass cylinders. Nevertheless, the bearings are overdetermined with respect to angular momentum, which is neglected as gravity and friction within the bearings are the only expected forces. The bearings are greased and sealed using Nilos rings. As the sleeve representing the machine's inner diameter should be exchangeable, it can be removed via the right hand side. To enable non-destructive dismantling of the loose bearing, an additional ring has been fitted behind the bearing so that it can be pulled off via this ring on the inner circle. The drive side does not have to be dismantled for this purpose. The sleeve and the right-hand brass cylinder have threaded holes so that they can be removed using threaded rods. The whole rotating shaft including the brass cylinders and the sleeve has been balanced with balance holes on the outer face of the brass cylinder to the driving side, where the vacuum chamber should not be affected.

The test rig is designed such that most parameters influencing the inhomogeneous chamber state according to Sec. 5.2 can be varied. The variation of the absolute influence parameters is summarized in Tab. 8.1 The geometric ratio $D_\mathrm{o}/D_\mathrm{i}$ can be varied by exchanging the sleeve. Therefore, the outer diameter is fixed to $D_\mathrm{o} = 170$ mm but the inner diameter is $D_\mathrm{i} \in [100\ \mathrm{mm}, 120\ \mathrm{mm}]$. The gas rarefaction parameter δ can be varied proportional to the recipient pressure, while the speed ratio u_0 is a function of the rotor speed. The dimensionless mass flow rate C_0 can not be prescribed explicitly as fixed boundary condition, as it depends on the resulting pressure ratio $p_\mathrm{HP}/p_\mathrm{LP}$ itself, but a qualitative impact can be measured by adjusting the radial clearance $h_\mathrm{cl,r}$. Thus, for similar operation points and different clearances the mass flow rate through the radial gap differs. As no additional cooling is established, the temperature can vary due to friction in the bearings and therefore also impact the gas rarefaction parameter δ, the speed ratio u_0 and the dimensionless flow rate C_0. As the simplified chamber model is without lead, the impact of the geometric ratio D_o/s as well as the number of lobes Z cannot be varied. Instead a constant chamber width is set throughout all measurements. At last, there are different TMACs within the chamber due to the use of brass cylinders and steel housing, sleeve and counter contour respectively. Thus, opposite walls have equal TMACs, but different from the perpendicular ones. Originally the intention of using brass cylinders was to prevent micro welding on the long mating surfaces of the shaft. Nevertheless, as shown in Fig. 7.11 the thermodynamic impact is non-negligible as the resulting friction is highly reduced in rarefied gases compared to the steel surfaces.

TAB. 8.1 Data variation of the test rig.

D_o [mm]	D_i [mm]	w [mm]	$h_{cl,r}$ [mm]			$h_{cl,il}$ [mm]	$h_{cl,h}$ [mm]	f [Hz]		
170	100	15	0.2	0.3	0.4	0.1	0.15	41.67	75	100
170	120	15		0.2		0.15		41.67	75	100

8.2 Sensors

The relevant sensors for the determination of measurement results are summarized in Tab. 8.2 with specification of the resolution, accuracy and maximum measuring range. Each position where the pressure is measured has several capacitive pressure sensors in cascade arrangement (one sensor for each pressure decade) to ensure high accuracy and high resolution in all pressure regimes with a resolution of 10^{-3} % of full scale. The sensors' accuracy is 0.12 % of reading for sensors with full scale ≥ 1 mbar and 0.15 % of reading for the pressure sensors with a full scale of 0.1 mbar.

TAB. 8.2 Technical data of sensors in use.

sensor	resolution	accuracy	full scale (FS)
pressure sensors			
Baratron 627B[209]	10^{-3}% FS	±0.15% of reading	0.1 mbar
pressure sensors			
Baratron 627B[209]	10^{-3}% FS	±0.12% of reading	$1, 10, 100, 1000$ mbar
temperature sensors			
Thermocouple type T[210]	0.063 K	±0.5 K	−40 - 125 °C
distance sensors			
capaNCDT 6110 CS1[211]	0.002% FS	±0.15% of reading	1 mm
optical RGB sensor			
Sitron[212]	50 μs	–	10 kHz

In order to measure the temperature, thermocouple type T sensors are installed. One right before the throttle valve, where the ambient temperature is measured and one at the outer circle of the fixed and loose bearings each. The sensors have an accuracy of ±0.5 K and their temperature range is suitable for the application. The positions of the temperature sensors on the bearings are shown in Figs. C.1 and C.2.

The radial clearance $h_{cl,r}$ is measured implicitly using capacitive distance sensors with a dynamic resolution of 20 nm and an accuracy of ±0.15% of reading. The maximum possible distance is 1 mm.

The rotor frequency is measured using an optical RGB sensor with a resolution of 50 μs giving one pulse per revolution (see Fig. C.1).

Additionally two accelerometers[213] are placed to measure the horizontal and vertical vibrations for safety purposes as shown in Fig. C.2. The signal is integrated in time in order to observe the vibrational velocity. As they do not affect the experimental uncertainty, they are not listed here in detail.

All measurement data were recorded with the imc SPARTAN[214] and imc CRONOSflex[215] measurement systems and analysed with the software imc STUDIO[216] and imc FAMOS Enterprise[217].

8.3 Method of Measurement

A measurement series starts as follows: For predefined geometric conditions in Tab. 8.1 the system is evacuated by running the vacuum pumps including the rotary vane pump[218] until the system's ultimate pressure of about $p_{\mathrm{ult}} < 0.4$ Pa is reached. Therefore, the throttling valve is closed and the valve to the vacuum pump opened. Due to desorption effects[2] from the system's walls or out of the bearings' grease this can last up to a few hours if the system was fully at atmospheric pressure. Especially desorption of enclosed gas bubbles within the grease can be accelerated with the additional rotary vane pump at the bearing volumes and by slowly driving the motor. Once the system is evacuated, the rotary vane pump is only connected to the counter contour's back room to overcome large leakages due to the distance sensors' cables.

Now the rotor frequency is increased until the target frequency is reached and afterwards held constant during the whole measurement series. The run up process is shown in Fig. 8.3. It is observed that as long as the rotor stands still, $p_{\mathrm{LP}} \approx p_{\mathrm{HP}}$ and the pressure in the recipient p^*_{ch} is about 0.05 Pa lower than at the other positions. As the shaft starts rotating, the high pressure p_{HP} directly starts increasing with increasing rotational speed. On the other hand the low pressure p_{LP} decreases well below the recipient pressure p^*_{ch} which remains constant. The fact that the recipient pressure p^*_{ch} is below the other two pressure positions with zero rotational speed can be explained by a remaining leakage. Following a flow path of a possible leakage within the vacuum chamber model in Fig. 8.1, the direction of a mass flow rate in a steady state can be either through counter contour or the housing gaps from the bearing which is carried towards the vacuum pump. As such a flow is a Poiseuille flow, a pressure drop in flow direction is expected which results in a pressure difference between the pressure positions p_{LP} and p_{HP} to the recipient pressure p^*_{ch}. As such a leakage causes a systematic error in the pressure measurement, this will be taken into account in the uncertainty assumption in Sec. 8.5.

Once the steady rotor frequency is reached, a stationary measurement approach is chosen as shown in Fig. 8.4. A definite recipient pressure is adjusted by opening the throttle valve. A steady-state is kept for at least 1 minute until the throttle valve is opened a bit further to reach the next pressure level. The resulting pressure course as a function of time resembles a staircase. In the following, this is referred to as a measurement series. It is conspicuous that the relative difference between the three pressure curves shrinks with increasing pressure level until they seem to converge. Therefore, it can be seen, that the chamber pressure is more inhomogeneous the lower the pressure level within the vacuum chamber is. This is investigated in detail in Sec. 8.7.

8.4 Leakage

As mentioned in the previous section, there must be a non-negligible amount of leakage in the system as otherwise a pressure drop from the chamber to the recipient cannot be explained. In order to quantify the amount of leakage, the single-tank method[12] is used. Therefore, at first the system is evacuated. Then the valve to the vacuum pump is closed and the pressure rise with time is measured as shown in Fig. 8.5. The rotary vane pump shown in Fig. C.1 is only connected to the counter contour's back room to hold the same conditions as for the measurements. Once again it is obtained that at the beginning the recipient pressure p_{ch} is about 0.05 Pa smaller than p_{LP} and p_{HP}. As the valve gets shut, a short pulse affects the recipient pressure sensors. Then the system's

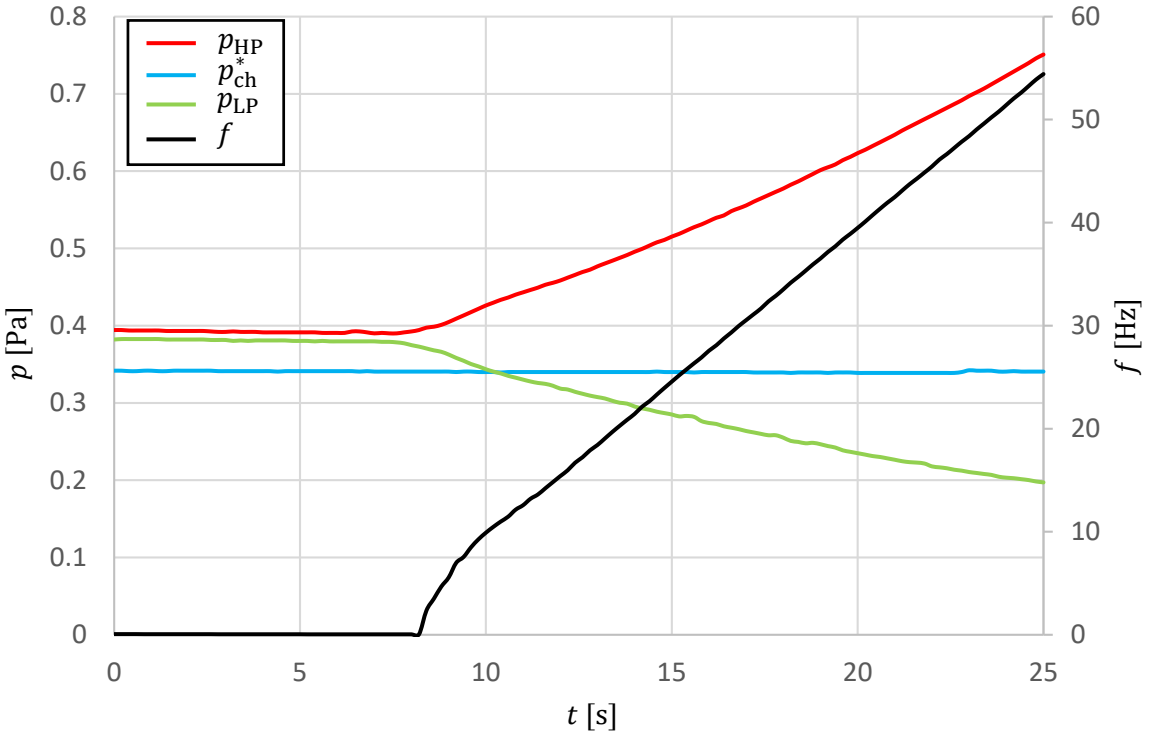

FIG. 8.3 Start of a measurement series.

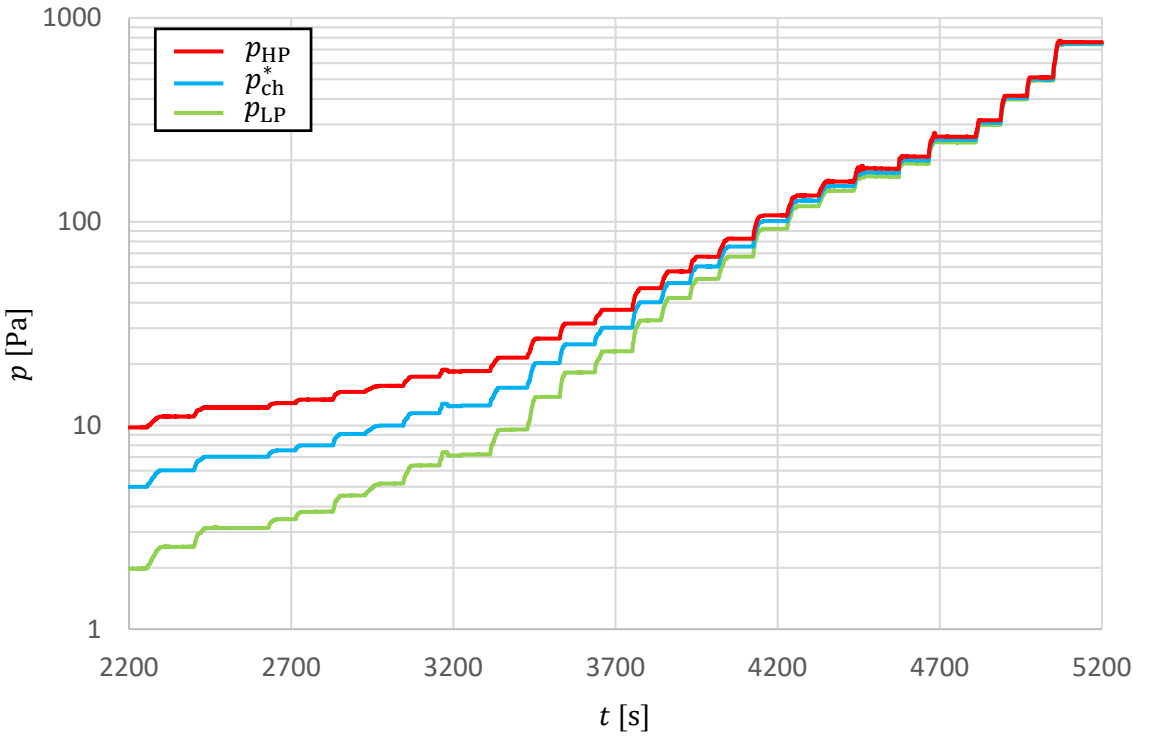

FIG. 8.4 Stationary measurement series in discrete time intervals for constant rotor frequency.

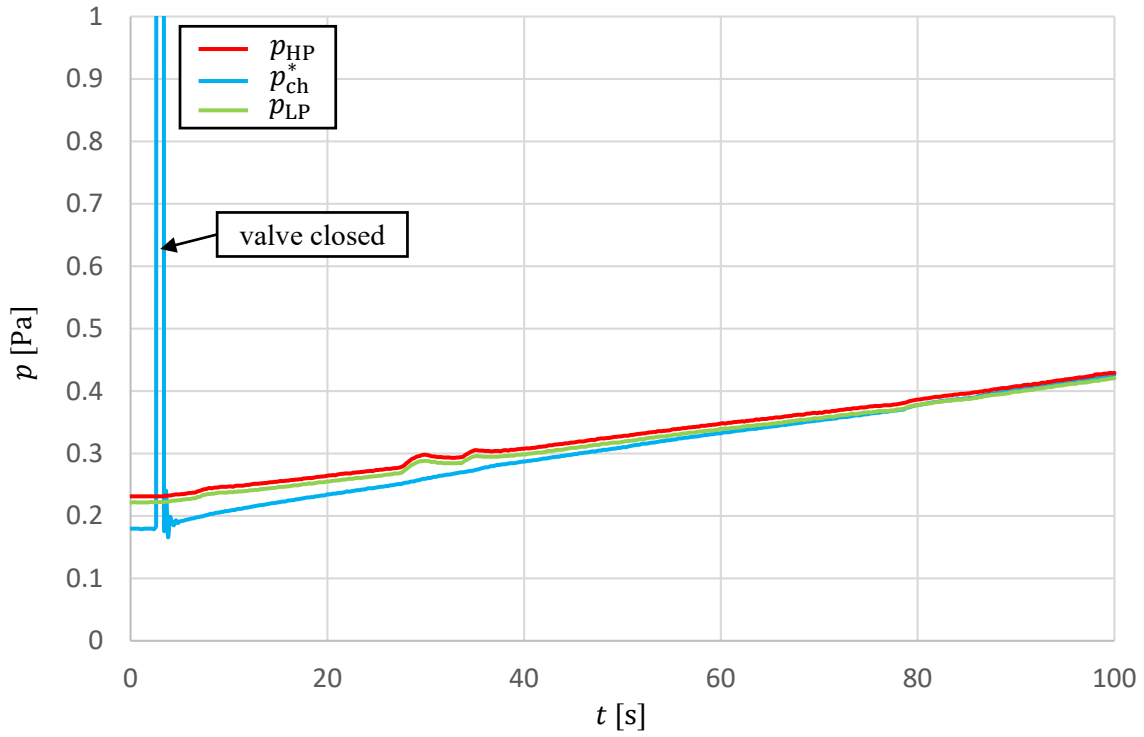

FIG. 8.5 Leakage measurement via single-tank method.

pressure rises at all three pressure positions and converges. The largest gradient is therefore seen at the recipient pressure p_{ch}, which is used to quantify the leakage $\mathbb{L}$ in a period $\Delta t = 600\,\mathrm{s}$ with a system's volume $V_{system} \approx 15\,\mathrm{l}$

$$\mathbb{L} = \frac{\Delta p_{ch} \cdot V_{system}}{\Delta t} \approx 3.5 \cdot 10^{-4}\ \frac{\mathrm{mbar} \cdot \mathrm{l}}{\mathrm{s}} \tag{8.1}$$

according to Ref. [2].

8.5 Uncertainty

As already mentioned in the previous sections, there are uncertainties regarding the measurands. Therefore, in this section an error estimation ΔX for all relevant measured quantities X is performed taking into account uncertainties due to the sensor ΔX_{sensor}, statistical errors ΔX_{stat} evaluating the empirical standard deviation s_X according to Eq. (4.59) and systematic errors ΔX_{SE}. The absolute uncertainty ΔY of the result quantity Y depending on different measurands X is calculated using the error propagation law according to Gauss, as required in DIN 1319-3[219]

$$\Delta Y = \sum_{i=1}^{N} \sqrt{\left(\frac{\partial Y}{\partial X_i} \Delta X_i\right)^2} \tag{8.2}$$

where ΔX_i is the absolute uncertainty of measurand X_i. Now the uncertainties of the different measurands are discussed.

8.5.1 Pressure

A zero adjustment of all pressure sensors is performed using a turbo molecular pump[220] in combination with the rotary vane pump which together can evacuate the system to a pressure $< 2 \cdot 10^{-6}$ Pa which is defined as zero. Therefore, the uncertainty of the absolute pressure transducers Δp_{sensor} can be taken from Tab. 8.2. In order to quantify the statistical error, each operation point is averaged over a time interval of 60 seconds. The empirical standard deviation s_p of each pressure position during this time interval is evaluated and the statistical error is defined as three times the empirical standard deviation $\Delta p_{\text{stat}} = 3 s_p$. A systematic error is obtained due to leakage as explained in the previous section. In some measurement series the error was even a bit larger than shown here, presumably due to pending desorption effects. Nevertheless, in most measurement series where the offset was recorded, the difference was ≤ 0.05 Pa. Although comparisons to the 1D model in Sec. 8.10 indicate that the leakage could be even larger when the shaft is rotating, this could not be proved. Therefore, the error bars are calculated using a systematic uncertainty $\Delta p_{\text{SE}} \approx 0.05$ Pa. The uncertainty of each pressure position is

$$\Delta p = \Delta p_{\text{sensor}} + 3 s_P + \Delta p_{\text{SE}} \ . \tag{8.3}$$

The three uncertainties act very differently. The sensor error Δp_{sensor} provides a constant relative uncertainty in any pressure regime. Due to a constant offset, the systematic uncertainty Δp_{SE} is large when the measured pressure is low and becomes negligible for high pressure values. The statistical error is almost negligible in most cases despite the last measurement series described in Sec. 8.7.

8.5.2 Temperature

Measuring the temperature directly within the vacuum chamber without causing a large amount of leakage is a difficult task. Furthermore, in rarefied gases the absolute heat capacity is small due to low density with the effect that after short periods the gas temperature is in equilibrium with the surrounding wall temperatures. Measured are the ambient temperature T_{amb} and the temperature at the outer rings of the bearings. In Fig. 8.2 it is shown, that the vacuum chamber is placed in the middle of the two bearings. Furthermore, Fourier's law of heat conduction is linear but heat transfer is sluggish. Therefore, if a heat flow outside the system was neglected, the temperature of the rotating shaft located in the middle between the two bearings will tend asymptotically towards the average bearing temperature

$$T_{\text{B}} = \frac{T_{\text{LB}} + T_{\text{FB}}}{2} \tag{8.4}$$

where T_{LB} is the loose bearing's temperature and T_{FB} is the fixed bearing's temperature. In order to verify this assumption, measurements are done where at first the machine is run up at $t = 0$. The machine is stopped after about $t = 90$ min until it is heated up with bearing temperatures $\vartheta_{\text{FB}} \approx 92°\text{C}$ and $\vartheta_{\text{LB}} \approx 72°\text{C}$. Then, an additional thermocouple sensor type T's tip is held on the vacuum chamber's inner diameter. Therefore, the suction line to the recipient was dismantled in the time 90 min $< t <$ 95 min. The result is shown in Fig. 8.6. It is obtained that the fixed bearing's temperature T_{FB} is larger than the loose bearing's temperature T_{LB}. This might be caused by the vicinity to the magnetic coupling. The temperature course of the blue curve has this shape because the sensor is handled manually and can be put into four different time sections. At the

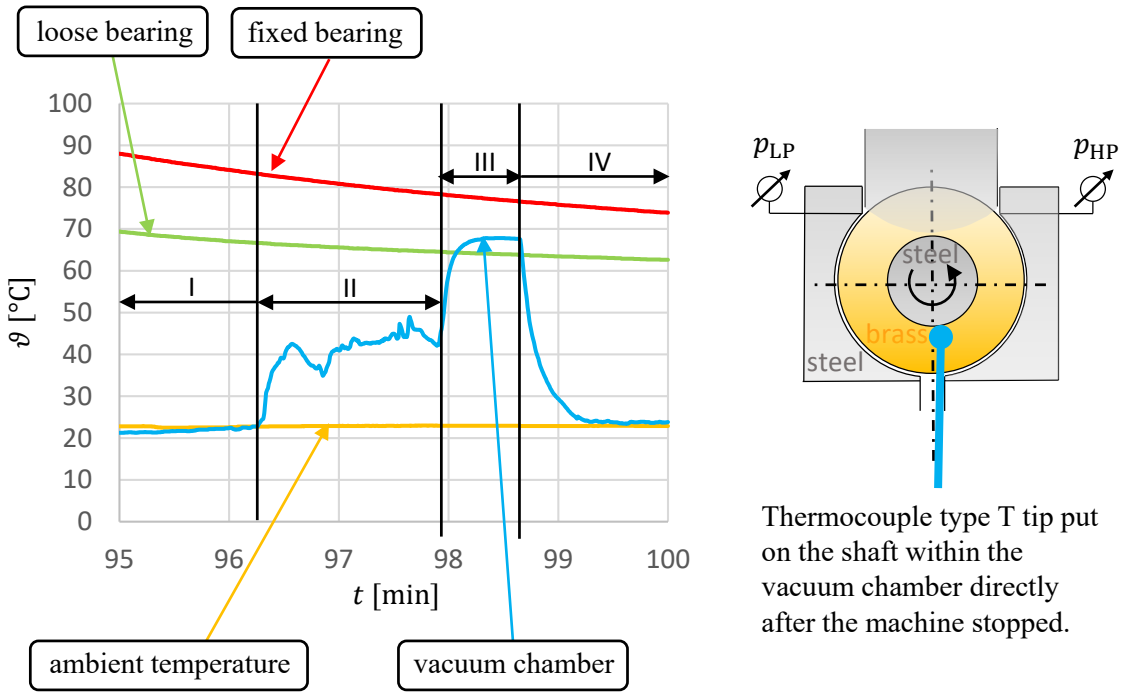

FIG. 8.6 Determination of the uncertainty of temperature within the vacuum chamber.

beginning in section I, the sensor is outside the machine and shows ambient temperature. Then in section II it is put into the machine through the flange and scratched at the side walls until the rotor's inner diameter is hit in section III. This is held for about a minute, and the sensor is thrown out of the machine again and tends towards ambient temperature in section IV. This shows that the temperature within the vacuum chamber is higher than T_{LB}, but lower than the average bearing temperature when the machine is heated up. Nevertheless, this occurs after more than 90 minutes. Especially at the start of the measuring series when the machine starts cold, the average temperature is more likely to be close to the ambient temperature. Furthermore, there is a heat flow going out through the housing to the atmosphere, and fresh air coming into the system when the pressure rises will at first be at ambient temperature and heat up due to the surrounding walls. After some time the vacuum chamber will heat up, but it will not be hotter than the average bearing temperature. Due to this uncertainty the ambient temperature T_{amb} is used to evaluate the measurement data and a systematic error $\Delta T_{\mathrm{SE,OP}}$ for the temperature measurement is added as the difference between the average bearing temperature T_{B} to the ambient temperature as an upper limit, while the lower limit remains T_{amb}:

$$\Delta T^{+}_{\mathrm{SE,OP}} = T_{\mathrm{B}} - T_{\mathrm{amb}} \tag{8.5}$$

As one operation point is defined in a period of 60 seconds, the systematic error is given as a time averaged value $\Delta \bar{T}_{\mathrm{SE,OP}}$. The resulting uncertainty for one operation point, which is used to evaluate the gas rarefaction parameter δ as a function of $\bar{T}_{\mathrm{OP}}$ is

$$\Delta T^{+}_{\mathrm{OP}} = \Delta T_{\mathrm{sensor}} + \Delta \bar{T}^{+}_{\mathrm{SE,OP}} \tag{8.6}$$

while the experimental standard deviation is neglected compared to the systematic uncertainty.

The results of a measurement series is given for a fixed value of u_0. But the temperature during one series is not completely constant as the temperature rises from a cold start. Therefore, for the speed ratio the time averaging to estimate the uncertainty ΔT^+ is performed over the whole measurement series and not only for a single operation point.

8.5.3 Rotational Speed

An uncertainty of the optical sensor which is used to detect the rotational speed is neglected. But there is a small statistical uncertainty due to fluctuations of the rotor frequency. Therefore, the uncertainty is defined by three times the empirical standard deviation over the whole measurement series without the run up and run down phase:

$$\Delta f = 3 s_f \tag{8.7}$$

8.5.4 Geometry

Due to the small gaps, all relevant parts of the test rig are manufactured with high precision, thus the resulting tolerances are small compared to most geometric scales like outer diameter D_o, inner diameter D_i and chamber width w which equals the radial gap width $w_\mathrm{cl,r}$. The radial clearance $h_\mathrm{cl,r}$ is adjusted by moving the counter contour in radial direction and measured with the distance sensors sketched in Fig. 8.2. The sensor error is $\Delta h_\mathrm{cl,r,sensor} = 0.0015 \cdot h_\mathrm{cl,r}$. A clearance of zero is defined if the shaft is blocked due to the counter contour. Nevertheless, due to the indirect measurement concept and the possibility of misalignment of the plate where the distance sensors are set, an additional uncertainty of about $\Delta h_\mathrm{cl,r,SE} = 0.01$ mm is assumed. Additional statistical errors are neglected. Therefore, the assumed uncertainty of the radial clearance is $\Delta h_\mathrm{cl,r} = \Delta h_\mathrm{cl,r,sensor} + \Delta h_\mathrm{cl,r,SE}$. The inter-lobe clearance is adjusted using a grinded test piece, which also ensures symmetry of both inter-lobe gaps. The uncertainty of each is assumed to be $\Delta h_\mathrm{cl,il} = 0.01$ mm. The inter-lobe gap width is equal to the chamber height $h = (D_\mathrm{o} - D_\mathrm{i})/2$ and is much larger than the uncertainty. The uncertainties with respect to clearances are not represented in the error bars of the measurements as the effect is highly non-linear. Nevertheless, this uncertainty could affect the calculated mass flow rates using the 1D model as explained in Sec. 8.6.

8.5.5 Uncertainties of Dimensionless Numbers

Applying Eq. (8.2) to a pressure ratio Π, the gas rarefaction parameter δ and the speed ratio u_0 with the estimated uncertainties of the measurands, one obtains the relative uncertainties given in Tab. 8.3. p_1 and p_2 are place holders for the certain evaluated pressure position. As the uncertainties of pressure are assumed to be symmetric, the resulting uncertainty of the pressure ratio Π is symmetric, too. The uncertainty of temperature is only added to the positive temperature range, therefore the resulting uncertainties of the gas rarefaction parameter δ and the speed ratio u_0 are non-symmetric.

8.6 1D Modelling of the Test Rig

In order to be able to make a validation, the essential physics within the test rig have to be reproduced as accurately as possible. The 1D model proposed in Sec. 5.3 with a solved closure

TAB. 8.3 Relative uncertainties of the dimensionless numbers.

name	equation	relative uncertainty
pressure ratio	$\Pi = \frac{p_1}{p_2}$	$\frac{\Delta\Pi}{\Pi} = \sqrt{\left(\frac{\Delta p_1}{p_1}\right)^2 + \left(\frac{\Delta p_2}{p_2}\right)^2}$
gas rarefaction	$\delta^* = \frac{p^*_{\mathrm{ch}} w}{\mu\sqrt{2RT}}$	$\frac{\Delta\delta^+}{\delta^*} = \sqrt{\left(\frac{\Delta p^*_{\mathrm{ch}}}{p^*_{\mathrm{ch}}}\right)^2}$
		$\frac{\Delta\delta^-}{\delta^*} = \sqrt{\left(\frac{\Delta p^*_{\mathrm{ch}}}{p^*_{\mathrm{ch}}}\right)^2 + \left(\frac{\Delta T^+_{\mathrm{OP}}}{2T}\right)^2}$
speed ratio	$u_0 = \frac{\pi f D_{\mathrm{o}}}{\sqrt{2RT}}$	$\frac{\Delta u_0^+}{u_0} = \sqrt{\left(\frac{\Delta f}{f}\right)^2}$
		$\frac{\Delta u_0^-}{u_0} = \sqrt{\left(\frac{\Delta f}{f}\right)^2 + \left(\frac{\Delta T^+_{\mathrm{OP}}}{2T}\right)^2}$

problem in Chap. 6 is used. The geometric data is given in Tab. 8.1 and therefore the channel length, width, height and the corresponding wall velocities can be calculated as described in Sec. 5.1. A rectangular channel is defined where the top wall is the static housing, the bottom wall is the root circle with velocity at the inner diameter according to Eq. 5.3 and the left and right walls are defined by the brass cylinders' faces. As proved in Sec. 6.2, without loss of generality the average wall velocity can be used for these faces, which is the velocity at the pitch circle. Due to the choice of the materials steel and brass, the top and bottom walls have a TMAC corresponding to the pair of steel and air ($\alpha \approx 0.92$), while the left and right wall have a TMAC according to the pair of brass and air ($\alpha \approx 0.71$) summarized in Tab. 5.1. The pressure p^*_{ch} is prescribed in the middle of the chamber at $z = L/2$ with the recipient pressure and defines an initial value problem in positive and negative direction as explained in Sec. 5.3 to get the high pressure p_{HP} at $z = L$ and the low pressure p_{LP} at $z = 0$ as done in Sec. 7.2.

A problem that arises is that the tangential mass flow rate in Eq. (5.20) needs to be known, which is the combined mass flow rate through the radial gap and the two inter-lobe gaps in the test rig:

$$\dot{m}_{\mathrm{cl,t}} = \dot{m}_{\mathrm{cl,r}} + 2 \cdot \dot{m}_{\mathrm{cl,il}} \tag{8.8}$$

The radial gap mass flow rate is calculated with the same model, but a different geometry. The model is validated for the calculation of such gap mass flow rates in Refs. [12, 47, 48]. While the width $w_{\mathrm{cl,r}} = w$ is constant and equal to the chamber width w, the length is defined as

$$L_{\mathrm{cl,r}} = \alpha_{\mathrm{CL}} \cdot D_{\mathrm{pc}} = \pi \cdot D_{\mathrm{pc}} - L \tag{8.9}$$

with L being defined in Eq. (5.9) and the gap height curve is

$$h_{\mathrm{r}}(z_{\mathrm{cl,r}}) = \frac{D_{\mathrm{i}}}{2} - \sqrt{\left(\frac{D_{\mathrm{i}}}{2}\right)^2 - \left(z_{\mathrm{cl,r}} - \frac{L_{\mathrm{cl,r}}}{2}\right)^2} + \frac{D_{\mathrm{o}}}{2} - \sqrt{\left(\frac{D_{\mathrm{o}}}{2}\right)^2 - \left(z_{\mathrm{cl,r}} - \frac{L_{\mathrm{cl,r}}}{2}\right)^2} + h_{\mathrm{cl,r}} \tag{8.10}$$

being symmetric around the minimum gap height $h_{\mathrm{cl,r}}$ at $z = L_{\mathrm{cl,r}}/2$ with $z_{\mathrm{cl,r}} \in [0, L_{\mathrm{cl,r}}]$.

The velocity curve of the lower wall is calculated as

$$U_{\mathrm{cl,r}}(z_{\mathrm{cl,r}}) = \pi \cdot f \cdot D_{\mathrm{i}} \cdot \sqrt{1 - \left(\frac{2z_{\mathrm{cl,r}} - L_{\mathrm{cl,r}}}{D_{\mathrm{i}}}\right)^2} \tag{8.11}$$

which is only the part of the wall velocity projected in 1D flow direction. As the counter contour is static and the gap width is much greater than the clearance, the other wall velocities are set to zero. The TMACs of the upper and lower wall are set to those of the pair of steel and air ($\alpha \approx 0.92$), while the TMACs of the left and right wall are set to the pair of brass and air ($\alpha \approx 0.71$). The inlet pressure is defined as the vacuum chamber's high pressure p_{HP} and the mass flow rate is found solving the differential equation as a boundary value problem thus the gap's outlet pressure matches the vacuum chamber's low pressure p_{LP}. This is again done using the 5th order Dormand-Prince-Method with adaptive step size with an accuracy of 10^{-9} from the boost library[191] while the correct mass flow rate $\dot{m}_{\mathrm{cl,r}}$ is found via bisection method.

The two inter-lobe gaps are handled more pragmatically as they are geometrically defined as long plane channels with a small clearance and comparably large wall velocity. Due to the large amount of friction in rarefied gases the Poiseuille flow rate for this channel is negligible compared to the Couette flow. According to Refs. [12, 47] such a gap flow can be approximated with a pure plane Couette flow calculated with the inlet conditions. Therefore, the mass flow rate $\dot{m}_{\mathrm{cl,il}}$ of each inter-lobe gap is calculated as

$$\dot{m}_{\mathrm{cl,il}} = \pi \cdot D_{\mathrm{pc}} \cdot f \cdot \frac{p_{\mathrm{HP}}}{RT} \cdot h_{\mathrm{cl,il}} \cdot w_{\mathrm{cl,il}} \cdot G_C \tag{8.12}$$

where the brass cylinder's face is regarded as top wall and the counter contour's face as bottom wall. The gap width $w_{\mathrm{cl,il}}$ equals the chamber height h_{ch}. Due to the linear behaviour of the Couette flow, only the average wall velocity is used, which is the velocity at the pitch circle. The inlet pressure is defined as the vacuum chamber's high pressure p_{HP} and the reduced flow rate for different TMACs with the above definitions is calculated using Eq. (6.97).

Now the problem that arises is that the boundary conditions of the gaps depend on the solution of the pressure distribution within the chamber which is affected by the amount of the gap mass flow rates. This is solved using a correction loop. In the first step the mass flow rates $\dot{m}_{\mathrm{cl,il}}$ of the inter-lobe gaps are calculated assuming a homogeneous pressure distribution equal to p^*_{ch}, neglecting a radial gap mass flow rate $\dot{m}_{\mathrm{cl,r}}$. Then a pressure distribution is calculated based on the initial gap mass flow rates. With the new boundary condition the gap mass flow rates are calculated leading to a new pressure distribution afterwards. This correction loop typically converges after about five or fewer iterations.

8.7 Comparison Between Measurements and 1D Model Simulation

Now a comparison of the experimental results to the 1D model is performed similar to the comparison of 3D CFD simulations in Chap. 7 to show that the model is suitable to predict the phenomena occurring within a machine. The data shown in the diagrams is given in tabulated form in App. D. In Fig. 8.7 the pressure ratio $p_{\mathrm{HP}}/p_{\mathrm{LP}}$ is shown as a function of the gas rarefaction parameter δ^* evaluated at the recipient pressure p^*_{ch} for different speed ratios u_0. Green refers to a speed ratio $u_0 = 0.054$ with the corresponding rotational speed $f \approx 41.67$ Hz, blue to a speed ratio $u_0 = 0.097$ with a corresponding rotational speed $f = 75$ Hz and red to a speed ratio $u_0 = 0.13$ with a corresponding rotational speed $f = 100$ Hz. The straight lines are related to results of the 1D model while the symbols with error bars are related to the measurements. The radial clearance is $h_{\mathrm{cl,r}} = 0.2$ mm and the inner diameter is $D_{\mathrm{i}} = 100$ mm. As shown before in Sec. 7.2 the pressure

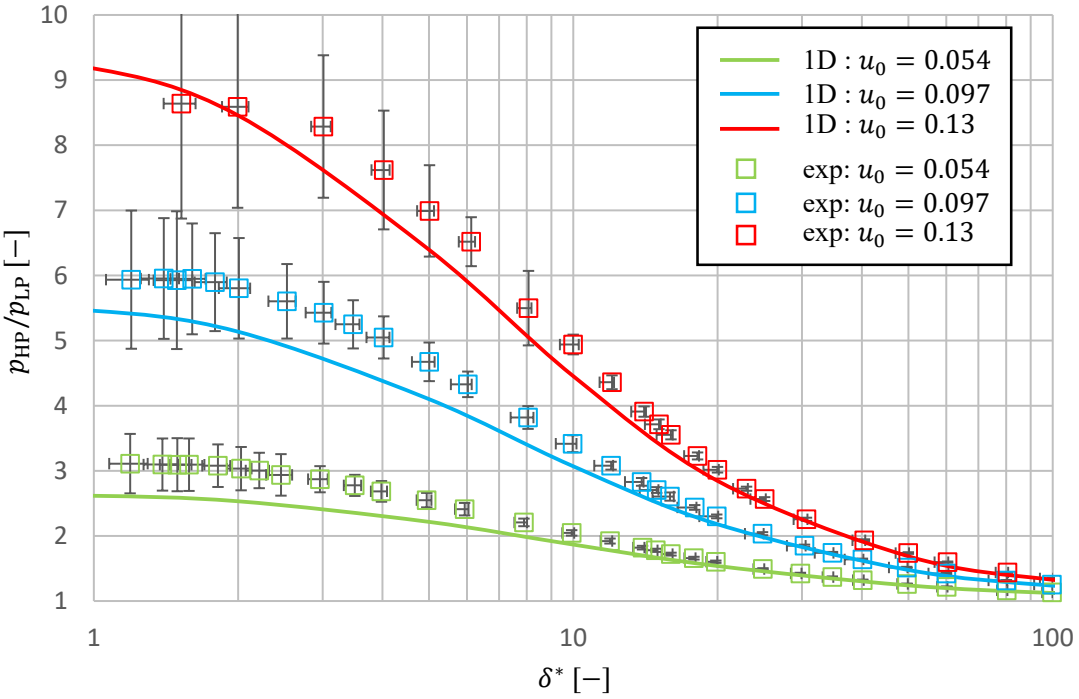

FIG. 8.7 Pressure ratio p_{HP}/p_{LP} as a function of the gas rarefaction parameter δ^*. Comparison of the 1D model to measurements for $D_o/D_i = 1.7$, $h_{cl,r} = 0.2$ mm and different speed ratios u_0.

ratio increases with increasing speed ratio u_0 and with decreasing gas rarefaction parameter δ^*. It was not possible to measure operation points with $\delta^* < 1$ and for $\delta > 100^*$ the curves converge, so only $1 \leq \delta^* \leq 100$ is shown. The uncertainty of measurement is small for large values of δ^* and increases for low values of δ^* due to the systematic error caused by the leakage. If the absolute values of the pressure are small, a small constant offset leads to a large spread of the error bars. Overall, the experimental results are in good agreement with the results of the 1D model although the model seems to slightly underrate the pressure ratio outside the assumed uncertainty of the measurements. A possible explanation could be the choice of the TMACs as the results are quite sensitive to the correct value as indicated in Figs. 7.10 and 7.11. Nevertheless, it is not intended to do a curve fit with different values here, but to show that the general behaviour of the experimental results are depicted by the model.

In Fig. 8.8 the impact of the temperature is highlighted for the measurement series $u_0 = 0.13$. The red line and symbols are identical to those in Fig. 8.7 where the ambient temperature is taken to calculate the gas rarefaction parameter δ^* and the speed ratio u_0. The black curve represents the corresponding results if the average bearing temperature T_B is used. For the experiments the change of the evaluated temperature results in a shift towards lower values of the gas rarefaction parameter, while the pressure ratio is not affected whereas the 1D model shows much lower values of the pressure ratio due to the decrease of the speed ratio from $u_0 = 0.13$ at ambient temperature to $u_0 = 0.12$ at average bearing temperature. Therefore, a higher temperature not only affects the gas rarefaction parameter, but also acts similarly to a reduction of the rotational speed. Thus, especially at low gas rarefaction parameters where the machine is still cold, large deviations between measurements and simulations occur if the average bearing temperature is taken. For larger values of the gas rarefaction parameter this influence shrinks because of two reasons. The first one is

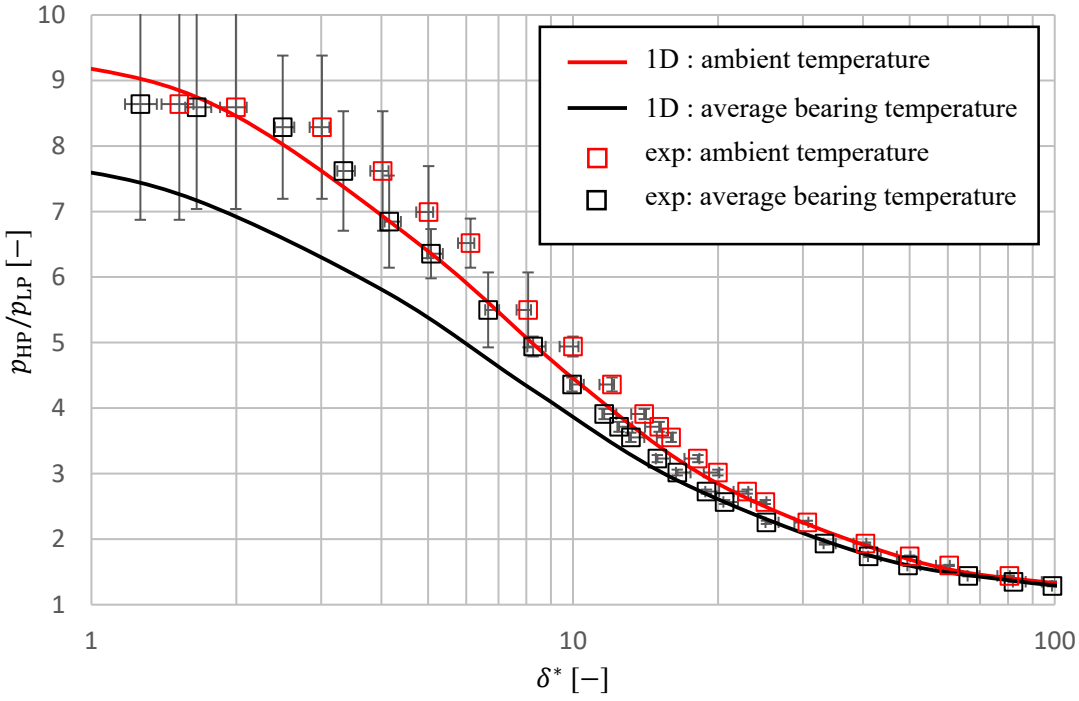

FIG. 8.8 Pressure ratio p_{HP}/p_{LP} as a function of the gas rarefaction parameter δ^*. Comparison of the 1D model to measurements for $D_o/D_i = 1.7$, $h_{cl,r} = 0.2$ mm and rotational speed $f = 100$ Hz. Investigation of the impact of the temperature on the pressure ratio. $T_{amb} = 294.77$ K $\Rightarrow u_0 = 0.13$, $T_B = 344.11$ K $\Rightarrow u_0 = 0.12$.

that the pressure ratio itself decreases, so that the difference between experiment and simulation shrinks, but the machine also gets hotter with time and the average temperature within the chamber approaches the average bearing temperature. Nevertheless, all following results are evaluated with ambient temperature as reference, taking the uncertainty explained in Sec. 8.5.2 into account in the error bars.

Figure 8.9 shows the pressure ratio p_{HP}/p^*_{ch} as a function of the gas rarefaction parameter δ^* for the same variation as in Fig. 8.7. The general behaviour is similar to that of the pressure ratio p_{HP}/p_{LP} but on a lower level, as the recipient pressure p^*_{ch} in the middle of the chamber is taken as reference to the high pressure. As before, the pressure ratio increases with increasing speed ratio u_0 and decreasing gas rarefaction parameter δ^* which is shown in both measurements and simulation results. Nevertheless, for $\delta^* < 10$ the simulation results tend to a maximum at $\delta^* \approx 1$ similar to the results in Fig. 7.2 while the measurements do not show an inflection point and therefore the two curves diverge for decreasing δ^*. This is somewhat contradictory to the results for the pressure ratio p_{HP}/p_{LP} as a maximum or asymptotic behaviour is reached. A possible explanation could be the pressure offset which is measured between the recipient p^*_{ch} and the two pressure locations p_{LP} and p_{HP} with zero rotational speed, which is related to leakage. If the measured pressure in the recipient is systematically too low compared to the pressure in the middle of the chamber, the resulting pressure ratio p_{HP}/p^*_{ch} is too large with increasing effect for lower system pressure.

To investigate this further, the 1D model is modified with a pressure offset p_{off} such that the pressure in the middle of the chamber is $p^*_{ch} + p_{off}$, but the pressure ratio p_{HP}/p^*_{ch} and the gas rarefaction parameter δ^* are evaluated using p^*_{ch} similar to the experimental results. This is shown

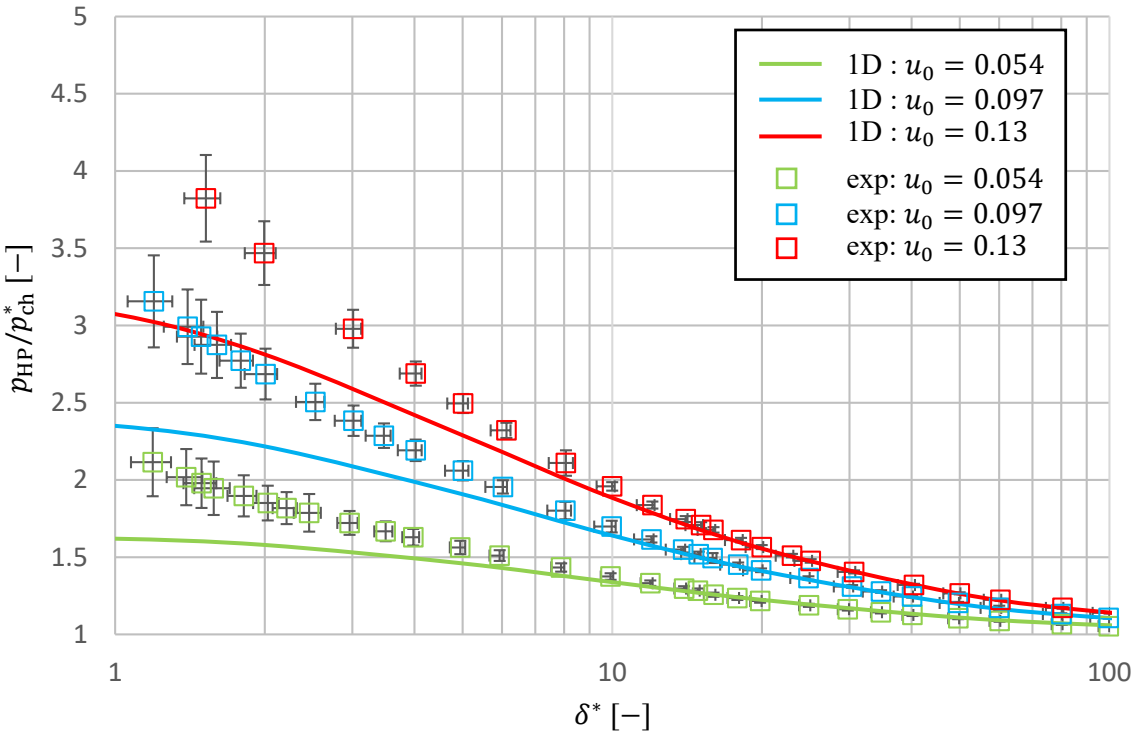

FIG. 8.9 Pressure ratio p_{HP}/p^*_{ch} as a function of the gas rarefaction parameter δ^*. Comparison of the 1D model to measurements for $D_o/D_i = 1.7$, $h_{cl,r} = 0.2$ mm and different speed ratios u_0.

in Fig. 8.10 for the series $u_0 = 0.13$ where the measurements are compared to the 1D model for different pressure offsets p_{off}. It is obtained that the deviation between experimental results and 1D model could be explained by a pressure offset $p_{off} = 0.25$ Pa, although only $p_{off} \approx 0.05$ Pa is measured at zero rotational speed. So it seems that the pressure difference between the middle of the chamber and the recipient is large when the machine is rotating. A possible explanation would be a larger leakage, for example because gas bubbles still desorb from the lubricated bearings or due to gas periodically getting into the system through the flanges due to vibrations. Nevertheless, this is only a possible explanation for the deviations and could not be directly measured. Therefore, for the rest of the results a pressure offset $p_{off} = 0$ is shown with the uncertainty explained in Sec. 8.5.1 with the hint that a possible larger offset is not depicted by the error bars. The pressure ratio p_{HP}/p_{LP} is hardly affected by such an offset as shown in Fig. 8.11.

In Fig. 8.12 the pressure ratio p_{HP}/p_{LP} is shown as a function of the gas rarefaction parameter δ^* for different radial clearances $h_{cl,r}$ for a speed ratio $u_0 = 0.13$. Green refers to $h_{cl,r} = 0.4$ mm, blue to $h_{cl,r} = 0.3$ mm and red to $h_{cl,r} = 0.2$ mm. The symbols represent the measurement, solid lines the results of the 1D model and the dotted lines the measured average bearing temperature T_B for the corresponding pressure ratios on the secondary axis. Both measurements and 1D model show the same qualitative behaviour, which is that the pressure ratio decreases with increasing clearance due to a larger tangential gap mass flow rate $\dot{m}_{cl,t}$ as already explained in Sec. 7.2. Nevertheless, in the experiment the impact of the mass flow rate seems to be larger than in the 1D model. There are two possible explanations for this difference. The first one is that the gap flow models implemented in the 1D model underestimate the mass flow rates to the corresponding clearances. This is unlikely as the model is validated with good agreement by Huck[12]. The second explanation is the temperature within the chamber. For the 1D model the ambient temperature is

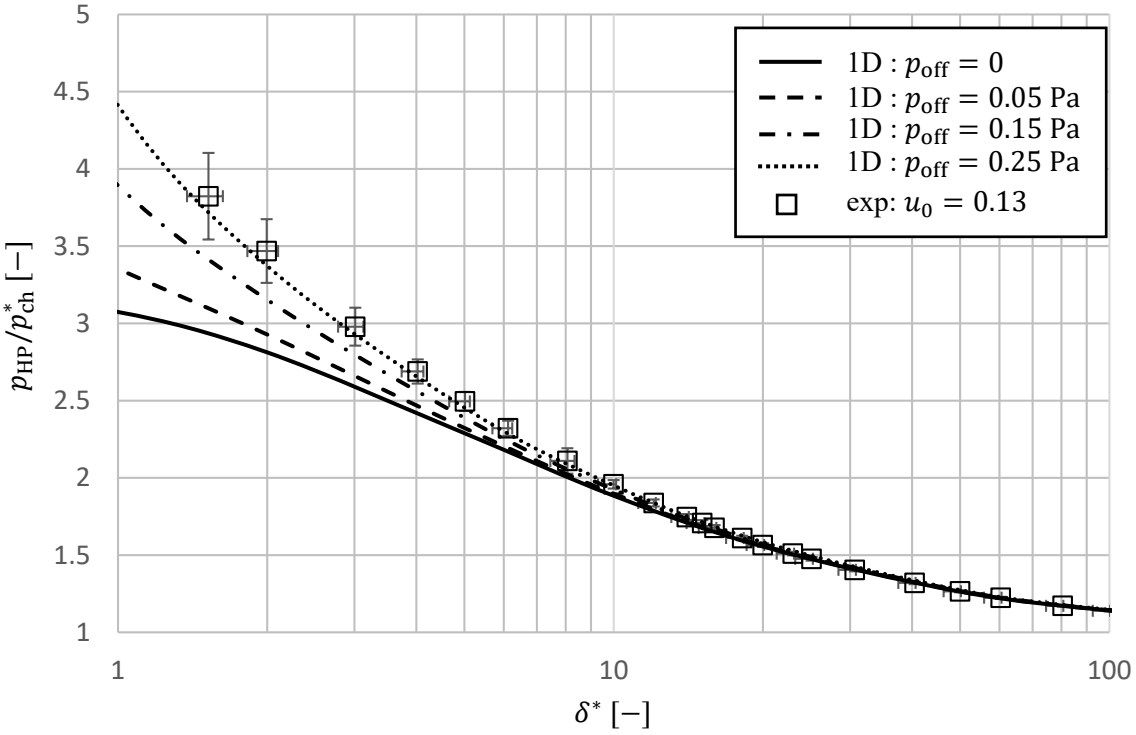

FIG. 8.10 Pressure ratio $p_{\mathrm{HP}}/p^*_{\mathrm{ch}}$ as a function of the gas rarefaction parameter δ^*. Impact of a pressure offset p_{off} for the recipient pressure p^*_{ch} on the pressure ratio $p_{\mathrm{HP}}/p^*_{\mathrm{ch}}$ for $D_{\mathrm{o}}/D_{\mathrm{i}} = 1.7$, $h_{\mathrm{cl,r}} = 0.2$ mm and $u_0 = 0.13$.

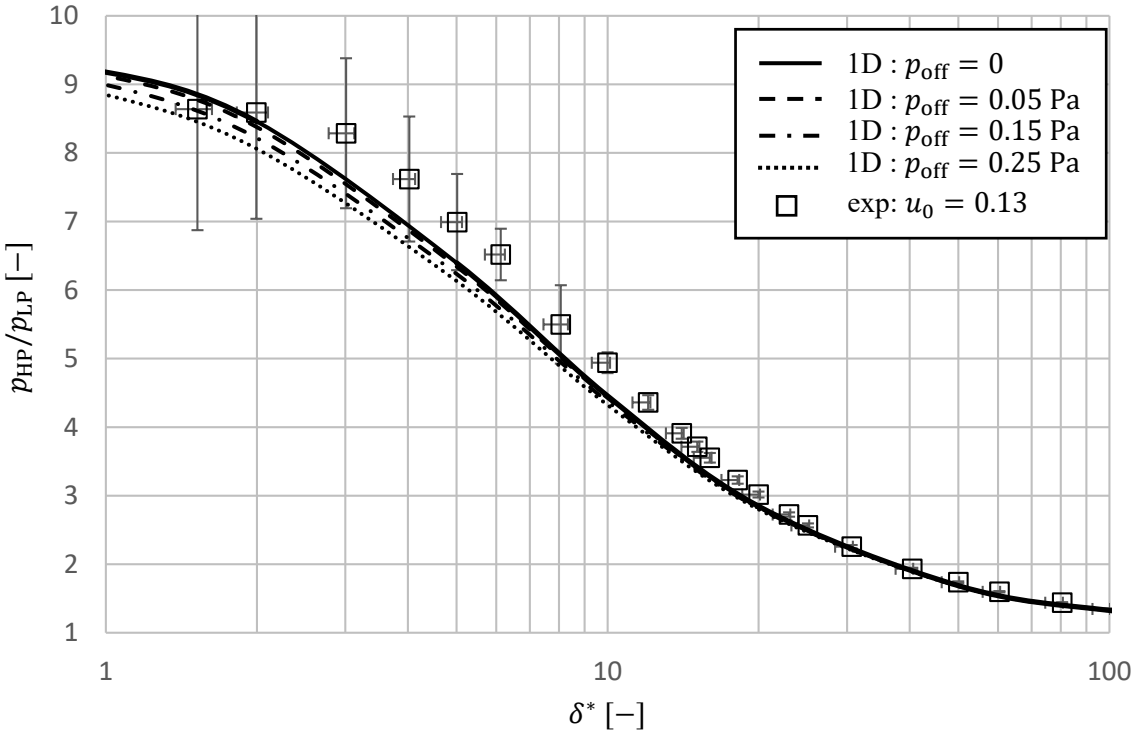

FIG. 8.11 Pressure ratio $p_{\mathrm{HP}}/p_{\mathrm{LP}}$ as a function of the gas rarefaction parameter δ^*. Impact of a pressure offset p_{off} for the recipient pressure p^*_{ch} on the pressure ratio $p_{\mathrm{HP}}/p_{\mathrm{LP}}$ for $D_{\mathrm{o}}/D_{\mathrm{i}} = 1.7$, $h_{\mathrm{cl,r}} = 0.2$ mm and $u_0 = 0.13$.

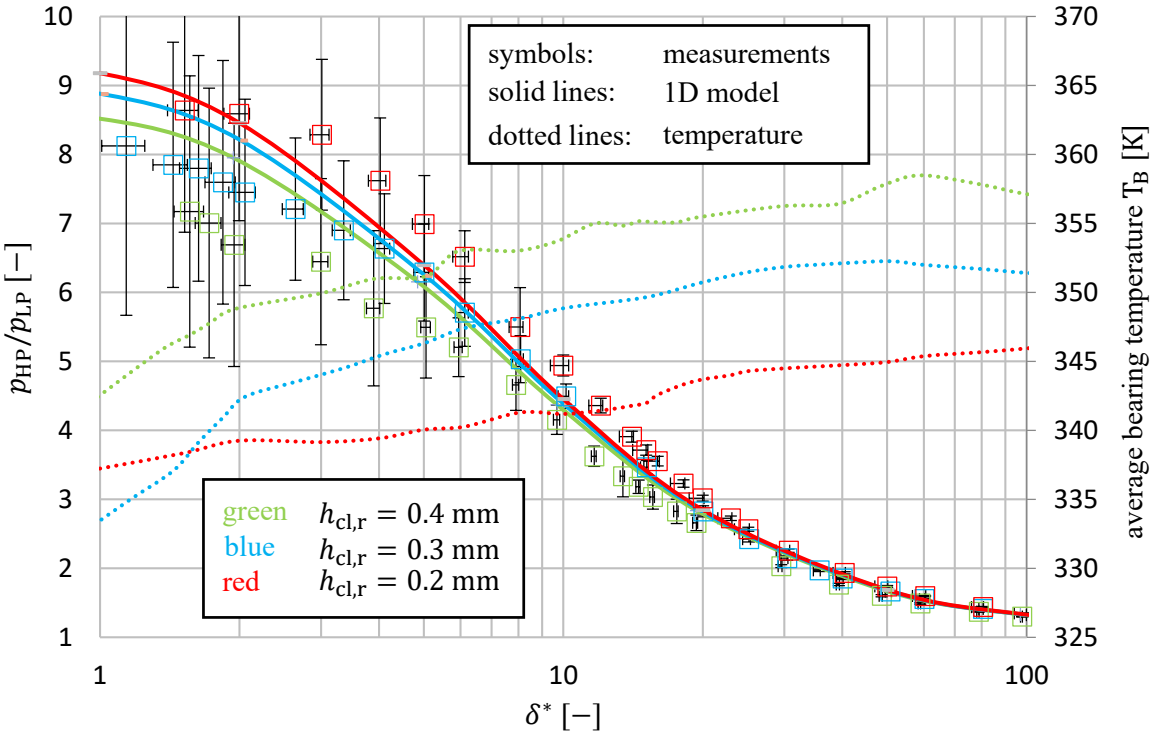

FIG. 8.12 Pressure ratio p_{HP}/p_{LP} as a function of the gas rarefaction parameter δ^*. Comparison of the 1D model to measurements for $D_o/D_i = 1.7$, $u_0 = 0.13$ and different radial clearances $h_{cl,r}$ The dotted lines show the average bearing temperature on the secondary axis.

always used. Looking at the average bearing temperature for the corresponding pressure ratios it is obtained that the measurement series for the highest clearance also shows the largest temperature. As shown in Fig. 8.8 this can have a very large impact on the results, because the rotational speed of all measurements here is the same, but the average bearing temperature differs, which probably leads to a different temperature within the chamber. Therefore, it is more likely that the larger deviations of the pressure ratio are dominated by a different speed ratio u_0 caused by different temperatures than by the change of the clearance. Besides these explanations regarding the uncertainty of measurements, only the main trend is discussed and in consequence both the experiments and the 1D model show that the gap flows only slightly affect the pressure distribution within the chamber, while the main trend shows the same qualitative behaviour. This is similarly seen in Fig. 8.13 for a speed ratio $u_0 = 0.054$. The ordinate range is adjusted to show the differences, as these are much smaller still than for the speed ratio $u_0 = 0.13$. This is explained by a much lower overall gap mass flow rate which depends on the inlet density, the gap pressure ratio and the wall velocities. All three influence parameters are smaller at lower rotational speed. The wall velocities for the gaps depend linearly on the rotor frequency, the inlet pressure or inlet density and the gap pressure ratio decrease with a decreasing pressure ratio within the chamber. Therefore, it is clear that the overall effect must be much smaller for same clearances and this is depicted for both measurements and 1D model.

Finally, a different chamber geometry is investigated. Therefore, the steel sleeve for the inner diameter is exchanged to $D_o = 120$ mm. As described in Sec. 8.1, the width of the new counter contour is 0.1 mm smaller leading to an increased inter-lobe clearance of $h_{cl,il} = 0.15$ mm each. In Fig. 8.14 the pressure ratio p_{HP}/p_{LP} is shown as a function of the gas rarefaction parameter δ^* for

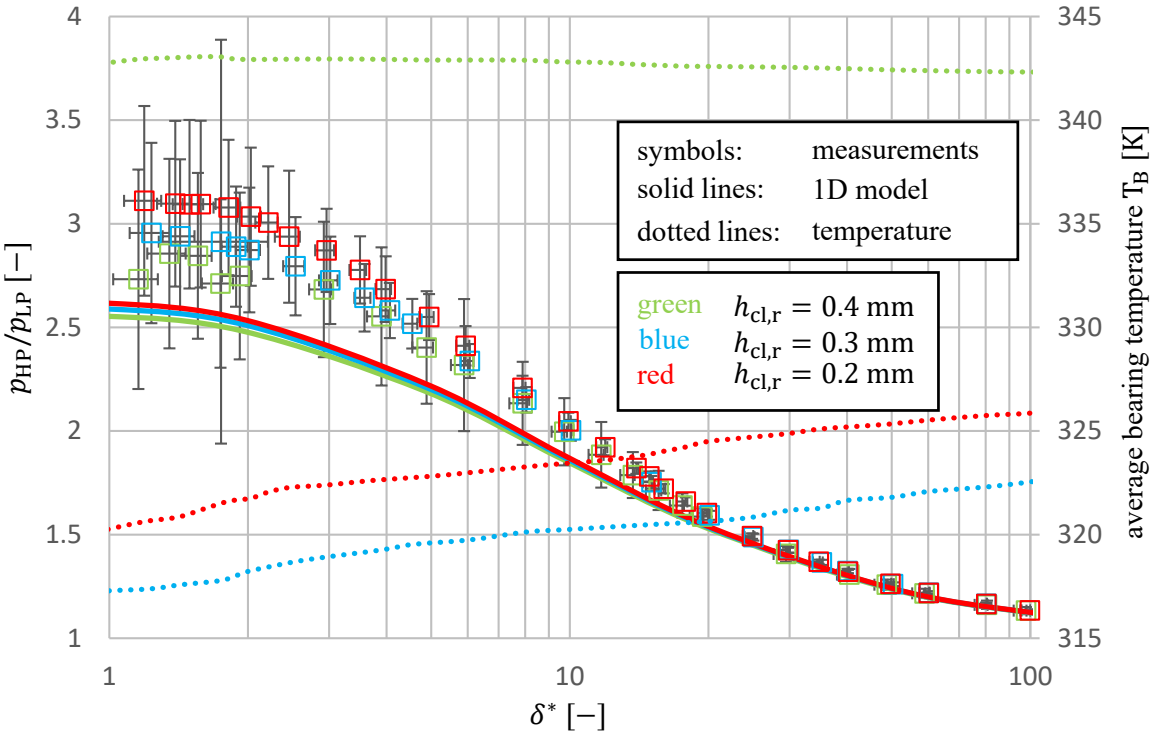

FIG. 8.13 Pressure ratio p_{HP}/p_{LP} as a function of the gas rarefaction parameter δ^*. Comparison of the 1D model to measurements for $D_o/D_i = 1.7$, $u_0 = 0.054$ and different radial clearances $h_{cl,r}$ The dotted lines show the average bearing temperature on the secondary axis.

different speed ratios u_0 for a radial clearance $h_{cl,r} = 0.2$ mm similar to Fig. 8.7. The qualitative behaviour is the same as before for an inner diameter $D_i = 100$ mm but on a higher level. Therefore, larger values of the pressure ratio are obtained for each measurement series. Due to the larger inner diameter, the pitch circle diameter is increased (Eq. (5.8)). This leads to an effective larger chamber length according to Eq. (5.9) and larger wall velocities of the inner diameter and average values of the brass faces according to Eqs. (5.3) and (6.82). As a result the ratio of the Couette mass flow rate to the Poiseuille mass flow rate is increased which leads to larger values of the pressure ratio. This is in good qualitative and quantitative agreement for measurements and 1D model except for low values of the gas rarefaction parameter and a speed ratio of $u_0 = 0.13$. It is shown that the pressure ratio for the measurements is lower than for the 1D model while the error bars become extremely large. The large error bars can be explained with Fig. 8.15 where the three pressure positions are plotted as a function of time t for the measurement series $u_0 = 0.13$ similar to Fig. 8.4 in Sec. 8.3. It is shown that although the high pressure p_{HP} and the recipient pressure p^*_{ch} are in steady state, the low pressure sensor p_{LP} fluctuates with time. This leads to a increasing standard deviation and thus to the large error bars. A possible reason is a significant increase of vibrations for a rotational speed $f = 100$ Hz which is much larger after the change of the inner diameter sleeve up to effective values of vibrational velocities of 10 mm/s which is about twice the values observed before the change of the sleeve. The vibrations are measured with the acceleration sensors in radial direction (horizontal and vertical) of the loose bearing. Due to the fluctuations of the lowest pressure sensor's signal the experimental results in this regime are questionable. Exchanging the pressure sensors of p_{HP} and p_{LP} leads to similar problems, so that a sensor failure itself does not seem to be the problem and further measurement results on this rotational speed are omitted.

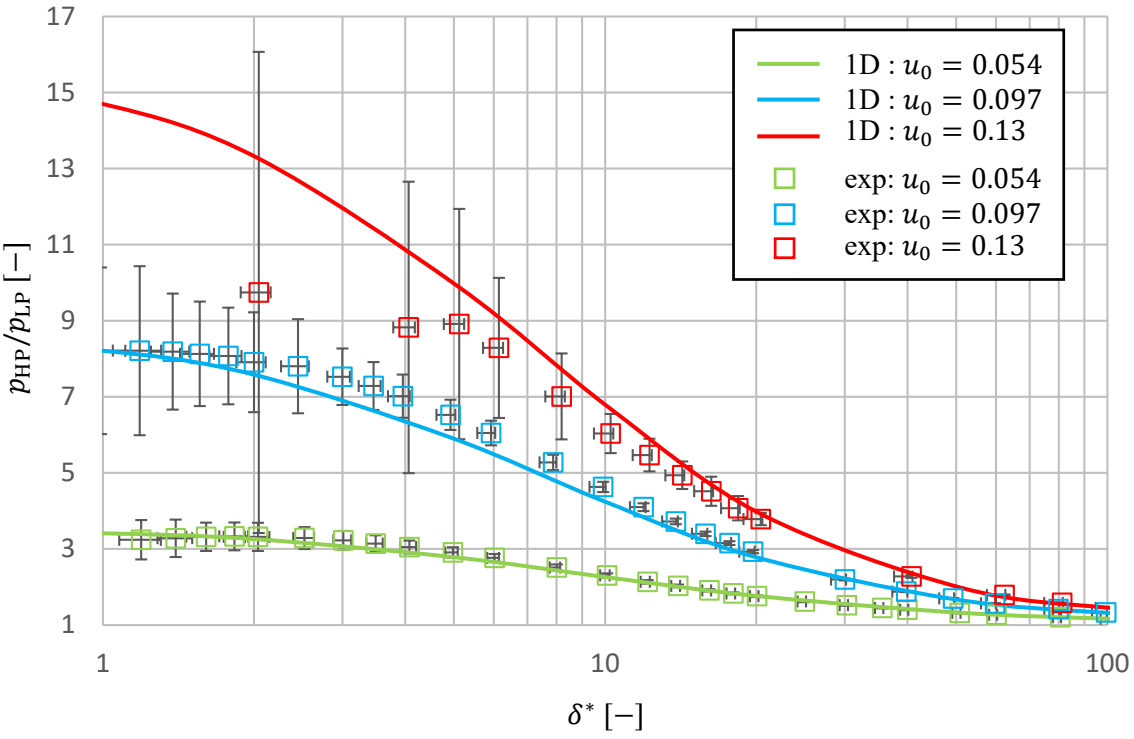

FIG. 8.14 Pressure ratio $p_{\mathrm{HP}}/p_{\mathrm{LP}}$ as a function of the gas rarefaction parameter δ^*. Comparison of the 1D model to measurements for $D_{\mathrm{o}}/D_{\mathrm{i}} = 1.4167$, $h_{\mathrm{cl,r}} = 0.2$ mm, $h_{\mathrm{cl,il}} = 0.15$ mm and different speed ratios u_0.

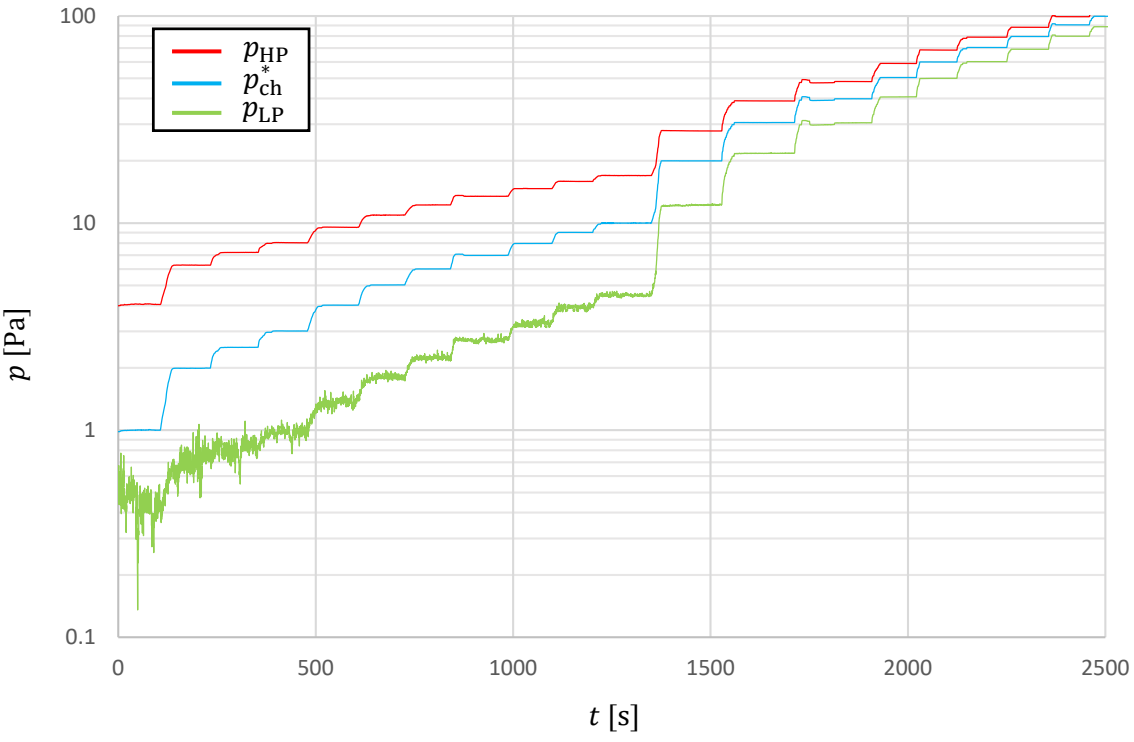

FIG. 8.15 Stationary measurements in discrete time intervals for speed ratio $u_0 = 0.13$. Fluctuations of p_{LP} occur, which are presumably caused by large vibrations.

8.8 Conclusion

As a short summary, in this chapter a test rig to investigate inhomogeneous pressure distributions in a simplified model of a chamber in SSVPs is presented where the chamber's low pressure p_{LP}, high pressure p_{HP} and the midpoint pressure in recipient p^*_{ch} are measured. The method of measurement is a stationary approach where different operation points can be adjusted and average values in a definite time interval can be evaluated. The uncertainties of measurement are discussed and although they are not negligible in every point, the main trends are depicted and show reasonable results with the most important verification that there exist significant inhomogeneous chamber states depending on the operation points. The pressure ratios $p_{\mathrm{HP}}/p_{\mathrm{LP}}$ and $p_{\mathrm{HP}}/p^*_{\mathrm{ch}}$ are investigated for different gas rarefaction parameters δ^*, speed ratios u_0, and a different geometric ratio $D_{\mathrm{o}}/D_{\mathrm{i}}$. The impact of the dimensionless mass flow rate C^*_0 is implicitly investigated by varying the clearances $h_{\mathrm{cl,r}}$. A comparison between experimental and 1D simulation results show that overall a great agreement is obtained. Thus the 1D model can be seen to be validated to be suitable to calculate inhomogeneous chamber states in positive displacement vacuum pumps. Due to the investigations in Chap. 7 this holds also for the 3D CFD simulations and for the regression functions Eqs. (7.1) and (7.2) in the described limits.

9 Transient Chamber Filling

Until now, only closed chambers are investigated where the change of the volume with time is negligible leading to a quasi-static approach. This is not the case for open chambers where the chamber volume linear increases (suction phase) or decreases (discharge) with time. Nevertheless, as the discharge phase is typically related to atmospheric conditions where according to previous investigations inhomogeneous effects are negligible only the suction phase is investigated further. In order to investigate the chamber filling in SSVPs, transient Computational Fluid Dynamics simulations (CFD) using ANSYS CFX 2021 R2[167] are performed.[I]

9.1 Domain and Boundary Conditions

Therefore, the suction chamber is abstracted as shown in Figs. 9.1 and 9.2. As a first simplification the rotor curvature is neglected. The mean chamber height as well as the chamber length and flank velocities along the pitch circle are then evaluated as shown in Chap. 5. This simplification is verified in Ref. [187] and in Chap. 7, where identical results are obtained using the 1D model with the mentioned geometric abstraction and full 3D CFD simulations including the curvature and linear rising wall velocities along the radius. As a second simplification, the rotor lead and therefore the axial movement of the chamber is neglected.

Figure 9.1 shows the used boundary conditions of the static domain (Fig. 9.1a), which is the connection to the machine's low pressure port and the boundary conditions of the moving domain which is the suction chamber (Fig. 9.1b). The two domains are connected with a conservative interface. The housing is marked in purple, while the red planes are openings where the suction pressure is prescribed. The green planes mark the machine's root circle and the black planes are the flanks with the average absolute velocity of the pitch circle. In Fig. 9.1a, the top plane and the upper front plane are symmetry planes. The moving domain is marked with a transparent orange and explained in Fig. 9.1b where the purple back plane is the housing while the green front plane marks the machine's root circle. The top (not coloured) and bottom plane (black) are the flanks and the yellow plane is the abstracted intersection edge with the cut lens, which is modelled as a no slip wall. For all other walls Maxwell slip boundary conditions according to Eqs. (3.102), (3.106) and (4.27) are used in order to improve the results for the slip regime.

In Fig. 9.2 two different time steps are shown. While the rotor moves clock wise along the y axis, the suction chamber grows according to Eq. (5.26). With the assumptions that curvature and rotor

[I] Parts of this chapter are reproduced from "H. Pleskun, A. Syring and A. Brümmer, "Transient chamber filling in rotary positive displacement vacuum pumps," IOP Conf. Ser.: Mater. Sci. Eng. **1267**, 012016 (2022)", with permission of IOP Publishing published under the CC BY license.[188]

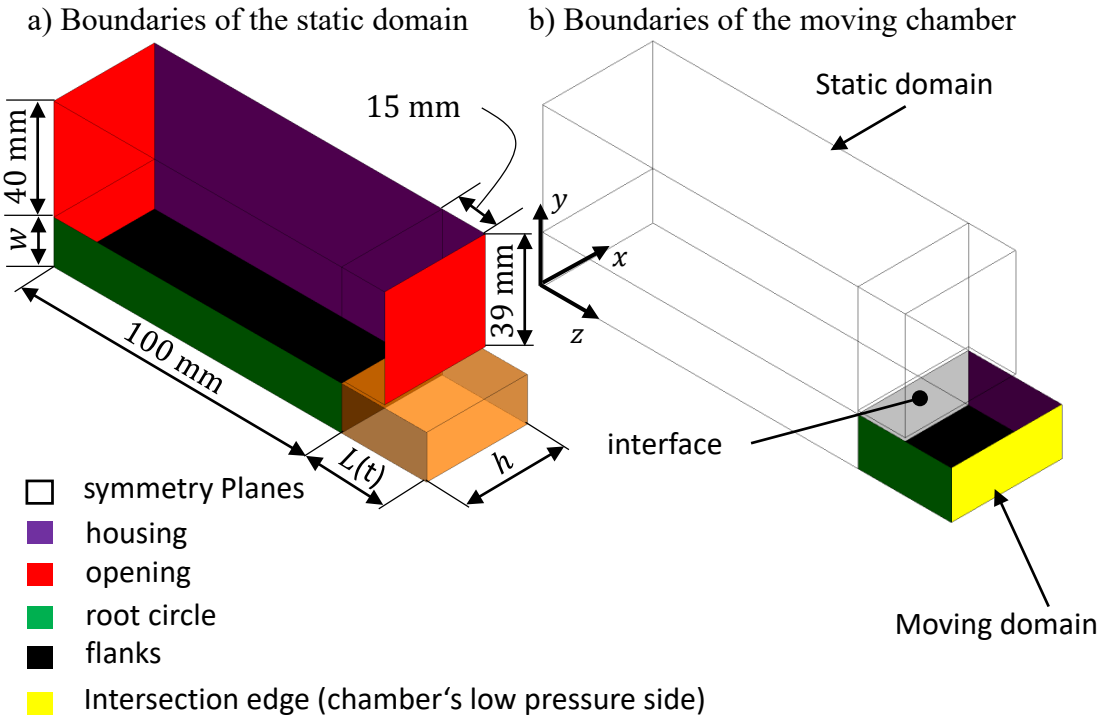

FIG. 9.1 Boundary conditions and 3D domains in Ansys CFX.

lead are neglected, the right hand side of the chamber is fixed and the inlet with the interface moves with constant velocity in negative z-direction in the absolute system. As this would cause problems with the boundary conditions in Ansys CFX because openings are not to be moved in normal direction[221], a change of the reference frame according to Sec. 3.3 is carried out which is the relative system of the rotating inlet area. Thus the inlet domain on the left hand side in Fig. 9.2 is fixed and the chamber elongates in positive z-direction. To achieve the same physical state, the relative velocity

$$U_{\mathrm{r,inlet}} = -\pi D_{\mathrm{pc}} f \tag{9.1}$$

is subtracted from each boundary condition. Therefore, the wall velocities within the CFD simulations are as follows:

$$U_{\mathrm{r,pc}} = U_{\mathrm{pc}} - U_{\mathrm{r,inlet}} = -\pi D_{\mathrm{pc}} f + \pi D_{\mathrm{pc}} f = 0 \tag{9.2}$$

$$U_{\mathrm{r,h}} = 0 - U_{\mathrm{r,inlet}} = \pi D_{\mathrm{pc}} f \tag{9.3}$$

$$U_{\mathrm{r,root}} = -\pi D_{\mathrm{i}} f + \pi D_{\mathrm{pc}} f = \pi f \left(D_{\mathrm{pc}} - D_{\mathrm{i}}\right) \tag{9.4}$$

with $U_{\mathrm{r,pc}}$ the relative velocity of the pitch circle, $U_{\mathrm{r,h}}$ the relative velocity of the housing and $U_{\mathrm{r,root}}$ the relative velocity of the root circle without rotor lead. The simulations are initialised with the suction pressure and the negative relative velocity $-U_{\mathrm{r,inlet}}$ with an initial chamber volume of 2.5 % of the whole chamber using a constant node number which is stretched with time. Comparing the pressure and velocity distribution within the two time steps in Fig. 9.2 in the middle of the domain in z direction, a constant pressure is obtained in the static domain, while the pressure within the suction chamber shrinks over x. Regarding the velocity fields a large velocity in x direction is obtained in the static domain with velocity close to zero at the flanks which cause stagnation

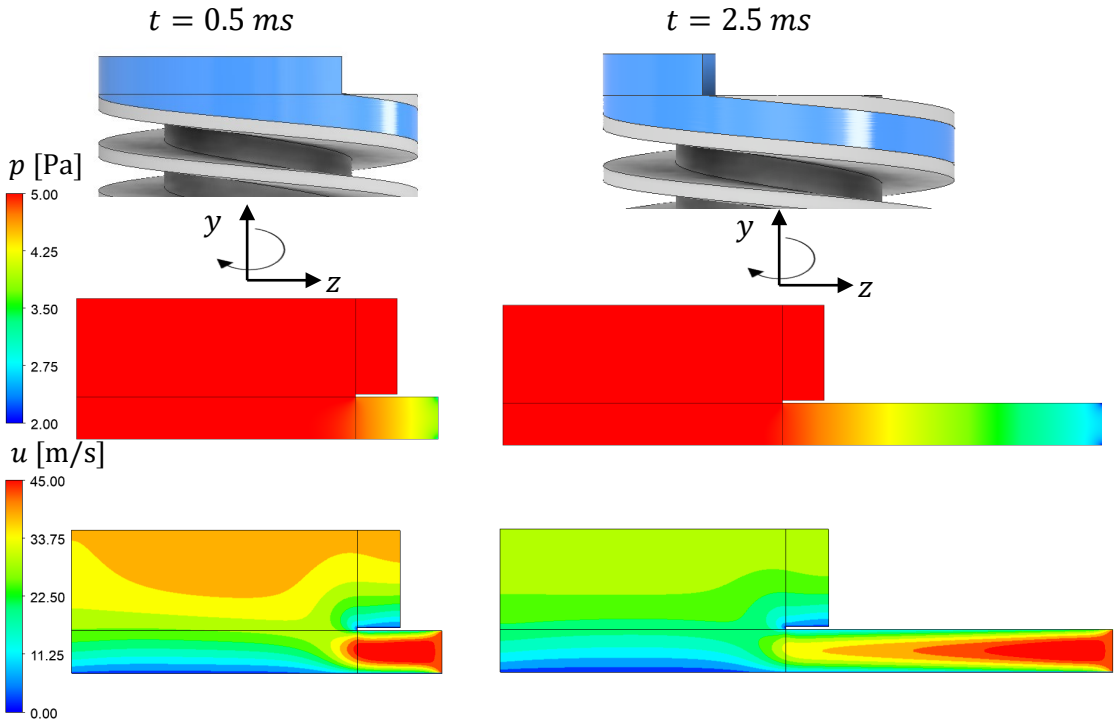

FIG. 9.2 Geometric abstraction of the CFD domain and with pressure and velocity distribution of two time steps.

points at the chamber's inlet with a large boundary layer due to the low gas rarefaction parameter and Reynolds number. At the earlier time step the velocity at the top is still higher due to the initialization.

As the pressure in the openings p_{HP} with

$$\delta_{\mathrm{HP}} = \frac{\min(h, w) \cdot p_{\mathrm{HP}}}{\mu \cdot c_{\mathrm{m}}} \tag{9.5}$$

is prescribed and the mass and volume in the moving domain changes in each time step, the mass averaged pressure as well as the chamber's low pressure p_{LP} are calculated as follows:

$$p_{\mathrm{ch}}(t) = \frac{RT}{V(t)} \int \rho(t)\, \mathrm{d}V(t) \tag{9.6}$$

$$p_{\mathrm{LP}}(t) = \frac{1}{A} \int p(t)\, \mathrm{d}S_{\mathrm{LP}} \tag{9.7}$$

$V(t)$ is the volume of the moving domain and $\mathrm{d}S_{\mathrm{LP}}$ is a surface increment of the chamber's low pressure side.

9.2 Error Estimation

All simulations are transient with a 2nd order backward Euler scheme, isothermal, laminar ($Re \ll 1$) with Maxwell slip boundary conditions with diffuse wall scattering and applied high resolution scheme for the convection terms[221]. In order to make an error estimation, a mesh study and a time step study are done. Therefore, a reference case is created with the machine boundary conditions given in Tab. 9.1 with 279500 nodes in the static domain and 255000 nodes in the moving domain.

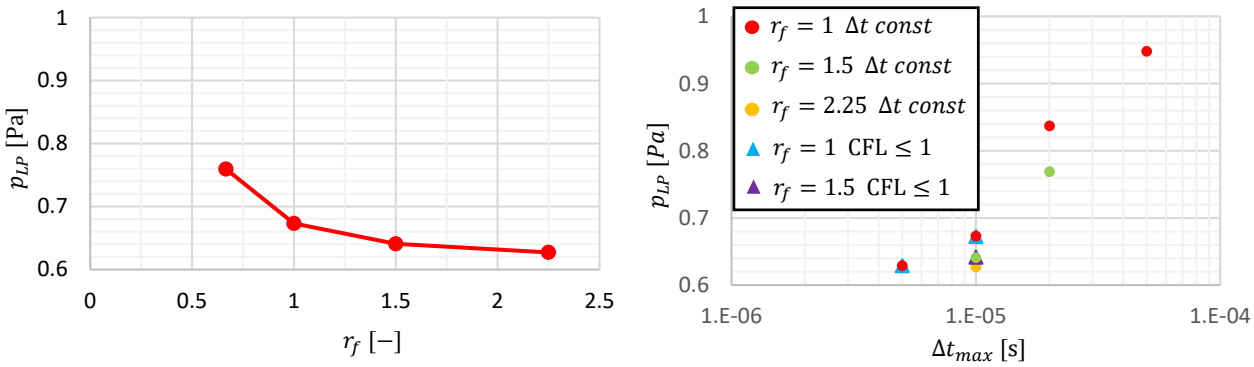

(a) Impact of the mesh refinement with $\Delta t = 10^{-5}\,s$

(b) Impact of the time step Δt

FIG. 9.3 Impact of mesh and time step on the chamber's low pressure p_{LP} at $L = L_{\max}$ for the reference case and $\delta = 10$

Starting from this reference mesh, different meshes with a constant refinement factor r_{f} ($r_{\mathrm{f}} = 1$ is the reference mesh) in each direction in the whole domain have been created and the resulting low pressure p_{LP} is evaluated at $L_{\max}$ with a constant time step $\Delta t = 10^{-5}\,\mathrm{s}$. This is shown in Fig. 9.3a, where p_{LP} has an asymptotic course with further refinement. A Richardson extrapolation according to Refs. [205] and [206] provides that the discretization error of the reference mesh is about 7 % regarding p_{LP} and about 2 % regarding the mass within the chamber. It needs to be noted that the maximum Courant-Friedrichs-Levy (CFL) number according to Eq. (4.22) is about 17 at the start of the simulations and smaller than 0.5 at the end for the reference mesh as the cell size grows with time. Therefore, the impact of the time step is investigated in Fig. 9.3b which shows p_{LP} as a function of the maximum time step. Three different meshes are used with a constant time step and two meshes with an adaptive time step with CFL ≤ 1. It is shown that there is no significant impact whether the CFL number is smaller than one or the time step is set constant, but the choice of the maximum time step is crucial and by reducing the time step the difference between the finest mesh and the reference mesh can be neglected, but the simulation time can be reduced from about a day to about three hours. Therefore, the reference mesh is used with a constant time step $\Delta t = 5 \cdot 10^{-6}\,\mathrm{s}$. The results can be explained by the movement of the mesh. Thus, a smaller time step also provides a better geometric resolution and the change of p with time is smaller.

TAB. 9.1 Data of the reference case

D_{o} [m]	D_{i} [m]	w [m]	f [Hz]	T [K]	δ_{HP} [−]	R [J kg^{-1} K^{-1}]	μ [Pa s]
0.17	0.1	0.015	100	298.15	10	287.1	$1.8351e-5$

9.3 Strouhal Number

In this section it is investigated how different boundary conditions influence the chamber filling. Therefore, starting from the reference case in Tab. 9.1, at first different time steps are evaluated. For each time step the mass averaged pressure and the low pressure within the moving domain

are calculated according to Eqs. (9.6) and (9.7). Then the Strouhal number related to the mass averaged pressure p_{ch} is evaluated explicitly using Eq. (5.29) with the current chamber length:

$$St = \mathcal{P} = \frac{L(t)}{p_{\mathrm{ch}}} \left.\frac{\partial p}{\partial z}\right|_{\mathrm{ch}} = \frac{L(t)}{\min(h,w) G_{\mathrm{P}}} \left(\frac{2\sum_{i=1}^{4} G_{\mathrm{C},i} U_i}{c_{\mathrm{m}}} - \frac{C_0}{\sqrt{\pi}} \right) \tag{9.8}$$

This is done every 0.5 ms until the chamber's full length according to Eq. (5.9) is reached. Figure 9.4 shows the pressure ratio $p_{\mathrm{ch}}/p_{\mathrm{HP}}$ as a function of the Strouhal number St for different boundary conditions while the impact of a mass flow rate of adjacent clearances is neglected ($C_0 = 0$). The different colours are related to a fixed gas rarefaction parameter δ_{HP} which is evaluated at the inlet, while the different symbols show different rotor frequencies which affect the wall velocities and the chamber speed $\mathrm{d}L/\mathrm{d}t$. The filled symbols are related to the width of the reference case $w = 0.015\,\mathrm{m}$ while the empty symbols have a width $w = 0.03\,\mathrm{m}$. It is obtained that all different chamber states are reduced to a single curve which can be approximated with an approximative logarithmic function according to Eq. (9.9) which is shown as the black dash-dot line (ln is the natural logarithm).

$$\frac{p_{\mathrm{HP}}}{p_{\mathrm{ch}}} \approx 1 + \ln\left(\frac{St}{2} + 1\right) \tag{9.9}$$

As the pressure ratio $p_{\mathrm{ch}}/p_{\mathrm{HP}}$ is the same as the actual mass within the chamber related to the mass if the chamber was filled homogeneously, it can be deduced that with higher Strouhal number the chamber gets less and less filled and therefore at $St \approx 3$ only about half of the theoretical mass is sucked into the machine without taking clearances into account. Thus the shown ratio $p_{\mathrm{ch}}/p_{\mathrm{HP}}$ can be seen as a filling efficiency. Furthermore, it is seen that large Strouhal numbers are obtained by low gas rarefaction parameters, by high rotor frequencies and by small values of the chamber width compared to the height. Now a comparison between the filling efficiency of single start and two start SSVPs can be done assuming $w \leq h$. Inserting Eq. (5.7) in Eq. (5.13) it is obtained that $p_{\mathrm{ch}}(t) = \frac{2Z\delta\mu c_{\mathrm{m}}}{s\cos(\varphi(D_{\mathrm{pc}}))}$. So if the same machine configuration is used and only the number of lobes is set from $Z = 2$ to $Z = 1$ for same δ the pressure ratio $\frac{p_{\mathrm{ch}}(t,Z=2)}{p_{\mathrm{ch}}(t,Z=1)} \approx 2$ and furthermore, according to Fig. 9.4 the single start SSVP has a better filling efficiency as the width w is larger. So all in all, the filling efficiency of a single start SSVP is better than that of a two start SSVP.

Similar results are obtained when the pressure ratio $p_{\mathrm{LP}}/p_{\mathrm{ch}}$ is evaluated which is illustrated in Fig. 9.5. This curve can be fitted by the approximative exponential function in Eq. (9.10).

$$\frac{p_{\mathrm{ch}}}{p_{\mathrm{LP}}} \approx \exp(0.58 \cdot St) \tag{9.10}$$

Next the impact of a mass flow rate through adjacent clearances on the transient chamber filling is investigated. Two different cases are studied. The first is a mass flow rate that comes from the direction of a cut lens tangential to the rotor lobe combined by radial clearance, inter-lobe clearance and blow hole. This is modelled by mass sources equally distributed on the chamber's low pressure side (yellow area in Fig. 9.1b). The mass flux per area increment is calculated in a way that the combined mass flow rate can be normalised with a constant suction pressure which is the chamber's high pressure p_{HP}:

$$C_{0,\mathrm{HP,t}} = \frac{\dot{m}_{\mathrm{cl,t}} \cdot \sqrt{\pi} c_{\mathrm{m}}}{p_{\mathrm{HP}} \cdot hw} \tag{9.11}$$

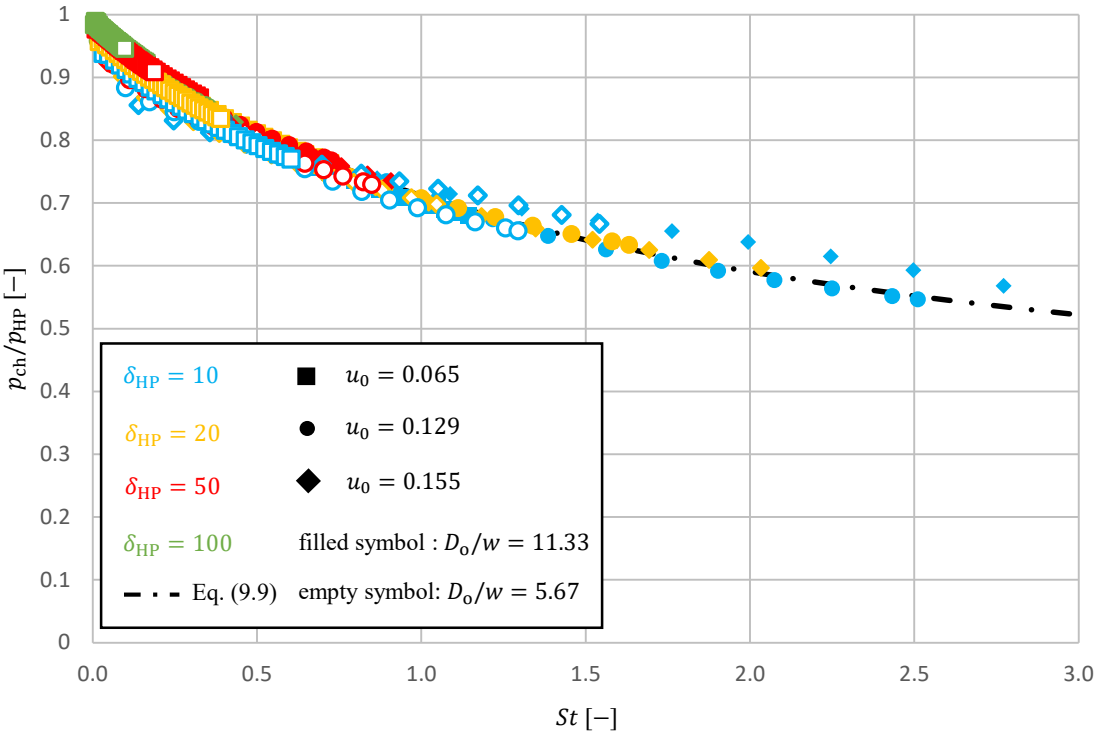

FIG. 9.4 Pressure ratio p_{ch}/p_{HP} as a function of the Strouhal number for different thermodynamic and geometric boundary conditions and $C_0 = 0$.

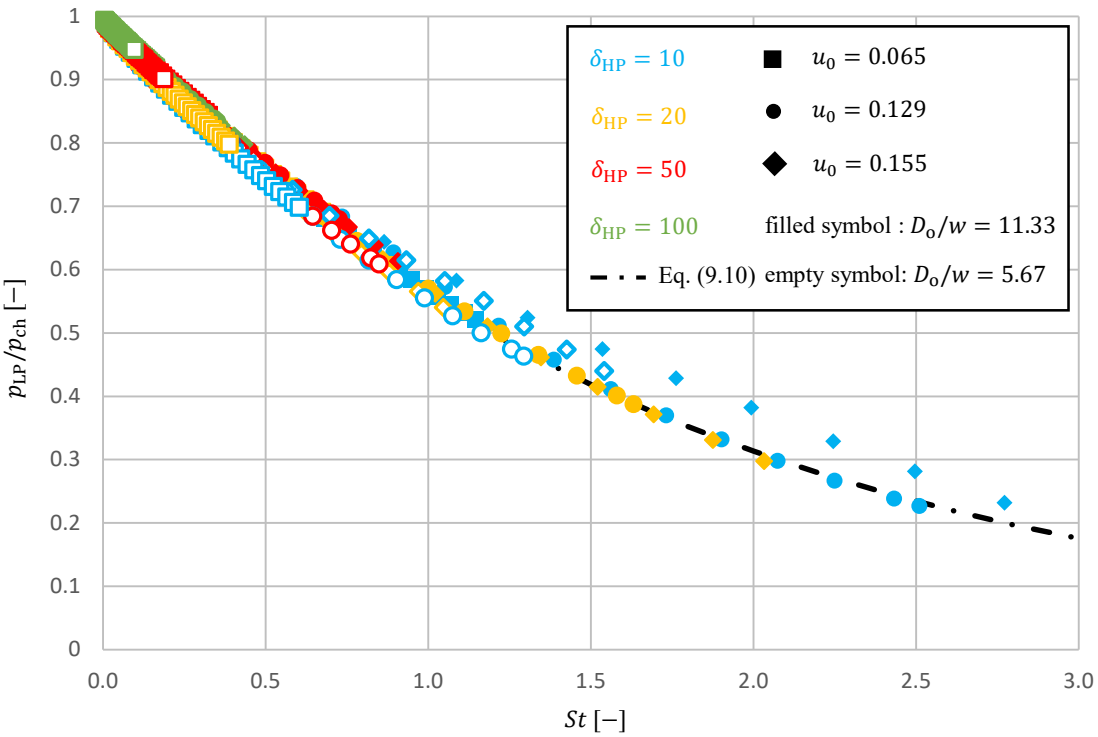

FIG. 9.5 Pressure ratio p_{LP}/p_{ch} as a function of the Strouhal number for different thermodynamic and geometric boundary conditions and $C_0 = 0$.

The prescribed mass flux per area increment is:

$$\frac{\dot{m}}{hw} = \frac{C_{0,\mathrm{HP,t}} \cdot p_{\mathrm{HP}}}{\sqrt{\pi} c_{\mathrm{m}}} \tag{9.12}$$

In order to evaluate the Strouhal number St at the mass averaged pressure according to Eq. (5.29), the normalised mass flow rate is calculated as follows:

$$C_{0,\mathrm{t}} = C_{0,\mathrm{HP,t}} \cdot \frac{p_{\mathrm{HP}}}{p_{\mathrm{ch}}(t)} \tag{9.13}$$

The second case is a prescribed mass flux for the housing clearance (purple area in Fig. 9.1b). Again the source term of the resulting inflowing mass flow rate $\dot{m}_{\mathrm{h}}$ of the housing is normalised using the chamber's constant high pressure p_{HP} with the definition:

$$C_{0,\mathrm{HP,h}} = \frac{\dot{m}_{\mathrm{h}} \cdot \sqrt{\pi} c_{\mathrm{m}}}{p_{\mathrm{HP}} \cdot hw} \tag{9.14}$$

Due to the different area of the housing clearance, the respective mass flux per area increment is calculated as follows:

$$\frac{\dot{m}_{\mathrm{h}}}{L(t)w} = \frac{C_{0,\mathrm{HP,h}} \cdot p_{\mathrm{HP}}}{\sqrt{\pi} c_{\mathrm{m}}} \frac{h}{L(t)} \tag{9.15}$$

As explained in Sec. 7.3, for the quasi-static simulations only half of the housing clearance mass flow rate is used to calculate the Strouhal number at the mass averaged pressure because it is equally distributed along the whole chamber. So when evaluating the pressure ratios $p_{\mathrm{ch}}/p_{\mathrm{HP}}$ and $p_{\mathrm{LP}}/p_{\mathrm{ch}}$ for the certain paths from about the middle of the chamber (p^*_{ch}) to the respective chamber ends, only about half of this value impacts the pressure gradient with the assumption that the positions of p_{ch} and p^*_{ch} do not differ much. Therefore, the normalised mass flow rate for the housing clearance used to evaluate the Strouhal number at the mass averaged pressure p_{ch} is calculated by

$$C_{0,\mathrm{h}} = \frac{C_{0,\mathrm{HP,h}}}{2} \cdot \frac{p_{\mathrm{HP}}}{p_{\mathrm{ch}}(t)} \,. \tag{9.16}$$

The resulting overall reduced mass flow rate to calculate the Strouhal number is:

$$C_0 = C_{0,\mathrm{t}} + C_{0,\mathrm{h}} \tag{9.17}$$

Figure 9.6 shows the impact of the adjacent mass flow rates on the pressure ratio $p_{\mathrm{ch}}/p_{\mathrm{HP}}$ for the reference case with $D_{\mathrm{o}}/w = 11.33$ and $u_0 = 0.129$. As before, the different colours show the different gas rarefaction parameters related to the chamber's high pressure p_{HP} and the symbols represent the cases: without any adjacent mass flow rates (circles), with a mass flow rate at the chamber's low pressure side (squares) and a mass flow rate through the housing (diamonds). It is seen that the certain mass flow rates lead to higher pressure ratios and smaller Strouhal numbers, so that the approximative Eq. (9.9) still fits very well and the impact of clearance mass flow rates on the filling efficiency is depicted with the above assumptions.

Figure 9.7 shows the impact of the adjacent clearance mass flow rates on the pressure ratio $p_{\mathrm{LP}}/p_{\mathrm{ch}}$ for the same boundary conditions. It is obtained that the housing clearance matches the functional of Eq. (9.10) very well. The tangential mass flow rates on the chamber's low pressure side lead to

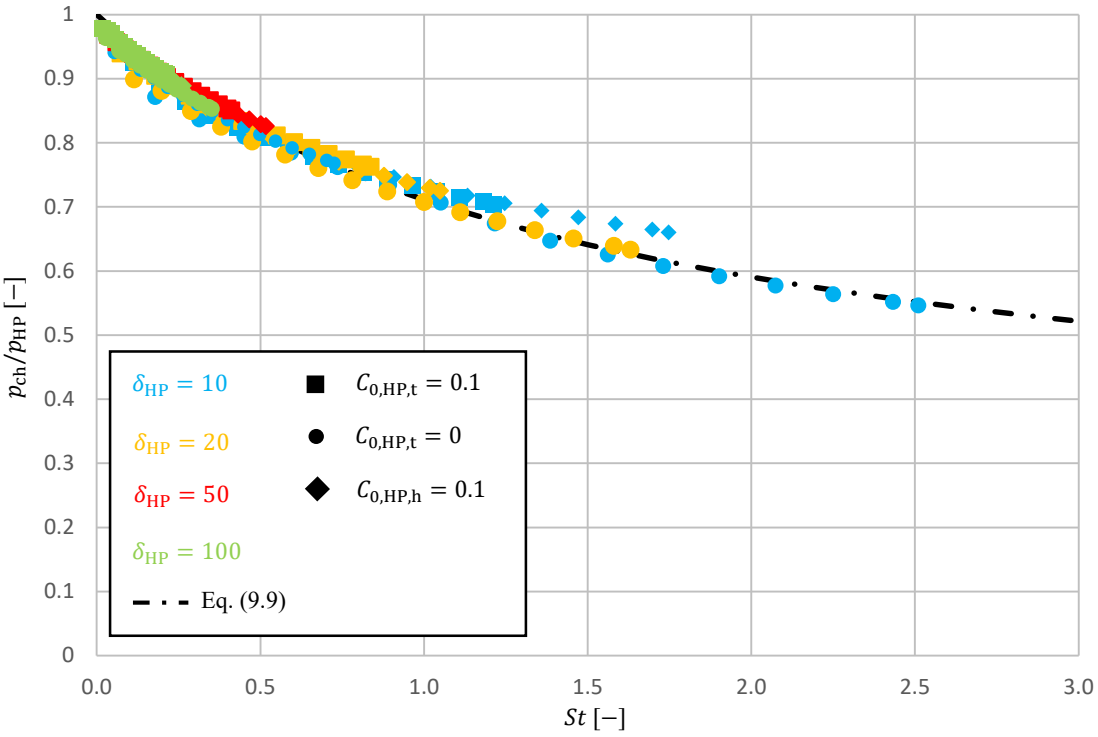

FIG. 9.6 Pressure ratio p_{ch}/p_{HP} as a function of the Strouhal number for different thermodynamic and geometric boundary conditions with $D_o/w = 11.33$ and $u_0 = 0.129$.

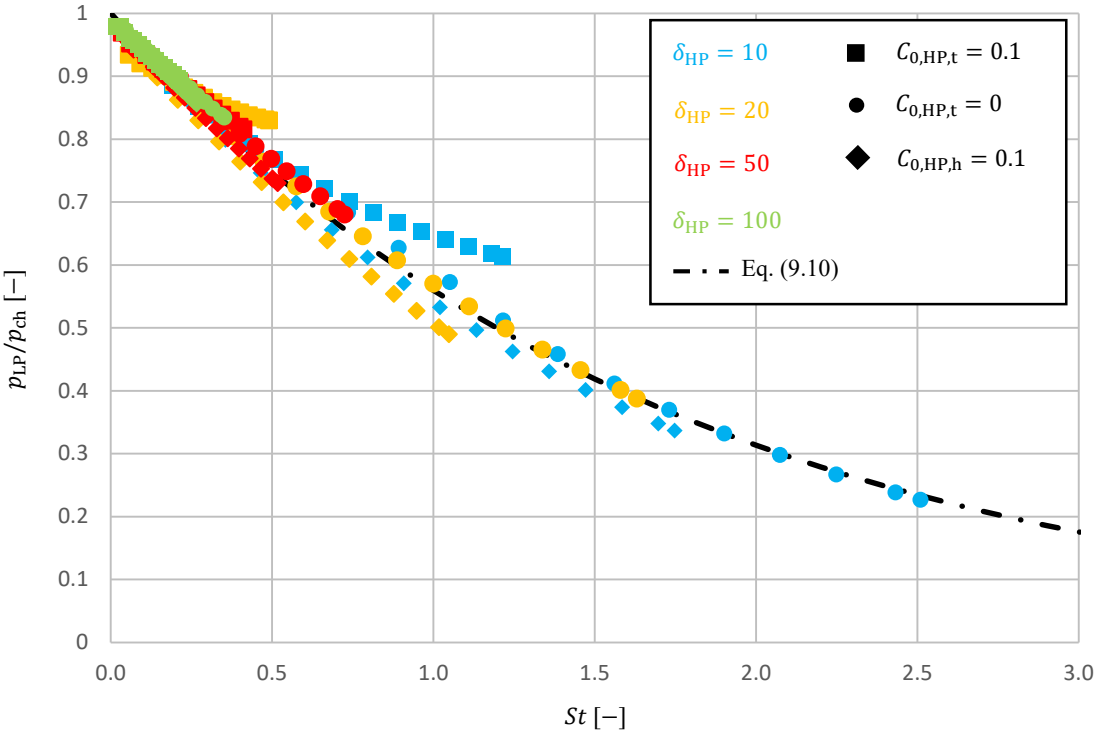

FIG. 9.7 Pressure ratio p_{LP}/p_{ch} as a function of the Strouhal number for different thermodynamic and geometric boundary conditions with $D_o/w = 11.33$ and $u_0 = 0.129$.

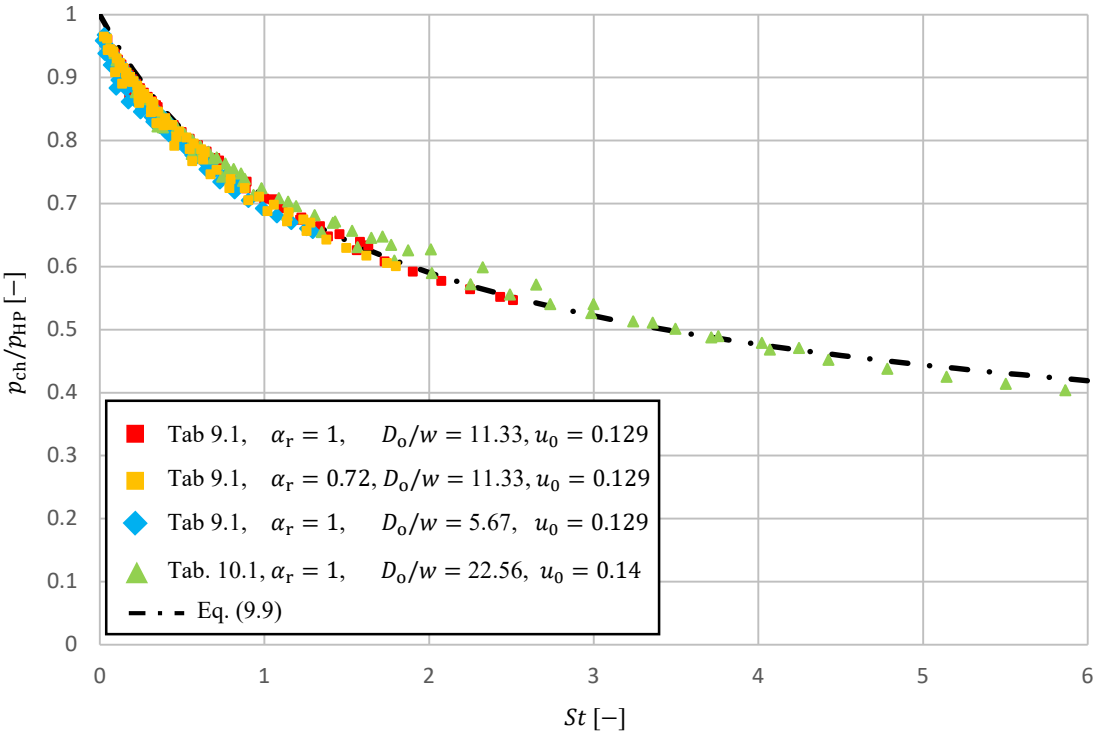

FIG. 9.8 Pressure ratio p_{ch}/p_{HP} as a function of the Strouhal number for different thermodynamic and geometric boundary conditions.

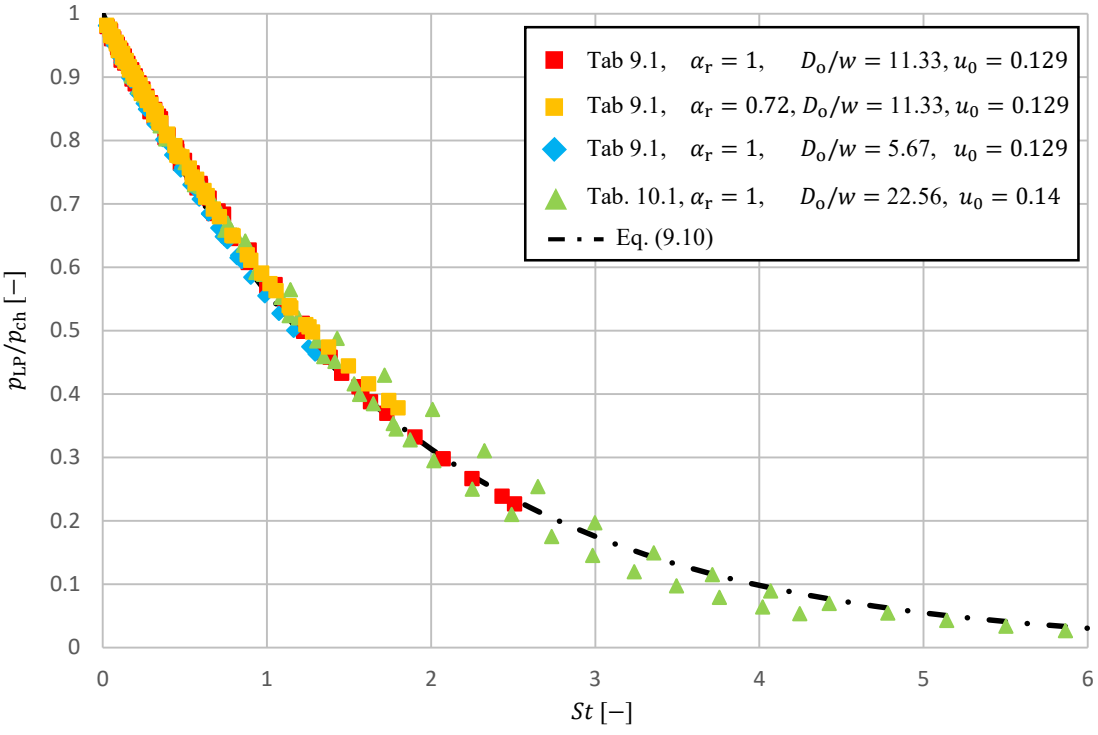

FIG. 9.9 Pressure ratio p_{LP}/p_{ch} as a function of the Strouhal number for different thermodynamic and geometric boundary conditions.

slightly higher pressure ratios which might be due to the fact that the mass sources are placed on the same plane where the low pressure is evaluated. If a small volume was modelled like the end

volumes within the cut lens, this might not be the case. Nevertheless, the differences are not too big, so even if there is a modelling error using Eq. (9.10) for large values of the tangential mass flow rate, it is neglected in this work. As already stated in Sec. 7.3 the chamber's low pressure side has a much lower impact on the machine performance, as it only corrects the outlet pressure for the determination of the gap mass flow rates and this impact is quite low in the low pressure regime.

Now at first the rotor material for the reference case (Tab. 9.1) is exchanged to aluminium and therefore the TMAC $\alpha_\mathrm{r} = 0.72$ (see Ref. [116]) while the TMAC of the housing is still $\alpha_\mathrm{h} = 1$. Furthermore, the geometric data of Tab. 10.1 is used with a rotor frequency $f = 83.33\,\mathrm{Hz}$ but diffuse wall scattering. All simulations are shown for $\delta_\mathrm{HP} = [10, 20, 50, 100]$ in Figs. 9.8 and 9.9. Again Eqs. (9.9) and (9.10) predict the simulation data. The change of the rotor material can lead to smaller Strouhal numbers with otherwise same boundary conditions and therefore improve the chamber filling process. Nevertheless, the gap mass flow rates will also be affected by the TMACs and therefore this does not necessarily mean that the overall machine is better if the rotor is made of a different material or is coated. This needs further investigation.

Although the impact of the rotor lead is neglected within the scope of the CFD simulations, it can be considered in order to calculate the Strouhal number St. As the rotor lead slightly affects the chamber length as well as the wall velocities (as shown in Sec. 5.1), the rotor lead slightly increases the resulting Strouhal number and with the help of Eqs. (9.9) and (9.10) p_LP and p_HP can be calculated.

9.4 Comparison Between Transient and Quasi-Static Chamber Filling

In this section a comparison between the transient simulation for the chamber filling process and the quasi-static approach of the 1D model is discussed. As described in the previous section, the pressure ratio $p_\mathrm{ch}/p_\mathrm{HP}$ is equal to the filling efficiency under isothermal conditions and can be calculated by an approximative functional (Eq. (9.9)) of the Strouhal number St which equals the normalised pressure gradient $\mathcal{P}$ according to Eq. (5.29). In Chap. 7 a similar approximative functional for the same pressure ratio (Eq. (7.1)) is derived for a closed chamber using a steady-state approach via 1D model which is validated with CFD and measurements. In order to calculate a quasi-static chamber filling process by neglecting the transient terms, Eq. (7.1) can be used by inserting the current chamber length $L(t)$ into the normalised pressure gradient, as it is done to calculate the Strouhal number in Eq. (9.8).

Figure 9.10 shows the pressure ratio $p_\mathrm{ch}/p_\mathrm{HP}$ as a function of the Strouhal number St or the respective normalised pressure gradient $\mathcal{P}$. The green curve is calculated via the approximative functional Eq. (9.9) derived from the transient simulations and the red curve shows the results from the quasi-static approach using Eq. (7.1) for $\delta = 10$. The fixed gas rarefaction parameter is chosen because the CFD simulations are valid here, so the difference between both curves is related to the transient terms considered in the green curve and are neglected in the quasi-static approach. It is obtained that both approaches start at $p_\mathrm{ch}/p_\mathrm{HP} = 1$ for $St = \mathcal{P} = 0$ with a decreasing filling efficiency for an increasing Strouhal number or respective normalised pressure gradient. Nevertheless, both curves diverge and a worse filling efficiency is predicted using the quasi-static approach. Therefore, Fig. 9.10 shows the impact of the transient inertial forces on the chamber filling process. Regarding the non-dimensional momentum equation in Eq. (3.117), the quasi-static

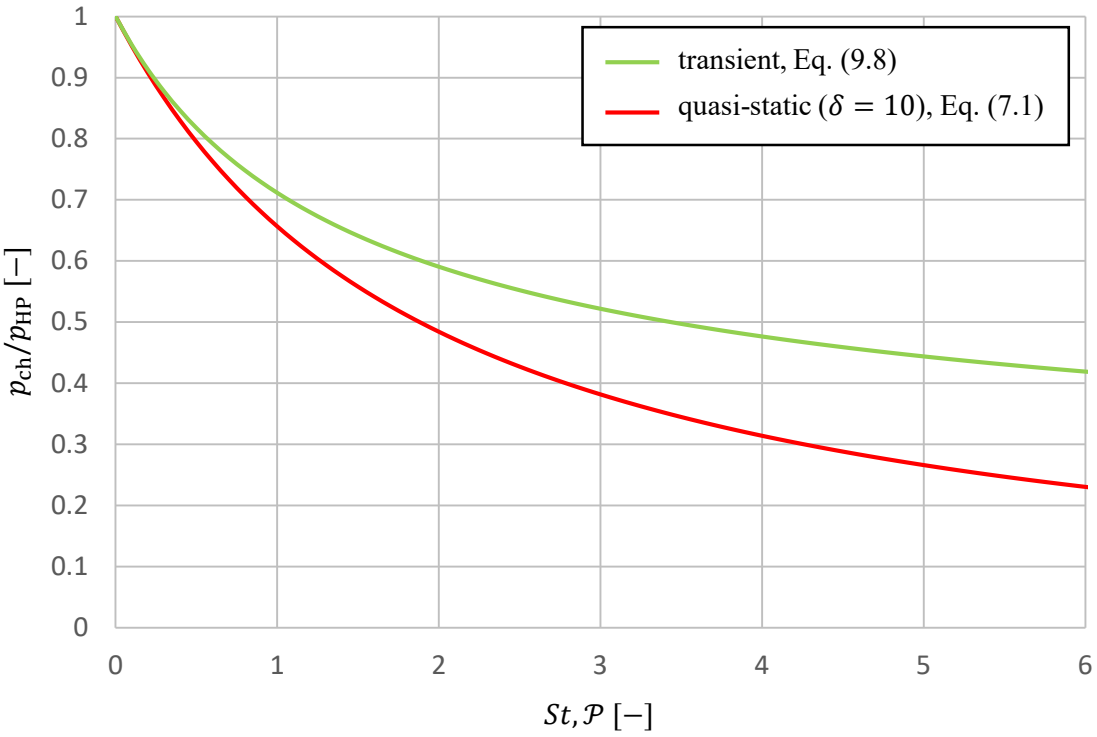

FIG. 9.10 Comparison between transient simulation and a quasi-static approach for the chamber filling process.

approach calculates a balance between pressure forces and fluid friction while all inertial forces and external body forces are neglected. The transient simulations include inertial forces, but the advective forces are negligible due to low Reynolds numbers.

As shown in Fig. 7.3 for $\delta < 10$ the results of the kinetic theory of gases and the Navier-Stokes equations with Maxwell slip boundary conditions diverge as the ratio of gas-surface interactions to intermolecular collisions is increased. This leads to a an error in the modelled friction force using the Navier-Stokes equations. Nevertheless, due to the increasing inertial forces in the transient simulations for higher Strouhal numbers, the relative impact of the friction forces on the resulting pressure ratio decreases. Therefore, it can be justified to use Eq. (9.9) for $\delta < 10$ because the expected integral error is small, as the filling efficiency is close to one for low values of the Strouhal number and the transient inertial forces dominate for high Strouhal numbers.

10 Chamber Model Simulation

In this chapter the new models for inhomogeneous chamber states and the chamber filling process are validated in the context of chamber model simulation. Therefore, at first the principal procedure of the simulation tool *KaSim* developed at the Chair of Fluidics at TU Dortmund University and the implementation of the new models are explained. Then the geometric abstraction of a test machine is described whose experimental machine performance is available due to previous investigations. This data is compared to the simulation results of the chamber model simulation including the new investigated models.[I]

10.1 The Simulation Tool *KaSim*

The solver *KaSim* is based on the fill and discharge method, which forms the basis for the thermodynamic calculation of positive displacement machines by means of chamber model simulation. In this case, the process variables under consideration are only considered as a function of time, but not as a function of space. The solver is written in the object based programming language C++ and there are mainly two types of objects used within the chamber model scope: capacities and connections. Capacities such as fluid volumes or rigid bodies contain mass and energy and can either be finite (such as chambers) or infinite (such as a drive or the atmosphere). Connections only transfer mass or energy between the different capacities during a time step. Therefore, the solver is based on the conservation of mass and energy using an explicit quasi-static time step algorithm[36]. As already sketched in Sec. 1.1.2 the machine is abstracted into chambers (capacities) and connecting gaps (connections). While the chambers transport mass and energy from suction to discharge port, due to the gaps mass and energy can be transferred in the opposite direction and heat can be exchanged through the surrounding surfaces. Transferring Eqs. (3.97) and (3.99) into the relative system of the moving chamber similarly to Chap. 5, the mass and energy equation for a chamber with index i can be written in the following forms:

$$\frac{\mathrm{d}m_i(t)}{\mathrm{d}t} = \sum_j \dot{m}_{\mathrm{r},j} \tag{10.1}$$

$$\frac{\mathrm{d}E_{\mathrm{t},i}(t)}{\mathrm{d}t} = \sum_j h_{\mathrm{t},j}\dot{m}_{\mathrm{r},j} + p\frac{\mathrm{d}V}{\mathrm{d}t} + \sum_j \dot{Q}_j \tag{10.2}$$

[I] Parts of this chapter are reproduced from "H. Pleskun, T. Jünemann and A. Brümmer, "Validation of inhomogeneous chamber states in rotary positive displacement vacuum pumps," IOP Conf. Ser.: Mater. Sci. Eng. **1267**, 012010 (2022)" and "H. Pleskun, A. Syring and A. Brümmer, "Transient chamber filling in rotary positive displacement vacuum pumps," IOP Conf. Ser.: Mater. Sci. Eng. **1267**, 012016 (2022)", with permission of IOP Publishing published under the CC BY license.[187,188]

Therefore, the change of mass m_i within chamber i with time is related to the sum of the relative mass flow rates $\dot{m}_{\mathrm{r},j}$ between the adjacent chambers or the openings to the ports of each time step. Similarly, the change of the total inner energy

$$E_{\mathrm{t},i} = \int_{\Omega_i} \rho e_{\mathrm{t},i} \, \mathrm{d}V \tag{10.3}$$

of chamber i is related to the sum of relative total enthalpy flows between the adjacent chambers, the rates of heat flow through the surrounding surfaces and the power due to change of volume similar to the work in Eq. (3.50). Therefore, the pressure term in Eq. (3.99) is split as follows:

$$\oint_{\mathcal{S}(t)} \rho e_{\mathrm{t}} (\boldsymbol{u} - \boldsymbol{v}_{\mathcal{S}}) \cdot \boldsymbol{n} \, \mathrm{d}A + \oint_{\mathcal{S}(t)} p (\boldsymbol{u} \cdot \boldsymbol{n}) \, \mathrm{d}A = \underbrace{\oint_{\mathcal{S}(t)} \rho h_{\mathrm{t}} (\boldsymbol{u} - \boldsymbol{v}_{\mathcal{S}}) \cdot \boldsymbol{n} \, \mathrm{d}A}_{\sum_j h_{\mathrm{t},j} \dot{m}_{\mathrm{r},j}} + \underbrace{\oint_{\mathcal{S}(t)} p (\boldsymbol{v}_{\mathcal{S}} \cdot \boldsymbol{n}) \, \mathrm{d}A}_{p \frac{\mathrm{d}V}{\mathrm{d}t}} \tag{10.4}$$

Body forces as well as friction power is neglected and only used to calculate mass flow rates and the pressure distribution within the chamber. The latter is justified because a rotating reference frame could be used where the friction power at the rotor is zero, but instead centrifugal forces are present which according to Sec. 3.6.3 are negligible in the context of rarefied gases. The kinetic energy is considered small as well and can thus be neglected.

The conservation of momentum $\boldsymbol{\mathcal{M}}$ and angular momentum $\boldsymbol{\mathcal{L}}$ is assumed to be decoupled from the conservation of mass and energy and is used to calculate the resulting pressure forces and torques on the rotors. Other fluid forces are assumed to be small. Therefore, the resulting forces $\boldsymbol{\mathcal{F}}$ and torques $\boldsymbol{\mathcal{T}}$ on the rotors are calculated as follows:

$$\frac{\mathrm{d}\boldsymbol{\mathcal{M}}}{\mathrm{d}t} = \boldsymbol{\mathcal{F}} = -\oint_{\mathcal{S}(t)} p \boldsymbol{n} \, \mathrm{d}A \tag{10.5}$$

$$\frac{\mathrm{d}\boldsymbol{\mathcal{L}}}{\mathrm{d}t} = \frac{\mathrm{d}\left(I\boldsymbol{\omega}\right)}{\mathrm{d}t} = \boldsymbol{\mathcal{T}} - \boldsymbol{l} \times \boldsymbol{\mathcal{F}} = \boldsymbol{\mathcal{T}} + \oint_{\mathcal{S}(t)} p \left(\boldsymbol{l} \times \boldsymbol{n}\right) \, \mathrm{d}A \tag{10.6}$$

I is the mass moment of inertia around the rotation axis z,

$$\boldsymbol{\omega} = \begin{pmatrix} 0 \\ 0 \\ \omega \end{pmatrix} \tag{10.7}$$

is the vector of the respective angular frequency and $\boldsymbol{l}$ is the lever of the respective area increment related to the origin which is located on the axis on the rotor's high pressure side. Both rotors are kinematically coupled with

$$\boldsymbol{\omega}_{\mathrm{GR}} = -i \cdot \boldsymbol{\omega}_{\mathrm{MR}} \tag{10.8}$$

where

$$i = \frac{Z_{\mathrm{MR}}}{Z_{\mathrm{GR}}} \tag{10.9}$$

is the lobe ratio of main rotor MR and gate rotor GR respectively which is equal to 1 in the present work. The machine's inner power is calculated as

$$P = z_{\mathrm{MR}} \cdot f_{\mathrm{MR}} \cdot \int p \, \mathrm{d}V = \omega_{\mathrm{MR}} \cdot \mathcal{T}_{z,\mathrm{MR}} + \omega_{\mathrm{GR}} \cdot \mathcal{T}_{z,\mathrm{GR}} \tag{10.10}$$

where the change of chamber volume with time on both rotors is calculated with respect to the main rotor's rotational speed f_{MR}. Due to geometric periodicity this needs to be calculated only for one tooth pitch angle

$$\Phi = \frac{2\pi}{Z_{\mathrm{MR}}} \tag{10.11}$$

and the result is multiplied with the number of starts Z_{MR}.[13,36,38]

The resulting algorithm is sketched in Fig. 10.1. The solver starts with the model input. Therefore, the geometric data such as the chamber volumes and cross-section areas of the gaps as well as the surface areas need to be known as a function of the main rotor's phase angle

$$\phi = \frac{\alpha}{\Phi} \tag{10.12}$$

with the main rotor's rotation angle α. Due to a multi-chamber approach where all occurring chambers are simulated simultaneously, the starting rotor position is arbitrary. After the model input, the chambers are initialised, for example, with the low pressure and ambient temperature. The next step is to calculate the current time step and phase angle according to the number of steps per phase angle chosen in the input file. In the next step the thermodynamic and mechanic change of state is calculated starting with the resulting pressure forces and torques according to Eqs. (10.5) and (10.6) in the current phase angle. Then the mass, energy and heat flows between the respective capacities are calculated as a function of the boundary conditions in the current phase angle. The following step is related to asymmetric machines where the blow hole on one side is so large that the connected chambers can be considered as one chamber. Therefore, mass and energy between these chambers are exchanged until both chambers have the same thermodynamic state. This is similarly done in any connection in case that the mass increment exchanged within a time step is too large, such that the new pressure of the capacity with the higher initial pressure is lower than the new pressure of the connected capacity with lower initial pressure. After concluding and saving the thermodynamic and mechanic changes of states in this time step the rotor frequency is updated in case of a prescribed torque according to Eq. (10.6) and accordingly the frequency dependent objects such as wall velocities as explained in Chap. 5 and Sec. 10.3 are updated. If the end of a period is not reached ($\phi < 1$), the next time step is calculated. Otherwise ($\phi = 1$) convergence is checked. Therefore, the maximum relative deviation of mass m_i^n or energy E_i^n in any chamber i to the previous period $n-1$ is calculated and compared to a convergence criterium $\varepsilon_{\max}$[13]:

$$\varepsilon = \max \left[\left| \frac{m_i^n - m_i^{n-1}}{m_i^{n-1}} \right| ; \left| \frac{E_i^n - E_i^{n-1}}{E_i^{n-1}} \right| \right] \leq \varepsilon_{\max} \tag{10.13}$$

The machine's mass flow rate is the effective mass Δm_n exchanged within the last period between chambers and an infinite fluid capacity times the chamber frequency

$$\dot{m} = \Delta m_n Z_{\mathrm{MR}} f_{\mathrm{MR}} \tag{10.14}$$

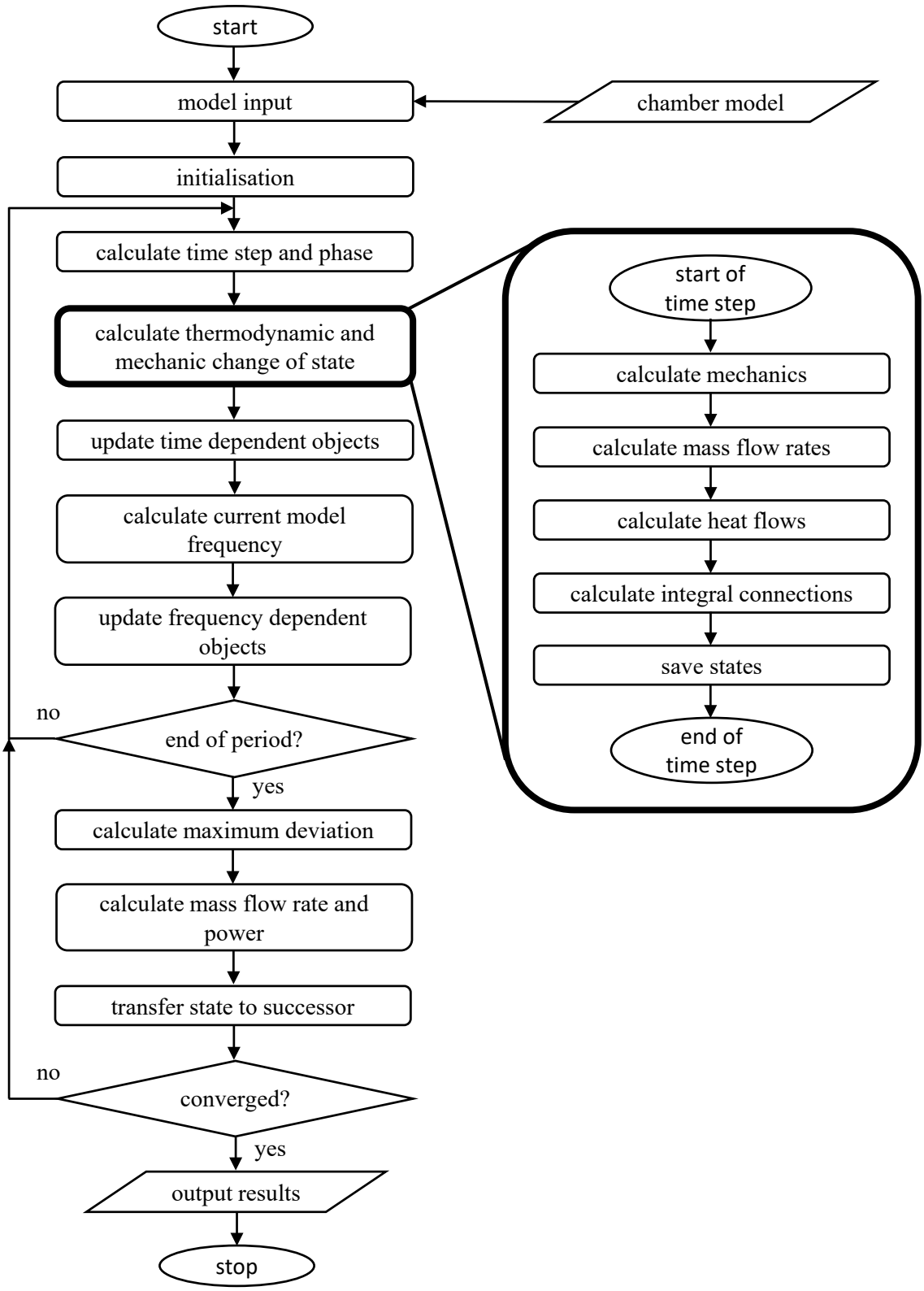

FIG. 10.1 Flow chart of the chamber model simulation tool *KaSim*[13].

and the power is calculated according to Eq. (10.10). As any capacity is defined within a scope of a phase $\phi \in [0, 1]$, at the end of the period the fluid state needs to be transferred to the successor which is defined one phase angle later. If the convergence criterium of Eq. (10.13) is reached, an output is created, otherwise the next period is calculated. Detailed information about the implementation, available sub-models for the calculations of mass flow rates, rates of heat flow or adsorption and

desorption, mechanic calculations and validations are given in Refs. [13, 22, 28, 35, 36, 38, 39, 41, 45]. As the convergence criterium defined in Eq. (10.13) is very strict, in this work a simulation is also considered to be converged if the change of the mass flow rate in five consecutive periods is less then 1 %.

10.2 Inhomogeneous Chamber States

The previously explained version of *KaSim* where states are stored as scalar values in capacities, is based on the assumption of homogeneous distributions within the chambers. To extend this structure, a new object type, the *fluid access interface*, is added. These interfaces are connected to the corresponding chamber and they are also assigned a normalised position so that the boundary conditions for the gap flows can be calculated accordingly. In the current definition, position 0 corresponds to the low pressure side of the chamber. Position 0.5 describes the average state and position 1 is the high pressure side of the chamber. Subsequently, the gaps are not directly connected to the chamber, but to the corresponding interface, as shown in Fig. 10.2. Therefore, the housing gaps are connected with the chamber's average chamber state on the same rotor. The blow holes connect two high pressure sides or two low pressure sides of adjacent chambers on different rotors and the radial and inter-lobe gap connect a high pressure side of one chamber that is closer to the discharge port with a low pressure side of another chamber that is closer to the suction port. Furthermore, the suction port is connected with an open chamber's high pressure side and the discharge port is connected with an open chamber's low pressure side. These connections can be explained with the relative wall velocity movement sketched in Figs. 2.1 and 5.1.

Within the interface no fluid state is stored itself, apart from the effective transferred mass increment of the last time step. Therefore, the resulting relative mass flow rate through each interface is calculated as

$$\dot{m}_\mathrm{r}(t) = \frac{1}{\Delta t} \sum_j \Delta m_j(t) \tag{10.15}$$

with j the index of the connection to the respective interface. Therefore, the housing mass flow rate $\dot{m}_\mathrm{h}$ is stored in the fluid access interface with position 0.5 and the tangential mass flow rates $\dot{m}_\mathrm{LP}$ and $\dot{m}_\mathrm{HP}$ are stored in the fluid access interfaces at positions 0 and 1 respectively. These mass flow rates are stored at each time step and are used to calculate the effective tangential mass flow rate carried through the chamber with the following simplification:

$$\dot{m}_\mathrm{cl,t} \approx \min\left(\left|\dot{m}_\mathrm{LP}\right|, \left|\dot{m}_\mathrm{HP}\right|\right) + \frac{\dot{m}_\mathrm{h}}{2} \tag{10.16}$$

The model to evaluate the chamber's low pressure p_LP and high pressure p_HP using Eqs. (7.1) and (7.2) with the help of the dimensionless pressure gradient in Eq. (5.21) for closed chambers uses a steady-state assumption. Thus, the mass flow rate flowing into the chamber needs to equal the mass flow rate flowing out of the chamber. Therefore, the minimum function is used within the chamber model. For open chambers the min function is not needed as the mass flow rate only comes from the chamber's low pressure side. In this case Eqs. (9.9) and (9.10) with the help of the Strouhal number in Eq. (5.29) are used to calculate the chamber's low and high pressure. The reason why only half of the housing gap mass flow rate is used is explained in Sec. 7.2.

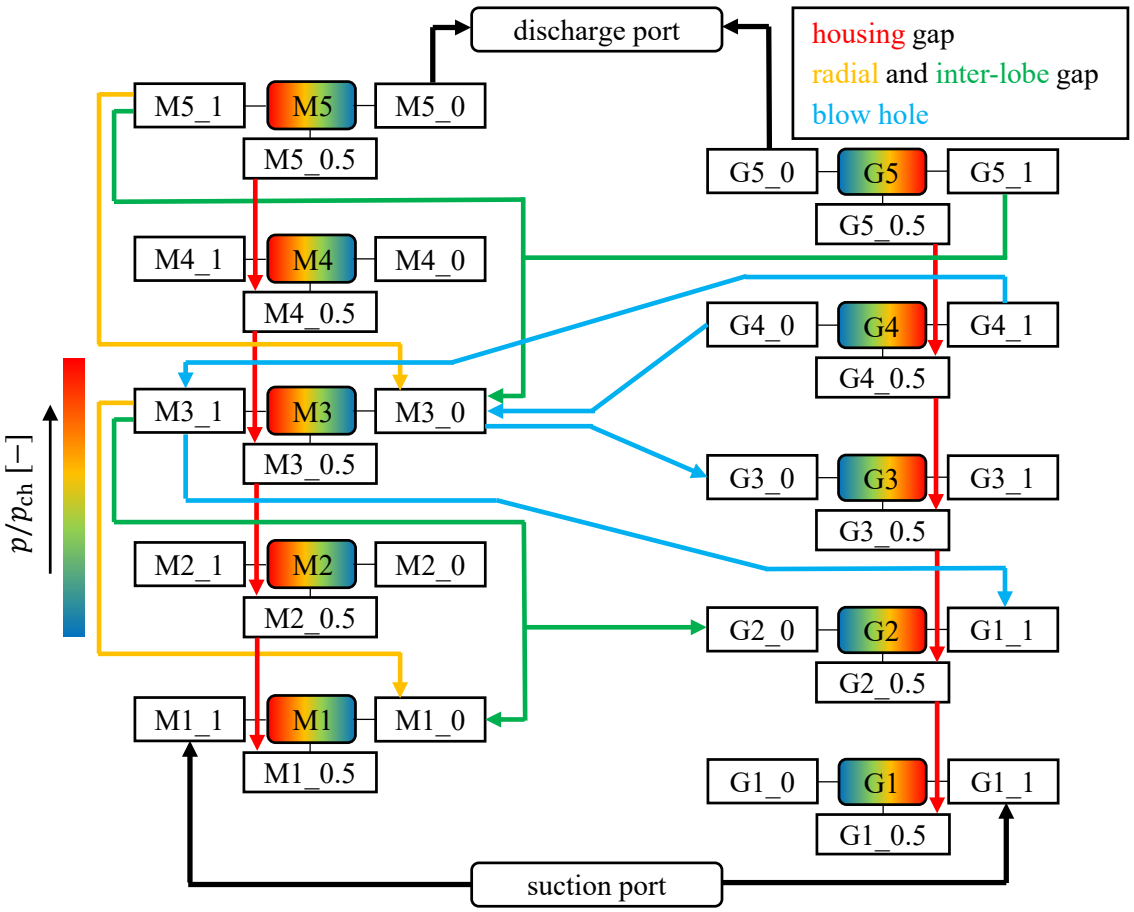

FIG. 10.2 Simplified sketch of the chamber model with inhomogeneous chamber states for 5 male rotor chambers (M1-M5) and 5 gate rotor chambers (G1-G5). The gaps are now connected with chamber access objects which are located at certain positions of the respective chamber. The suction port is connected to the chambers' high pressure side and the discharge port is connected to the chamber's low pressure side. For better clarity, only the connections to chamber M3 have been drawn for most gaps.

Furthermore, due to convergence problems the maximum mass flow rate through the chamber has been capped by the following expression:

$$0 \leq C_0/\pi \leq \sum_i G_{\mathrm{C},i} U_i / c_{\mathrm{m}} \tag{10.17}$$

This avoids a change of the pressure distribution in the opposite direction which in very few operation points led to change of signs in the resulting mass flow rates in each iteration step and did not converge.

The last step needed to evaluate the chamber's high and low pressure is the geometry for the 1D model. Within the chamber model simulation the total chamber volume with the given chamber mass and energy for each rotation angle is available. Due to the geometric abstraction made in Chap. 5 there is a discrepancy between the 1D model's chamber volume

$$V_{\mathrm{mod}} = L(t) h w \tag{10.18}$$

and the total chamber volume V_t to set the boundary conditions uniquely for the different gaps (blow hole, radial gap and inter-lobe gap) that are modelled separately. Furthermore, in the case of open chambers, only the part which is already covered by the trailing rotor tooth is assumed to be inhomogeneous. As long as there is a direct connection to the port, it is assumed that the respective port pressure is imposed as sketched in Fig. 9.2. Thus, the total chamber volume is divided as follows

$$V_\mathrm{t} = V_\mathrm{s} + V_\mathrm{mod} + V_\mathrm{e} \tag{10.19}$$

where $V_\mathrm{s} = V_\mathrm{e}$ are the chamber's start and end volume within the cut lens respectively. This classification is performed as the total mass m_t within the chamber is distributed on these three volumes with the linearisation

$$m_\mathrm{s} + m_\mathrm{e} = \int_{\Omega_\mathrm{s}} \rho \, \mathrm{d}V_\mathrm{s} + \int_{\Omega_\mathrm{e}} \rho \, \mathrm{d}V_\mathrm{e} \approx \frac{p_\mathrm{ch}}{RT}(V_\mathrm{s} + V_\mathrm{e}) \tag{10.20}$$

which assumes a linear pressure distribution within the chamber. As either the start and end volumes are small compared to the total chamber volume or the deviation from the linear pressure distribution is negligible in case that V_mod is small, the total error of this assumption is considered small. Therefore, the current chamber length for the model can be calculated by

$$L(t) = \frac{V_\mathrm{t}(t) - V_\mathrm{s} - V_\mathrm{e}}{hw} \tag{10.21}$$

without changing the mass averaged pressure for the model or violating conservation of mass. In case of a variable rotor lead an average chamber width for each phase angle is proposed using Eqs. (5.1) and (5.7) by using the linearisation for the current rotor lead

$$s(\phi) = 2\pi \frac{\Delta z(\phi)}{\Delta \psi(\phi)} = 2\pi \frac{z_\mathrm{max}(\phi) - z_\mathrm{min}(\phi)}{\psi(z_\mathrm{max}(\phi)) - \psi(z_\mathrm{min}(\phi))} \tag{10.22}$$

where $z_\mathrm{max}(\phi)$ is the maximum z-coordinate of a chamber in the current rotation angle with the the respective wrap angle $\psi_\mathrm{max}(\phi)$, and $z_\mathrm{min}(\phi)$ and $\psi_\mathrm{min}(\phi)$ are the corresponding minimum values.

10.3 Gap Flow Models

The mass flow rates through the different gaps are calculated by a theoretical mass flow rate that can be calculated by analytical means multiplied by a flow coefficient or reduced mass flow rate. The latter depends on the certain gap shape, the wall velocities and the boundary conditions given by the fluid states of the chamber position or the suction and discharge port.

10.3.1 Theoretical Mass Flow Rates

There are two basic concepts used to calculate a theoretic mass flow rate for perfect gases in this work. One is the approach by Saint Venant and Wantzel[91] where the gap mass flow rate can be calculated as follows:

$$\dot{m}_\mathrm{SVW} = A \cdot p_\mathrm{in} \cdot \sqrt{\frac{2\gamma}{(\gamma - 1) \cdot R \cdot T_\mathrm{in}}} \cdot \sqrt{\Pi_\mathrm{cl}^{\frac{2}{\gamma}} - \Pi_\mathrm{cl}^{\frac{\gamma+1}{\gamma}}} \tag{10.23}$$

This approach assumes a pure Poiseuille flow which is adiabatic and frictionless until the gap exit at minimum height is reached and the remaining kinetic energy is dissipated in the low pressure reservoir. For pressure ratios

$$\Pi_{\mathrm{cl}} = \frac{p_{\mathrm{out}}}{p_{\mathrm{in}}} \leq \Pi_{\mathrm{cl,crit}} = \left(\frac{2}{\gamma+1}\right)^{\frac{\gamma}{\gamma-1}} \tag{10.24}$$

the flow is choked and reaches $M = 1$ in the smallest cross-section area A. Therefore, the resulting mass flow rate cannot be increased by reducing the outlet pressure. In this case the maximum theoretical mass flow rate is reached and is independent of the outlet pressure:[36]

$$\dot{m}_{\mathrm{SVW,max}} = A \cdot p_{\mathrm{in}} \cdot \sqrt{\frac{2\gamma}{(\gamma+1)\cdot R \cdot T_{\mathrm{in}}}} \cdot \left(\frac{2}{\gamma+1}\right)^{\frac{1}{\gamma-1}} \tag{10.25}$$

This consideration is useful to estimate physical limits in the continuum regime and therefore defines a maximum.

Another theoretical mass flow rate used is the already defined effusion mass flow rate

$$\dot{m}_{\mathrm{eff}} = \frac{p_{\mathrm{in}} A}{c_{\mathrm{m}}\sqrt{\pi}} \tag{10.26}$$

which is independent of the pressure ratio and the heat capacity ratio γ. This approach defines a limit in the free molecular regime as a flow through a frictionless slit and has an advantage in the context of rarefied gases when using dimensional analysis. As for rarefied gases a complete heat exchange can often be assumed, γ is not an influencing parameter and the reduced flow rate

$$C_0^{\mathrm{cl}} = \frac{\dot{m}}{\dot{m}_{\mathrm{eff}}} \tag{10.27}$$

will lead to equal results if the dimensionless parameters in Sec. 5.2 are constant when the gas is exchanged for example from air to helium which has a different heat capacity ratio. This would not be the case if Eqs. (10.23) or (10.25) were used as normalising condition.

10.3.2 Friction Models

The simplest approach for a friction model is to choose a fixed dimensionless mass flow rate $C_0^{\mathrm{cl}} \in [0, 1]$ with one of the theoretical mass flow rate definitions. This provides reasonable results and is applied in the context of compressors or expanders in the continuum regime using Eqs. (10.23) and (10.25)[36,38,39] with

$$C_{0,\mathrm{SVW}}^{\mathrm{cl}} = \frac{\dot{m}}{\dot{m}_{\mathrm{SVW}}} \ . \tag{10.28}$$

In the context of vacuum pumps Stratmann[41] and Pfaller[28] used this procedure to model an inlet and outlet throttling by connecting the open chambers with the ports with such a gap model. Pfaller used a constant value of $C_{0,\mathrm{SVW}}^{\mathrm{cl}} = 0.8$ and Stratmann used a constant value of $C_{0,\mathrm{SVW}}^{\mathrm{cl}} = 1$ and found out that due to the large axial opening areas this effect is very small anyway[41]. In this work Stratmann's value is adopted.

For rarefied gap flows, this model is not useful, as the frictional effects as well as the Couette flow are dominant. Therefore, Wenderott[45] created a database where he measured the actual mass flow

rates through different gap geometries in a great variety of boundary conditions with static walls. He normalised his results using Eq. (10.25) as the effect of the pressure ratio in Eq. (10.23) is not represented well in friction dominated flows. As the blowhole can be considered a slit where the impact of moving walls is small, this database is used to calculate the mass flow rate for this gap in this work.

Stratmann[41] extended this data base by simulations of the test particle method through the same gap geometries but with moving boundaries. The results of the free molecular regime are interpolated with the measurements in the following way:

$$\dot{m} = \dot{m}_{\mathrm{exp}} \cdot (1 - F) + \dot{m}_{\mathrm{sim}} \cdot F \tag{10.29}$$

$$F = \begin{cases} 0 & Kn < 0.01 \\ \frac{\ln\left(Kn^{-1}\right) - \ln(2)}{\ln(100) - \ln(2)} & 0.01 \leq Kn \leq 0.5 \\ 1 & Kn > 0.5 \end{cases} \tag{10.30}$$

Therefore, for a Knudsen number $Kn = 0.5$ the free molecular regime is defined, where only his simulation data $\dot{m}_{\mathrm{sim}}$ of the test particle method is used and for $Kn = 0.01$ the continuum limit is defined where the impact of moving walls is neglected and only the experimental data $\dot{m}_{\mathrm{exp}}$ of Wenderott is used. This extension of the data base significantly increased the simulation accuracy for screw spindle vacuum pumps as the mass flow rates through the gaps increase with increasing rotational speed which significantly influences the predicted machine performance[24]. The model itself is questionable though. The chosen limits do not refer to the state of the art especially regarding the free molecular regime as shown in the previous chapters. In the continuum regime the Couette flow is completely neglected and the interpolation approach in the defined intermediate regime is not validated and for some boundary conditions it was even possible to get smaller resulting mass flow rates with a small moving boundary velocity in flow direction than with static walls, which is a result of the interpolation procedure specifically. Nevertheless, as for the inter-lobe gap the flow path is not completely clear, the approach of modelling this connection by Stratmann is adopted for this gap.

For the housing gap and the radial gap the 1D model developed and validated by Jünemann[49,50] is used. With the help of this model, a new database is created based on dimensionless parameters which are similar to those described in Sec. 5.2. A difference is that the mass flow rate is now the target parameter and the pressure ratio a dimensionless boundary condition. Furthermore, the heat capacity ratio is non-negligible in the continuum flow regime which is set to $\gamma = 1.4$ for air in the current implementation and can be extended in pending works for other gas types. Additionally a diffuse wall scattering is used for the sake of simplicity. Therefore, the dimensionless mass flow rate C_0^{cl} is calculated with a multi-variate interpolation approach as a function of the gas rarefaction parameter δ, the pressure ratio

$$\Pi^{\mathrm{cl}} = \frac{p_{\mathrm{out}}}{p_{\mathrm{in}}} \tag{10.31}$$

and the speed ratio

$$u_0^{\mathrm{cl}} = \frac{U^{\mathrm{cl}}}{c_{\mathrm{m}}} \tag{10.32}$$

for a constant heat capacity ratio and diffuse wall scattering where U^{cl} is the relative wall velocity in the gap. For the housing gap the height to length ratio $h_{\mathrm{cl,h}}/L_{\mathrm{h}}$ is varied and the respective wall

velocity $U^{\mathrm{cl,h}} = U_{\mathrm{h,normal}}$ according to Eq. (5.5). The width $w \gg h$ is considered large for both gaps, so that an influence of the gap width is neglected.

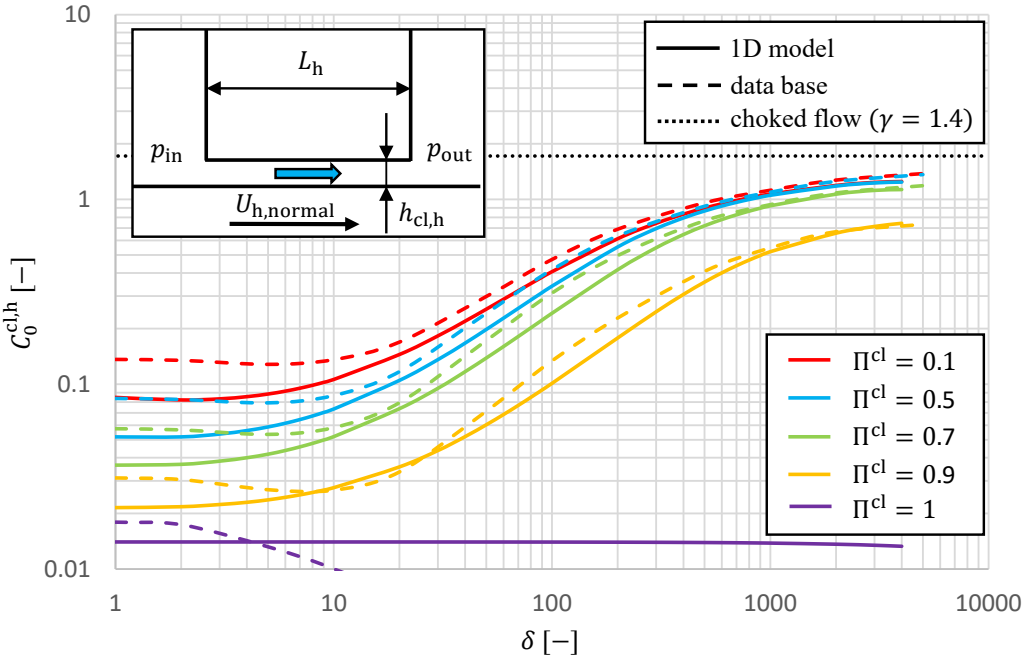

FIG. 10.3 Reduced mass flow rates C_0^{h} for the test machine's housing gap as a function of the gas rarefaction parameter δ for different pressure ratios Π^{cl}, a speed ratio $u_0^{\mathrm{cl}} = 0.008$ and a geometric ratio $h_{\mathrm{cl,h}}/L_{\mathrm{h}} = 0.03$. A comparison between 1D model according to Jünemann[49,50] to the data base of Wenderott[45] and Stratmann[41].

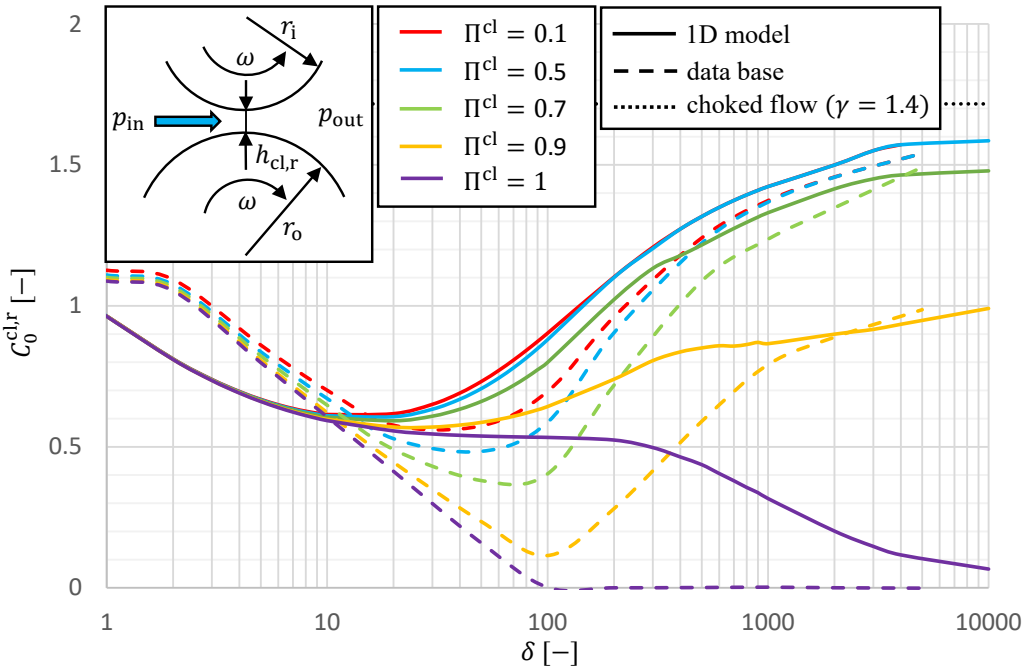

FIG. 10.4 Reduced mass flow rates $C_0^{\mathrm{cl,r}}$ for the test machine's radial gap as a function of the gas rarefaction parameter δ for different pressure ratios Π^{cl}, a speed ratio $u_0^{\mathrm{cl}} = 0.14$ and geometric ratios $r_{\mathrm{o}}/r_{\mathrm{i}} = 1.57$ and $h_{\mathrm{cl,r}}/r_{\mathrm{o}} = 0.0027$. A comparison between 1D model according to Jünemann[49,50] to the data base of Wenderott[45] and Stratmann[41].

Figure 10.3 shows a sketch of the housing gap including the absolute input parameters and the diagram shows the reduced housing gap mass flow of the test machine in Tab. 10.1 as a function of the gas rarefaction parameter for different pressure ratios at a fixed speed ratio $u_0^{\mathrm{cl}} = 0.008$ and height to length ratio $h_{\mathrm{cl,h}}/L_{\mathrm{h}} = 0.03$. It is noticeable that the 1D model in the continuum regime - where the influence of the moving boundary is small - agrees almost exactly with the measurements of the Wenderott database as long as the pressure ratio is smaller than one. The resulting mass flow rate is well below the theoretical limit of a choked flow. With a pressure ratio $\Pi^{\mathrm{cl}} = 1$ on the one hand, the old database neglects the Couette flow which is represented in the 1D model. For small gas rarefaction parameters, on the other hand, it is noticeable that Stratmann's simulations depict a systematically larger gap mass flow than the 1D model. This can be explained by the fact that Stratmann assumed that free molecular flow already takes place at $\delta \approx 2$ and intermolecular collisions are thus negligible. In the transition regime it is shown that the interpolation approach chosen by Stratmann achieves plausible results for this gap configuration and that both approaches achieve similar results.

For the radial gap both walls have a wall velocity according to Eqs. (10.51) and (10.52) and two geometric ratios are used: The ratio gap height to outer radius $h_{\mathrm{cl,r}}/r_{\mathrm{o}}$ and the ratio of the outer to inner radius $r_{\mathrm{o}}/r_{\mathrm{i}}$. Figure 10.4 shows a sketch of the radial gap with the used parameters and the diagram shows the respective reduced mass flow rate as a function of the gas rarefaction parameter δ for different pressure ratios Π^{cl}. The geometric ratios are fixed to $r_{\mathrm{o}}/r_{\mathrm{i}} = 1.57$ and $h_{\mathrm{cl,r}}/r_{\mathrm{o}} = 0.0027$ and the speed ratio related to the outer diameter is $u_0^{\mathrm{cl}} = 0.14$. This gap has a large amount of Couette flow compared to the housing gap, as both walls move in the direction of flow with the circumferential speed of the outer and inner diameters. In this case, it can be seen that the moving boundary cannot be neglected even for the continuum flow. This becomes particularly clear at a pressure ratio $\Pi_{\mathrm{cl}} = 1$, where the database determines a mass flow rate of zero for $\delta > 100$, which cannot be justified due to large circumferential speeds. But also in the transition regime, the influence of the wall velocities is clearly underestimated by the interpolation approach. The curves calculated by means of the 1D model for the different pressure ratios are much smoother. As a result, the gap mass flow rate calculated by means of the 1D model for $\delta > 10$ is almost always greater than that determined by the database. However, this turns around again for $\delta < 10$ due to the incorrectly assumed limit for the free molecular flow at $\delta \approx 2$. However, it needs to be noted that the pragmatic approach of Stratmann significantly improved the accuracy of the simulation results compared to the previous state of the art and determined the main tendencies correctly. The integral impact on the predicted machine performance of the new gap flow models compared to those of the old data base is shown in Ref. [187].

10.4 Geometry Model

In this section the geometric abstraction of the machine is explained beginning with the definition of the face section as shown in Fig. 10.5. A symmetrical two-start cycloidal profile is sketched in which both rotors are identical. In addition to the outer circles, inner circles and pitch circles already introduced in Chap. 5, the generating circles are of particular importance. The size of these generating circles determines the shape of the tooth flanks. These are formed by the rolling of the generating circles inside and outside the pitch circle over the resulting path curve corresponding to an epicycloid outside the pitch circle and a hypocycloid inside the pitch circle. However, at the

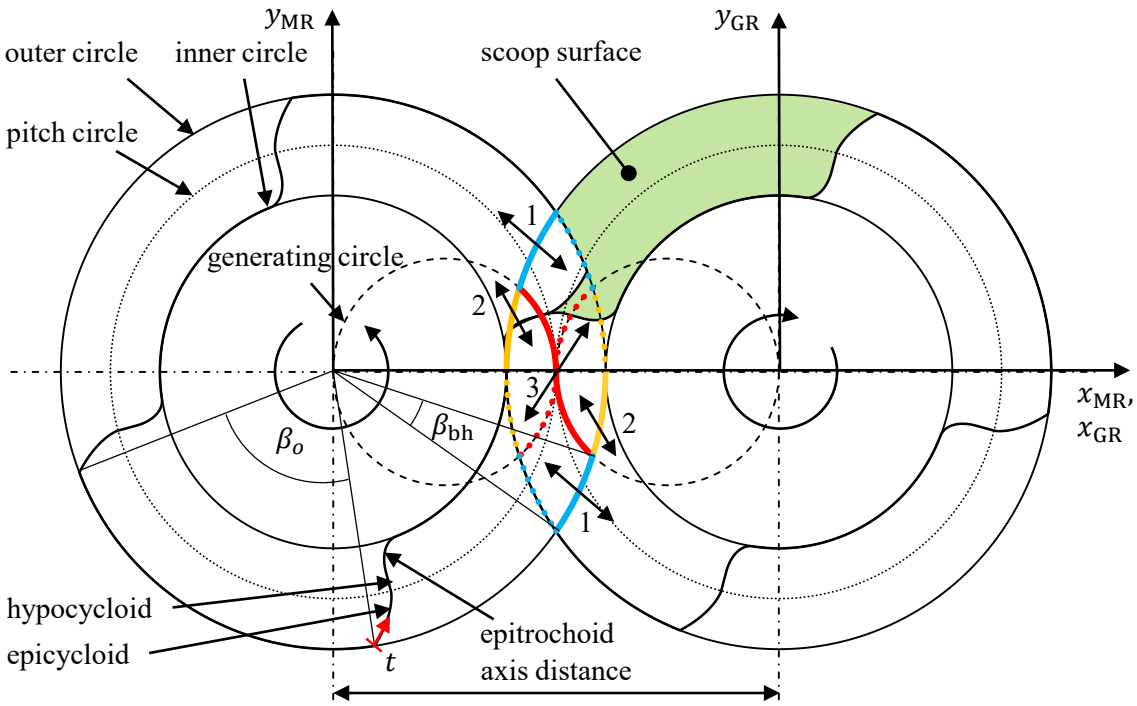

FIG. 10.5 Sketch of a symmetric two-start cycloid profile. The blowhole (1) connects two adjacent chambers of main and gate rotor. The inter-lobe gap is defined by the contact line and is divided in two parts. The flank-to-tip clearance (2) that is formed by the tip of one rotor flank and the envelope of the other rotor (epitrochoid) and the flank-to-flank clearance (3) that is formed by the two flanks of both rotors rolling off each other. The chambers are separated by the contact line within the cut lens.[29]

transition from the cycloid flank to the inner circle, this would create an unnecessary hole within the profile engagement, which is closed by an envelope (epitrochoid). The resulting contact line within the cut lens of the two rotors - i.e. the connection of the points of contact in the clearance-free profile - separates the main rotor chambers from the gate rotor chambers and can be divided into two parts. On the one hand, the rotors touch each other on a curve that is created by the generating circles through the rolling of two tooth flanks on each other until the outer circle is reached. The resulting gap is also called flank-to-flank clearance (3) and connects main rotor chambers with gate rotor chambers. From the outer point of the contact line, the gap is closed by the envelope which is only formed by the rolling of the outer flank point on the outer circle onto the opposite tooth flank and is accordingly called flank-to-tip clearance (2) which connects chambers on the same rotor. The resulting profile engagement runs along the outer circle of one rotor until the inner circle of the other rotor is reached. At this point, the outer circle of one rotor and the inner circle of the other rotor roll off each other. The resulting gap is also called a radial gap which also connects chambers on the same rotor. The solid lines of the contact line shown in Fig. 10.5 are formed by the trailing tooth flanks of the right rotor and the leading flanks of the left rotor. The dashed lines refer to the opposite flanks, whose design is identical in the symmetrical profile. The blue lines in Fig. 10.5 represent the blowholes (1). As the contact of the rotors only takes place on the line of engagement, a profile-related gap is formed along the connecting line between the outermost contact point to the cusps.[29]

10.4.1 Mathematical Rotor Description

The cycloid flank that connects the inner and outer circle is created by the epicycloid (ec) outside the pitch circle with

$$\begin{pmatrix} x \\ y \end{pmatrix}_{\mathrm{ec}} = \begin{pmatrix} (r_{\mathrm{pc}} + r_{\mathrm{gen}}) \cdot \cos(t_{\mathrm{ec,max}} - t_{\mathrm{ec}}) - r_{\mathrm{gen}} \cdot \cos\left(\left(1 + \frac{r_{\mathrm{pc}}}{r_{\mathrm{gen}}}\right)(t_{\mathrm{ec,max}} - t_{\mathrm{ec}})\right) \\ -(r_{\mathrm{pc}} + r_{\mathrm{gen}}) \cdot \sin(t_{\mathrm{ec,max}} - t_{\mathrm{ec}}) + r_{\mathrm{gen}} \cdot \sin\left(\left(1 + \frac{r_{\mathrm{pc}}}{r_{\mathrm{gen}}}\right)(t_{\mathrm{ec,max}} - t_{\mathrm{ec}})\right) \end{pmatrix} \tag{10.33}$$

$$0 \leq t_{\mathrm{ec}} \leq t_{\mathrm{ec,max}} \tag{10.34}$$

and a hypocycloid (hc) inside the pitch circle with

$$\begin{pmatrix} x \\ y \end{pmatrix}_{\mathrm{hc}} = \begin{pmatrix} (r_{\mathrm{pc}} - r_{\mathrm{gen}}) \cdot \cos(t_{\mathrm{hc}}) + r_{\mathrm{gen}} \cdot \cos\left(\left(\frac{r_{\mathrm{pc}}}{r_{\mathrm{gen}}} - 1\right) t_{\mathrm{hc}}\right) \\ (r_{\mathrm{pc}} - r_{\mathrm{gen}}) \cdot \sin(t_{\mathrm{hc}}) - r_{\mathrm{gen}} \cdot \sin\left(\left(\frac{r_{\mathrm{pc}}}{r_{\mathrm{gen}}} - 1\right) t_{\mathrm{hc}}\right) \end{pmatrix} \tag{10.35}$$

$$0 \leq t_{\mathrm{hc}} \leq t_{\mathrm{hc,max}}$$

where the maximum parameters of the epicycloid and hypocycloid are equal due to same radii r_{gen} of the generating circles:

$$t_{\mathrm{ec,max}} = t_{\mathrm{hc,max}} = \frac{r_{\mathrm{gen}}}{r_{\mathrm{pc}}} \cdot \arccos\left(\frac{(r_{\mathrm{pc}} + r_{\mathrm{gen}})^2 + r_{\mathrm{gen}}^2 - r_{\mathrm{o}}^2}{2 \cdot r_{\mathrm{gen}} \cdot (r_{\mathrm{gen}} + r_{\mathrm{pc}})}\right)$$

The radius where the hypocycloid ends can be calculated by

$$r_{\mathrm{hc,min}} = \sqrt{\left(x_{\mathrm{hc}}(t_{\mathrm{hc,max}})\right)^2 + \left(y_{\mathrm{hc}}(t_{\mathrm{hc,max}})\right)^2} \tag{10.36}$$

accordingly and defines the end parameter of the following epitrochoid (et) that connects the inner circle with the hypocycloid:

$$\begin{pmatrix} x \\ y \end{pmatrix}_{\mathrm{et},0} = \begin{pmatrix} a \cdot \cos\left(t_{\mathrm{et,max}} - t_{\mathrm{et}}\right) - r_{\mathrm{o}} \cdot \cos\left(2 \cdot \left(t_{\mathrm{et,max}} - t_{\mathrm{et}}\right)\right) \\ a \cdot \sin\left(t_{\mathrm{et,max}} - t_{\mathrm{et}}\right) - r_{\mathrm{o}} \cdot \sin\left(2 \cdot \left(t_{\mathrm{et,max}} - t_{\mathrm{et}}\right)\right) \end{pmatrix} \tag{10.37}$$

$$0 \leq t_{\mathrm{et}} \leq t_{\mathrm{et,max}} \quad t_{\mathrm{et,max}} = \arccos\left(\frac{a^2 + r_{\mathrm{o}}^2 - r_{\mathrm{hc,min}}^2}{2 \cdot a \cdot r_{\mathrm{o}}}\right)$$

a is the axis distance. The epitrochoid then needs to be rotated by an angle

$$\Delta\theta_{\mathrm{et}} = \arctan\left(\frac{y_{\mathrm{hc}}(t_{\mathrm{hc,max}})}{x_{\mathrm{hc}}(t_{\mathrm{hc,max}})}\right) - \arctan\left(\frac{y_{\mathrm{et},0}(t_{\mathrm{et}} = 0)}{x_{\mathrm{et},0}(t_{\mathrm{et}} = 0)}\right) \tag{10.38}$$

thus the start and end points of both curves match. The final epitrochoid curve then reads:

$$\begin{pmatrix} x \\ y \end{pmatrix}_{\mathrm{et}} = \begin{pmatrix} x_{\mathrm{et},0} \cdot \cos(\Delta\theta_{\mathrm{et}}) - y_{\mathrm{et},0} \cdot \sin(\Delta\theta_{\mathrm{et}}) \\ x_{\mathrm{et},0} \cdot \sin(\Delta\theta_{\mathrm{et}}) + y_{\mathrm{et},0} \cdot \cos(\Delta\theta_{\mathrm{et}}) \end{pmatrix} \tag{10.39}$$

The trailing cycloid flank (tr) is calculated similarly in reverse order with a negative sign on the $y-$coordinate and is then rotated by half the tooth pitch angle

$$\theta_{\mathrm{tr}} = \frac{\Phi}{2} = \frac{\pi}{Z} \ . \tag{10.40}$$

The inner circle (i) and outer circle (o) can be parameterized as follows:

$$\begin{pmatrix} x \\ y \end{pmatrix}_{\mathrm{i}} = r_{\mathrm{i}} \cdot \begin{pmatrix} \cos\left(t_{\mathrm{i}}\right) \\ \sin\left(t_{\mathrm{i}}\right) \end{pmatrix} \quad t_{\mathrm{i,min}} \leq t_{\mathrm{i}} \leq \frac{\pi}{z} - t_{\mathrm{i,min}} \quad t_{\mathrm{i,min}} = \arctan\left(\frac{y_{\mathrm{et}}(t_{\mathrm{et,max}})}{x_{\mathrm{et}}(t_{\mathrm{et,max}})}\right) \tag{10.41}$$

$$\begin{pmatrix} x \\ y \end{pmatrix}_{\mathrm{o}} = r_{\mathrm{o}} \cdot \begin{pmatrix} \cos\left(t_{\mathrm{o}}\right) \\ \sin\left(t_{\mathrm{o}}\right) \end{pmatrix} \quad t_{\mathrm{o,min}} \leq t_{\mathrm{o}} \leq \frac{3 \cdot \pi}{z} - t_{\mathrm{o,min}} \quad t_{\mathrm{o,min}} = \frac{\pi}{z} - \arctan\left(\frac{y_{\mathrm{ec}}(t_{\mathrm{ec}} = 0)}{x_{\mathrm{ec}}(t_{\mathrm{ec}} = 0)}\right) \tag{10.42}$$

The generating radius can vary in the following limits:

$$\frac{r_{\mathrm{o}} - r_{\mathrm{i}}}{4} \leq r_{\mathrm{gen}} \leq r_{\mathrm{pc}} \tag{10.43}$$

For the lower limit the epitrochoid segment vanishes and the hypocycloid is directly connected with the root circle. For the upper limit the hypocycloid segment vanishes and the epitrochoid directly starts at the pitch circle. The latter case is also used and described in Ref. [30].

The profile is then described as a mathematical curve depending on a combined normalised parameter t within the $xy-$section starting at the outer circle as shown in Fig. 10.5:

$$\boldsymbol{r}(t) = \begin{pmatrix} x(t) \\ y(t) \end{pmatrix} \ , \ t \in [0, 1] \tag{10.44}$$

A rotation of the main rotor profile about the angle φ leads to the description

$$\boldsymbol{r}(t, \varphi) = \begin{pmatrix} x(t) \cdot \cos(\varphi) - y(t) \cdot \sin(\varphi) \\ x(t) \cdot \sin(\varphi) + y(t) \cdot \cos(\varphi) \\ \varphi \end{pmatrix} \tag{10.45}$$

which can be interpreted as the surface of a rotor of infinite length with the normalised lead $\hat{s} = 2\pi$. This is called the normal rotor and shows a periodicity along the $\varphi-$axis with the period length of the tooth pitch angle.

This is similarly done with the female rotor. Subsequently, edges are defined which lie on the surfaces of the normal rotor and define the chamber boundaries. These are the rotor profiles themselves, the contact lines, the blow holes and housing clearance. With these bounding edges, so-called trimmed surfaces are defined. The trimmed surfaces of the main and gate rotors can then be combined to form the working chambers of which an infinite number can be found along the $\varphi-$axis due to periodicity. The resulting surface model is at first independent of the rotor length and the lead curve. In order to model the real rotor and not the normal rotor, the wrap angle curve

$$\psi(z) = \psi_0 + 2\pi \int_0^z s\left(z\right)^{-1} \ \mathrm{d}z \tag{10.46}$$

needs to be defined. Together with the angle of rotation α for a specified position of the rotor, a correlation between the defined angle φ in the normal rotor and that of the real rotor can be given as

$$\varphi(z) = \psi(z) + \alpha \ . \tag{10.47}$$

If this results in a chamber that extends over the rotor end faces, the surface definition must be limited accordingly to the interval $z \in [0, L_\mathrm{R}]$ where L_R is the rotor length.

10.4.2 Volume Curves and Opening Areas

To form the volume curve, the chamber's surface model of the normal rotor is intersected with discrete planes along the φ-axis. The determined curves are directly available by inserting the corresponding φ-coordinate into the surface definition. The intersection area enclosed within the contour is then calculated numerically after a discretization to a polygon. The chamber volume for a normalised rotor position ϕ (Eq. (10.12)) can be determined by integrating the course of the scoop area A_s (shown in Fig. 10.5) over the z-axis:

$$V(\phi) = \int_0^{L_\mathrm{R}} A_\mathrm{s}\left(\varphi(z)\right) \ \mathrm{d}z \tag{10.48}$$

The resulting volume curves for the main and gate rotor are identical for the symmetrical profile with the chosen separation procedure within the cut lens. This is not the case if the procedure introduced in Refs. [13, 22, 36] is used, where every scoop area part lying within the cut lens is assigned to the gate rotor.

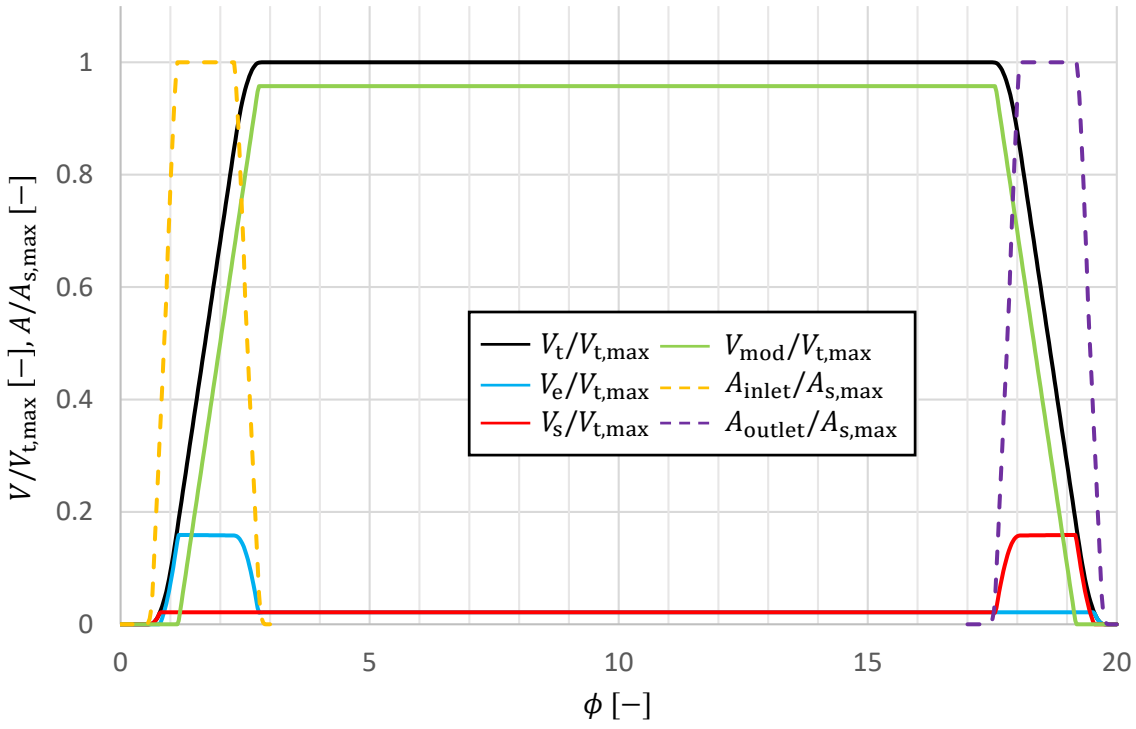

FIG. 10.6 Normalised chamber volume and axial opening area as a function of the phase angle ϕ for the isochoric test machine investigated in Sec. 10.5. The total chamber volume V_t as well as the model volume to determine the inhomogeneous pressure distribution V_mod and the respective start and end volumes V_s and V_e are shown.

The axial inlet and outlet area curves are also defined by the scoop area $A_s(\phi)$. Figure 10.6 shows the volume curves and opening area curves as a function of the phase angle ϕ for the isochoric test machine (constant rotor lead s without end plates) investigated in Sec. 10.5. The machine's total chamber volume V_t starts growing with the axial inlet area. The scoop area shown in Fig. 10.5 increases as soon as the leading tooth flank has passed the cut lens and reaches its maximum $A_{s,max}$ when the entire tooth space is outside the cut lens. From here on, the volume curve increases linearly until the scoop area on the other side rejoins the cut lens. The maximum chamber volume is reached as soon as it has completely disappeared again and the axial inlet area vanishes. Due to the constant rotor lead, the total chamber volume is constant until the high pressure side is reached and starts decreasing as the outlet area opens and the chamber vanishes in a reverse manner. Beside the total chamber volume the model volume V_{mod} for the inhomogeneous pressure distribution as well as the start and end volumes V_s and V_e are shown. The first part of the total chamber volume V_t of the resulting working chamber is assigned to the start volume V_s, where the local chamber low pressure is located later. The subsequent chamber volume is assigned to the chamber end volume V_e until the maximum scoop area is reached. The then newly created chamber volume is enclosed by the housing and the rotor profile, so that this is assigned to the volume of the model V_{mod}. The chamber end volume, to which the local chamber high pressure is assigned, however, remains constant until the scoop area decreases again when the cut lens is reached, until it has the same size as the start volume due to symmetry. Due to the constant gradient, these partial volumes move axially through the machine with further rotation until the high-pressure side working chamber opens, where the process takes place in reverse order.

10.4.3 Housing Gap

As shown in Figs. 2.1 and 10.3, the housing gap can be abstracted as a plane gap between the rotor's outer diameter and the surrounding housing where the curvature is neglected. It connects two adjacent chambers on the same rotor. The gap height $h_{cl,h}$ is defined by the clearance and the gap width

$$w_h = (\pi - \alpha_{CL}) \cdot D_o \cdot \sqrt{1 + \left(\frac{s}{\pi D_o}\right)^2} \tag{10.49}$$

is defined by the spiral of the outer diameter from cusp to cusp and is similar to the channel length described in Chap. 5, but with a different diameter. The gap length is defined as the shortest distance between two chambers and can be calculated as

$$L_h = \frac{s\beta_o}{2\pi\sqrt{1 + \left(\frac{s}{\pi D_o}\right)^2}} \tag{10.50}$$

where β_o is the polar angle of the profile's outer diameter shown in Fig. 10.5. In the relative system introduced in Chap. 5, the wall velocity of the rotor in the direction of flow is zero. The housing moves with the relative velocity according to Eq. (5.5).

10.4.4 Radial Gap

The radial gap sketched in Figs. 2.1 and 10.4 is placed between both rotors and formed by the inner diameter of one rotor and the outer diameter of the other rotor. The gap height $h_{cl,r}$ is defined by the prescribed clearance and the gap width w_r can be calculated as the housing gap's

length according to Eq. (10.50). As the gap height is much smaller than the gap width, the friction caused by the channel side walls is neglected and a converging diverging channel of infinite width is calculated. For the remaining top and bottom walls the circumferential speed of the respective diameter is applied with

$$U_\mathrm{t} = \pi \cdot D_\mathrm{i} \cdot f \tag{10.51}$$

and

$$U_\mathrm{b} = \pi \cdot D_\mathrm{o} \cdot f \ . \tag{10.52}$$

The gap connects chambers on the same rotor where one chamber each is leapfrogged.

10.4.5 Blow Hole

The blowhole is a slit-like opening between one chamber of the main rotor and one of the gate rotor. According to the definition used in the geometry model, the opening lies on a cylindrical surface of the spatial cut lens. The size of the area A_bh is determined numerically using the geometry model analogous to the determination of the volume curve. To be able to treat the blowhole as a rectangular slit, it is assigned a width

$$w_\mathrm{bh} = \beta_\mathrm{bh} \cdot r_\mathrm{o} \tag{10.53}$$

which corresponds to the circular arc shown in Fig. 10.5. The height is then defined as

$$h_\mathrm{bh} = \frac{A_\mathrm{bh}}{w_\mathrm{bh}} \tag{10.54}$$

to conserve the total gap area. This is a geometric simplification from a trapezoidal flow surface to a rectangle, so that the Wenderott flow model can be used to calculate the mass flow rate.

10.4.6 Inter-Lobe Gap

The actual flow path through the inter-lobe gap is hard to determine by theoretical means. The line of smallest approach is given by the contact line sketched in Fig. 10.5. This is divided as shown in a part that connects two chambers of the same rotor formed by the flank-to-tip clearance (2) and a part that connects chambers of different rotors formed by the flank-to-flank clearance (3). The respective gap width w_il is calculated as the length of the contact line with a prescribed clearance $h_\mathrm{cl,il}$. Nevertheless, it is expected that the stream lines of a purely pressure-driven flow differ from that of purely shear-driven flow and as a result, the effective flow area in different flow regimes where either of the flows dominate would change. In this work, the flow area as described above is used, applying an average wall velocity for the whole gap where both the top and bottom wall have a velocity

$$U_\mathrm{il,t} = U_\mathrm{il,b} = \pi \cdot D_\mathrm{pc} \cdot f \tag{10.55}$$

according to the circumferential speed of the pitch circle. It is expected that this leads to larger mass flow rates for rarefied gases where the Couette flow dominates, as the effective flow gap width here would more likely be the difference of the outer radius to the inner radius. A blending of the gap areas according to the expected stream lines is omitted here, but could be investigated in future work.

10.5 Simulation of a Test Machine

In order to work out the impact of the new investigated model for inhomogeneous chamber states, simulations for a test machine are performed and compared to measurements. This machine is an isochoric two start cycloid profiled SSVP with $r_{\mathrm{gen}}/r_{\mathrm{pc}} = 0.5$. The dimensionless data is given in Tab. 10.1, where L_{R} is the rotor length, $h_{\mathrm{cl,h}}$, $h_{\mathrm{cl,il}}$ and $h_{\mathrm{cl,r}}$ are clearances of the housing gap, the inter-lobe gap and the radial gap respectively and ψ_{t} is the machine's total wrap angle. As the machine is cooled, it is assumed to be fully isothermal at ambient temperature $T = 293$ K. The machine neither has a radial inlet area nor a pressure relief valve.

TAB. 10.1 Data of the reference case

$D_{\mathrm{o}}/D_{\mathrm{i}}$ [−]	D_{o}/s [−]	$D_{\mathrm{o}}/L_{\mathrm{R}}$ [−]	$D_{\mathrm{o}}/h_{\mathrm{cl,h}}$ [−]	$D_{\mathrm{o}}/h_{\mathrm{cl,il}}$ [−]	$D_{\mathrm{o}}/h_{\mathrm{cl,r}}$ [−]	ψ_{t} [°]	Z [−]
1.571	5.641	0.667	880	733.33	733.33	3474	2

Figure 10.7 shows the machine's volumetric efficiency, which is the ratio of the machine's suction speed

$$\dot{V} = \frac{\dot{m} \cdot R \cdot T}{p_{\mathrm{suction}}} \tag{10.56}$$

to the theoretical suction speed

$$\dot{V}_{\mathrm{th}} = 2 \cdot V_{\mathrm{t,max}} \cdot f \cdot Z \tag{10.57}$$

as a function of the suction pressure p_{suction}. $\dot{m}$ is the effective mass flow rate of the machine. The discharge pressure is always 10^5 Pa. The results are in steady-state with a constant rotational speed $f = 83.33$ Hz. Comparing the results of *KaSim* with homogeneous chambers (red curve) without applying the new model, a good agreement is obtained for large values of the suction pressure. But with the decrease of the suction pressure those two curves diverge. The measurements (black curve with symbols) show that the machine cannot evacuate the low pressure volume lower than about 6 Pa at the given rotational speed, while the simulated suction speed is still at a high value. Regarding the results obtained by the inhomogeneous model (green curve) as described in Sec. 10.2 the curve is not affected in the high pressure regime, but declines at low suction pressures in good agreement with the measurements. The simulated ultimate pressure is still a bit better than the measured one. This might be caused by the fact that external leakage is neglected within the chamber model simulation. As a leakage causes a constant mass flow rate independent of the system pressure, this impact increases with decreasing system pressure and is a possible explanation for the discrepancy. The blue curve is also obtained by simulations of the inhomogeneous model, but the impact of the gap mass flow rates on the inhomogeneity within the chambers is neglected by setting $\dot{m}_{\mathrm{cl,t}} = 0$ within the 1D model. This does not mean that the overall simulation is performed without gap flows, but the inhomogeneity within the chambers is slightly overestimated. Nevertheless, this is the easiest and most conservative modelling method presented, as the actual machine is likely to be better than the simulated one.

For the purple curve it is assumed that the open chambers are homogeneous and become inhomogeneous when the chambers are encapsulated. Therefore, a perfect chamber filling is modelled. This could be achieved by a radial inlet area, that closes at the same time as the axial connection vanishes due to an overlapping of the pending profile tooth. Due to a radial inlet, a lengthwise connection

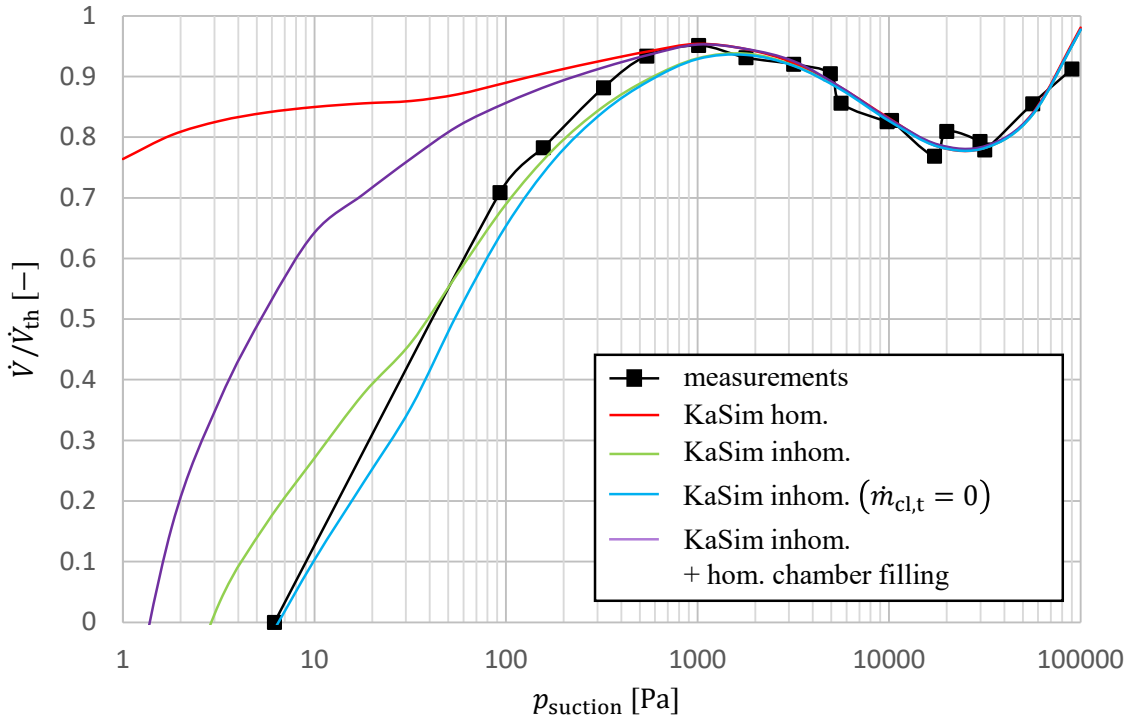

FIG. 10.7 Comparison of the suction speed curves of measurements and chamber model simulation with homogeneous and inhomogeneous pressure distribution within the chambers for a rotational speed $f = 83.33$ Hz.

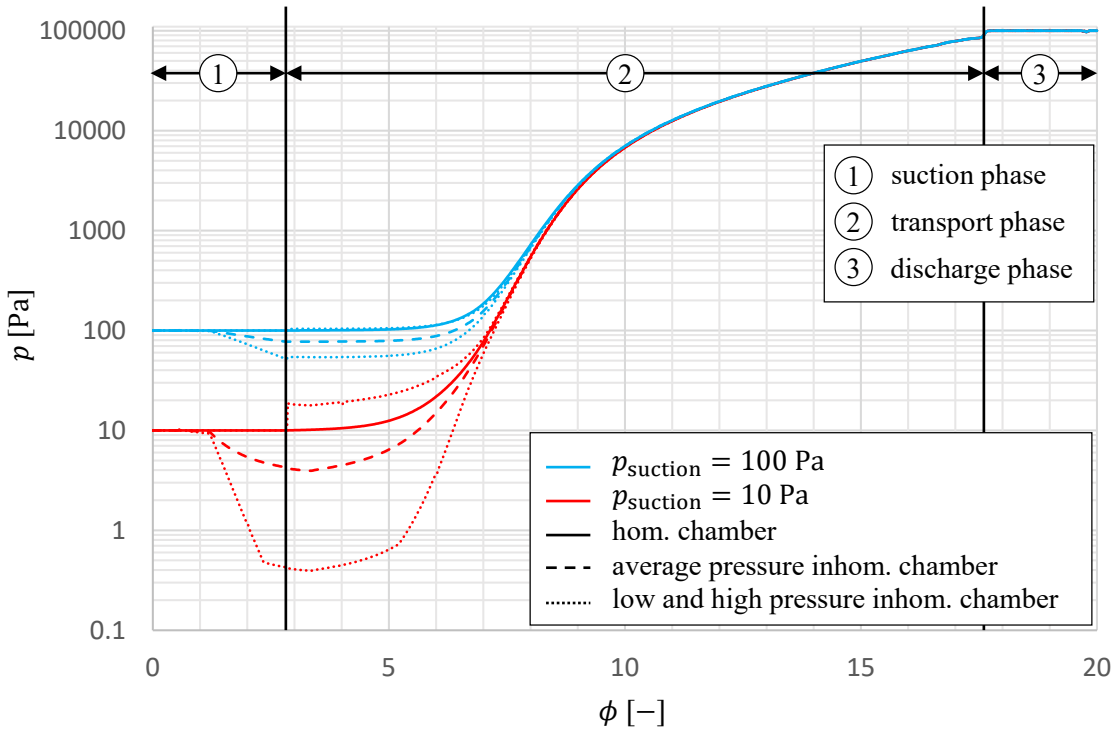

FIG. 10.8 Pressure p as a function of the phase angle ϕ for a rotational speed $f = 83.33$ Hz and suction pressures $p_{\mathrm{suction}} = 10$ Pa (blue) and $p_{\mathrm{suction}} = 100$ Pa (red). The straight lines refer to homogeneous chambers, the dashed lines refer to the average pressure in inhomogeneous chambers and the dotted lines to the chamber's low and high pressure.

of the chamber to the suction port would be established. Again this only affects the results for lower values of the suction pressure and would significantly increase the machine's performance regarding the volumetric efficiency as well as the ultimate pressure. Therefore, this approach provides an estimation for the potential of a deeper design complexity.

The green curve even declines at higher intake pressures, than the purple curve, due to incomplete chamber filling. Therefore, the average pressure in the first enclosed chamber is below the suction pressure as seen in Fig. 10.8 which shows the pressure distribution within the male chambers as a function of the phase angle ϕ for a suction pressure $p_{\text{suction}} = 10$ Pa (red curves) and $p_{\text{suction}} = 100$ Pa (blue curves). The solid lines refer to homogeneous chamber states and the dashed lines to the chamber's average pressure with inhomogeneous chamber states. The dotted lines are the chamber's low and high pressure respectively. The shown operation points refer to the red and blue curves in Fig. 10.7. It is obtained that as long as the chamber is opened, the local high pressure equals the suction pressure and lies on the same curve as the homogeneous simulation. Nevertheless, the average chamber pressure of the inhomogeneous simulations decreases until the filling process is completed. This results in the average pressure in the working chamber just closed being lower than the suction pressure. Therefore, the suction speed curve already collapses at slightly higher suction pressures. Afterwards the average chamber pressure increases until the high pressure side is reached. The fact that the chamber's low and high pressure curves are discontinuous at the point where the chamber closes is caused by the change of the model from Eqs. (9.9) and (9.10) for chamber filling to Eqs. (7.1) and (7.2) for closed chambers. A blending between both approaches along the phase angle around the point where the chamber closes would be possible to avoid this.

In Fig. 10.9 the difference between the homogeneous and inhomogeneous model is highlighted by the yellow dotted curve on the secondary axis. The operation points shown are the same as in Fig. 10.7. The yellow curve provides an approximation for the increase of the gap mass flow rates due to the inhomogeneous model evaluating the pressure ratio $p_{\text{HP}}/p_{\text{ch}}$ with Eq. (7.1) for a closed chamber with the assumption that the average pressure equals the suction pressure ($p_{\text{ch}} = p_{\text{suction}}$). The resulting pressure ratio is used to give an approximation for the increase of the mass flow rates:

$$\text{Increase of mass flow rates} \approx \left(\frac{p_{\text{HP}}}{p_{\text{ch}}} - 1 \right) \cdot 100\ \% \tag{10.58}$$

Thus it is seen that the purple curve starts to separate from the red curve when the yellow curve increases. This indicates that Eq. (7.1) is useful for design purposes as this function can be evaluated analytically including all relevant operation parameters without the need of a simulation. If this function delivers a large pressure ratio for a desired operation point, the machine is likely to be worse than expected and a different design should be chosen for example by increasing the rotor lead s on the machine's low pressure side, by decreasing the number of starts from $Z = 2$ to $Z = 1$ or by scaling the machine geometrically to a larger diameter and reducing the rotational speed f at constant theoretical suction speed $\dot{V}_{\text{th}}$. These relationships can be derived from Eqs. (5.7), (5.13), (5.21), (7.1) and (10.57).

The green curve even separates at higher suction pressures as the assumption the first enclosed chamber has an average pressure equal to the suction pressure is wrong as explained in Fig. 10.8. This effect could be adjusted by establishing a radial inlet area. Nevertheless, the difference between the red and purple curve will remain.

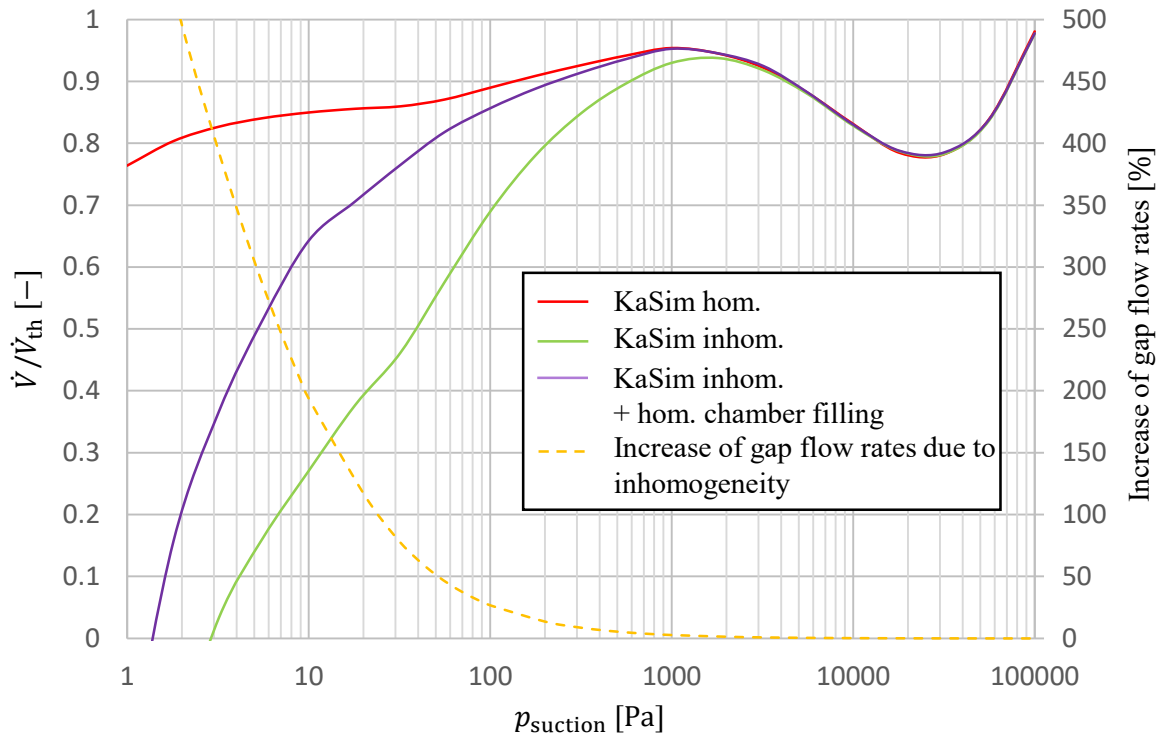

FIG. 10.9 Comparison of the suction speed curves of measurements and chamber model simulation with homogeneous and inhomogeneous pressure distribution within the chambers for a rotational speed $f = 83.33$ Hz. The dashed yellow curve represents an approximation of the increase of gap mass flow rates due to the inhomogeneity within the chambers.

11 Conclusion and Outlook

Dry-running oil-free screw spindle vacuum pumps (SSVP) play an important role in the semiconductor, pharmaceutical, chemical and food industries to avoid contaminations by auxiliary fluids. As a machine-describing characteristic map, the suction speed curve describes the intake volume flow in relation to the suction pressure, according to which system designers select their machines. A central design criterion for such machines is therefore the best possible suction speed curve with simultaneous energy efficiency. In order to keep prototype construction to a minimum during development, upstream theoretical considerations and simulations are useful. For the purpose of predicting the actual operating behaviour, it is necessary to know the flow conditions within the machine as precisely as possible. Due to the complexity of the machine, the chamber model simulation in which the machine is abstracted into working chambers and connecting gaps is particularly suitable. However, while there is excellent agreement between simulation and experiment in the range of higher suction pressure, in the past it turned out that the actual machine performance at low suction pressures is significantly worse than theoretically expected. This problem is solved in this work and it is shown that the original assumption that working chambers are homogeneous is not generally valid, but that due to the circumferential speed of the rotors at low pressures a considerable inhomogeneous pressure distribution occurs within the working chambers. This leads to increased leakage mass flow rates due to the operational gaps and to poorer chamber filling. The focus of this work is the theoretical and experimental investigation of these mechanisms, the mathematical description and the implementation in the chamber model simulation software *KaSim* developed at the Chair of Fluidics at TU Dortmund University.

In order to describe the inhomogeneous chamber state mathematically, a working chamber is first abstracted geometrically as a rectangular channel in which the walls have a velocity in the longitudinal direction based on the kinematic relationships of an SSVP. The wall velocities cause a mass flow that is dammed up due to the spatial limitation of the working chambers, so that a pressure gradient is caused in the opposite direction. The quasi-steady state in the working chamber can be described by a Couette-Poiseuille flow, which can be numerically calculated via a non-linear differential equation with a closure problem. The closure problem can be solved by means of dimensional analysis where the dimensionless flow rates of the purely pressure-driven and purely shear-driven flows are a function of the dimensionless channel shape, the gas rarefaction parameter and the tangential momentum accommodation coefficient (TMAC), which is a material parameter that models the amount of friction at the wall in rarefied gases. For large values of the gas rarefaction parameter in the continuum and slip regime analytical solutions are derived for both the Poiseuille flow and the Couette flow in a rectangular channel, while in the transitional and free molecular regime simulations based on the kinetic theory of gases are performed. Due to a linearisation

approach, the results of a channel with diffuse wall scattering can be used to calculate the flow rates with arbitrary TMACs, which is validated by simulations using the direct simulation Monte Carlo (DSMC) method. For the Couette flow, an analytical solution with diffuse wall scattering for the free molecular regime is derived as well.

The derived one-dimensional model is validated in two ways. At first, three-dimensional simulations are performed by means of the computational fluid dynamics (CFD) software Ansys CFX where the pressure distribution in a single chamber of an SSVP without rotor lead is simulated. For the application of slightly rarefied gases Maxwell slip boundary conditions at the walls are implemented via user-defined functions. Both approaches show perfect agreement in the slip regime, while the results diverge in the transition regime so that the CFD simulations predict too large pressure ratios within the working chamber. This can be explained by the fact that the Navier-Stokes equations on which the CFD simulations are based are no longer valid here. Nevertheless, the good agreement in the slip range shows that the flow inside the working chamber can be characterised by means of a one-dimensional model. Accordingly, the results of the one-dimensional model in the area of the transition flow are also plausible, since it takes into account the properties of the kinetic gas theory.

For experimental validation, a test rig is built with which the pressure distribution within a working chamber without lead can be measured. The working chamber is formed on a rotating shaft between two rotating brass sleeves, the enclosing housing and a counter contour embedded above the housing, which models the gearing of the gate rotor. The pressure in the working chamber can be measured on both sides of the counter contour and in the middle of the working chamber. When the shaft rotates, the pressure at the measuring point upstream the counter contour (in direction of rotation) is significantly higher than downstream the counter contour and the pressure in the middle of the working chamber is in between. This effect is intensified as a result of higher rotational speeds and lower average pressures. At pressures close to ambient pressure, the chamber can be considered homogeneous, so that the effect can be attributed to the high friction in rarefied gases. The experimental results and those of the one-dimensional model agree well if the influence of the gas-wall interaction is correctly represented by means of adapted TMACs, so that the brass components cause less fluid friction than the steel components. The assumption of purely diffuse wall scattering, on the other hand, leads to higher simulated pressure ratios.

For open working chambers, the assumption of a quasi-steady flow is insufficient, as the chamber volume changes continuously. To investigate the influence of the inhomogeneity on the chamber filling, CFD simulations are carried out within a rotor fixed reference frame. The pressure in the low-pressure port is prescribed. The filling efficiency can then be determined via the actual mass in the expanding working chamber related to the theoretical mass if the chamber was filled homogeneously with the suction pressure. Again, the lower the pressure and the higher the rotational speed, the more inhomogeneous the chamber is and the worse it is filled.

With the help of a dimensional analysis it can be seen that both the results of the closed chamber and those of the open chamber each coincide on a single curve when the pressure ratio within the working chamber is represented at different points as a function of the dimensionless pressure gradient evaluated at the mass averaged chamber pressure. The dimensionless pressure gradient follows from the one-dimensional model and can be calculated analytically for a given point as a

function of geometry, the mass averaged chamber state, gas type, TMACs and rotational speed. In this way, the inhomogeneous chamber state can be calculated via derived approximative functionals without having to solve a differential equation.

The approximative functionals are implemented in *KaSim* to investigate the influence of the inhomogeneous pressure distribution in the chambers on the integral operating behaviour of an SSVP. By comparing the suction speed curve of simulations with and without inhomogeneous pressure distribution in the working chambers with measurements of a test machine, it is shown that the simulation results are significantly improved with the help of the new model. Furthermore, the suction speed curve collapses at the point where the working chambers become inhomogeneous. This offers a new possibility to use the approximative functional for the design of machines. By specifying the geometry and the required operating point, the expected chamber inhomogeneity can be evaluated. Thus, the size, lead on the suction side, number of starts and the rotational speed of the machine can be adjusted to minimise this unfavourable mechanism. Furthermore, the potential of a radial inlet is shown. For this purpose, it is assumed that the pressure distribution within the suction working chamber with radial inlet is homogeneous. In this way, the suction speed curve can also be significantly improved in the low pressure range. With the help of the inhomogeneous model it can be estimated whether the more complex design of the low-pressure port is required for an efficient machine at the desired operating points.

As shown in this work, the surface material chosen has a significant influence on the gas-surface interaction, which affects both the gap flow and the pressure distribution in the working chambers in the rarefied gas regime which leads to possible investigations in future works. The choice of brass instead of steel results in reduced wall friction when conveying air, which leads to a reduction of inhomogeneity in the working chambers. On the other hand, reduced friction can also lead to an increase in gap mass flows, so that a closer investigation is desirable here and an overall improvement might be achieved for example through coating. Furthermore, investigations regarding surface structures in SSVPs would be interesting. A surface structure could lead to molecules being scattered back on average in the opposite direction from which they came. This would lead to a reduction of the gap mass flow rates and thus to an improvement of the machine without harming operation safety due to reduced clearances. The housing gap would be particularly suitable for this purpose. This is particularly interesting as Kösters[14] showed the idea to increase the clearance on the low pressure side in combination with a larger inner compression ratio to avoid over-compression at the machine's start-up. With the help of the surface structures, this could be achieved without increasing the gap mass flows at low suction pressures as the gap would become more sealed again due to the greater influence of the gas-surface interaction in the area of rarefied gases.

Bibliography

[1] *Vacuum technology - vocabulary*, Norm, ISO 3529-1, 2019.

[2] K. Jousten, *Wutz - Handbuch der Vakuumtechnik*, **12** (Vieweg+Teubner, Wiesbaden, 2018).

[3] E. Clapeyron, *Poissance motrice de la chaleur*, Journal de l'Ecole Polytechnique **14**, 153 (1835).

[4] A. Krönig, *Grundzüge einer Theorie der Gase*, Annalen der Physik **175**, 177 (1856).

[5] R. Clausius, *Ueber die Art der Bewegung, welche wir Wärme nennen*, Annalen der Physik **176**, 353 (1857).

[6] J. C. Maxwell, *V. Illustrations of the dynamical theory of gases.-Part I. On the motions and collisions of perfectly elastic spheres*, The London, Edinburgh, and Dublin Philosophical Magazine and Journal of Science **19**, 19 (1860).

[7] L. Boltzmann, *Zur Priorität der Auffindung der Beziehung zwischen dem zweiten Hauptsatze der mechanischen Wärmetheorie und dem Principe der kleinsten Wirkung*, Annalen der Physik **219**, 161 (1871).

[8] M. Knudsen, *Die Gesetze der Molekularströmung und der inneren Reibungsströmung der Gase durch Röhren*, Annalen der Physik **333(1)**, 75 (1909).

[9] G. A. Bird, *Molecular gas dynamics and the direct simulation of gas flows* (Clarendon Press, Oxford, 1994).

[10] A. Beskok, *Validation of a new velocity-slip model for separated gas microflows*, Numer. Heat Transfer, Part B **40**, 451 (2001).

[11] Deutsches Institut für Normung, *Abnahmeregeln für Rotationsverdrängervakuumpumpen*, DIN 28426, 1983.

[12] C. Huck, *Verdünnte Strömung in Spalten von Vakuumpumpen mit bewegter Berandung*, Diss. (Technische Universität Dortmund, Logos Verlag, 2020).

[13] K. Nadler, *Modellierung und Analyse von Schraubenvakuumpumpen im Blowerbetrieb*, Diss. (Technische Universität Dortmund, Logos Verlag, 2017).

[14] H. Kösters and J. Eickhoff, *Trockene Schraubenvakuumpumpe mit hoher innerer Verdichtung*, Schraubenmaschinen 2006, VDI-Berichte **1932**, 423 (2006).

[15] T. Dreifert and R. Müller, *Screw vacuum pumps - The state of the art*, International Conference on Screw Machines 2014, VDI-Berichte **2228**, 29 (2014).

[16] L. Rinder, *Schraubenverdichter* (Springer-Verlag, Wien, 1979), ISBN: 978-3-211-81535-9.

[17] P. Buthmann, *Rechnergestützte Schraubenverdichterprofilentwicklung und -rotorauslegung unter Berücksichtigung der betriebsbedingten Verformungen*, Diss. (Ruhr-Universität Bochum, 1985).

[18] N. Stošić and K. Hanjalic, *Development and optimization of screw machines with a simulation model—Part I: Profile generation*, ASME J. Fluids Eng. **119**, 659 (1997).

[19] N. Stošić, *On gearing of helical screw compressor rotors*, J. Mech. Eng. Sci. **212**, 587 (1998).

[20] M. Helpertz, *Methode zur stochastischen Optimierung von Schraubenrotorprofilen*, Diss. (Universität Dortmund, 2003).

[21] Y.-R. Wu and Z.-H. Fong, *Rotor profile design for the twin-screw compressor based on the normal-rack generation method*, ASME J. Mech. Des. **130**, 042601 (2008).

[22] M. Utri, *Potenzial von nicht-konstanter Rotorsteigung für Schraubenkompressoren*, Diss. (Technische Universität Dortmund, Logos Verlag, 2020).

[23] S. Patil et al., *Contribution of modern rotor profiles to energy efficiency of screw compressors*, IOP Conf. Ser.: Mater. Sci. Eng. **1267**, 012006 (2022).

[24] C. Huck and A. Brümmer, *Thermodynamical operation behaviour of screw vacuum pumps with cycloid- and quimby-toothed rotors*, International Conference on Screw Machines 2014, VDI-Berichte **2228**, 331 (2014).

[25] H. Kösters, *Trockenlaufende Schraubenspindelvakuumpumpen in der Prozessindustrie - Anforderungen an die Thermodynamik und deren Umsetzung*, Schraubenmaschinen 2002, VDI-Berichte **1715**, 267 (2002).

[26] T. Dreifert and K. Rofall, *Trockenlaufende Schraubenvakuumpumpe für industrielle Vakuumanwendungen*, Schraubenmaschinen 2002, VDI-Berichte **1715**, 267 (2002).

[27] D. Pfaller et al., *Options for internal compression in screw-type vacuum pumps and their influence on operational behaviour*, International Conference on Compressors and their Systems: Chandos Publishing, 241 (2007).

[28] D. Pfaller, *Einfluss der Verdrängergeometrie auf die Auslegung von Schraubenspindel-Vakuumpumpen*, Diss. (Technische Universität Dortmund, 2012).

[29] T. Jünemann and A. Brümmer, *Optimisation of screw spindle vacuum pumps with variable rotor pitch regarding load-lock operation*, IOP Conf. Ser.: Mater. Sci. Eng. **425**, 012028 (2018).

[30] T. W. Moesch et al., *Thermodynamic analysis of a conical screw spindle compressor for R718*, ICR2023 - 26th International Congress of Refrigeration **1267**, 012016 (2023).

[31] Busch, *Vacuum Solutions*, `https://www.buschvacuum.com`, Last accessed 2022-11-04, 2022.

[32] Hüthig, *Chemie Technik*, `www.chemietechnik.de/anlagentechnik/foerdertechnik/schrauben-vakuumpumpen-cobra-nx.html`, Last accessed 2022-11-04, 2022.

[33] J.-G. Persson, *Design parameter study to extend the capacity range of dry twin screw compressors*, IOP Conf. Ser.: Mater. Sci. Eng. **1267**, 012009 (2022).

[34] T. Ohbayashi et al., *Study on the performance prediction of screw vacuum pump*, Appl. Surf. Sci. **169-170**, 768 (2001).

[35] A. Rohe, *Wärmehaushalt von Schraubenspindel-Vakuumpumpen*, Diss. (Universität Dortmund, 2005).

[36] M. Janicki, *Modellierung und Simulation von Rotationsverdrängermaschinen*, Diss. (Universität Dortmund, 2007).

[37] K. Kauder et al., *Thermodynamic simulation of rotary displacement machines*, Schraubenmaschinen 2002, VDI-Berichte **1715**, 1 (2002).

[38] J. Temming, *Stationärer und instationärer Betrieb eines unsynchronisierten Schraubenladers*, Diss. (Universität Dortmund, 2007).

[39] J. Hütker, *Energiewandlung in trockenlaufenden Schraubenmotoren*, Diss. (Universität Dortmund, Logos Verlag, 2016).

[40] M. Grieb and A. Brümmer, *Thermodynamic simulation and experimental validation of an oil-free twin-screw expander*, IOP Conf. Ser.: Mater. Sci. Eng. **1267**, 012015 (2022).

[41] D. Stratmann, *Kennfeldverhalten zweiwelliger Rotationsverdrängervakuumpumpen*, Diss. (Technische Universität Dortmund, 2010).

[42] D. Li et al., *Simulation of dry screw vacuum pumps based on chamber model and thermal resistance network*, Applied Thermal Engineering **211**, 118460 (2022).

[43] M. Utri, S. Höckenkamp and A. Brümmer, *Fluid flow through male rotor housing clearances of dry running screw machines using dimensionless numbers*, IOP Conf. Ser.: Mater. Sci. Eng. **425**, 012033 (2018).

[44] M. Heselmann and A. Brümmer, *Analysis of the flow through the blowhole of twin-screw machines with different rotor profiles using dimensionless numbers*, IOP Conf. Ser.: Mater. Sci. Eng. **1267**, 012008 (2022).

[45] D. Wenderott, *Spaltströmungen im Vakuum*, Diss. (Universität Dortmund, 2001).

[46] R. Müller, *Spaltströmung mit Wärmeübertragung in Vakuumpumpen*, Diss. (Universität Kaiserslautern, 2013).

[47] C. Huck, H. Pleskun and A. Brümmer, *Measurement and simulation of rarefied Couette Poiseuille flow with variable cross section*, J. Vac. Sci. Technol. A **36**, 031606 (2018).

[48] C. Huck and A. Brümmer, *Limits of one dimensional modeling of rarefied Couette Poiseuille clearance flow in vacuum pumps*, IOP Conf. Ser.: Mater. Sci. Eng. **425**, 012027 (2018).

[49] T. Jünemann and A. Brümmer, *One-dimensional simulation of Couette–Poiseuille flow with variable cross section for the full range of gas rarefaction*, J. Vac. Sci. Technol. B **38**, 044201 (2020).

[50] T. Jünemann and A. Brümmer, *One-dimensional calculation approach for gaseous clearance flows*, IOP Conf. Ser.: Mater. Sci. Eng. **1267**, 012004 (2022).

[51] C. Fost, *Ein Beitrag zur Verbesserung der Kammerfüllung von Schraubenmotoren*, Diss. (Universität Dortmund, 2003).

[52] N. T. P. Le et al., *Langmuir-Maxwell and Langmuir-Smoluchowski boundary conditions for thermal gas flow simulations in hypersonic aerodynamics*, Int. J. Heat Mass Transfer **55**, 5032 (2012).

[53] T. Jünemann, H. Pleskun and A. Brümmer, *Maxwell velocity slip and Smoluchowski temperature jump boundary condition for ANSYS CFX*, IOP Conf. Ser.: Mater. Sci. Eng. **1180**, 012037 (2021).

[54] G. Abbate, B. J. Thijsse and C. R. Kleijn, *Coupled Navier-Stokes/DSMC method for transient and steady-state gas flows*, Computational Science – ICCS 2007 **4487**, 842 (2007).

[55] Z. Tang, *Investigation on a coupled CFD/DSMC method for continuum-rarefied flows*, AIP Conference Proceedings **1501**, 535 (2012).

[56] A. Kovačević, *Three dimensional numerical analysis for flow prediction in positive displacement screw machines*, Diss. (City University London, 2002).

[57] A. Kovačević, N. Stošić and I. K. Smith, *Three dimensional numerical analysis of screw compressor performance*, J. Comput. Methods Sci. Eng. **3**, 259 (2003).

[58] S. Rane, A. Kovačević and N. Stošić, *Analytical grid generation for accurate representation of clearances in CFD for screw machines*, IOP Conf. Ser.: Mater. Sci. Eng. **90**, 012008 (2015).

[59] A. Kovačević and S. Rane, *3D CFD analysis of a twin screw expander*, 8th International Conference on Compressors and their Systems, 417 (2013).

[60] A. Kovačević et al., *Influence of approaches in CFD solvers on performance prediction in screw compressors*, International Compressor Engineering Conference (2014).

[61] D. Rowinski, A. Nikolov and A. Brümmer, *Modeling a dry running twin-screw expander using a coupled thermal-fluid solver with automatic mesh generation*, IOP Conf. Ser.: Mater. Sci. Eng. **425**, 012019 (2018).

[62] R. Andres et al., *CFD simulation of a two stage twin screw compressor including leakage flows and comparison with experimental data*, IOP Conf. Ser.: Mater. Sci. Eng. **425**, 012018 (2018).

[63] R. Andres, J. Hesse and A. Spille, *Investigation of radial gap size change under load and the impact on performance for a twin screw compressor using numerical simulation*, IOP Conf. Ser.: Mater. Sci. Eng. **1267**, 012007 (2022).

[64] A. H. Moghaddam et al., *Experimental investigations and 3D simulations by the overset grid method on twin-screw machines in both pump and turbine mode*, IOP Conf. Ser.: Mater. Sci. Eng. **1267**, 012012 (2022).

[65] K. Nadler and A. Brümmer, *Teilchenorientierte Modellierung der Strömungsverhältnisse in einer Wälzkolbenvakuumpumpe*, Schraubenmaschinen **14**, 68 (2011).

[66] H. Schlichting and K. Gersten, *Grenzschicht-Theorie*, **10** (Springer-Verlag, 2006).

[67] J. C. Maxwell, *On stresses in rarified gases arising from inequalities of temperature*, Phil. Trans. R. Soc. **170**, 231 (1879).

[68] S. K. Loyalka and S. A. Hamoodi, *Poiseuille flow of a rarefied gas in a cylindrical tube: Solution of linearized Boltzmann equation*, Phys. Fluids A **2**, 2061 (1990).

[69] F. Sharipov and V. D. Seleznev, *Rarefied gas flow through a long tube at any pressure ratio*, J. Vac. Sci. Technol. A **12**, 2933 (1994).

[70] T. C. Lilly et al., *Measurements and computations of mass flow and momentum flux through short tubes in rarefied gases*, Phys. Fluids **18**, 093601 (2006).

[71] J. H. Spurk and N. Aksel, *Strömungslehre - Einführung in die Theorie der Strömungen*, **8** (Springer-Verlag Berlin Heidelberg, 2010).

[72] F. M. White, *Viscous fluid flow*, **2** (McGraw-Hill, New York, 1991), ISBN: 0-07-069712-4.

[73] C. Cercignani and A. Daneri, *Flow of a rarefied gas between two parallel plates*, J. Appl. Phys. **34**, 3509 (1963).

[74] C. Cercignani and C. D. Pagani, *Variational approach to boundary-value problems in kinetic theory*, Phys. Fluids **9**, 1167 (1966).

[75] K. A. Hickey and S. K. Loyalka, *Plane Poiseuille flow: Rigid sphere gas*, J. Vac. Sci. Technol. A, 957 (1990).

[76] S. K. Loyalka and H. Lang, *Linearized Poiseuille flow between parallel plates*, Zeitschrift für angewandte Mathematik und Physik ZAMP **21**, 690 (1970).

[77] S. K. Loyalka, N. Petrellis and T. S. Storvick, *Some exact numerical results for the BGK model: Couette, Poiseuille and thermal creep flow between parallel plates*, **30**, 514 (1979).

[78] F. Sharipov, *Rarefied gas dynamics - Fundamentals for research and practice* (Wiley-VCH Verlag GmbH & Co. KGaA, 2016).

[79] E. B. Arkilic, K. S. Breuer and M. A. Schmidt, *Mass flow and tangential momentum accommodation in silicon micromachined channels*, J. Fluid Mech. **437**, 29 (2001).

[80] I. A. Graur, J. G. Méolans and D. E. Zeitoun, *Analytical and numerical description for isothermal gas flows in microchannels*, Microfluid Nanofluid **2**, 64 (2006).

[81] T. Ewart et al., *Mass flow rate measurements in gas micro flows*, Exp. Fluids **41**, 487 (2006).

[82] T. Ewart et al., *Mass flow rate measurements in a microchannel, from hydrodynamic to near free molecular regimes*, J. Fluid Mech. **584**, 337 (2007).

[83] S. Varoutis et al., *Computational and experimental study of gas flows through long channels of various cross sections in the whole range of the Knudsen number*, J. Vac. Sci. Technol. A **27**, 89 (2009).

[84] V. V. Zhvick and O. G. Friedlander, *Poiseuille flow in a capillary at all regimes of rarefied gas flows*, AIP Conf. Proc. **1501**, 830 (2012).

[85] J. G. Méolans et al., *Effects of two transversal finite dimensions in long microchannel: Analytical approach in slip regime*, Phys. Fluids **24**, 112005 (2012).

[86] V. A. Titarev and E. M. Shakhov, *Kinetic analysis of the isothermal flow in a long rectangular microchannel*, Comput. Math. Math. Phys. **50**, 1221 (2010).

[87] F. Sharipov, *Rarefied gas flow through a long rectangular channel*, J. Vac. Sci. Technol. A **17**, 3062 (1999).

[88] F. Sharipov, *Non-isothermal gas flow through rectangular microchannels*, J. Micromechanics Microengineering **9**, 394 (1999).

[89] I. Graur and M. T. Ho, *Rarefied gas flow through a long rectangular channel of variable cross section*, Vacuum **101**, 328 (2014).

[90] V. Hemadri et al., *Investigation of rarefied gas flow in microchannels of non-uniform cross section*, Phys. Fluids **28**, 022007 (2016).

[91] B. Saint-Venant and L. Wantzel, *Mémoire et expériences sure l'écoulement de l'air déterminé par des différences de pression considérables*, J. Ec. polytech. Math. **16**, 85 (1839).

[92] A. R. Kuhltau, *Air friction on rapidly moving surfaces*, J. Appl. Phys. **20**, 217 (1949).

[93] D. H. Gabis, S. K. Loyalka and T. S. Storvick, *Measurements of the tangential momentum accommodation coefficient in the transition flow regime with a spinning rotor gauge*, J. Vac. Sci. Technol., A **14**, 2592 (1996).

[94] J. A. Bentz, R. V. Tompson and S. K. Loyalka, *The spinning rotor gauge: measurements of viscosity, velocity slip coefficients, and tangential momentum accommodation coefficients for N2 and CH4*, Vacuum **48**, 817 (1997).

[95] C. Cercignani, M. Lampis and S. Lorenzani, *Plane Poiseuille-Couette problem in micro-electro-mechanical systems applications with gas-rarefaction effects*, Phys. Fluids **18**, 087102 (2006).

[96] F. Sharipov, L. M. G. Cumin and D. Kalempa, *Plane Couette flow of binary gaseous mixture in the whole range of the Knudsen number*, Eur. J. Mech. B/Fluids **23**, 899 (2004).

[97] M. N. Kogan, *Rarefied gas dynamics* (Plenum Press, 1969), ISBN: 978-1-4899-6189-1.

[98] F.-b. Bao, J.-z. Lin and X. Shi, *Simulation of flow and heat transfer in micro Couette flow*, 2006 1st IEEE International Conference on Nano/Micro Engineered and Molecular Systems, 110 (2006).

[99] W. Su et al., *Accurate and efficient computation of the Boltzmann equation for Couette flow: Influence of intermolecular potentials on Knudsen layer function and viscous slip coefficient*, J. Comp. Phys. **378**, 573 (2019).

[100] S. M. Nejand et al., *Modeling rarefied gas-solid surface interactions for Couette flow with different wall temperatures using an unsupervised machine learning technique*, Phys. Rev. E **104**, 015309 (2021).

[101] H. S. Rowell and D. Finlayson, *Screw viscosity pumps*, Engineering **126**, 249 (1928).

[102] O. Reynolds, *On certain dimensional properties of matter in the gaseous state*, Phil. Trans. R. Soc. **170**, 727 (1879).

[103] F. Sharipov, *Rarefied gas flow through a long tube at any temperature ratio*, J. Vac. Sci. Technol. A **14**, 2627 (1996).

[104] F. Sharipov, *Rarefied gas flow through a long tube at arbitrary pressure and temperature drops*, J. Vac. Sci. Technol. A **15**, 2434 (1997).

[105] C. E. Siewert, *Poiseuille and thermal-creep flow in a cylindrical tube*, J. Comput. Phys. **160**, 470 (2000).

[106] C. E. Siewert and F. Sharipov, *Model equations in rarefied gas dynamics: Viscous-slip and thermal-slip coefficients*, Phys. Fluids **14**, 4123 (2002).

[107] S. Fukui and R. Kaneko, *Analysis of ultra-thin gas film lubrication based on the linearized Boltzmann equation: Influence of accommodation coefficient*, Jsme Int J **30**, 1660 (1987).

[108] S. Fukui and R. Kaneko, *Analysis of ultra-thin gas film lubrication based on linearized Boltzmann equation: first report - Derivation of a generalized lubrication equation including thermal creep flow*, J. Tribol. **110**, 253 (1988).

[109] S. Fukui and R. Kaneko, *A database for interpolation of Poiseuille flow rates for high Knudsen number lubrication problems*, J. Tribol. **112**, 78 (1990).

[110] F. J. Alexander, A. L. Garcia and B. J. Alder, *Direct simulation Monte Carlo for thin-film bearings*, Phys. Fluids **6**, 3854 (1994).

[111] Y. Li and F. Hsieh, *Modeling of flow in a single screw extruder*, J. Food Eng. **27**, 353 (1996).

[112] F. Sharipov, P. Fahrenbach and A. Zipp, *Numerical modeling of the Holweck pump*, J. Vac. Sci. Technol. A **23**, 1331 (2005).

[113] A. H. Shapiro, *The dynamics and thermodynamics of compressible fluid flow, Volume 1* (Ronald Press, 1953).

[114] A. H. Shapiro, *The dynamics and thermodynamics of compressible fluid flow, Volume 2* (Ronald Press, 1953).

[115] D. Hänel, *Molekulare Gasdynamik* (Springer, 2004).

[116] T. Acharya et al., *Measurement of variation of momentum accommodation coefficients with molecular mass and structure*, J. Thermophy. Heat Trans. **33**, 733 (2019).

[117] M. Smoluchowski von Smolan, *Über Wärmeleitung in verdünnten Gasen*, Ann. Phys. (Berl.) **300**, 101 (1898).

[118] E. B. Arkilic, M. A. Schmidt and K. S. Breuer, *Gaseous slip flow in long microchannels*, J. Microelectromech. S. **6**, 167 (1997).

[119] E. B. Arkilic, *Measurement of the mass flow and tangential momentum accomodation coefficient in silicon micromachined channels*, Dissertation (Massachusetts Institute of Technology, 1997).

[120] I. A. Graur et al., *Measurements of tangential momentum accommodation coefficient for various gases in plane microchannel*, Phys. Fluids **21**, 102004 (2009).

[121] T. Missoni et al., *Extraction of tangential momentum and normal energy accommodation coefficients by comparing variational solutions of the Boltzmann equation with experiments on thermal creep gas flow in microchannels*, Fluids **6**, 445 (2021).

[122] S. K. Loyalka, *Theory of the spinning rotor gauge in the slip regime*, J. Vac. Sci. Technol., A **14**, 2940 (1996).

[123] T. Acharya et al., *Measurement of continuum breakdown during disk spindown in low-pressure air*, J. Thermophy. Heat. Trans. **29**, 281 (2015).

[124] T. Acharya et al., *Disk spin-down measurements in the free-molecular flow regime: A new method for measurement of tangential momentum accommodation coefficients*, Vacuum **126**, 70 (2016).

[125] T. Acharya and M. J. Martin, *Variation of momentum accommodation coefficients with molecular mass and structure*, AIAA Scitech 2019 Forum, 0623 (2019).

[126] F. Sharipov, *Application of the Cercignani-Lampis scattering kernel to calculations of rarefied gas flows. I. Plane flow between two parallel plates*, Eur. J. Mech. B. Fluids **21**, 113 (2002).

[127] F. Sharipov, *Application of the Cercignani-Lampis scattering kernel to calculations of rarefied gas flows. III. Poiseuille flow and thermal creep through a long tube*, Eur. J. Mech. B. Fluids **22**, 145 (2003).

[128] F. Sharipov and D. Kalempa, *Velocity slip and temperature jump coefficients for gaseous mixtures. I. Viscous slip coefficient*, Phys. Fluids **15**, 1800 (2003).

[129] C. Cercignani, M. Lampis and S. Lorenzani, *Variational approach to gas flows in microchannels*, Phys. Fluids **16**, 3426 (2004).

[130] T. C. Lilly et al., *Numerical and experimental investigation of microchannel flows with rough surfaces*, Phys. Fluids **19**, 106101 (2007).

[131] O. A. Aksenova and I. A. Khalidov, *Fractal and statistical models of rough surface interacting with rarefied gas flow*, AIP Conf. Proc. **762**, 993 (2005).

[132] O. A. Aksenova and I. A. Khalidov, *Analytic model of the effect of poly-Gaussian roughness on rarefied gas flow near the surface*, AIP Conf. Proc. **1786**, 100007 (2016).

[133] O. A. Aksenova and I. A. Khalidov, *Inverse problem of finding surface roughness parameters in rarefied gas flow*, AIP Conf. Proc. **2132**, 170005 (2019).

[134] C. Zhang et al., *Role of rough surface topography on gas slip flow in microchannels*, Physical Review E **86**, 016319 (2012).

[135] H. Yan, W.-M. Zhang and Z.-K. Peng, *Effect of random surface topography on the gaseous flow in microtubes with an extended slip model*, Microfluid Nanofluid **18**, 897 (2015).

[136] W. Su et al., *Rarefaction cloaking: Influence of the fractal rough surface in gas slider bearings*, Phys. Fluids **29**, 102003 (2017).

[137] O. Sazhin, *Regarding a benchmark problem: Rarefied gas flow through a rough-surfaced channel*, Comp. Math. and Math. Phys. **58**, 1640 (2018).

[138] O. Sazhin, *The effect of surface roughness on internal free molecular gas flow*, Vacuum **159**, 287 (2019).

[139] O. Sazhin, *Rarefied gas flow through a rough channel into a vacuum*, Microfluid Nanofluid **24**, 27 (2020).

[140] G. Karniadakis, A. Beskok and N. Aluru, *Microflows and Nanoflows - Fundamentals and Simulation* (Springer Science+Business Media, Inc., 2005).

[141] G. Narendran, D. A. Perumal and N. Gnanasekaran, *A review of Lattice Boltzmann method computational domains for micro- and nanoregime applications*, Nanosci. Technol.: An Internat. J. **11**, 343 (2020).

[142] A. Taassob et al., *A review of rarefied gas flow in irregular micro/nanochannels*, J. Micromech. Microeng. **31**, 113002 (2021).

[143] G. L. Morini et al., *A critical review of the measurement techniques for the analysis of gas microflows through microchannels*, Exp Therm Fluid Sci **35**, 849 (2011).

[144] R. P. Feynman, R. B. Leighton and M. Sands, *The Feynman lectures on physics. Vol. I*, Diss. (California Institute of Technology, 2013).

[145] A. Einstein, *Ist die Trägheit eines Körpers von seinem Energiegehalt abhängig?*, Annalen der physik **323**, 639 (1905).

[146] C. Shen, *Rarefied gas dynamics - fundamentals, simulations and micro flows* (Springer Science + Business Media, Inc., 2005).

[147] M. Fang et al., *DSMC modeling of rarefied ionization reactions and applications to hypervelocity spacecraft reentry flows*, Adv. Aerodyn. **2**, 7 (2020).

[148] G. A. Bird, *The Q-K model for gas-phase chemical reaction rates*, Phys. Fluids **23**, 106101 (2011).

[149] P. L. Bhatnagar, E. P. Gross and M. Krook, *A model for collision processes in gases. I. Small amplitude processes in charged and neutral one-component systems*, Phys. Rev. **94**, 511 (1954).

[150] E. M. Shakhov, *Generalization of the Krook kinetic relaxation equation*, Fluid Dynam. **3**, 95 (1968).

[151] L. H. Holway, *New statistical models for kinetic theory: Methods of construction*, Phys. Fluids **9**, 1658 (1966).

[152] J. Mathiaud, L. Mieussens and M. Pfeiffer, *An ES-BGK model for diatomic gases with correct relaxation rates for internal energies*, Europ. J. Mech. B Fluids **96**, 65 (2022).

[153] F. Sharipov and V. Seleznev, *Data on internal rarefied gas flows*, J. Phys. Chem. Ref. Data **27**, 657 (1998).

[154] B. Widom, *Statistical mechanics: A concise introduction for chemists* (Cambridge University Press, 2002), ISBN: 0-521-81119-8.

[155] D. Richter, *Mechanik der Gase* (Berlin-Heidelberg: Springer-Verlag, 2010), ISBN: 978-3-642-12722-9.

[156] C. Cercignani and M. Lampis, *Kinetic models for gas-surface interactions*, Transport Theor Stat **1**, 101 (1971).

[157] R. G. Lord, *Application of the Cercignani-Lampis scattering kernel to direct simulation Monte Carlo calculations* (VCH, Weinheim, 1991), S. 1427.

[158] M. S. Woronowicz and D. F. G. Rault, *Cercignani-Lampis-Lord gas-surface interaction model: Comparisons between theory and simulation*, J. Spacecraft **31**, 532 (1994).

[159] C. Hirsch, *Numerical computation of internal and external flows. Introduction to the fundamentals of CFD*, **2** (Butterworth-Heinemann, 2007).

[160] J. H. Ferziger and M. Perić, *Numerische Strömungsmechanik* (Springer, 2008).

[161] J. C. Maxwell, *On stresses in rarefied gases arising from inequalities of temperature*, Proc. Roy. Soc. London **27**, 304 (1878).

[162] F. Sharipov, *Data on the velocity slip and temperature jump on a gas-solid interface*, J. Phys. Chem. Ref. Data **40**, 023101 (2011).

[163] E. Truckenbrodt, *Fluidmechanik - Band 1: Gundlagen und elementare Strömungsvorgänge dichtebeständiger Fluide*, **4** (Springer-Verlag Berlin Heidelberg, 2008).

[164] A. Ebrahimi and E. Roohi, *Flow and thermal fields investigation in divergent micro/nano channels*, J. therm. Eng. **2**, 709 (2016).

[165] A. Ebrahimi and E. Roohi, *DSMC investigation of rarefied gas flow through diverging micro- and nanochannels*, Microfluid Nanofluid **21**, 18 (2017).

[166] A. Ebrahimi, V. Shahabi and E. Roohi, *Pressure-driven nitrogen flow in divergent microchannels with isothermal walls*, Appl. Sci. **11**, 3602 (2021).

[167] I. Ansys, *Ansys CFX-Solver Theory Guide Release 2021 R2*, Techn. Ber. (2021).

[168] G. A. Bird, *Approach to translational equilibrium in a rigid sphere gas*, Phys. Fluids **6**, 1518 (1963).

[169] R. C. Palharini, *Atmospheric reentry modelling using an open-source DSMC code*, Diss. (University of Strathclyde, 2014).

[170] E. Piekos and K. Breuer, *DSMC modeling of micromechanical devices*, 30th AIAA Thermophysics Conference, 10.2514/6.1995-2089 (1995).

[171] O. Boulon, R. Mathes and J.-P. Thibault, *Direct simulation Monte Carlo method for molecular and transitional flow regimes in vacuum components with static and moving surfaces*, J. Vac. Sci. Technol. A **17**, 2080 (1999).

[172] M. A. Gallis et al., *DSMC simulations of turbulent flows at moderate Reynolds numbers*, AIP Conf. Proc. **2132**, 070010 (2019).

[173] C. White et al., *DsmcFoam+: An OpenFOAM based direct simulation Monte Carlo solver*, Comput. Phys. Comm. **224**, 22 (2018).

[174] T. J. Scanlon et al., *An open source, parallel DSMC code for rarefied gas flows in arbitrary geometries*, Comput. Fluids **39**, 2078 (2010).

[175] E. Arlemark, G. Markelov and S. Nedea, *Rebuilding of Rothe's nozzle measurements with OpenFOAM software*, J. Phys.: Conf. Ser. **362**, 012040 (2012).

[176] C. White, *Benchmarking, development and application of an open source DSMC solver*, Diss. (University of Strathclyde, 2013).

[177] C. White et al., *A DSMC investigation of gas flows in micro-channels with bends*, Comp. Fluids **71**, 261 (2013).

[178] H.-O. Georgii, *Stochastik - Einführung in die Wahrscheinlichkeitstheorie und Statistik*, **2** (Walter de Gruyter GmbH & Co. KG, Berlin, 2004), ISBN: 3-11-018282-3.

[179] M. Wang and Z. Li, *Simulations for gas flows in microgeometries using the direct simulation Monte Carlo method*, Int. J. Heat Fluid Flow **25**, 975 (2004).

[180] A. Linkamp, *Nichtreflektierende Rand- und Kopplungsbedingung zur instationären Strömungssimulation von Fluidenergiemaschinen in Anlagen*, Diss. (Technische Universität Dortmund, Logos Verlag, 2019).

[181] R. P. Nance, H. A. Hassan and D. B. Hash, *Role of boundary conditions in Monte Carlo simulation of MEMS devices*, 35th Aerospace Sciences Meeting and Exhibit, 375 (1997).

[182] W. W. Liou and Y. Fang, *Heat transfer in microchannel devices using DSMC*, J. Microelectromech. Sys. **10**, 274 (2001).

[183] Y. Fang and W. W. Liou, *Computations of the flow and heat transfer in microdevices using DSMC with implicit boundary conditions*, J. Heat Trans. **124**, 338 (2002).

[184] C. Ratcliffe and B. Ratcliffe, *Doubt-free uncertainty in measurement* (Springer International Publishing, Switzerland, 2015).

[185] L. Fahrmeir et al., *Statistik - Der Weg zur Datenanalyse*, **8** (Springer, Berlin-Heidelberg, 2016), ISBN: 978-3-662-50371-3.

[186] H. Pleskun et al., *Modelling of inhomogeneous chamber states in rotary positive displacement vacuum pumps*, IOP Conf. Ser.: Mater. Sci. Eng. **1180**, 12009 (2021).

[187] H. Pleskun, T. Jünemann and A. Brümmer, *Validation of inhomogeneous chamber states in rotary positive displacement vacuum pumps*, IOP Conf. Ser.: Mater. Sci. Eng. **1267**, 012010 (2022).

[188] H. Pleskun, A. Syring and A. Brümmer, *Transient chamber filling in rotary positive displacement vacuum pumps*, IOP Conf. Ser.: Mater. Sci. Eng. **1267**, 012016 (2022).

[189] J. F. M. Velthuis and L. van Bokhoven, *Measurement of the tangential momentum accommodation coefficient of H2 on stainless steel, extreme ultraviolet-resist, and polyimide*, J. Vac. Sci. Technol. A **31**, 061605 (2013).

[190] E. Buckingham, *On physically similar systems - Illustrations of the use of dimensional equations*, Phys. Rev. **4**, 345 (1914).

[191] Boost, *Boost C++ Libraries version 1.77.0*, `http://www.boost.org/`, Last accessed 2022-07-19, 2021.

[192] H. Pleskun, T. Bode and A. Brümmer, *Couette flow in a rectangular channel in the whole range of the gas rarefaction*, Phys. Fluids **34**, 032004 (2022).

[193] H. Pleskun and A. Brümmer, *Gas-surface interactions of a Couette-Poiseuille flow in a rectangular channel*, Phys. Fluids **34**, 082009 (2022).

[194] B. John, X.-J. Gu and D. R. Emerson, *Nonequilibrium gaseous heat transfer in pressure-driven plane Poiseuille flow*, Physical Review E **88**, 013018 (2013).

[195] V. Varade et al., *Low mach number slip flow through diverging microchannel*, Computers and Fluids **111**, 46 (2015).

[196] M. M. Smirnov, *Problems on the equations of mathematical physics* (Noordhoff, 1967).

[197] J. Jang and T. Wereley, *Effective heights and tangential momentum accommodation coefficients of gaseous slip flows in deep reactive ion etching rectangular microchannels*, J. Micromech. Microeng. **16**, 493 (2006).

[198] S. K. Loyalka, *Kinetic theory of thermal transpiration and mechanocaloric effect*, J. Chem. Phys. **63**, 4054 (1975).

[199] S. K. Loyalka and K. A. Hickey, *Kinetic theory of thermal transpiration and the mechanocaloric effect: Planar flow of a rigid sphere gas with arbitrary accommodation at the surface*, J. Vac. Sci. Technol., A **9**, 158 (1991).

[200] G. A. Bird, *Sophisticated DSMC*, Notes for a short course at the DSMC07 meeting (2007).

[201] O. Forster, *Analysis 1: Differential- und Integralrechnung einer Veränderlichen*, **9** (Vieweg, 2008), ISBN: 978-3-8348-0395-5.

[202] W. H. Press et al., „Numerical recipes: the art of scientific computing“, **3** (Cambridge University Press, Cambridge, 2007).

[203] G. A. F. Seber and C. J. Wild, *Nonlinear regression* (Wiley-Interscience, 2003), ISBN: 0-471-47135-6.

[204] MATLAB, *version 9.1.0 (R2016b)* (The MathWorks Inc., Natick, Massachusetts, 2016).

[205] L. F. Richardson and J. A. Gaunt, *VIII. The deferred approach to the limit*, Philosophical Transactions of the Royal Society of London. Series A, Containing Papers of a Mathematical or Physical Character **226**, 299 (1927).

[206] J. H. Ferziger and M. Peric, *Computational methods for fluid dynamics*, **3** (Springer, 2002).

[207] MATLAB, *version 9.11.0 (R2021b)* (The MathWorks Inc., Natick, Massachusetts, 2021).

[208] *SP 250 - Trockenverdichtende Schrauben-Vakuumpumpe*, manual, Oerlikon Leybold Vacuum, 2010.

[209] *MKS Baratron Type 627B absolute pressure transducer:, MKS instruments Deutschland GmbH*, www.nanophys.kth.se/nanolab/aja/manuals-pdf/MKS_627B_BARATRON.pdf, manual, Last accessed 2024-01-30, 1999.

[210] *TC Mess- & Regeltechnik GmbH*, https://www.tcgmbh.de/thermoelemente/typ-t-thermoelemente.html, Last accessed 2022-11-04, 2022.

[211] *capaNCDT 6110/6120, CS1, Micro-Epsilon Messtechnik GmbH und Co. KG*, manual, 2016.

[212] *Sitron sensors, RGB-Sensor E3ZM-V86 - Optischer Sensor zur Druckmarkenerfassung von Sitron Sensor - Prospekt*, https://www.sitron.de/de/produktedownloads/vision-sensoren-code-lesesysteme-farb-sensoren/, manual, Last accessed 2022-11-04, 2010.

[213] *CCLD Accelerometers with TEDS: Type 4533-B*, Product data, Brüel & Kjær, 2013.

[214] *imc SPARTAN 11*, manual, imc Test & Measurement GmbH, 2022.

[215] *imc CRONOS 8.4*, manual, imc Test & Measurement GmbH, 2020.

[216] *imc Studio 5.2*, manual, imc Test & Measurement GmbH, 2017.

[217] *imc Famos 7.2*, manual, imc Test & Measurement GmbH, 2017.

[218] *TRIVAC E 2 - D 5 E / D 10 E / D 16 E - Dual-Stage Rotary Vane Vacuum Pump*, manual, Leybold Vacuum GmbH, 2001.

[219] *Grundlagen der Messtechnik Teil 3: Auswetung von Messungen einer einzelnen Messgröße - Messunsicherheit*, Norm, DIN 1319 - 3, 1999.

[220] *TURBOVAC TW 250 S - Wide-Range Turbo-Molekularpumpe mit integriertem oder externem Frequenzwandler*, manual, Oerlikon Leybold Vacuum, Nov. 2009.

[221] *Ansys, Inc., Ansys CFX-Solver Modeling Guide Release 2021 R2*, Techn. Ber. (2021).

A Proof of Couette Flow Properties

A.1 Shape Factor

Plane slip flow using Eq. 6.97:

$$\sum_i G_{C,i} = G_{C,t} + G_{C,b} = \frac{\delta/2 + \sigma_b}{\delta + \sigma_b + \sigma_t} + \frac{\delta/2 + \sigma_t}{\delta + \sigma_b + \sigma_t} = \frac{\cancel{\delta + \sigma_b + \sigma_t}}{\cancel{\delta + \sigma_b + \sigma_t}} = 1 \tag{A.1}$$

Free molecular flow using Eq. 6.114:

$$\sum_{i=1}^{4} G_{C,i} = \frac{1}{2\pi}\Bigg[\left(\eta - \frac{1}{\eta}\right)\ln\left(\eta^2+1\right) - 2\eta\ln(\eta) + 4\arctan(\eta) \tag{A.2}$$

$$+ \left(\frac{1}{\eta} - \eta\right)\ln\left(\eta^{-2}+1\right) - \frac{2}{\eta}\ln\left(\frac{1}{\eta}\right) + 4\arctan\left(\frac{1}{\eta}\right)\Bigg] \tag{A.3}$$

$$= \frac{1}{2\pi}\Bigg[\cancel{\left(\eta - \frac{1}{\eta}\right)\ln\left(\eta^2+1\right)} - \cancel{\left(\eta - \frac{1}{\eta}\right)\ln\left(\eta^2+1\right)} + 2\cancel{\left(\eta - \frac{1}{\eta}\right)\ln(\eta)} \tag{A.4}$$

$$\cancel{-2\left(\eta - \frac{1}{\eta}\right)\ln(\eta)} + 4\left(\arctan(\eta) + \arctan\left(\frac{1}{\eta}\right)\right)\Bigg] = \frac{1}{2\pi}\left[4\frac{\pi}{2}\right] = 1 \tag{A.5}$$

using

$$\ln\left(\frac{1}{\eta}\right) = -\ln(\eta) \tag{A.6}$$

$$\ln\left(\eta^{-2}+1\right) = \ln\left(\eta^2+1\right) - 2\ln(\eta) \tag{A.7}$$

$$\arctan(\eta) + \arctan\left(\frac{1}{\eta}\right) = \frac{\pi}{2} \quad \forall \eta \in \mathbb{R}^+ \tag{A.8}$$

A.2 High Wall Velocities

TAB. A.1 Reduced mass flow rate for $\delta = 1$ and $\tilde{\eta} = 5$ and different velocity ratios $u_0 = U_i/c_\mathrm{m}$. Reproduced from Ref. [192], with the permission of AIP Publishing.

$u_0 = U_i/c_\mathrm{m}$	G_C	$\left(1 - \frac{G_C(u_0)}{G_C(u_0=0.01)}\right)\cdot 100$
0.01	0.431	0
0.1	0.431	0
1	0.43	0.23
2	0.427	0.93
3	0.422	2.09

In this section at first the impact of the velocity ratio $u_0 = U/c_\mathrm{m}$ is investigated. Therefore DSMC simulations are performed for the case $\delta = 1$ and $\tilde{\eta} = 5$ for different values of velocity ratio u_0. The results are given in Tabelle A.1. It is obtained that the reduced flow rate is only affected by the absolute value of the wall velocity if it is in the range of the molecule's most probable speed. Even for a value $u_0 = 3$ the reduced flow rate G_C is only about 2% lower than the reduced flow rate at $u_0 = 0.01$. Therefore the impact of this ratio can be neglected.

A.3 Superposition Principle

In the free molecular regime, the slip and the hydrodynamic regime, the validation of superposition principle of several moving walls can be shown mathematically. In this section this is shown for the transition regime especially at high wall velocities. Therefore DSMC simulations are performed with all four walls moving with different wall velocities according to Fig. 6.13:

$$U_{t,0}/c_\mathrm{m} = U_{t,1}/c_\mathrm{m} = 1 \tag{A.9}$$

$$U_{r,0}/c_\mathrm{m} = U_{r,1}/c_\mathrm{m} = 3/4 \tag{A.10}$$

$$U_{b,0}/c_\mathrm{m} = U_{b,1}/c_\mathrm{m} = 1/2 \tag{A.11}$$

$$U_{l,0}/c_\mathrm{m} = U_{l,1}/c_\mathrm{m} = 1/4 \tag{A.12}$$

TAB. A.2 Comparison between the mass flow rate $\dot{m}$ using the superposition principle in Eq. 6.72 and data of Tab. B.5 and direct results of the DSMC method $\dot{m}_\mathrm{DSMC}$ with boundary conditions of Eqs. A.9-A.12. Reproduced from Ref. [192], with the permission of AIP Publishing.

δ	η	$\dot{m}$ [kg s^{-1}]	$\dot{m}_\mathrm{DSMC}$ [kg s^{-1}]	deviation [%]
0.1	1	$2.814 \cdot 10^{-8}$	$2.814 \cdot 10^{-8}$	0.0093
	2	$5.979 \cdot 10^{-8}$	$5.979 \cdot 10^{-8}$	0.0002
	5	$1.587 \cdot 10^{-7}$	$1.587 \cdot 10^{-7}$	0.0118
	10	$3.266 \cdot 10^{-7}$	$3.266 \cdot 10^{-7}$	0.0028
1	1	$2.814 \cdot 10^{-7}$	$2.812 \cdot 10^{-7}$	0.0548
	2	$6.037 \cdot 10^{-7}$	$6.037 \cdot 10^{-7}$	0.0040
	5	$1.611 \cdot 10^{-6}$	$1.61 \cdot 10^{-6}$	0.0760
	10	$3.298 \cdot 10^{-6}$	$3.298 \cdot 10^{-6}$	0.0202
10	1	$2.814 \cdot 10^{-6}$	$2.814 \cdot 10^{-6}$	0.0217
	2	$6.127 \cdot 10^{-6}$	$6.124 \cdot 10^{-6}$	0.0473
	5	$1.626 \cdot 10^{-5}$	$1.626 \cdot 10^{-5}$	0.0559
	10	$3.313 \cdot 10^{-5}$	$3.312 \cdot 10^{-5}$	0.0582

Argon at $T = 293.15\,\mathrm{K}$ is simulated. The gas rarefaction parameter δ is calculated with a dynamic viscosity $\mu = 2.251 \cdot 10^{-5}\,\mathrm{Pa \cdot s}$ and the channel height is set to $h = 0.01\,\mathrm{m}$. Therefore the pressure scales with δ. Tab. A.2 shows the resulting mass flow rates for different gas rarefaction parameters δ and cross section ratios η. For $\dot{m}$ the superposition principle of Eq. (6.72) is used with the tabulated data of Tab. B.5 and Eq. (6.117). The density is calculated using Eq. (3.40). $\dot{m}_\mathrm{DSMC}$ is directly calculated by the DSMC method with a statistical accuracy of 0.1 % or better. The deviation in percent between both results is given and is smaller than the given accuracy of the results. This indicates that even for high values of the wall velocity the superposition principle for more than one moving wall can also be applied in the transitional regime.

B DSMC Data

TAB. B.1 Reduced flow rates $G_{\mathrm{P}}(\delta,\eta)$ of the Poiseuille flow in a rectangular channel for $\alpha_{\mathrm{h}} = \alpha_{\mathrm{v}} = 0.71$. DSMC results shown in Fig. 6.6.[I]

δ [−] \ η [−]	1	2	10
0	1.200	1.570	2.529
0.01	1.180	1.549	2.474
0.1	1.157	1.537	2.267
0.2	1.148	1.532	2.176
0.5	1.115	1.501	2.088
1	1.124	1.550	2.067
2	1.146	1.585	2.122
5	1.327	1.898	2.429

TAB. B.2 Reduced flow rates $G_{\mathrm{P}}(\delta,\eta)$ of the Poiseuille flow in a rectangular channel for $\alpha_{\mathrm{h}} = 0.92, \alpha_{\mathrm{v}} = 0.71$. DSMC results shown in Fig. 6.7.[I]

δ [−] \ η [−]	1	2	10
0	1.041	1.301	2.078
0.01	1.024	1.296	2.032
0.1	0.981	1.273	1.847
0.2	0.992	1.254	1.696
0.5	0.958	1.232	1.587
1	0.964	1.219	1.574
2	0.997	1.297	1.555
5	1.167	1.595	2.017

TAB. B.3 Reduced flow rates $G_{\mathrm{P}}(\delta,\eta)$ of the Poiseuille flow in a rectangular channel for $\alpha_{\mathrm{h}} = 0.92, \alpha_{\mathrm{v}} = 0.5$. DSMC results shown in Fig. 6.8.[I]

δ [−] \ η [−]	1	2	10
0	1.191	1.433	2.138
0.01	1.164	1.429	2.096
0.1	1.141	1.392	1.835
0.2	1.107	1.375	1.789
0.5	1.107	1.342	1.630
1	1.105	1.351	1.582
2	1.145	1.399	1.628
5	1.291	1.694	2.019

TAB. B.4 Reduced flow rates $G_{\mathrm{P}}(\delta,\eta)$ of the Poiseuille flow in a rectangular channel for $\alpha_{\mathrm{t}} = 0.7, \alpha_{\mathrm{b}} = 0.8, \alpha_{\mathrm{r}} = 0.9, \alpha_{\mathrm{l}} = 1$. DSMC results shown in Fig. 6.9.[I]

δ [−] \ η [−]	1	2	10
0	0.991	1.383	2.352
0.01	0.965	1.352	2.307
0.1	0.943	1.335	2.075
0.2	0.965	1.343	2.019
0.5	0.932	1.348	1.925
1	0.940	1.330	1.948
2	0.973	1.410	-
5	1.145	-	-

[I] Reproduced from Ref. [193], with the permission of AIP Publishing.

TAB. B.5 Tabulated data for $G_C(\delta, \tilde{\eta})$. Values for $\delta = 0$ are obtained by Eq. (6.114), values for $\delta \to \infty$ are obtained by Eq. (6.83). Intermediate states are calculated via DSMC method.[IV]

δ \ $\tilde{\eta}$	1	2	5	10	20	50	100	∞[I]
0[II]	0.250	0.324	0.401	0.439	0.464	0.483	0.490	0.500
0.01	0.250	0.324	0.402	0.442	0.467	0.485	0.492	0.500
0.02	0.250	0.325	0.404	0.443	0.468	0.487	0.493	0.500
0.05	0.250	0.326	0.407	0.447	0.472	0.488	0.494	0.500
0.1	0.250	0.328	0.410	0.451	0.475	0.490	0.495	0.500
0.2	0.250	0.330	0.416	0.456	0.478	0.491	0.496	0.500
0.5	0.250	0.336	0.424	0.462	0.481	0.492	0.496	0.500
1	0.250	0.341	0.431	0.465	0.483	0.493	0.497	0.500
2	0.250	0.348	0.437	0.468	0.484	0.494	0.497	0.500
5	0.250	0.356	0.441	0.471	0.485	0.494	0.497	0.500
10	0.250	0.361	0.444	0.472	0.486	0.494	0.497	0.500
20	0.250	0.363	0.445	0.472	0.486	0.495	0.497	0.500
50	0.250	0.364	0.445	0.473	0.486	0.495	0.497	0.500
∞[III]	0.250	0.365	0.446	0.473	0.486	0.495	0.497	0.500

TAB. B.6 Reduced flow rates $G_C(\delta, \eta)$ of the Couette flow in a rectangular channel for $\alpha_h = \alpha_v = 0.71$. Results of the DSMC method are shown in Fig. 6.17.[IV]

δ [−] \ η [−]	1	2	10
0	0.250	0.327	0.444
0.01	0.250	0.327	0.446
0.1	0.249	0.329	0.453
0.2	0.250	0.331	0.456
0.5	0.250	0.336	0.461
1	0.250	0.340	0.464
2	0.250	0.346	0.467
5	0.250	0.353	0.470
10	0.250	0.359	0.471

TAB. B.7 Reduced flow rates $G_C(\delta, \eta)$ of the Couette flow in a rectangular channel for $\alpha_h = 0.71, \alpha_v = 0.92$. Results of the DSMC method are shown in Fig. 6.18.[IV]

δ [−] \ η [−]	1	2	10
0	0.214	0.292	0.430
0.01	0.214	0.292	0.446
0.1	0.213	0.295	0.440
0.2	0.212	0.397	0.445
0.5	0.213	0.302	0.452
1	0.212	0.308	0.456
2	0.215	0.318	0.461
5	0.220	0.333	0.466
10	0.228	0.344	0.468

[I] Values for the well-known plane Couette flow can also be derived for example from [78,97,140].
[II] Values obtained by Eq. (6.114).
[III] Values obtained by Eq. (6.83).
[IV] Reproduced from Ref. [192], with the permission of AIP Publishing.

TAB. B.8 Reduced flow rates $G_{\mathrm{C}}(\delta, \eta)$ of the Couette flow in a rectangular channel for $\alpha_{\mathrm{h}} = 0.92, \alpha_{\mathrm{v}} = 0.71$. Results of the DSMC method are shown in Fig. 6.19.[V]

δ [−] \ η [−]	1	2	10
0	0.287	0.357	0.454
0.01	0.287	0.357	0.455
0.1	0.287	0.358	0.462
0.2	0.287	0.363	0.465
0.5	0.288	0.367	0.470
1	0.287	0.371	0.472
2	0.286	0.374	0.474
5	0.280	0.376	0.475
10	0.273	0.374	0.474

[V] Reproduced from Ref. [192], with the permission of AIP Publishing.

C Experimental Setup

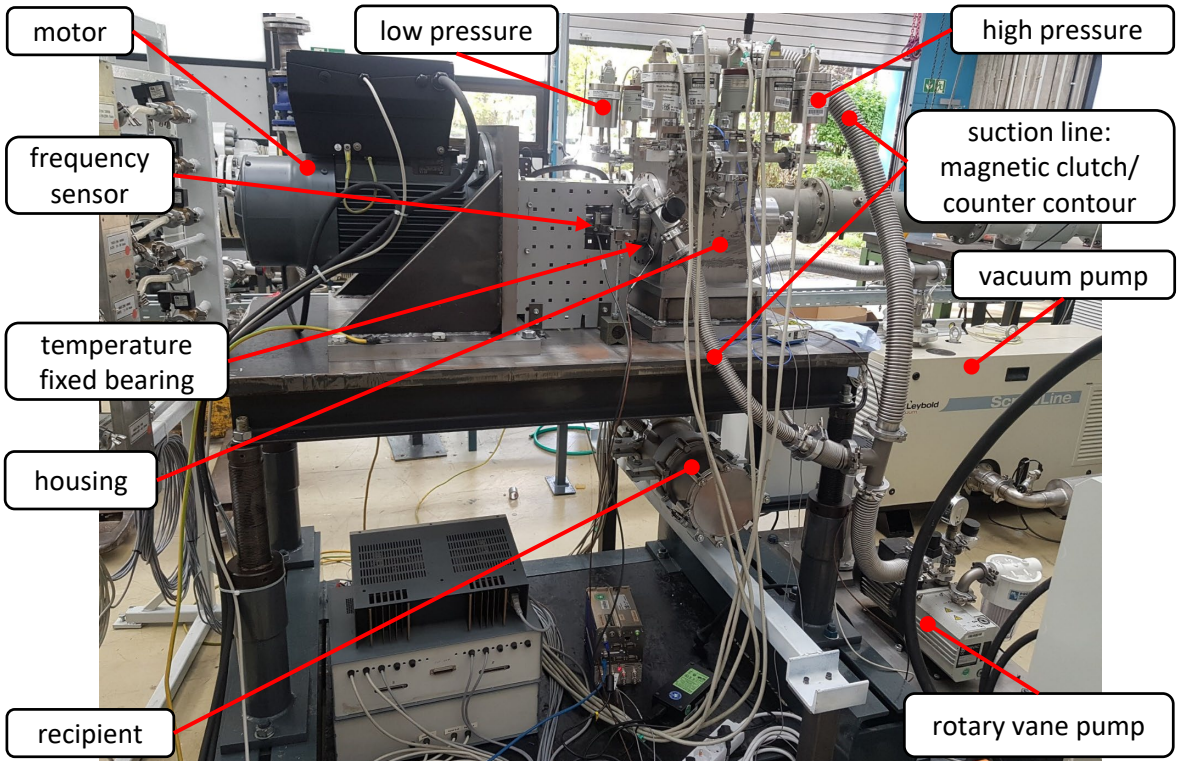

FIG. C.1 Picture of the vacuum test rig.

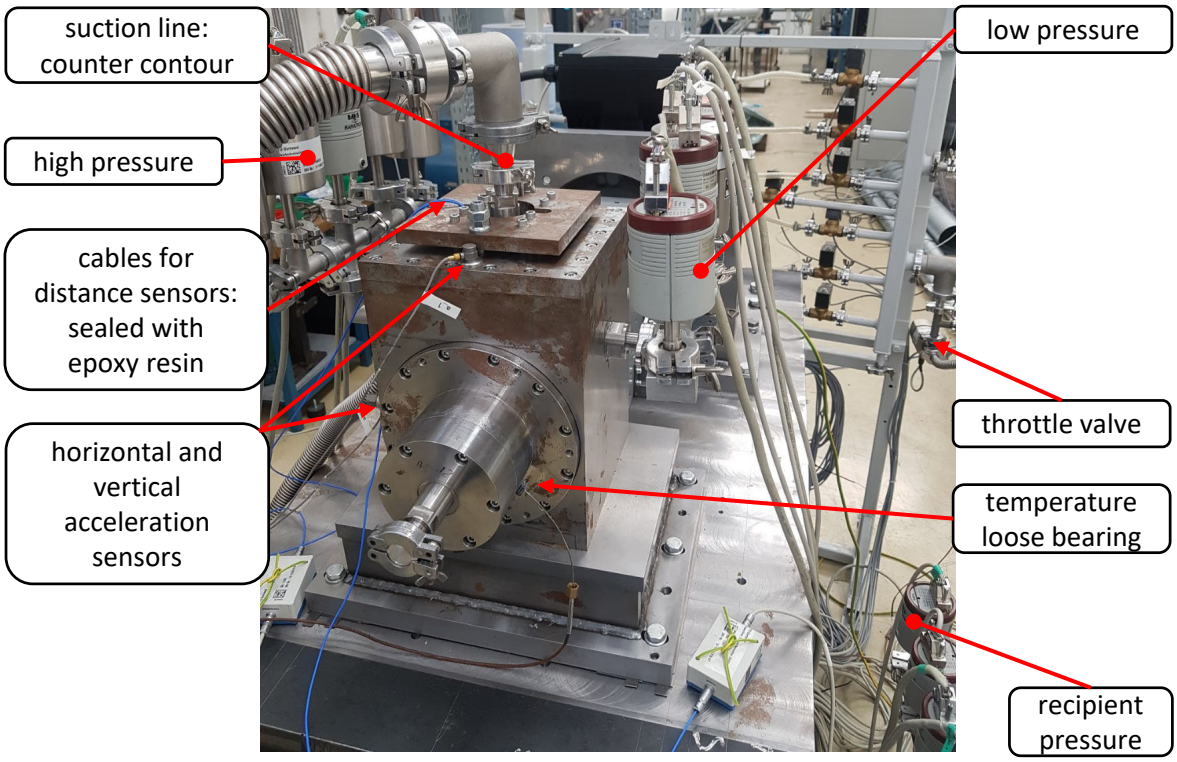

FIG. C.2 Picture of the vacuum test rig.

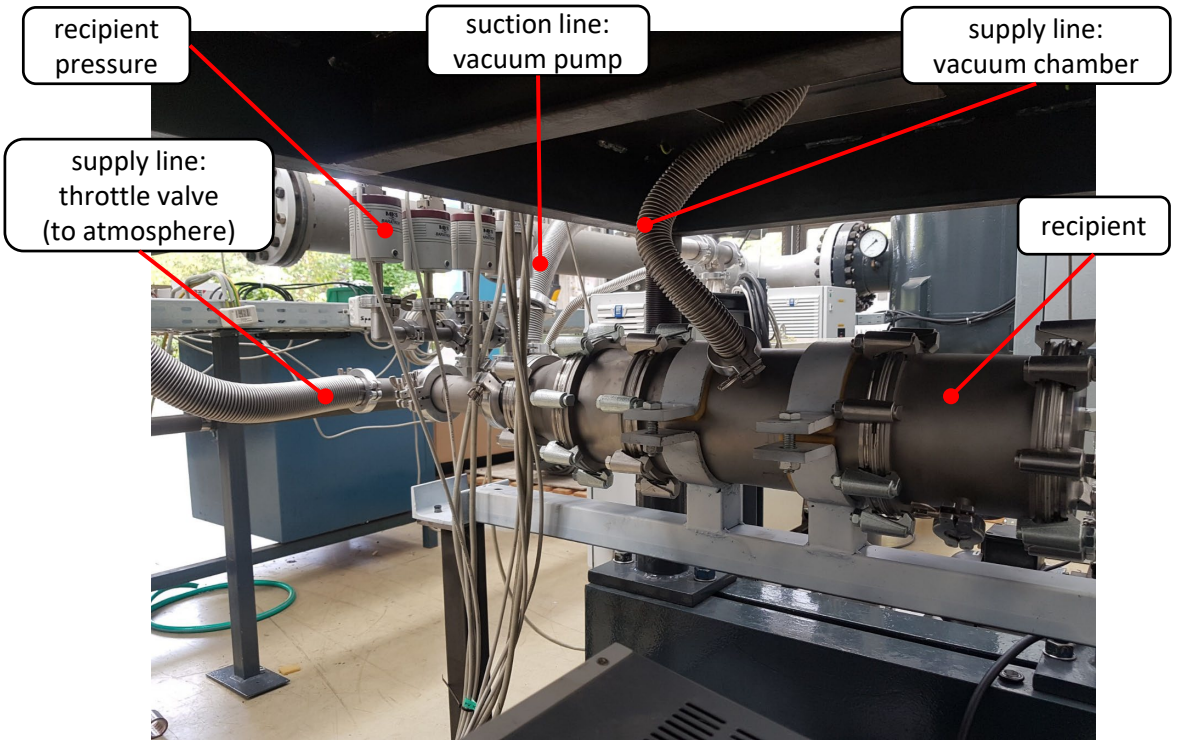

FIG. C.3 Picture of the vacuum test rig.

D Measurement Data

TAB. D.1 Measurements for $D_o/D_i = 1.7$, $h_{cl,r} = 0.2\,\mathrm{mm}$ and $u_0 = 0.13^{+0.0004}_{-0.01}$ at $T_{amb} = 294.8\,\mathrm{K}$ shown in Figs. 8.7 -8.13.

p^*_{ch} [Pa]	p_{HP} [Pa]	p_{LP} [Pa]	T_B [K]	δ^* [−]	p_{HP}/p^*_{ch} [−]	p_{HP}/p_{LP} [−]
$0.50^{+0.053}_{-0.053}$	$2.24^{+0.073}_{-0.073}$	$0.26^{+0.110}_{-0.110}$	$337.2^{+1.04}_{-1.04}$	$1.0^{+0.107}_{-0.124}$	$4.482^{+0.502}_{-0.502}$	$8.498^{+3.552}_{-3.552}$
$0.76^{+0.053}_{-0.053}$	$2.91^{+0.070}_{-0.070}$	$0.34^{+0.068}_{-0.068}$	$338.4^{+1.54}_{-1.54}$	$1.5^{+0.106}_{-0.145}$	$3.823^{+0.280}_{-0.280}$	$8.639^{+1.766}_{-1.766}$
$1.00^{+0.055}_{-0.055}$	$3.46^{+0.080}_{-0.080}$	$0.40^{+0.072}_{-0.072}$	$339.3^{+1.37}_{-1.37}$	$2.0^{+0.109}_{-0.172}$	$3.468^{+0.206}_{-0.206}$	$8.590^{+1.551}_{-1.551}$
$1.50^{+0.058}_{-0.058}$	$4.48^{+0.069}_{-0.069}$	$0.54^{+0.071}_{-0.071}$	$339.2^{+0.55}_{-0.55}$	$3.0^{+0.115}_{-0.230}$	$2.979^{+0.123}_{-0.123}$	$8.286^{+1.093}_{-1.093}$
$2.01^{+0.054}_{-0.054}$	$5.41^{+0.061}_{-0.061}$	$0.71^{+0.085}_{-0.085}$	$339.4^{+0.64}_{-0.64}$	$4.0^{+0.108}_{-0.289}$	$2.689^{+0.078}_{-0.078}$	$7.619^{+0.911}_{-0.911}$
$2.51^{+0.056}_{-0.056}$	$6.25^{+0.064}_{-0.064}$	$0.91^{+0.089}_{-0.089}$	$340.1^{+0.65}_{-0.65}$	$5.0^{+0.112}_{-0.356}$	$2.495^{+0.061}_{-0.061}$	$6.846^{+0.702}_{-0.702}$
$3.06^{+0.057}_{-0.057}$	$7.11^{+0.068}_{-0.068}$	$1.09^{+0.058}_{-0.058}$	$340.3^{+0.87}_{-0.87}$	$6.1^{+0.113}_{-0.429}$	$2.321^{+0.049}_{-0.049}$	$6.513^{+0.353}_{-0.353}$
$4.03^{+0.134}_{-0.134}$	$8.51^{+0.174}_{-0.174}$	$1.55^{+0.158}_{-0.158}$	$341.3^{+0.61}_{-0.61}$	$8.1^{+0.268}_{-0.617}$	$2.110^{+0.082}_{-0.082}$	$5.498^{+0.572}_{-0.572}$
$5.00^{+0.060}_{-0.060}$	$9.78^{+0.070}_{-0.070}$	$1.98^{+0.059}_{-0.059}$	$341.2^{+0.56}_{-0.56}$	$10.0^{+0.119}_{-0.698}$	$1.958^{+0.027}_{-0.027}$	$4.940^{+0.152}_{-0.152}$
$6.02^{+0.060}_{-0.060}$	$11.06^{+0.078}_{-0.078}$	$2.54^{+0.059}_{-0.059}$	$341.4^{+0.76}_{-0.76}$	$12.0^{+0.121}_{-0.841}$	$1.837^{+0.023}_{-0.023}$	$4.360^{+0.106}_{-0.106}$
$7.02^{+0.062}_{-0.062}$	$12.27^{+0.077}_{-0.077}$	$3.14^{+0.060}_{-0.060}$	$341.8^{+0.58}_{-0.58}$	$14.1^{+0.123}_{-0.985}$	$1.747^{+0.019}_{-0.019}$	$3.910^{+0.079}_{-0.079}$
$7.54^{+0.068}_{-0.068}$	$12.88^{+0.082}_{-0.082}$	$3.47^{+0.066}_{-0.066}$	$342.0^{+0.59}_{-0.59}$	$15.1^{+0.137}_{-1.062}$	$1.708^{+0.019}_{-0.019}$	$3.714^{+0.075}_{-0.075}$
$7.99^{+0.065}_{-0.065}$	$13.39^{+0.088}_{-0.088}$	$3.77^{+0.070}_{-0.070}$	$342.6^{+0.91}_{-0.91}$	$16.0^{+0.129}_{-1.134}$	$1.677^{+0.017}_{-0.017}$	$3.554^{+0.070}_{-0.070}$
$9.08^{+0.067}_{-0.067}$	$14.62^{+0.082}_{-0.082}$	$4.53^{+0.071}_{-0.071}$	$343.3^{+0.82}_{-0.82}$	$18.2^{+0.135}_{-1.305}$	$1.611^{+0.015}_{-0.015}$	$3.229^{+0.054}_{-0.054}$
$9.99^{+0.066}_{-0.066}$	$15.64^{+0.084}_{-0.084}$	$5.18^{+0.069}_{-0.069}$	$343.7^{+0.81}_{-0.81}$	$20.0^{+0.133}_{-1.443}$	$1.566^{+0.013}_{-0.013}$	$3.016^{+0.043}_{-0.043}$
$11.49^{+0.069}_{-0.069}$	$17.35^{+0.081}_{-0.081}$	$6.36^{+0.068}_{-0.068}$	$344.0^{+0.62}_{-0.62}$	$23.0^{+0.139}_{-1.668}$	$1.510^{+0.012}_{-0.012}$	$2.726^{+0.032}_{-0.032}$
$12.53^{+0.075}_{-0.075}$	$18.50^{+0.086}_{-0.086}$	$7.21^{+0.077}_{-0.077}$	$344.3^{+0.75}_{-0.75}$	$25.1^{+0.149}_{-1.828}$	$1.476^{+0.011}_{-0.011}$	$2.567^{+0.030}_{-0.030}$
$15.32^{+0.082}_{-0.082}$	$21.52^{+0.093}_{-0.093}$	$9.53^{+0.093}_{-0.093}$	$344.5^{+0.77}_{-0.77}$	$30.6^{+0.165}_{-2.241}$	$1.405^{+0.010}_{-0.010}$	$2.257^{+0.024}_{-0.024}$
$20.22^{+0.087}_{-0.087}$	$26.70^{+0.102}_{-0.102}$	$13.81^{+0.100}_{-0.100}$	$344.7^{+0.58}_{-0.58}$	$40.5^{+0.174}_{-2.967}$	$1.320^{+0.008}_{-0.008}$	$1.934^{+0.016}_{-0.016}$
$24.98^{+0.091}_{-0.091}$	$31.63^{+0.118}_{-0.118}$	$18.20^{+0.112}_{-0.112}$	$345.0^{+0.68}_{-0.68}$	$50.0^{+0.183}_{-3.677}$	$1.266^{+0.007}_{-0.007}$	$1.738^{+0.012}_{-0.012}$
$30.17^{+0.104}_{-0.104}$	$36.94^{+0.132}_{-0.132}$	$23.10^{+0.109}_{-0.109}$	$345.4^{+0.66}_{-0.66}$	$60.4^{+0.209}_{-4.473}$	$1.224^{+0.006}_{-0.006}$	$1.599^{+0.009}_{-0.009}$
$40.24^{+0.125}_{-0.125}$	$47.16^{+0.159}_{-0.159}$	$32.77^{+0.126}_{-0.126}$	$345.7^{+0.64}_{-0.64}$	$80.5^{+0.250}_{-5.992}$	$1.172^{+0.005}_{-0.005}$	$1.439^{+0.007}_{-0.007}$
$49.99^{+0.136}_{-0.136}$	$56.99^{+0.164}_{-0.164}$	$42.25^{+0.153}_{-0.153}$	$345.9^{+0.66}_{-0.66}$	$100.0^{+0.272}_{-7.476}$	$1.140^{+0.005}_{-0.005}$	$1.349^{+0.006}_{-0.006}$
$60.28^{+0.172}_{-0.172}$	$67.31^{+0.209}_{-0.209}$	$52.35^{+0.143}_{-0.143}$	$346.2^{+0.68}_{-0.68}$	$120.6^{+0.345}_{-9.057}$	$1.117^{+0.005}_{-0.005}$	$1.286^{+0.005}_{-0.005}$
$75.52^{+0.204}_{-0.204}$	$82.56^{+0.239}_{-0.239}$	$67.37^{+0.177}_{-0.177}$	$346.6^{+0.77}_{-0.77}$	$151.1^{+0.409}_{-11.419}$	$1.093^{+0.004}_{-0.004}$	$1.226^{+0.005}_{-0.005}$
$100.7^{+0.248}_{-0.248}$	$107.4^{+0.330}_{-0.330}$	$92.30^{+0.197}_{-0.197}$	$347.1^{+0.74}_{-0.74}$	$201.6^{+0.496}_{-15.361}$	$1.066^{+0.004}_{-0.004}$	$1.164^{+0.004}_{-0.004}$
$126.8^{+0.352}_{-0.352}$	$134.5^{+0.411}_{-0.411}$	$119.0^{+0.312}_{-0.312}$	$347.7^{+0.75}_{-0.75}$	$253.7^{+0.704}_{-19.500}$	$1.061^{+0.004}_{-0.004}$	$1.131^{+0.005}_{-0.005}$
$149.4^{+0.527}_{-0.527}$	$157.4^{+0.559}_{-0.559}$	$141.8^{+0.504}_{-0.504}$	$347.8^{+0.69}_{-0.69}$	$299.0^{+1.055}_{-23.051}$	$1.053^{+0.005}_{-0.005}$	$1.110^{+0.006}_{-0.006}$
$174.4^{+1.161}_{-1.161}$	$182.6^{+1.203}_{-1.203}$	$166.8^{+1.138}_{-1.138}$	$347.6^{+0.58}_{-0.58}$	$349.0^{+2.323}_{-26.887}$	$1.047^{+0.010}_{-0.010}$	$1.095^{+0.010}_{-0.010}$
$200.5^{+1.150}_{-1.150}$	$208.9^{+1.188}_{-1.188}$	$193.0^{+1.118}_{-1.118}$	$347.5^{+0.58}_{-0.58}$	$401.2^{+2.302}_{-30.813}$	$1.042^{+0.008}_{-0.008}$	$1.082^{+0.009}_{-0.009}$
$252.3^{+0.821}_{-0.821}$	$261.2^{+0.861}_{-0.861}$	$245.1^{+0.783}_{-0.783}$	$347.4^{+0.57}_{-0.57}$	$504.9^{+1.644}_{-38.648}$	$1.035^{+0.005}_{-0.005}$	$1.066^{+0.005}_{-0.005}$
$305.4^{+0.913}_{-0.913}$	$314.7^{+0.945}_{-0.945}$	$298.4^{+0.849}_{-0.849}$	$347.3^{+0.54}_{-0.54}$	$611.2^{+1.827}_{-46.683}$	$1.031^{+0.004}_{-0.004}$	$1.055^{+0.004}_{-0.004}$
$404.6^{+1.046}_{-1.046}$	$414.7^{+1.109}_{-1.109}$	$397.9^{+1.000}_{-1.000}$	$347.3^{+0.55}_{-0.55}$	$809.6^{+2.093}_{-61.813}$	$1.025^{+0.004}_{-0.004}$	$1.042^{+0.004}_{-0.004}$
$499.6^{+1.079}_{-1.079}$	$510.5^{+1.114}_{-1.114}$	$493.2^{+1.015}_{-1.015}$	$347.2^{+0.52}_{-0.52}$	$999.7^{+2.159}_{-76.249}$	$1.022^{+0.003}_{-0.003}$	$1.035^{+0.003}_{-0.003}$
$748.5^{+1.659}_{-1.659}$	$761.2^{+1.701}_{-1.701}$	$742.9^{+1.633}_{-1.633}$	$347.2^{+0.56}_{-0.56}$	$1498^{+3.320}_{-114.268}$	$1.017^{+0.003}_{-0.003}$	$1.025^{+0.003}_{-0.003}$
$1005^{+2.044}_{-2.044}$	$1013^{+2.167}_{-2.167}$	$996.7^{+2.155}_{-2.155}$	$347.2^{+0.61}_{-0.61}$	$2011^{+4.091}_{-153.361}$	$1.008^{+0.003}_{-0.003}$	$1.017^{+0.003}_{-0.003}$

TAB. D.2 Measurements for $D_o/D_i = 1.7$, $h_{cl,r} = 0.2\,\mathrm{mm}$ and $u_0 = 0.097^{+0.0011}_{-0.0091}$ at $T_{amb} = 296.3\,\mathrm{K}$ shown in Figs. 8.7 and 8.9.

p^*_{ch} [Pa]	p_{HP} [Pa]	p_{LP} [Pa]	T_B [K]	δ^* [−]	p_{HP}/p^*_{ch} [−]	p_{HP}/p_{LP} [−]
$0.50^{+0.055}_{-0.055}$	$1.70^{+0.070}_{-0.070}$	$0.29^{+0.056}_{-0.056}$	$345.6^{+0.54}_{-0.54}$	$1.0^{+0.109}_{-0.131}$	$3.385^{+0.398}_{-0.398}$	$5.871^{+1.156}_{-1.156}$
$0.60^{+0.053}_{-0.053}$	$1.90^{+0.061}_{-0.061}$	$0.32^{+0.056}_{-0.056}$	$345.8^{+0.61}_{-0.61}$	$1.2^{+0.106}_{-0.137}$	$3.156^{+0.298}_{-0.298}$	$5.935^{+1.061}_{-1.061}$
$0.70^{+0.053}_{-0.053}$	$2.11^{+0.059}_{-0.059}$	$0.35^{+0.054}_{-0.054}$	$345.9^{+0.62}_{-0.62}$	$1.4^{+0.106}_{-0.147}$	$2.992^{+0.241}_{-0.241}$	$5.953^{+0.928}_{-0.928}$
$0.75^{+0.058}_{-0.058}$	$2.19^{+0.059}_{-0.059}$	$0.37^{+0.065}_{-0.065}$	$345.9^{+0.55}_{-0.55}$	$1.5^{+0.115}_{-0.158}$	$2.928^{+0.239}_{-0.239}$	$5.927^{+1.058}_{-1.058}$
$0.81^{+0.054}_{-0.054}$	$2.32^{+0.075}_{-0.075}$	$0.39^{+0.054}_{-0.054}$	$346.1^{+0.62}_{-0.62}$	$1.6^{+0.107}_{-0.158}$	$2.874^{+0.214}_{-0.214}$	$5.948^{+0.851}_{-0.851}$
$0.90^{+0.052}_{-0.052}$	$2.50^{+0.062}_{-0.062}$	$0.42^{+0.053}_{-0.053}$	$346.4^{+0.59}_{-0.59}$	$1.8^{+0.104}_{-0.167}$	$2.772^{+0.175}_{-0.175}$	$5.897^{+0.752}_{-0.752}$
$1.01^{+0.056}_{-0.056}$	$2.71^{+0.069}_{-0.069}$	$0.47^{+0.061}_{-0.061}$	$347.0^{+0.83}_{-0.83}$	$2.0^{+0.111}_{-0.185}$	$2.685^{+0.164}_{-0.164}$	$5.803^{+0.772}_{-0.772}$
$1.27^{+0.054}_{-0.054}$	$3.19^{+0.066}_{-0.066}$	$0.57^{+0.057}_{-0.057}$	$347.4^{+0.65}_{-0.65}$	$2.5^{+0.107}_{-0.216}$	$2.505^{+0.118}_{-0.118}$	$5.603^{+0.572}_{-0.572}$
$1.52^{+0.056}_{-0.056}$	$3.62^{+0.068}_{-0.068}$	$0.67^{+0.057}_{-0.057}$	$347.6^{+0.77}_{-0.77}$	$3.0^{+0.111}_{-0.251}$	$2.383^{+0.098}_{-0.098}$	$5.428^{+0.475}_{-0.475}$
$1.75^{+0.054}_{-0.054}$	$4.00^{+0.061}_{-0.061}$	$0.76^{+0.052}_{-0.052}$	$347.9^{+0.61}_{-0.61}$	$3.5^{+0.108}_{-0.282}$	$2.287^{+0.079}_{-0.079}$	$5.250^{+0.370}_{-0.370}$
$2.02^{+0.056}_{-0.056}$	$4.44^{+0.068}_{-0.068}$	$0.88^{+0.055}_{-0.055}$	$347.8^{+0.61}_{-0.61}$	$4.0^{+0.112}_{-0.321}$	$2.192^{+0.069}_{-0.069}$	$5.048^{+0.323}_{-0.323}$
$2.52^{+0.065}_{-0.065}$	$5.19^{+0.082}_{-0.082}$	$1.11^{+0.068}_{-0.068}$	$348.1^{+0.88}_{-0.88}$	$5.0^{+0.130}_{-0.398}$	$2.060^{+0.063}_{-0.063}$	$4.674^{+0.296}_{-0.296}$
$3.03^{+0.057}_{-0.057}$	$5.93^{+0.066}_{-0.066}$	$1.37^{+0.060}_{-0.060}$	$348.7^{+0.98}_{-0.98}$	$6.0^{+0.114}_{-0.471}$	$1.955^{+0.043}_{-0.043}$	$4.328^{+0.196}_{-0.196}$
$4.05^{+0.105}_{-0.105}$	$7.29^{+0.128}_{-0.128}$	$1.91^{+0.081}_{-0.081}$	$348.6^{+0.62}_{-0.62}$	$8.0^{+0.209}_{-0.645}$	$1.801^{+0.056}_{-0.056}$	$3.819^{+0.175}_{-0.175}$
$5.02^{+0.093}_{-0.093}$	$8.52^{+0.108}_{-0.108}$	$2.49^{+0.089}_{-0.089}$	$348.6^{+0.94}_{-0.94}$	$10.0^{+0.185}_{-0.778}$	$1.698^{+0.038}_{-0.038}$	$3.416^{+0.130}_{-0.130}$
$6.03^{+0.061}_{-0.061}$	$9.74^{+0.075}_{-0.075}$	$3.16^{+0.058}_{-0.058}$	$349.4^{+0.78}_{-0.78}$	$12.0^{+0.122}_{-0.929}$	$1.615^{+0.021}_{-0.021}$	$3.079^{+0.062}_{-0.062}$
$6.99^{+0.064}_{-0.064}$	$10.82^{+0.079}_{-0.079}$	$3.82^{+0.076}_{-0.076}$	$349.5^{+0.91}_{-0.91}$	$13.9^{+0.128}_{-1.074}$	$1.549^{+0.018}_{-0.018}$	$2.830^{+0.060}_{-0.060}$
$7.51^{+0.064}_{-0.064}$	$11.41^{+0.077}_{-0.077}$	$4.22^{+0.064}_{-0.064}$	$350.3^{+0.97}_{-0.97}$	$14.9^{+0.127}_{-1.169}$	$1.520^{+0.017}_{-0.017}$	$2.706^{+0.045}_{-0.045}$
$8.01^{+0.142}_{-0.142}$	$11.97^{+0.142}_{-0.142}$	$4.59^{+0.098}_{-0.098}$	$351.3^{+0.83}_{-0.83}$	$15.9^{+0.283}_{-1.288}$	$1.495^{+0.032}_{-0.032}$	$2.605^{+0.064}_{-0.064}$
$9.02^{+0.070}_{-0.070}$	$13.09^{+0.074}_{-0.074}$	$5.37^{+0.074}_{-0.074}$	$351.7^{+0.81}_{-0.81}$	$17.9^{+0.140}_{-1.432}$	$1.452^{+0.014}_{-0.014}$	$2.438^{+0.036}_{-0.036}$
$10.02^{+0.068}_{-0.068}$	$14.18^{+0.078}_{-0.078}$	$6.17^{+0.071}_{-0.071}$	$352.2^{+0.73}_{-0.73}$	$19.9^{+0.136}_{-1.601}$	$1.415^{+0.012}_{-0.012}$	$2.300^{+0.029}_{-0.029}$
$12.48^{+0.071}_{-0.071}$	$17.05^{+0.088}_{-0.088}$	$8.38^{+0.086}_{-0.086}$	$352.6^{+0.65}_{-0.65}$	$24.8^{+0.140}_{-2.004}$	$1.366^{+0.010}_{-0.010}$	$2.035^{+0.023}_{-0.023}$
$15.28^{+0.083}_{-0.083}$	$20.02^{+0.089}_{-0.089}$	$10.82^{+0.090}_{-0.090}$	$352.9^{+0.68}_{-0.68}$	$30.4^{+0.164}_{-2.462}$	$1.311^{+0.009}_{-0.009}$	$1.850^{+0.018}_{-0.018}$
$17.47^{+0.083}_{-0.083}$	$22.32^{+0.099}_{-0.099}$	$12.82^{+0.090}_{-0.090}$	$353.2^{+0.64}_{-0.64}$	$34.7^{+0.166}_{-2.827}$	$1.278^{+0.008}_{-0.008}$	$1.741^{+0.014}_{-0.014}$
$20.17^{+0.091}_{-0.091}$	$25.13^{+0.097}_{-0.097}$	$15.32^{+0.103}_{-0.103}$	$353.4^{+0.68}_{-0.68}$	$40.1^{+0.180}_{-3.274}$	$1.246^{+0.007}_{-0.007}$	$1.640^{+0.013}_{-0.013}$
$24.96^{+0.098}_{-0.098}$	$30.06^{+0.107}_{-0.107}$	$19.83^{+0.112}_{-0.112}$	$353.6^{+0.61}_{-0.61}$	$49.6^{+0.195}_{-4.061}$	$1.204^{+0.006}_{-0.006}$	$1.516^{+0.010}_{-0.010}$
$30.20^{+0.289}_{-0.289}$	$35.40^{+0.252}_{-0.252}$	$24.86^{+0.199}_{-0.199}$	$353.8^{+0.54}_{-0.54}$	$60.0^{+0.574}_{-4.955}$	$1.172^{+0.014}_{-0.014}$	$1.424^{+0.015}_{-0.015}$
$40.28^{+0.123}_{-0.123}$	$45.61^{+0.152}_{-0.152}$	$34.63^{+0.124}_{-0.124}$	$353.9^{+0.54}_{-0.54}$	$80.1^{+0.244}_{-6.579}$	$1.132^{+0.005}_{-0.005}$	$1.317^{+0.006}_{-0.006}$
$50.14^{+0.135}_{-0.135}$	$55.53^{+0.153}_{-0.153}$	$44.29^{+0.145}_{-0.145}$	$354.0^{+0.58}_{-0.58}$	$99.7^{+0.267}_{-8.197}$	$1.108^{+0.004}_{-0.004}$	$1.254^{+0.005}_{-0.005}$
$60.57^{+0.165}_{-0.165}$	$65.98^{+0.198}_{-0.198}$	$54.59^{+0.146}_{-0.146}$	$354.2^{+0.56}_{-0.56}$	$120.4^{+0.329}_{-9.935}$	$1.089^{+0.004}_{-0.004}$	$1.209^{+0.005}_{-0.005}$
$69.97^{+0.186}_{-0.186}$	$75.37^{+0.218}_{-0.218}$	$63.90^{+0.155}_{-0.155}$	$354.3^{+0.63}_{-0.63}$	$139.1^{+0.370}_{-11.49}$	$1.077^{+0.004}_{-0.004}$	$1.180^{+0.004}_{-0.004}$
$74.82^{+0.178}_{-0.178}$	$80.22^{+0.196}_{-0.196}$	$68.72^{+0.164}_{-0.164}$	$354.4^{+0.57}_{-0.57}$	$148.8^{+0.353}_{-12.31}$	$1.072^{+0.004}_{-0.004}$	$1.167^{+0.004}_{-0.004}$
$80.08^{+0.182}_{-0.182}$	$85.47^{+0.194}_{-0.194}$	$73.94^{+0.167}_{-0.167}$	$354.5^{+0.54}_{-0.54}$	$159.2^{+0.362}_{-13.19}$	$1.067^{+0.003}_{-0.003}$	$1.156^{+0.004}_{-0.004}$
$91.02^{+0.221}_{-0.221}$	$96.40^{+0.237}_{-0.237}$	$84.78^{+0.203}_{-0.203}$	$354.6^{+0.61}_{-0.61}$	$181.0^{+0.438}_{-15.01}$	$1.059^{+0.004}_{-0.004}$	$1.137^{+0.004}_{-0.004}$
$100.3^{+0.217}_{-0.217}$	$105.3^{+0.302}_{-0.302}$	$93.95^{+0.202}_{-0.202}$	$354.8^{+0.59}_{-0.59}$	$199.3^{+0.432}_{-16.59}$	$1.050^{+0.004}_{-0.004}$	$1.121^{+0.004}_{-0.004}$
$125.1^{+0.338}_{-0.338}$	$131.0^{+0.354}_{-0.354}$	$119.0^{+0.319}_{-0.319}$	$354.8^{+0.59}_{-0.59}$	$248.7^{+0.672}_{-20.71}$	$1.048^{+0.004}_{-0.004}$	$1.101^{+0.004}_{-0.004}$
$150.4^{+2.235}_{-2.235}$	$156.6^{+2.211}_{-2.211}$	$144.5^{+2.103}_{-2.103}$	$354.9^{+0.62}_{-0.62}$	$299.1^{+4.444}_{-25.31}$	$1.041^{+0.021}_{-0.021}$	$1.084^{+0.022}_{-0.022}$
$176.2^{+1.180}_{-1.180}$	$182.6^{+1.207}_{-1.207}$	$170.4^{+1.156}_{-1.156}$	$354.7^{+0.58}_{-0.58}$	$350.2^{+2.347}_{-29.17}$	$1.036^{+0.010}_{-0.010}$	$1.072^{+0.010}_{-0.010}$
$201.6^{+1.153}_{-1.153}$	$208.3^{+1.193}_{-1.193}$	$196.0^{+1.144}_{-1.144}$	$354.8^{+0.62}_{-0.62}$	$400.9^{+2.292}_{-33.41}$	$1.033^{+0.008}_{-0.008}$	$1.063^{+0.009}_{-0.009}$
$256.1^{+1.118}_{-1.118}$	$263.1^{+1.156}_{-1.156}$	$250.6^{+1.105}_{-1.105}$	$354.8^{+0.52}_{-0.52}$	$509.1^{+2.223}_{-42.40}$	$1.028^{+0.006}_{-0.006}$	$1.050^{+0.007}_{-0.007}$
$306.0^{+0.858}_{-0.858}$	$313.4^{+0.876}_{-0.876}$	$300.8^{+0.833}_{-0.833}$	$354.9^{+0.56}_{-0.56}$	$608.3^{+1.706}_{-50.66}$	$1.024^{+0.004}_{-0.004}$	$1.042^{+0.004}_{-0.004}$
$505.9^{+1.184}_{-1.184}$	$514.7^{+1.233}_{-1.233}$	$501.5^{+1.165}_{-1.165}$	$354.8^{+0.56}_{-0.56}$	$1006^{+2.354}_{-83.66}$	$1.017^{+0.003}_{-0.003}$	$1.026^{+0.003}_{-0.003}$
$752.3^{+1.596}_{-1.596}$	$762.6^{+1.635}_{-1.635}$	$748.6^{+1.567}_{-1.567}$	$354.5^{+0.74}_{-0.74}$	$1496^{+3.173}_{-123.9}$	$1.014^{+0.003}_{-0.003}$	$1.019^{+0.003}_{-0.003}$
$1016^{+2.318}_{-2.318}$	$1022^{+2.211}_{-2.211}$	$1004^{+2.496}_{-2.496}$	$354.4^{+0.73}_{-0.73}$	$2019^{+4.609}_{-167.0}$	$1.007^{+0.003}_{-0.003}$	$1.018^{+0.003}_{-0.003}$

TAB. D.3 Measurements for $D_o/D_i = 1.7$, $h_{cl,r} = 0.2\,\mathrm{mm}$ and $u_0 = 0.054^{+0.00044}_{-0.0026}$ at $T_{amb} = 296.4\,\mathrm{K}$ shown in Figs. 8.7 and 8.9.

p^*_{ch} [Pa]	p_{HP} [Pa]	p_{LP} [Pa]	T_B [K]	δ^* [−]	p_{HP}/p^*_{ch} [−]	p_{HP}/p_{LP} [−]
$0.50^{+0.056}_{-0.056}$	$1.11^{+0.062}_{-0.062}$	$0.36^{+0.058}_{-0.058}$	$320.3^{+0.59}_{-0.59}$	$1.0^{+0.111}_{-0.117}$	$2.220^{+0.277}_{-0.277}$	$3.093^{+0.530}_{-0.530}$
$0.60^{+0.053}_{-0.053}$	$1.27^{+0.070}_{-0.070}$	$0.41^{+0.055}_{-0.055}$	$320.6^{+0.61}_{-0.61}$	$1.2^{+0.105}_{-0.114}$	$2.115^{+0.220}_{-0.220}$	$3.110^{+0.457}_{-0.457}$
$0.70^{+0.054}_{-0.054}$	$1.41^{+0.064}_{-0.064}$	$0.46^{+0.055}_{-0.055}$	$320.8^{+0.59}_{-0.59}$	$1.4^{+0.108}_{-0.121}$	$2.018^{+0.182}_{-0.182}$	$3.097^{+0.400}_{-0.400}$
$0.75^{+0.053}_{-0.053}$	$1.49^{+0.059}_{-0.059}$	$0.48^{+0.060}_{-0.060}$	$321.0^{+0.61}_{-0.61}$	$1.5^{+0.105}_{-0.120}$	$1.979^{+0.160}_{-0.160}$	$3.094^{+0.406}_{-0.406}$
$0.79^{+0.061}_{-0.061}$	$1.55^{+0.068}_{-0.068}$	$0.50^{+0.061}_{-0.061}$	$321.2^{+0.60}_{-0.60}$	$1.6^{+0.122}_{-0.137}$	$1.946^{+0.173}_{-0.173}$	$3.095^{+0.402}_{-0.402}$
$0.91^{+0.055}_{-0.055}$	$1.73^{+0.062}_{-0.062}$	$0.56^{+0.056}_{-0.056}$	$321.6^{+0.56}_{-0.56}$	$1.8^{+0.110}_{-0.131}$	$1.897^{+0.133}_{-0.133}$	$3.078^{+0.327}_{-0.327}$
$1.02^{+0.053}_{-0.053}$	$1.89^{+0.060}_{-0.060}$	$0.62^{+0.065}_{-0.065}$	$321.8^{+0.59}_{-0.59}$	$2.0^{+0.105}_{-0.133}$	$1.851^{+0.113}_{-0.113}$	$3.034^{+0.333}_{-0.333}$
$1.11^{+0.054}_{-0.054}$	$2.02^{+0.062}_{-0.062}$	$0.67^{+0.057}_{-0.057}$	$322.1^{+0.61}_{-0.61}$	$2.2^{+0.107}_{-0.139}$	$1.818^{+0.104}_{-0.104}$	$3.005^{+0.271}_{-0.271}$
$1.24^{+0.068}_{-0.068}$	$2.21^{+0.088}_{-0.088}$	$0.75^{+0.076}_{-0.076}$	$322.3^{+0.52}_{-0.52}$	$2.5^{+0.136}_{-0.169}$	$1.787^{+0.122}_{-0.122}$	$2.938^{+0.318}_{-0.318}$
$1.49^{+0.056}_{-0.056}$	$2.57^{+0.062}_{-0.062}$	$0.89^{+0.059}_{-0.059}$	$322.4^{+0.54}_{-0.54}$	$3.0^{+0.112}_{-0.165}$	$1.722^{+0.077}_{-0.077}$	$2.872^{+0.201}_{-0.201}$
$1.76^{+0.055}_{-0.055}$	$2.94^{+0.067}_{-0.067}$	$1.06^{+0.057}_{-0.057}$	$322.6^{+0.58}_{-0.58}$	$3.5^{+0.109}_{-0.181}$	$1.668^{+0.064}_{-0.064}$	$2.777^{+0.162}_{-0.162}$
$2.00^{+0.054}_{-0.054}$	$3.26^{+0.061}_{-0.061}$	$1.22^{+0.068}_{-0.068}$	$322.7^{+0.55}_{-0.55}$	$4.0^{+0.108}_{-0.197}$	$1.630^{+0.054}_{-0.054}$	$2.685^{+0.158}_{-0.158}$
$2.49^{+0.057}_{-0.057}$	$3.89^{+0.061}_{-0.061}$	$1.53^{+0.062}_{-0.062}$	$322.8^{+0.60}_{-0.60}$	$4.9^{+0.114}_{-0.235}$	$1.563^{+0.043}_{-0.043}$	$2.550^{+0.111}_{-0.111}$
$2.99^{+0.056}_{-0.056}$	$4.51^{+0.061}_{-0.061}$	$1.87^{+0.069}_{-0.069}$	$323.0^{+0.58}_{-0.58}$	$5.9^{+0.112}_{-0.273}$	$1.511^{+0.035}_{-0.035}$	$2.411^{+0.095}_{-0.095}$
$3.97^{+0.059}_{-0.059}$	$5.69^{+0.064}_{-0.064}$	$2.58^{+0.062}_{-0.062}$	$323.3^{+0.55}_{-0.55}$	$7.9^{+0.117}_{-0.354}$	$1.434^{+0.027}_{-0.027}$	$2.208^{+0.059}_{-0.059}$
$4.99^{+0.061}_{-0.061}$	$6.87^{+0.066}_{-0.066}$	$3.36^{+0.060}_{-0.060}$	$323.5^{+0.63}_{-0.63}$	$9.9^{+0.121}_{-0.439}$	$1.375^{+0.021}_{-0.021}$	$2.047^{+0.042}_{-0.042}$
$6.00^{+0.062}_{-0.062}$	$8.00^{+0.070}_{-0.070}$	$4.16^{+0.075}_{-0.075}$	$323.6^{+0.55}_{-0.55}$	$11.9^{+0.123}_{-0.525}$	$1.332^{+0.018}_{-0.018}$	$1.921^{+0.038}_{-0.038}$
$7.02^{+0.063}_{-0.063}$	$9.10^{+0.070}_{-0.070}$	$5.00^{+0.064}_{-0.064}$	$323.8^{+0.59}_{-0.59}$	$13.9^{+0.124}_{-0.613}$	$1.297^{+0.015}_{-0.015}$	$1.821^{+0.027}_{-0.027}$
$7.48^{+0.063}_{-0.063}$	$9.60^{+0.070}_{-0.070}$	$5.39^{+0.063}_{-0.063}$	$323.9^{+0.56}_{-0.56}$	$14.9^{+0.125}_{-0.654}$	$1.284^{+0.014}_{-0.014}$	$1.781^{+0.025}_{-0.025}$
$8.05^{+0.065}_{-0.065}$	$10.11^{+0.071}_{-0.071}$	$5.88^{+0.063}_{-0.063}$	$324.0^{+0.57}_{-0.57}$	$16.0^{+0.130}_{-0.705}$	$1.257^{+0.014}_{-0.014}$	$1.721^{+0.022}_{-0.022}$
$8.98^{+0.068}_{-0.068}$	$11.10^{+0.076}_{-0.076}$	$6.69^{+0.067}_{-0.067}$	$324.2^{+0.61}_{-0.61}$	$17.9^{+0.134}_{-0.791}$	$1.236^{+0.013}_{-0.013}$	$1.660^{+0.020}_{-0.020}$
$9.98^{+0.067}_{-0.067}$	$12.14^{+0.078}_{-0.078}$	$7.57^{+0.065}_{-0.065}$	$324.5^{+0.62}_{-0.62}$	$19.8^{+0.132}_{-0.883}$	$1.217^{+0.011}_{-0.011}$	$1.604^{+0.017}_{-0.017}$
$12.52^{+0.080}_{-0.080}$	$14.87^{+0.081}_{-0.081}$	$9.96^{+0.067}_{-0.067}$	$324.7^{+0.59}_{-0.59}$	$24.9^{+0.159}_{-1.114}$	$1.188^{+0.010}_{-0.010}$	$1.493^{+0.013}_{-0.013}$
$14.98^{+0.081}_{-0.081}$	$17.43^{+0.087}_{-0.087}$	$12.23^{+0.080}_{-0.080}$	$324.9^{+0.62}_{-0.62}$	$29.8^{+0.162}_{-1.337}$	$1.163^{+0.009}_{-0.009}$	$1.425^{+0.012}_{-0.012}$
$17.46^{+0.086}_{-0.086}$	$19.97^{+0.091}_{-0.091}$	$14.59^{+0.083}_{-0.083}$	$325.1^{+0.60}_{-0.60}$	$34.7^{+0.171}_{-1.567}$	$1.143^{+0.008}_{-0.008}$	$1.369^{+0.010}_{-0.010}$
$20.22^{+0.087}_{-0.087}$	$22.77^{+0.088}_{-0.088}$	$17.23^{+0.086}_{-0.086}$	$325.2^{+0.57}_{-0.57}$	$40.2^{+0.173}_{-1.817}$	$1.127^{+0.007}_{-0.007}$	$1.322^{+0.008}_{-0.008}$
$25.00^{+0.097}_{-0.097}$	$27.62^{+0.106}_{-0.106}$	$21.87^{+0.100}_{-0.100}$	$325.3^{+0.57}_{-0.57}$	$49.7^{+0.194}_{-2.255}$	$1.105^{+0.006}_{-0.006}$	$1.263^{+0.008}_{-0.008}$
$30.27^{+0.104}_{-0.104}$	$32.92^{+0.107}_{-0.107}$	$27.01^{+0.098}_{-0.098}$	$325.5^{+0.55}_{-0.55}$	$60.1^{+0.207}_{-2.743}$	$1.088^{+0.005}_{-0.005}$	$1.219^{+0.006}_{-0.006}$
$40.38^{+0.121}_{-0.121}$	$43.06^{+0.125}_{-0.125}$	$36.95^{+0.112}_{-0.112}$	$325.7^{+0.61}_{-0.61}$	$80.2^{+0.241}_{-3.683}$	$1.066^{+0.004}_{-0.004}$	$1.166^{+0.005}_{-0.005}$
$50.18^{+0.138}_{-0.138}$	$52.86^{+0.142}_{-0.142}$	$46.61^{+0.129}_{-0.129}$	$325.9^{+0.54}_{-0.54}$	$99.7^{+0.275}_{-4.590}$	$1.053^{+0.004}_{-0.004}$	$1.134^{+0.004}_{-0.004}$
$59.85^{+0.164}_{-0.164}$	$62.51^{+0.168}_{-0.168}$	$56.18^{+0.159}_{-0.159}$	$326.1^{+0.58}_{-0.58}$	$118.9^{+0.325}_{-5.505}$	$1.044^{+0.004}_{-0.004}$	$1.113^{+0.004}_{-0.004}$
$69.92^{+0.168}_{-0.168}$	$72.55^{+0.171}_{-0.171}$	$66.16^{+0.160}_{-0.160}$	$326.2^{+0.61}_{-0.61}$	$138.9^{+0.334}_{-6.454}$	$1.038^{+0.003}_{-0.003}$	$1.097^{+0.004}_{-0.004}$
$74.83^{+0.185}_{-0.185}$	$77.45^{+0.187}_{-0.187}$	$71.04^{+0.176}_{-0.176}$	$326.3^{+0.58}_{-0.58}$	$148.7^{+0.368}_{-6.936}$	$1.035^{+0.004}_{-0.004}$	$1.090^{+0.004}_{-0.004}$
$80.10^{+0.190}_{-0.190}$	$82.70^{+0.193}_{-0.193}$	$76.27^{+0.179}_{-0.179}$	$326.4^{+0.55}_{-0.55}$	$159.2^{+0.377}_{-7.433}$	$1.032^{+0.003}_{-0.003}$	$1.084^{+0.004}_{-0.004}$
$89.87^{+0.221}_{-0.221}$	$92.43^{+0.226}_{-0.226}$	$85.96^{+0.214}_{-0.214}$	$326.5^{+0.57}_{-0.57}$	$178.6^{+0.439}_{-8.369}$	$1.028^{+0.004}_{-0.004}$	$1.075^{+0.004}_{-0.004}$
$100.1^{+0.216}_{-0.216}$	$102.4^{+0.225}_{-0.225}$	$96.15^{+0.213}_{-0.213}$	$326.5^{+0.55}_{-0.55}$	$199.0^{+0.430}_{-9.340}$	$1.022^{+0.003}_{-0.003}$	$1.064^{+0.003}_{-0.003}$
$124.9^{+0.331}_{-0.331}$	$128.2^{+0.325}_{-0.325}$	$121.6^{+0.324}_{-0.324}$	$326.7^{+0.54}_{-0.54}$	$248.2^{+0.658}_{-11.705}$	$1.026^{+0.004}_{-0.004}$	$1.054^{+0.004}_{-0.004}$
$150.2^{+0.505}_{-0.505}$	$153.6^{+0.543}_{-0.543}$	$147.0^{+0.542}_{-0.542}$	$326.8^{+0.55}_{-0.55}$	$298.5^{+1.004}_{-14.147}$	$1.023^{+0.005}_{-0.005}$	$1.045^{+0.005}_{-0.005}$
$200.2^{+0.924}_{-0.924}$	$204.1^{+0.948}_{-0.948}$	$197.2^{+0.910}_{-0.910}$	$327.2^{+0.57}_{-0.57}$	$397.8^{+1.837}_{-19.081}$	$1.019^{+0.007}_{-0.007}$	$1.035^{+0.007}_{-0.007}$

TAB. D.4 Measurements for $D_o/D_i = 1.7$, $h_{cl,r} = 0.3\,\mathrm{mm}$ and $u_0 = 0.129^{+0.0003}_{-0.012}$ at $T_{amb} = 293.3\,\mathrm{K}$ shown in Figs. 8.12 and 8.13.

p^*_{ch} [Pa]	p_{HP} [Pa]	p_{LP} [Pa]	T_B [K]	δ^* [−]	p_{HP}/p^*_{ch} [−]	p_{HP}/p_{LP} [−]
$0.57^{+0.067}_{-0.067}$	$2.40^{+0.120}_{-0.120}$	$0.30^{+0.088}_{-0.088}$	$334.8^{+1.99}_{-1.99}$	$1.1^{+0.136}_{-0.153}$	$4.247^{+0.549}_{-0.549}$	$8.124^{+2.456}_{-2.456}$
$0.71^{+0.052}_{-0.052}$	$2.71^{+0.072}_{-0.072}$	$0.35^{+0.078}_{-0.078}$	$337.1^{+1.71}_{-1.71}$	$1.4^{+0.105}_{-0.141}$	$3.802^{+0.296}_{-0.296}$	$7.849^{+1.778}_{-1.778}$
$0.81^{+0.056}_{-0.056}$	$2.97^{+0.076}_{-0.076}$	$0.38^{+0.079}_{-0.079}$	$339.1^{+1.79}_{-1.79}$	$1.6^{+0.114}_{-0.159}$	$3.669^{+0.272}_{-0.272}$	$7.799^{+1.636}_{-1.636}$
$0.91^{+0.059}_{-0.059}$	$3.23^{+0.096}_{-0.096}$	$0.43^{+0.098}_{-0.098}$	$340.9^{+1.53}_{-1.53}$	$1.8^{+0.119}_{-0.176}$	$3.532^{+0.252}_{-0.252}$	$7.596^{+1.766}_{-1.766}$
$1.02^{+0.055}_{-0.055}$	$3.47^{+0.070}_{-0.070}$	$0.47^{+0.084}_{-0.084}$	$342.4^{+1.27}_{-1.27}$	$2.1^{+0.111}_{-0.185}$	$3.403^{+0.196}_{-0.196}$	$7.449^{+1.351}_{-1.351}$
$1.31^{+0.053}_{-0.053}$	$4.07^{+0.068}_{-0.068}$	$0.56^{+0.080}_{-0.080}$	$343.5^{+1.23}_{-1.23}$	$2.6^{+0.108}_{-0.223}$	$3.105^{+0.137}_{-0.137}$	$7.208^{+1.032}_{-1.032}$
$1.67^{+0.055}_{-0.055}$	$4.75^{+0.073}_{-0.073}$	$0.69^{+0.100}_{-0.100}$	$344.5^{+1.10}_{-1.10}$	$3.4^{+0.111}_{-0.275}$	$2.847^{+0.104}_{-0.104}$	$6.900^{+1.007}_{-1.007}$
$2.04^{+0.057}_{-0.057}$	$5.40^{+0.072}_{-0.072}$	$0.81^{+0.097}_{-0.097}$	$345.5^{+1.04}_{-1.04}$	$4.1^{+0.115}_{-0.334}$	$2.646^{+0.082}_{-0.082}$	$6.635^{+0.795}_{-0.795}$
$2.49^{+0.060}_{-0.060}$	$6.12^{+0.073}_{-0.073}$	$0.97^{+0.108}_{-0.108}$	$346.3^{+1.18}_{-1.18}$	$5.0^{+0.121}_{-0.405}$	$2.462^{+0.066}_{-0.066}$	$6.289^{+0.705}_{-0.705}$
$3.04^{+0.057}_{-0.057}$	$6.96^{+0.070}_{-0.070}$	$1.22^{+0.104}_{-0.104}$	$347.4^{+0.75}_{-0.75}$	$6.1^{+0.116}_{-0.495}$	$2.288^{+0.049}_{-0.049}$	$5.707^{+0.490}_{-0.490}$
$4.02^{+0.058}_{-0.058}$	$8.32^{+0.072}_{-0.072}$	$1.65^{+0.111}_{-0.111}$	$348.1^{+0.96}_{-0.96}$	$8.1^{+0.118}_{-0.653}$	$2.073^{+0.035}_{-0.035}$	$5.032^{+0.341}_{-0.341}$
$5.04^{+0.060}_{-0.060}$	$9.65^{+0.082}_{-0.082}$	$2.15^{+0.082}_{-0.082}$	$348.9^{+0.98}_{-0.98}$	$10.1^{+0.121}_{-0.824}$	$1.916^{+0.028}_{-0.028}$	$4.495^{+0.177}_{-0.177}$
$7.52^{+0.065}_{-0.065}$	$12.58^{+0.106}_{-0.106}$	$3.63^{+0.098}_{-0.098}$	$349.7^{+1.03}_{-1.03}$	$15.1^{+0.132}_{-1.238}$	$1.673^{+0.020}_{-0.020}$	$3.465^{+0.098}_{-0.098}$
$9.95^{+0.068}_{-0.068}$	$15.26^{+0.122}_{-0.122}$	$5.40^{+0.146}_{-0.146}$	$350.7^{+1.14}_{-1.14}$	$20.0^{+0.137}_{-1.660}$	$1.533^{+0.016}_{-0.016}$	$2.827^{+0.080}_{-0.080}$
$12.49^{+0.077}_{-0.077}$	$18.03^{+0.129}_{-0.129}$	$7.44^{+0.114}_{-0.114}$	$351.5^{+0.65}_{-0.65}$	$25.2^{+0.156}_{-2.105}$	$1.443^{+0.014}_{-0.014}$	$2.423^{+0.041}_{-0.041}$
$15.11^{+0.080}_{-0.080}$	$20.78^{+0.140}_{-0.140}$	$9.67^{+0.128}_{-0.128}$	$351.9^{+0.69}_{-0.69}$	$30.4^{+0.161}_{-2.558}$	$1.376^{+0.012}_{-0.012}$	$2.149^{+0.032}_{-0.032}$
$17.74^{+0.083}_{-0.083}$	$23.53^{+0.113}_{-0.113}$	$11.94^{+0.088}_{-0.088}$	$352.0^{+0.64}_{-0.64}$	$35.7^{+0.166}_{-3.008}$	$1.326^{+0.009}_{-0.009}$	$1.971^{+0.017}_{-0.017}$
$19.89^{+0.088}_{-0.088}$	$25.75^{+0.127}_{-0.127}$	$13.89^{+0.111}_{-0.111}$	$352.1^{+0.57}_{-0.57}$	$40.0^{+0.177}_{-3.377}$	$1.295^{+0.009}_{-0.009}$	$1.854^{+0.017}_{-0.017}$
$25.23^{+0.100}_{-0.100}$	$31.28^{+0.137}_{-0.137}$	$18.80^{+0.146}_{-0.146}$	$352.3^{+0.71}_{-0.71}$	$50.8^{+0.201}_{-4.292}$	$1.240^{+0.007}_{-0.007}$	$1.664^{+0.015}_{-0.015}$
$29.86^{+0.105}_{-0.105}$	$36.02^{+0.134}_{-0.134}$	$23.16^{+0.108}_{-0.108}$	$352.0^{+0.77}_{-0.77}$	$60.1^{+0.211}_{-5.059}$	$1.206^{+0.006}_{-0.006}$	$1.555^{+0.009}_{-0.009}$
$39.97^{+0.131}_{-0.131}$	$46.31^{+0.194}_{-0.194}$	$32.80^{+0.145}_{-0.145}$	$351.7^{+0.67}_{-0.67}$	$80.5^{+0.264}_{-6.741}$	$1.159^{+0.006}_{-0.006}$	$1.412^{+0.009}_{-0.009}$
$50.61^{+0.140}_{-0.140}$	$57.04^{+0.190}_{-0.190}$	$43.12^{+0.156}_{-0.156}$	$351.4^{+0.71}_{-0.71}$	$101.9^{+0.282}_{-8.501}$	$1.127^{+0.005}_{-0.005}$	$1.323^{+0.007}_{-0.007}$
$74.60^{+0.214}_{-0.214}$	$81.13^{+0.286}_{-0.286}$	$66.58^{+0.181}_{-0.181}$	$351.2^{+0.62}_{-0.62}$	$150.2^{+0.430}_{-12.500}$	$1.088^{+0.005}_{-0.005}$	$1.218^{+0.005}_{-0.005}$
$99.72^{+0.261}_{-0.261}$	$105.8^{+0.375}_{-0.375}$	$91.36^{+0.212}_{-0.212}$	$351.5^{+0.64}_{-0.64}$	$200.8^{+0.525}_{-16.778}$	$1.061^{+0.005}_{-0.005}$	$1.158^{+0.005}_{-0.005}$
$126.1^{+0.342}_{-0.342}$	$134.7^{+0.405}_{-0.405}$	$119.5^{+0.308}_{-0.308}$	$351.6^{+0.54}_{-0.54}$	$253.9^{+0.689}_{-21.232}$	$1.068^{+0.004}_{-0.004}$	$1.126^{+0.004}_{-0.004}$
$150.0^{+0.916}_{-0.916}$	$158.9^{+1.002}_{-1.002}$	$143.6^{+0.838}_{-0.838}$	$351.9^{+0.77}_{-0.77}$	$302.1^{+1.845}_{-25.417}$	$1.059^{+0.009}_{-0.009}$	$1.106^{+0.010}_{-0.010}$
$175.9^{+1.737}_{-1.737}$	$185.0^{+1.834}_{-1.834}$	$169.7^{+1.680}_{-1.680}$	$352.4^{+0.71}_{-0.71}$	$354.2^{+3.497}_{-30.144}$	$1.052^{+0.015}_{-0.015}$	$1.091^{+0.015}_{-0.015}$
$202.5^{+1.513}_{-1.513}$	$211.9^{+1.597}_{-1.597}$	$196.4^{+1.422}_{-1.422}$	$352.8^{+0.87}_{-0.87}$	$407.7^{+3.047}_{-34.807}$	$1.046^{+0.011}_{-0.011}$	$1.079^{+0.011}_{-0.011}$
$251.5^{+1.243}_{-1.243}$	$261.4^{+1.344}_{-1.344}$	$245.7^{+1.133}_{-1.133}$	$353.5^{+0.82}_{-0.82}$	$506.5^{+2.503}_{-43.524}$	$1.039^{+0.007}_{-0.007}$	$1.064^{+0.007}_{-0.007}$
$300.7^{+1.099}_{-1.099}$	$311.2^{+1.189}_{-1.189}$	$295.1^{+0.985}_{-0.985}$	$353.9^{+0.83}_{-0.83}$	$605.6^{+2.213}_{-52.309}$	$1.035^{+0.005}_{-0.005}$	$1.054^{+0.005}_{-0.005}$
$399.6^{+1.177}_{-1.177}$	$411.0^{+1.282}_{-1.282}$	$394.4^{+1.062}_{-1.062}$	$354.2^{+0.57}_{-0.57}$	$804.7^{+2.369}_{-69.804}$	$1.029^{+0.004}_{-0.004}$	$1.042^{+0.004}_{-0.004}$
$506.7^{+1.282}_{-1.282}$	$519.2^{+1.346}_{-1.346}$	$502.0^{+1.188}_{-1.188}$	$354.1^{+0.67}_{-0.67}$	$1020^{+2.581}_{-88.307}$	$1.025^{+0.004}_{-0.004}$	$1.034^{+0.004}_{-0.004}$
$757.8^{+1.786}_{-1.786}$	$772.7^{+1.900}_{-1.900}$	$754.0^{+1.696}_{-1.696}$	$353.8^{+0.76}_{-0.76}$	$1526^{+3.597}_{-131.51}$	$1.020^{+0.003}_{-0.003}$	$1.025^{+0.003}_{-0.003}$
$1009^{+2.659}_{-2.659}$	$1018^{+2.448}_{-2.448}$	$1002^{+2.229}_{-2.229}$	$353.4^{+0.71}_{-0.71}$	$2031^{+5.355}_{-174.11}$	$1.009^{+0.004}_{-0.004}$	$1.015^{+0.003}_{-0.003}$

TAB. D.5 Measurements for $D_o/D_i = 1.7$, $h_{cl,r} = 0.3\,\mathrm{mm}$ and $u_0 = 0.054^{+0.007}_{-0.007}$ at $T_{amb} = 294.4\,\mathrm{K}$ shown in Figs. 8.12 and 8.13.

p^*_{ch} [Pa]	p_{HP} [Pa]	p_{LP} [Pa]	T_B [K]	δ^* [−]	p_{HP}/p^*_{ch} [−]	p_{HP}/p_{LP} [−]
$0.49^{+0.054}_{-0.054}$	$1.02^{+0.071}_{-0.071}$	$0.35^{+0.056}_{-0.056}$	$317.3^{+0.60}_{-0.60}$	$1.0^{+0.108}_{-0.114}$	$2.087^{+0.273}_{-0.273}$	$2.958^{+0.526}_{-0.526}$
$0.62^{+0.059}_{-0.059}$	$1.20^{+0.069}_{-0.069}$	$0.41^{+0.055}_{-0.055}$	$317.4^{+0.63}_{-0.63}$	$1.2^{+0.119}_{-0.127}$	$1.948^{+0.219}_{-0.219}$	$2.955^{+0.435}_{-0.435}$
$0.71^{+0.053}_{-0.053}$	$1.35^{+0.063}_{-0.063}$	$0.46^{+0.054}_{-0.054}$	$317.6^{+0.58}_{-0.58}$	$1.4^{+0.107}_{-0.119}$	$1.896^{+0.167}_{-0.167}$	$2.940^{+0.371}_{-0.371}$
$0.87^{+0.231}_{-0.231}$	$1.59^{+0.313}_{-0.313}$	$0.55^{+0.148}_{-0.148}$	$317.8^{+0.54}_{-0.54}$	$1.7^{+0.462}_{-0.467}$	$1.826^{+0.602}_{-0.602}$	$2.913^{+0.974}_{-0.974}$
$0.94^{+0.055}_{-0.055}$	$1.70^{+0.068}_{-0.068}$	$0.59^{+0.054}_{-0.054}$	$318.0^{+0.62}_{-0.62}$	$1.9^{+0.111}_{-0.132}$	$1.805^{+0.129}_{-0.129}$	$2.889^{+0.290}_{-0.290}$
$1.00^{+0.054}_{-0.054}$	$1.80^{+0.063}_{-0.063}$	$0.62^{+0.062}_{-0.062}$	$318.2^{+0.59}_{-0.59}$	$2.0^{+0.109}_{-0.133}$	$1.787^{+0.115}_{-0.115}$	$2.873^{+0.301}_{-0.301}$
$1.27^{+0.057}_{-0.057}$	$2.18^{+0.075}_{-0.075}$	$0.78^{+0.061}_{-0.061}$	$318.7^{+0.57}_{-0.57}$	$2.5^{+0.115}_{-0.151}$	$1.723^{+0.098}_{-0.098}$	$2.795^{+0.237}_{-0.237}$
$1.51^{+0.057}_{-0.057}$	$2.51^{+0.066}_{-0.066}$	$0.92^{+0.067}_{-0.067}$	$318.9^{+0.58}_{-0.58}$	$3.0^{+0.114}_{-0.164}$	$1.669^{+0.077}_{-0.077}$	$2.727^{+0.211}_{-0.211}$
$1.79^{+0.054}_{-0.054}$	$2.90^{+0.067}_{-0.067}$	$1.10^{+0.063}_{-0.063}$	$319.2^{+0.64}_{-0.64}$	$3.6^{+0.107}_{-0.178}$	$1.620^{+0.061}_{-0.061}$	$2.643^{+0.163}_{-0.163}$
$2.03^{+0.054}_{-0.054}$	$3.22^{+0.070}_{-0.070}$	$1.25^{+0.058}_{-0.058}$	$319.3^{+0.59}_{-0.59}$	$4.1^{+0.109}_{-0.195}$	$1.587^{+0.055}_{-0.055}$	$2.582^{+0.133}_{-0.133}$
$2.27^{+0.057}_{-0.057}$	$3.53^{+0.074}_{-0.074}$	$1.40^{+0.060}_{-0.060}$	$319.5^{+0.53}_{-0.53}$	$4.5^{+0.115}_{-0.215}$	$1.557^{+0.051}_{-0.051}$	$2.518^{+0.120}_{-0.120}$
$3.02^{+0.056}_{-0.056}$	$4.48^{+0.071}_{-0.071}$	$1.92^{+0.060}_{-0.060}$	$319.7^{+0.61}_{-0.61}$	$6.1^{+0.112}_{-0.269}$	$1.481^{+0.036}_{-0.036}$	$2.338^{+0.082}_{-0.082}$
$4.01^{+0.057}_{-0.057}$	$5.66^{+0.079}_{-0.079}$	$2.63^{+0.066}_{-0.066}$	$320.1^{+0.58}_{-0.58}$	$8.0^{+0.115}_{-0.349}$	$1.411^{+0.028}_{-0.028}$	$2.151^{+0.062}_{-0.062}$
$5.02^{+0.062}_{-0.062}$	$6.81^{+0.084}_{-0.084}$	$3.40^{+0.074}_{-0.074}$	$320.3^{+0.55}_{-0.55}$	$10.1^{+0.123}_{-0.431}$	$1.358^{+0.024}_{-0.024}$	$2.004^{+0.050}_{-0.050}$
$7.50^{+0.063}_{-0.063}$	$9.54^{+0.092}_{-0.092}$	$5.44^{+0.076}_{-0.076}$	$320.5^{+0.54}_{-0.54}$	$15.0^{+0.127}_{-0.636}$	$1.271^{+0.016}_{-0.016}$	$1.753^{+0.030}_{-0.030}$
$10.03^{+0.074}_{-0.074}$	$12.15^{+0.096}_{-0.096}$	$7.63^{+0.083}_{-0.083}$	$320.6^{+0.54}_{-0.54}$	$20.1^{+0.149}_{-0.851}$	$1.211^{+0.013}_{-0.013}$	$1.593^{+0.021}_{-0.021}$
$12.49^{+0.077}_{-0.077}$	$14.72^{+0.098}_{-0.098}$	$9.89^{+0.089}_{-0.089}$	$320.8^{+0.55}_{-0.55}$	$25.0^{+0.154}_{-1.061}$	$1.179^{+0.011}_{-0.011}$	$1.488^{+0.017}_{-0.017}$
$14.91^{+0.092}_{-0.092}$	$17.22^{+0.112}_{-0.112}$	$12.07^{+0.097}_{-0.097}$	$321.2^{+0.62}_{-0.62}$	$29.9^{+0.185}_{-1.281}$	$1.155^{+0.010}_{-0.010}$	$1.426^{+0.015}_{-0.015}$
$17.59^{+0.086}_{-0.086}$	$19.96^{+0.110}_{-0.110}$	$14.61^{+0.100}_{-0.100}$	$321.3^{+0.58}_{-0.58}$	$35.2^{+0.173}_{-1.510}$	$1.135^{+0.008}_{-0.008}$	$1.366^{+0.012}_{-0.012}$
$19.99^{+0.102}_{-0.102}$	$22.41^{+0.120}_{-0.120}$	$16.92^{+0.112}_{-0.112}$	$321.7^{+0.56}_{-0.56}$	$40.1^{+0.204}_{-1.739}$	$1.121^{+0.008}_{-0.008}$	$1.324^{+0.011}_{-0.011}$
$25.11^{+0.095}_{-0.095}$	$27.58^{+0.124}_{-0.124}$	$21.88^{+0.115}_{-0.115}$	$321.8^{+0.60}_{-0.60}$	$50.3^{+0.191}_{-2.188}$	$1.099^{+0.006}_{-0.006}$	$1.261^{+0.009}_{-0.009}$
$30.04^{+0.104}_{-0.104}$	$32.54^{+0.134}_{-0.134}$	$26.69^{+0.123}_{-0.123}$	$322.1^{+0.62}_{-0.62}$	$60.2^{+0.209}_{-2.639}$	$1.083^{+0.006}_{-0.006}$	$1.220^{+0.008}_{-0.008}$
$40.02^{+0.123}_{-0.123}$	$42.54^{+0.152}_{-0.152}$	$36.48^{+0.144}_{-0.144}$	$322.3^{+0.64}_{-0.64}$	$80.2^{+0.247}_{-3.539}$	$1.063^{+0.005}_{-0.005}$	$1.166^{+0.006}_{-0.006}$
$49.98^{+0.153}_{-0.153}$	$52.49^{+0.170}_{-0.170}$	$46.29^{+0.162}_{-0.162}$	$322.5^{+0.69}_{-0.69}$	$100.2^{+0.306}_{-4.454}$	$1.050^{+0.005}_{-0.005}$	$1.134^{+0.005}_{-0.005}$
$74.89^{+0.310}_{-0.310}$	$77.32^{+0.317}_{-0.317}$	$70.94^{+0.303}_{-0.303}$	$323.1^{+0.68}_{-0.68}$	$150.1^{+0.620}_{-6.806}$	$1.032^{+0.006}_{-0.006}$	$1.090^{+0.006}_{-0.006}$
$99.44^{+0.237}_{-0.237}$	$101.4^{+0.274}_{-0.274}$	$95.28^{+0.243}_{-0.243}$	$323.9^{+0.54}_{-0.54}$	$199.3^{+0.474}_{-9.239}$	$1.020^{+0.004}_{-0.004}$	$1.065^{+0.004}_{-0.004}$
$124.9^{+0.342}_{-0.342}$	$128.0^{+0.295}_{-0.295}$	$121.7^{+0.313}_{-0.313}$	$324.1^{+0.65}_{-0.65}$	$250.2^{+0.685}_{-11.668}$	$1.025^{+0.004}_{-0.004}$	$1.052^{+0.004}_{-0.004}$
$150.0^{+0.338}_{-0.338}$	$153.3^{+0.398}_{-0.398}$	$147.0^{+0.362}_{-0.362}$	$324.6^{+0.57}_{-0.57}$	$300.6^{+0.678}_{-14.229}$	$1.022^{+0.004}_{-0.004}$	$1.043^{+0.004}_{-0.004}$
$174.9^{+0.443}_{-0.443}$	$178.4^{+0.429}_{-0.429}$	$172.1^{+0.441}_{-0.441}$	$325.0^{+0.53}_{-0.53}$	$350.4^{+0.889}_{-16.758}$	$1.020^{+0.004}_{-0.004}$	$1.037^{+0.004}_{-0.004}$
$200.0^{+0.453}_{-0.453}$	$203.8^{+0.475}_{-0.475}$	$197.3^{+0.451}_{-0.451}$	$325.1^{+0.55}_{-0.55}$	$400.9^{+0.908}_{-19.229}$	$1.019^{+0.003}_{-0.003}$	$1.033^{+0.003}_{-0.003}$
$249.8^{+0.606}_{-0.606}$	$253.9^{+0.600}_{-0.600}$	$247.3^{+0.598}_{-0.598}$	$325.3^{+0.54}_{-0.54}$	$500.6^{+1.215}_{-24.146}$	$1.017^{+0.003}_{-0.003}$	$1.027^{+0.003}_{-0.003}$
$299.3^{+0.688}_{-0.688}$	$303.8^{+0.733}_{-0.733}$	$297.1^{+0.722}_{-0.722}$	$325.3^{+0.50}_{-0.50}$	$599.8^{+1.379}_{-28.985}$	$1.015^{+0.003}_{-0.003}$	$1.023^{+0.004}_{-0.004}$
$399.5^{+0.874}_{-0.874}$	$404.8^{+0.841}_{-0.841}$	$397.8^{+0.860}_{-0.860}$	$325.4^{+0.57}_{-0.57}$	$800.7^{+1.752}_{-38.790}$	$1.013^{+0.003}_{-0.003}$	$1.018^{+0.003}_{-0.003}$
$500.1^{+0.902}_{-0.902}$	$506.0^{+0.989}_{-0.989}$	$498.7^{+0.906}_{-0.906}$	$325.6^{+0.55}_{-0.55}$	$1002^{+1.809}_{-48.733}$	$1.012^{+0.003}_{-0.003}$	$1.015^{+0.003}_{-0.003}$
$750.0^{+1.507}_{-1.507}$	$757.1^{+1.525}_{-1.525}$	$749.4^{+1.512}_{-1.512}$	$325.7^{+0.53}_{-0.53}$	$1503^{+3.020}_{-73.457}$	$1.010^{+0.003}_{-0.003}$	$1.010^{+0.003}_{-0.003}$
$1003^{+2.558}_{-2.558}$	$1005^{+2.301}_{-2.301}$	$999.3^{+2.082}_{-2.082}$	$325.8^{+0.59}_{-0.59}$	$2010^{+5.127}_{-98.473}$	$1.001^{+0.003}_{-0.003}$	$1.005^{+0.003}_{-0.003}$

TAB. D.6 Measurements for $D_o/D_i = 1.7$, $h_{cl,r} = 0.4\,\mathrm{mm}$ and $u_0 = 0.128^{+0.0003}_{-0.011}$ at $T_{amb} = 302.2\,\mathrm{K}$ shown in Figs. 8.12 and 8.13.

p^*_{ch} [Pa]	p_{HP} [Pa]	p_{LP} [Pa]	T_B [K]	δ^* [−]	p_{HP}/p^*_{ch} [−]	p_{HP}/p_{LP} [−]
$0.81^{+0.054}_{-0.054}$	$3.24^{+0.072}_{-0.072}$	$0.45^{+0.123}_{-0.123}$	$346.9^{+0.90}_{-0.90}$	$1.6^{+0.105}_{-0.146}$	$4.023^{+0.284}_{-0.284}$	$7.173^{+1.968}_{-1.968}$
$0.89^{+0.056}_{-0.056}$	$3.40^{+0.069}_{-0.069}$	$0.48^{+0.135}_{-0.135}$	$347.7^{+0.85}_{-0.85}$	$1.7^{+0.108}_{-0.157}$	$3.832^{+0.253}_{-0.253}$	$7.006^{+1.954}_{-1.954}$
$1.00^{+0.055}_{-0.055}$	$3.64^{+0.078}_{-0.078}$	$0.54^{+0.143}_{-0.143}$	$348.8^{+1.06}_{-1.06}$	$1.9^{+0.106}_{-0.169}$	$3.630^{+0.212}_{-0.212}$	$6.690^{+1.764}_{-1.764}$
$1.55^{+0.057}_{-0.057}$	$4.63^{+0.090}_{-0.090}$	$0.72^{+0.134}_{-0.134}$	$349.9^{+1.60}_{-1.60}$	$3.0^{+0.111}_{-0.235}$	$2.998^{+0.126}_{-0.126}$	$6.446^{+1.205}_{-1.205}$
$2.01^{+0.055}_{-0.055}$	$5.39^{+0.073}_{-0.073}$	$0.93^{+0.182}_{-0.182}$	$351.0^{+0.69}_{-0.69}$	$3.9^{+0.107}_{-0.294}$	$2.685^{+0.082}_{-0.082}$	$5.770^{+1.125}_{-1.125}$
$2.61^{+0.062}_{-0.062}$	$6.28^{+0.069}_{-0.069}$	$1.14^{+0.152}_{-0.152}$	$351.2^{+0.66}_{-0.66}$	$5.1^{+0.120}_{-0.376}$	$2.412^{+0.063}_{-0.063}$	$5.493^{+0.735}_{-0.735}$
$3.07^{+0.058}_{-0.058}$	$6.93^{+0.065}_{-0.065}$	$1.33^{+0.108}_{-0.108}$	$353.0^{+0.59}_{-0.59}$	$5.9^{+0.112}_{-0.446}$	$2.259^{+0.047}_{-0.047}$	$5.205^{+0.427}_{-0.427}$
$4.08^{+0.110}_{-0.110}$	$8.28^{+0.140}_{-0.140}$	$1.78^{+0.138}_{-0.138}$	$353.0^{+0.61}_{-0.61}$	$7.9^{+0.214}_{-0.613}$	$2.032^{+0.065}_{-0.065}$	$4.659^{+0.370}_{-0.370}$
$5.00^{+0.062}_{-0.062}$	$9.44^{+0.077}_{-0.077}$	$2.27^{+0.114}_{-0.114}$	$353.7^{+0.55}_{-0.55}$	$9.7^{+0.120}_{-0.723}$	$1.889^{+0.028}_{-0.028}$	$4.154^{+0.212}_{-0.212}$
$6.01^{+0.064}_{-0.064}$	$10.55^{+0.089}_{-0.089}$	$2.91^{+0.116}_{-0.116}$	$355.0^{+0.57}_{-0.57}$	$11.7^{+0.125}_{-0.884}$	$1.755^{+0.024}_{-0.024}$	$3.624^{+0.147}_{-0.147}$
$6.94^{+0.066}_{-0.066}$	$11.63^{+0.082}_{-0.082}$	$3.49^{+0.312}_{-0.312}$	$354.8^{+0.79}_{-0.79}$	$13.4^{+0.128}_{-1.015}$	$1.677^{+0.020}_{-0.020}$	$3.335^{+0.300}_{-0.300}$
$7.50^{+0.064}_{-0.064}$	$12.27^{+0.083}_{-0.083}$	$3.85^{+0.114}_{-0.114}$	$355.2^{+0.61}_{-0.61}$	$14.5^{+0.124}_{-1.101}$	$1.636^{+0.018}_{-0.018}$	$3.183^{+0.097}_{-0.097}$
$8.05^{+0.065}_{-0.065}$	$12.90^{+0.088}_{-0.088}$	$4.25^{+0.244}_{-0.244}$	$355.1^{+0.57}_{-0.57}$	$15.6^{+0.125}_{-1.181}$	$1.602^{+0.017}_{-0.017}$	$3.034^{+0.175}_{-0.175}$
$9.06^{+0.066}_{-0.066}$	$14.04^{+0.083}_{-0.083}$	$4.97^{+0.308}_{-0.308}$	$355.1^{+0.59}_{-0.59}$	$17.6^{+0.127}_{-1.327}$	$1.549^{+0.015}_{-0.015}$	$2.826^{+0.176}_{-0.176}$
$9.99^{+0.067}_{-0.067}$	$15.06^{+0.088}_{-0.088}$	$5.66^{+0.237}_{-0.237}$	$355.4^{+0.94}_{-0.94}$	$19.4^{+0.131}_{-1.471}$	$1.506^{+0.013}_{-0.013}$	$2.659^{+0.113}_{-0.113}$
$15.23^{+0.098}_{-0.098}$	$21.36^{+0.142}_{-0.142}$	$10.52^{+0.084}_{-0.084}$	$356.2^{+0.63}_{-0.63}$	$29.5^{+0.189}_{-2.270}$	$1.402^{+0.013}_{-0.013}$	$2.031^{+0.021}_{-0.021}$
$20.29^{+0.089}_{-0.089}$	$26.66^{+0.140}_{-0.140}$	$15.10^{+0.128}_{-0.128}$	$356.4^{+0.70}_{-0.70}$	$39.3^{+0.172}_{-3.026}$	$1.314^{+0.009}_{-0.009}$	$1.766^{+0.018}_{-0.018}$
$25.09^{+0.095}_{-0.095}$	$31.55^{+0.174}_{-0.174}$	$19.70^{+0.164}_{-0.164}$	$357.7^{+1.06}_{-1.06}$	$48.7^{+0.184}_{-3.816}$	$1.257^{+0.008}_{-0.008}$	$1.602^{+0.016}_{-0.016}$
$30.40^{+0.104}_{-0.104}$	$36.97^{+0.175}_{-0.175}$	$24.80^{+0.149}_{-0.149}$	$358.5^{+0.75}_{-0.75}$	$58.9^{+0.201}_{-4.675}$	$1.216^{+0.007}_{-0.007}$	$1.491^{+0.011}_{-0.011}$
$40.64^{+0.130}_{-0.130}$	$47.48^{+0.168}_{-0.168}$	$34.63^{+0.124}_{-0.124}$	$357.9^{+0.98}_{-0.98}$	$78.8^{+0.252}_{-6.190}$	$1.168^{+0.006}_{-0.006}$	$1.371^{+0.007}_{-0.007}$
$50.43^{+0.146}_{-0.146}$	$57.43^{+0.206}_{-0.206}$	$44.18^{+0.158}_{-0.158}$	$357.2^{+0.85}_{-0.85}$	$97.8^{+0.284}_{-7.603}$	$1.139^{+0.005}_{-0.005}$	$1.300^{+0.007}_{-0.007}$
$60.83^{+0.174}_{-0.174}$	$67.93^{+0.243}_{-0.243}$	$54.43^{+0.167}_{-0.167}$	$356.8^{+0.58}_{-0.58}$	$118.0^{+0.338}_{-9.118}$	$1.117^{+0.005}_{-0.005}$	$1.248^{+0.006}_{-0.006}$
$70.31^{+0.174}_{-0.174}$	$77.44^{+0.242}_{-0.242}$	$63.86^{+0.198}_{-0.198}$	$356.9^{+1.15}_{-1.15}$	$136.3^{+0.338}_{-10.554}$	$1.101^{+0.004}_{-0.004}$	$1.212^{+0.005}_{-0.005}$
$75.38^{+0.191}_{-0.191}$	$82.44^{+0.284}_{-0.284}$	$68.99^{+0.218}_{-0.218}$	$358.5^{+1.47}_{-1.47}$	$146.2^{+0.371}_{-11.588}$	$1.094^{+0.005}_{-0.005}$	$1.195^{+0.006}_{-0.006}$
$80.44^{+0.198}_{-0.198}$	$87.47^{+0.253}_{-0.253}$	$74.08^{+0.184}_{-0.184}$	$359.4^{+0.82}_{-0.82}$	$156.0^{+0.384}_{-12.536}$	$1.087^{+0.004}_{-0.004}$	$1.181^{+0.005}_{-0.005}$
$90.34^{+0.212}_{-0.212}$	$97.41^{+0.283}_{-0.283}$	$83.90^{+0.221}_{-0.221}$	$359.7^{+1.05}_{-1.05}$	$175.2^{+0.411}_{-14.135}$	$1.078^{+0.004}_{-0.004}$	$1.161^{+0.005}_{-0.005}$
$100.4^{+0.228}_{-0.228}$	$106.8^{+0.332}_{-0.332}$	$93.98^{+0.257}_{-0.257}$	$360.5^{+0.89}_{-0.89}$	$194.7^{+0.443}_{-15.892}$	$1.064^{+0.004}_{-0.004}$	$1.137^{+0.005}_{-0.005}$
$149.5^{+0.453}_{-0.453}$	$157.5^{+0.561}_{-0.561}$	$142.9^{+0.367}_{-0.367}$	$360.8^{+0.61}_{-0.61}$	$289.8^{+0.878}_{-23.760}$	$1.054^{+0.005}_{-0.005}$	$1.103^{+0.005}_{-0.005}$
$176.4^{+1.440}_{-1.440}$	$184.8^{+1.579}_{-1.579}$	$169.9^{+1.345}_{-1.345}$	$361.1^{+0.63}_{-0.63}$	$342.0^{+2.792}_{-28.289}$	$1.047^{+0.012}_{-0.012}$	$1.087^{+0.013}_{-0.013}$
$199.2^{+1.200}_{-1.200}$	$207.7^{+1.340}_{-1.340}$	$192.8^{+1.096}_{-1.096}$	$361.6^{+0.88}_{-0.88}$	$386.2^{+2.327}_{-32.075}$	$1.043^{+0.009}_{-0.009}$	$1.077^{+0.009}_{-0.009}$
$254.7^{+1.435}_{-1.435}$	$263.8^{+1.565}_{-1.565}$	$248.5^{+1.303}_{-1.303}$	$361.8^{+0.69}_{-0.69}$	$493.8^{+2.782}_{-41.131}$	$1.036^{+0.008}_{-0.008}$	$1.062^{+0.008}_{-0.008}$
$506.8^{+1.456}_{-1.456}$	$518.3^{+1.604}_{-1.604}$	$501.2^{+1.310}_{-1.310}$	$362.2^{+0.60}_{-0.60}$	$982.6^{+2.824}_{-82.189}$	$1.023^{+0.004}_{-0.004}$	$1.034^{+0.004}_{-0.004}$
$600.7^{+1.513}_{-1.513}$	$613.0^{+1.627}_{-1.627}$	$595.4^{+1.396}_{-1.396}$	$362.3^{+0.62}_{-0.62}$	$1165^{+2.934}_{-97.487}$	$1.021^{+0.004}_{-0.004}$	$1.030^{+0.004}_{-0.004}$
$767.0^{+1.695}_{-1.695}$	$780.7^{+1.820}_{-1.820}$	$762.1^{+1.600}_{-1.600}$	$362.3^{+0.62}_{-0.62}$	$1487^{+3.286}_{-124.41}$	$1.018^{+0.003}_{-0.003}$	$1.024^{+0.003}_{-0.003}$
$994.3^{+2.127}_{-2.127}$	$1008^{+2.526}_{-2.526}$	$990.1^{+2.088}_{-2.088}$	$362.1^{+0.61}_{-0.61}$	$1928^{+4.124}_{-160.94}$	$1.013^{+0.003}_{-0.003}$	$1.018^{+0.003}_{-0.003}$

TAB. D.7 Measurements for $D_o/D_i = 1.7$, $h_{cl,r} = 0.4\,\mathrm{mm}$ and $u_0 = 0.054^{+0.002}_{-0.004}$ at $T_{amb} = 301.9\,\mathrm{K}$ shown in Figs. 8.12 and 8.13.

p^*_{ch} [Pa]	p_{HP} [Pa]	p_{LP} [Pa]	T_B [K]	δ^* [−]	p_{HP}/p^*_{ch} [−]	p_{HP}/p_{LP} [−]
$0.50^{+0.070}_{-0.070}$	$1.09^{+0.215}_{-0.215}$	$0.38^{+0.128}_{-0.128}$	$342.7^{+0.67}_{-0.67}$	$1.0^{+0.136}_{-0.148}$	$2.207^{+0.534}_{-0.534}$	$2.890^{+1.128}_{-1.128}$
$0.60^{+0.061}_{-0.061}$	$1.30^{+0.155}_{-0.155}$	$0.48^{+0.145}_{-0.145}$	$342.9^{+0.56}_{-0.56}$	$1.2^{+0.118}_{-0.137}$	$2.184^{+0.343}_{-0.343}$	$2.732^{+0.893}_{-0.893}$
$0.70^{+0.059}_{-0.059}$	$1.40^{+0.099}_{-0.099}$	$0.49^{+0.070}_{-0.070}$	$343.0^{+0.59}_{-0.59}$	$1.4^{+0.115}_{-0.141}$	$2.007^{+0.222}_{-0.222}$	$2.856^{+0.458}_{-0.458}$
$0.80^{+0.057}_{-0.057}$	$1.49^{+0.108}_{-0.108}$	$0.52^{+0.118}_{-0.118}$	$343.1^{+0.56}_{-0.56}$	$1.6^{+0.110}_{-0.145}$	$1.860^{+0.189}_{-0.189}$	$2.845^{+0.672}_{-0.672}$
$0.90^{+0.058}_{-0.058}$	$1.72^{+0.115}_{-0.115}$	$0.63^{+0.106}_{-0.106}$	$343.1^{+0.58}_{-0.58}$	$1.7^{+0.113}_{-0.155}$	$1.917^{+0.179}_{-0.179}$	$2.712^{+0.487}_{-0.487}$
$0.99^{+0.060}_{-0.060}$	$1.81^{+0.112}_{-0.112}$	$0.66^{+0.095}_{-0.095}$	$342.9^{+0.53}_{-0.53}$	$1.9^{+0.117}_{-0.165}$	$1.828^{+0.159}_{-0.159}$	$2.748^{+0.430}_{-0.430}$
$1.51^{+0.056}_{-0.056}$	$2.48^{+0.076}_{-0.076}$	$0.92^{+0.081}_{-0.081}$	$343.0^{+0.54}_{-0.54}$	$2.9^{+0.109}_{-0.208}$	$1.646^{+0.079}_{-0.079}$	$2.683^{+0.250}_{-0.250}$
$2.01^{+0.069}_{-0.069}$	$3.15^{+0.098}_{-0.098}$	$1.23^{+0.093}_{-0.093}$	$342.9^{+0.56}_{-0.56}$	$3.9^{+0.134}_{-0.272}$	$1.569^{+0.073}_{-0.073}$	$2.553^{+0.208}_{-0.208}$
$2.52^{+0.082}_{-0.082}$	$3.83^{+0.107}_{-0.107}$	$1.59^{+0.086}_{-0.086}$	$342.9^{+0.50}_{-0.50}$	$4.9^{+0.160}_{-0.336}$	$1.523^{+0.065}_{-0.065}$	$2.403^{+0.145}_{-0.145}$
$3.04^{+0.061}_{-0.061}$	$4.45^{+0.087}_{-0.087}$	$1.92^{+0.114}_{-0.114}$	$342.9^{+0.50}_{-0.50}$	$5.9^{+0.119}_{-0.376}$	$1.466^{+0.041}_{-0.041}$	$2.318^{+0.145}_{-0.145}$
$4.07^{+0.090}_{-0.090}$	$5.69^{+0.104}_{-0.104}$	$2.67^{+0.113}_{-0.113}$	$342.9^{+0.54}_{-0.54}$	$7.9^{+0.175}_{-0.509}$	$1.398^{+0.040}_{-0.040}$	$2.134^{+0.099}_{-0.099}$
$5.01^{+0.068}_{-0.068}$	$6.77^{+0.103}_{-0.103}$	$3.39^{+0.126}_{-0.126}$	$342.8^{+0.57}_{-0.57}$	$9.7^{+0.132}_{-0.602}$	$1.352^{+0.028}_{-0.028}$	$1.996^{+0.080}_{-0.080}$
$6.03^{+0.073}_{-0.073}$	$7.91^{+0.105}_{-0.105}$	$4.20^{+0.166}_{-0.166}$	$342.8^{+0.54}_{-0.54}$	$11.7^{+0.141}_{-0.720}$	$1.313^{+0.024}_{-0.024}$	$1.885^{+0.079}_{-0.079}$
$7.06^{+0.064}_{-0.064}$	$9.04^{+0.073}_{-0.073}$	$5.06^{+0.072}_{-0.072}$	$342.7^{+0.58}_{-0.58}$	$13.7^{+0.124}_{-0.835}$	$1.280^{+0.016}_{-0.016}$	$1.787^{+0.029}_{-0.029}$
$8.03^{+0.102}_{-0.102}$	$10.07^{+0.129}_{-0.129}$	$5.88^{+0.111}_{-0.111}$	$342.6^{+0.50}_{-0.50}$	$15.6^{+0.199}_{-0.959}$	$1.254^{+0.023}_{-0.023}$	$1.713^{+0.039}_{-0.039}$
$9.04^{+0.068}_{-0.068}$	$11.07^{+0.086}_{-0.086}$	$6.75^{+0.107}_{-0.107}$	$342.6^{+0.55}_{-0.55}$	$17.6^{+0.131}_{-1.063}$	$1.224^{+0.013}_{-0.013}$	$1.640^{+0.029}_{-0.029}$
$9.98^{+0.069}_{-0.069}$	$12.05^{+0.086}_{-0.086}$	$7.59^{+0.121}_{-0.121}$	$342.6^{+0.54}_{-0.54}$	$19.4^{+0.133}_{-1.172}$	$1.207^{+0.012}_{-0.012}$	$1.587^{+0.028}_{-0.028}$
$15.19^{+0.080}_{-0.080}$	$18.18^{+0.092}_{-0.092}$	$12.92^{+0.084}_{-0.084}$	$342.5^{+0.54}_{-0.54}$	$29.5^{+0.155}_{-1.777}$	$1.197^{+0.009}_{-0.009}$	$1.407^{+0.012}_{-0.012}$
$20.84^{+0.090}_{-0.090}$	$23.98^{+0.102}_{-0.102}$	$18.35^{+0.097}_{-0.097}$	$342.5^{+0.57}_{-0.57}$	$40.4^{+0.176}_{-2.431}$	$1.151^{+0.007}_{-0.007}$	$1.307^{+0.009}_{-0.009}$
$25.13^{+0.097}_{-0.097}$	$28.35^{+0.107}_{-0.107}$	$22.53^{+0.100}_{-0.100}$	$342.4^{+0.53}_{-0.53}$	$48.8^{+0.188}_{-2.927}$	$1.128^{+0.006}_{-0.006}$	$1.259^{+0.007}_{-0.007}$
$30.36^{+0.108}_{-0.108}$	$33.64^{+0.117}_{-0.117}$	$27.66^{+0.107}_{-0.107}$	$342.4^{+0.56}_{-0.56}$	$58.9^{+0.209}_{-3.532}$	$1.108^{+0.006}_{-0.006}$	$1.217^{+0.006}_{-0.006}$
$41.46^{+0.133}_{-0.133}$	$44.85^{+0.142}_{-0.142}$	$38.62^{+0.119}_{-0.119}$	$342.3^{+0.58}_{-0.58}$	$80.5^{+0.258}_{-4.818}$	$1.082^{+0.005}_{-0.005}$	$1.161^{+0.005}_{-0.005}$
$50.39^{+0.149}_{-0.149}$	$53.82^{+0.167}_{-0.167}$	$47.49^{+0.147}_{-0.147}$	$342.3^{+0.55}_{-0.55}$	$97.8^{+0.289}_{-5.852}$	$1.068^{+0.005}_{-0.005}$	$1.133^{+0.005}_{-0.005}$
$60.02^{+0.165}_{-0.165}$	$63.48^{+0.178}_{-0.178}$	$57.08^{+0.168}_{-0.168}$	$342.3^{+0.54}_{-0.54}$	$116.5^{+0.321}_{-6.968}$	$1.058^{+0.004}_{-0.004}$	$1.112^{+0.005}_{-0.005}$
$70.37^{+0.189}_{-0.189}$	$73.85^{+0.200}_{-0.200}$	$67.38^{+0.172}_{-0.172}$	$342.3^{+0.50}_{-0.50}$	$136.6^{+0.366}_{-8.167}$	$1.049^{+0.004}_{-0.004}$	$1.096^{+0.004}_{-0.004}$
$80.57^{+0.207}_{-0.207}$	$84.07^{+0.216}_{-0.216}$	$77.56^{+0.197}_{-0.197}$	$342.3^{+0.58}_{-0.58}$	$156.4^{+0.401}_{-9.342}$	$1.043^{+0.004}_{-0.004}$	$1.084^{+0.004}_{-0.004}$
$90.34^{+0.225}_{-0.225}$	$93.84^{+0.231}_{-0.231}$	$87.31^{+0.216}_{-0.216}$	$342.3^{+0.55}_{-0.55}$	$175.4^{+0.436}_{-10.480}$	$1.039^{+0.004}_{-0.004}$	$1.075^{+0.004}_{-0.004}$
$99.49^{+0.223}_{-0.223}$	$102.3^{+0.263}_{-0.263}$	$96.45^{+0.221}_{-0.221}$	$342.3^{+0.53}_{-0.53}$	$193.1^{+0.434}_{-11.537}$	$1.029^{+0.004}_{-0.004}$	$1.061^{+0.004}_{-0.004}$
$151.2^{+0.481}_{-0.481}$	$155.5^{+0.527}_{-0.527}$	$148.3^{+0.476}_{-0.476}$	$342.3^{+0.50}_{-0.50}$	$293.4^{+0.934}_{-17.540}$	$1.029^{+0.005}_{-0.005}$	$1.049^{+0.005}_{-0.005}$
$205.2^{+1.309}_{-1.309}$	$210.0^{+1.315}_{-1.315}$	$202.6^{+1.305}_{-1.305}$	$342.2^{+0.52}_{-0.52}$	$398.3^{+2.540}_{-23.894}$	$1.023^{+0.009}_{-0.009}$	$1.036^{+0.009}_{-0.009}$
$261.2^{+2.144}_{-2.144}$	$266.5^{+2.188}_{-2.188}$	$258.9^{+2.142}_{-2.142}$	$342.2^{+0.59}_{-0.59}$	$507.1^{+4.161}_{-30.512}$	$1.020^{+0.012}_{-0.012}$	$1.029^{+0.012}_{-0.012}$
$507.1^{+1.782}_{-1.782}$	$514.2^{+1.803}_{-1.803}$	$505.7^{+1.781}_{-1.781}$	$342.2^{+0.59}_{-0.59}$	$984.3^{+3.459}_{-58.729}$	$1.014^{+0.005}_{-0.005}$	$1.017^{+0.005}_{-0.005}$
$1000^{+2.599}_{-2.599}$	$1007^{+3.016}_{-3.016}$	$1000^{+2.621}_{-2.621}$	$342.2^{+0.59}_{-0.59}$	$1941.5^{+5.044}_{-115.70}$	$1.007^{+0.004}_{-0.004}$	$1.007^{+0.004}_{-0.004}$

TAB. D.8 Measurements for $D_o/D_i = 1.4167$, $h_{cl,r} = 0.2\,\mathrm{mm}$ and $u_0 = 0.13^{+0.0002}_{-0.011}$ at $T_{amb} = 290.3\,\mathrm{K}$ shown in Fig. 8.14.

p^*_{ch} [Pa]	p_{HP} [Pa]	p_{LP} [Pa]	T_B [K]	δ^* [−]	p_{HP}/p^*_{ch} [−]	p_{HP}/p_{LP} [−]
$1.00^{+0.056}_{-0.056}$	$4.06^{+0.081}_{-0.081}$	$0.42^{+0.270}_{-0.270}$	$326.8^{+2.45}_{-2.45}$	$2.0^{+0.114}_{-0.162}$	$4.055^{+0.240}_{-0.240}$	$9.745^{+6.326}_{-6.326}$
$1.99^{+0.057}_{-0.057}$	$6.27^{+0.072}_{-0.072}$	$0.71^{+0.308}_{-0.308}$	$330.8^{+1.89}_{-1.89}$	$4.1^{+0.117}_{-0.277}$	$3.146^{+0.097}_{-0.097}$	$8.825^{+3.832}_{-3.832}$
$2.51^{+0.056}_{-0.056}$	$7.22^{+0.071}_{-0.071}$	$0.81^{+0.275}_{-0.275}$	$332.9^{+1.50}_{-1.50}$	$5.1^{+0.115}_{-0.351}$	$2.873^{+0.070}_{-0.070}$	$8.913^{+3.027}_{-3.027}$
$3.01^{+0.058}_{-0.058}$	$8.04^{+0.079}_{-0.079}$	$0.97^{+0.215}_{-0.215}$	$335.4^{+1.48}_{-1.48}$	$6.1^{+0.118}_{-0.434}$	$2.668^{+0.057}_{-0.057}$	$8.286^{+1.840}_{-1.840}$
$4.01^{+0.060}_{-0.060}$	$9.55^{+0.086}_{-0.086}$	$1.36^{+0.219}_{-0.219}$	$337.5^{+1.22}_{-1.22}$	$8.2^{+0.121}_{-0.591}$	$2.378^{+0.041}_{-0.041}$	$7.010^{+1.128}_{-1.128}$
$5.03^{+0.062}_{-0.062}$	$10.93^{+0.082}_{-0.082}$	$1.81^{+0.154}_{-0.154}$	$339.2^{+0.60}_{-0.60}$	$10.3^{+0.127}_{-0.757}$	$2.174^{+0.032}_{-0.032}$	$6.036^{+0.516}_{-0.516}$
$6.01^{+0.062}_{-0.062}$	$12.24^{+0.082}_{-0.082}$	$2.24^{+0.174}_{-0.174}$	$339.6^{+0.72}_{-0.72}$	$12.3^{+0.126}_{-0.907}$	$2.037^{+0.025}_{-0.025}$	$5.467^{+0.428}_{-0.428}$
$6.98^{+0.064}_{-0.064}$	$13.47^{+0.081}_{-0.081}$	$2.73^{+0.200}_{-0.200}$	$340.3^{+0.71}_{-0.71}$	$14.2^{+0.130}_{-1.063}$	$1.929^{+0.021}_{-0.021}$	$4.937^{+0.363}_{-0.363}$
$7.97^{+0.065}_{-0.065}$	$14.67^{+0.097}_{-0.097}$	$3.25^{+0.275}_{-0.275}$	$340.6^{+0.70}_{-0.70}$	$16.3^{+0.133}_{-1.220}$	$1.841^{+0.019}_{-0.019}$	$4.518^{+0.383}_{-0.383}$
$9.02^{+0.068}_{-0.068}$	$15.90^{+0.091}_{-0.091}$	$3.90^{+0.306}_{-0.306}$	$341.1^{+0.75}_{-0.75}$	$18.4^{+0.138}_{-1.389}$	$1.763^{+0.017}_{-0.017}$	$4.072^{+0.320}_{-0.320}$
$10.01^{+0.073}_{-0.073}$	$16.97^{+0.085}_{-0.085}$	$4.48^{+0.188}_{-0.188}$	$341.7^{+0.59}_{-0.59}$	$20.4^{+0.149}_{-1.555}$	$1.696^{+0.015}_{-0.015}$	$3.785^{+0.160}_{-0.160}$
$19.97^{+0.090}_{-0.090}$	$27.86^{+0.116}_{-0.116}$	$12.24^{+0.202}_{-0.202}$	$342.2^{+0.63}_{-0.63}$	$40.7^{+0.183}_{-3.122}$	$1.395^{+0.009}_{-0.009}$	$2.277^{+0.039}_{-0.039}$
$30.59^{+0.108}_{-0.108}$	$38.89^{+0.123}_{-0.123}$	$21.73^{+0.130}_{-0.130}$	$342.7^{+0.71}_{-0.71}$	$62.4^{+0.219}_{-4.819}$	$1.271^{+0.006}_{-0.006}$	$1.790^{+0.012}_{-0.012}$
$39.84^{+0.121}_{-0.121}$	$48.25^{+0.164}_{-0.164}$	$30.50^{+0.134}_{-0.134}$	$344.1^{+0.94}_{-0.94}$	$81.3^{+0.246}_{-6.411}$	$1.211^{+0.006}_{-0.006}$	$1.582^{+0.009}_{-0.009}$
$50.47^{+0.137}_{-0.137}$	$59.01^{+0.179}_{-0.179}$	$40.68^{+0.166}_{-0.166}$	$344.6^{+1.69}_{-1.69}$	$103.0^{+0.280}_{-8.187}$	$1.169^{+0.005}_{-0.005}$	$1.451^{+0.007}_{-0.007}$
$59.98^{+0.157}_{-0.157}$	$68.46^{+0.219}_{-0.219}$	$50.02^{+0.150}_{-0.150}$	$346.6^{+1.33}_{-1.33}$	$122.4^{+0.320}_{-10.028}$	$1.142^{+0.005}_{-0.005}$	$1.369^{+0.006}_{-0.006}$
$70.47^{+0.170}_{-0.170}$	$79.02^{+0.189}_{-0.189}$	$60.20^{+0.161}_{-0.161}$	$345.9^{+0.61}_{-0.61}$	$143.8^{+0.347}_{-11.653}$	$1.121^{+0.004}_{-0.004}$	$1.313^{+0.005}_{-0.005}$
$79.60^{+0.196}_{-0.196}$	$88.20^{+0.225}_{-0.225}$	$69.09^{+0.177}_{-0.177}$	$345.7^{+0.63}_{-0.63}$	$162.4^{+0.399}_{-13.117}$	$1.108^{+0.004}_{-0.004}$	$1.277^{+0.005}_{-0.005}$
$90.63^{+0.209}_{-0.209}$	$99.22^{+0.242}_{-0.242}$	$79.87^{+0.191}_{-0.191}$	$345.6^{+0.62}_{-0.62}$	$184.9^{+0.426}_{-14.926}$	$1.095^{+0.004}_{-0.004}$	$1.242^{+0.004}_{-0.004}$
$99.66^{+0.225}_{-0.225}$	$107.7^{+0.308}_{-0.308}$	$88.75^{+0.206}_{-0.206}$	$345.6^{+0.54}_{-0.54}$	$203.3^{+0.460}_{-16.411}$	$1.081^{+0.004}_{-0.004}$	$1.213^{+0.004}_{-0.004}$
$200.6^{+1.866}_{-1.866}$	$212.7^{+1.939}_{-1.939}$	$192.2^{+1.804}_{-1.804}$	$345.6^{+0.60}_{-0.60}$	$409.2^{+3.808}_{-33.257}$	$1.060^{+0.014}_{-0.014}$	$1.106^{+0.014}_{-0.014}$
$253.4^{+1.125}_{-1.125}$	$266.1^{+1.202}_{-1.202}$	$245.3^{+1.079}_{-1.079}$	$346.0^{+0.61}_{-0.61}$	$517.0^{+2.295}_{-42.020}$	$1.050^{+0.007}_{-0.007}$	$1.085^{+0.007}_{-0.007}$
$503.8^{+1.536}_{-1.536}$	$519.2^{+1.650}_{-1.650}$	$496.4^{+1.495}_{-1.495}$	$346.0^{+0.56}_{-0.56}$	$1028^{+3.133}_{-83.483}$	$1.031^{+0.005}_{-0.005}$	$1.046^{+0.005}_{-0.005}$
$1004^{+3.046}_{-3.046}$	$1012^{+2.820}_{-2.820}$	$990.2^{+2.493}_{-2.493}$	$346.3^{+1.15}_{-1.15}$	$2048^{+6.214}_{-166.99}$	$1.008^{+0.004}_{-0.004}$	$1.022^{+0.004}_{-0.004}$

TAB. D.9 Measurements for $D_\mathrm{o}/D_\mathrm{i} = 1.4167$, $h_\mathrm{cl,r} = 0.2\,\mathrm{mm}$ and $u_0 = 0.097^{+0.0002}_{-0.0063}$ at $T_\mathrm{amb} = 298\,\mathrm{K}$ shown in Fig. 8.14.

p^*_ch [Pa]	p_HP [Pa]	p_LP [Pa]	T_B [K]	δ^* [−]	$p_\mathrm{HP}/p^*_\mathrm{ch}$ [−]	$p_\mathrm{HP}/p_\mathrm{LP}$ [−]
$0.50^{+0.059}_{-0.059}$	$1.82^{+0.076}_{-0.076}$	$0.22^{+0.058}_{-0.058}$	$330.3^{+1.24}_{-1.24}$	$1.0^{+0.116}_{-0.126}$	$3.620^{+0.451}_{-0.451}$	$8.209^{+2.191}_{-2.191}$
$0.60^{+0.062}_{-0.062}$	$2.10^{+0.181}_{-0.181}$	$0.26^{+0.066}_{-0.066}$	$331.7^{+1.06}_{-1.06}$	$1.2^{+0.122}_{-0.137}$	$3.499^{+0.471}_{-0.471}$	$8.212^{+2.223}_{-2.223}$
$0.70^{+0.055}_{-0.055}$	$2.34^{+0.067}_{-0.067}$	$0.29^{+0.053}_{-0.053}$	$332.9^{+1.04}_{-1.04}$	$1.4^{+0.109}_{-0.131}$	$3.353^{+0.281}_{-0.281}$	$8.189^{+1.526}_{-1.526}$
$0.79^{+0.053}_{-0.053}$	$2.57^{+0.070}_{-0.070}$	$0.32^{+0.053}_{-0.053}$	$333.8^{+0.82}_{-0.82}$	$1.6^{+0.105}_{-0.135}$	$3.258^{+0.237}_{-0.237}$	$8.129^{+1.375}_{-1.375}$
$0.90^{+0.056}_{-0.056}$	$2.83^{+0.073}_{-0.073}$	$0.35^{+0.054}_{-0.054}$	$334.3^{+0.81}_{-0.81}$	$1.8^{+0.110}_{-0.147}$	$3.145^{+0.211}_{-0.211}$	$8.072^{+1.270}_{-1.270}$
$1.01^{+0.055}_{-0.055}$	$3.09^{+0.073}_{-0.073}$	$0.39^{+0.064}_{-0.064}$	$334.7^{+0.72}_{-0.72}$	$2.0^{+0.109}_{-0.156}$	$3.053^{+0.181}_{-0.181}$	$7.907^{+1.313}_{-1.313}$
$1.24^{+0.062}_{-0.062}$	$3.59^{+0.171}_{-0.171}$	$0.46^{+0.070}_{-0.070}$	$335.1^{+0.72}_{-0.72}$	$2.4^{+0.122}_{-0.184}$	$2.897^{+0.200}_{-0.200}$	$7.803^{+1.237}_{-1.237}$
$1.52^{+0.053}_{-0.053}$	$4.16^{+0.074}_{-0.074}$	$0.55^{+0.054}_{-0.054}$	$335.5^{+0.69}_{-0.69}$	$3.0^{+0.105}_{-0.199}$	$2.737^{+0.108}_{-0.108}$	$7.527^{+0.743}_{-0.743}$
$1.75^{+0.057}_{-0.057}$	$4.59^{+0.068}_{-0.068}$	$0.63^{+0.054}_{-0.054}$	$335.9^{+0.73}_{-0.73}$	$3.5^{+0.113}_{-0.228}$	$2.616^{+0.094}_{-0.094}$	$7.285^{+0.629}_{-0.629}$
$2.00^{+0.064}_{-0.064}$	$5.04^{+0.080}_{-0.080}$	$0.72^{+0.057}_{-0.057}$	$336.2^{+0.71}_{-0.71}$	$4.0^{+0.127}_{-0.261}$	$2.515^{+0.090}_{-0.090}$	$7.016^{+0.569}_{-0.569}$
$2.49^{+0.056}_{-0.056}$	$5.87^{+0.068}_{-0.068}$	$0.90^{+0.054}_{-0.054}$	$336.6^{+0.68}_{-0.68}$	$4.9^{+0.111}_{-0.306}$	$2.353^{+0.060}_{-0.060}$	$6.525^{+0.398}_{-0.398}$
$3.00^{+0.058}_{-0.058}$	$6.67^{+0.066}_{-0.066}$	$1.10^{+0.058}_{-0.058}$	$336.9^{+0.70}_{-0.70}$	$5.9^{+0.114}_{-0.365}$	$2.221^{+0.048}_{-0.048}$	$6.049^{+0.323}_{-0.323}$
$3.99^{+0.058}_{-0.058}$	$8.11^{+0.066}_{-0.066}$	$1.54^{+0.057}_{-0.057}$	$337.3^{+0.70}_{-0.70}$	$7.9^{+0.114}_{-0.478}$	$2.030^{+0.034}_{-0.034}$	$5.274^{+0.201}_{-0.201}$
$5.02^{+0.060}_{-0.060}$	$9.48^{+0.068}_{-0.068}$	$2.05^{+0.058}_{-0.058}$	$337.6^{+0.75}_{-0.75}$	$9.9^{+0.119}_{-0.600}$	$1.889^{+0.026}_{-0.026}$	$4.632^{+0.135}_{-0.135}$
$6.04^{+0.060}_{-0.060}$	$10.72^{+0.075}_{-0.075}$	$2.62^{+0.063}_{-0.063}$	$338.0^{+0.65}_{-0.65}$	$11.9^{+0.119}_{-0.723}$	$1.774^{+0.022}_{-0.022}$	$4.099^{+0.103}_{-0.103}$
$7.01^{+0.063}_{-0.063}$	$11.89^{+0.076}_{-0.076}$	$3.19^{+0.061}_{-0.061}$	$338.2^{+0.62}_{-0.62}$	$13.8^{+0.124}_{-0.841}$	$1.696^{+0.019}_{-0.019}$	$3.723^{+0.075}_{-0.075}$
$8.03^{+0.066}_{-0.066}$	$13.09^{+0.075}_{-0.075}$	$3.85^{+0.062}_{-0.062}$	$338.5^{+0.62}_{-0.62}$	$15.8^{+0.130}_{-0.967}$	$1.630^{+0.016}_{-0.016}$	$3.397^{+0.058}_{-0.058}$
$8.96^{+0.068}_{-0.068}$	$14.16^{+0.076}_{-0.076}$	$4.49^{+0.067}_{-0.067}$	$338.8^{+0.71}_{-0.71}$	$17.7^{+0.134}_{-1.084}$	$1.580^{+0.015}_{-0.015}$	$3.153^{+0.050}_{-0.050}$
$9.99^{+0.069}_{-0.069}$	$15.31^{+0.083}_{-0.083}$	$5.23^{+0.067}_{-0.067}$	$339.0^{+0.71}_{-0.71}$	$19.7^{+0.136}_{-1.213}$	$1.533^{+0.013}_{-0.013}$	$2.929^{+0.041}_{-0.041}$
$15.21^{+0.085}_{-0.085}$	$21.49^{+0.094}_{-0.094}$	$9.78^{+0.091}_{-0.091}$	$339.3^{+0.64}_{-0.64}$	$30.0^{+0.168}_{-1.855}$	$1.413^{+0.010}_{-0.010}$	$2.197^{+0.023}_{-0.023}$
$20.16^{+0.092}_{-0.092}$	$26.73^{+0.102}_{-0.102}$	$14.22^{+0.096}_{-0.096}$	$339.5^{+0.68}_{-0.68}$	$39.8^{+0.181}_{-2.466}$	$1.326^{+0.008}_{-0.008}$	$1.880^{+0.015}_{-0.015}$
$24.99^{+0.100}_{-0.100}$	$31.75^{+0.108}_{-0.108}$	$18.70^{+0.108}_{-0.108}$	$339.7^{+0.64}_{-0.64}$	$49.3^{+0.198}_{-3.068}$	$1.270^{+0.007}_{-0.007}$	$1.698^{+0.011}_{-0.011}$
$30.28^{+0.104}_{-0.104}$	$37.18^{+0.119}_{-0.119}$	$23.71^{+0.102}_{-0.102}$	$339.9^{+0.71}_{-0.71}$	$59.7^{+0.205}_{-3.730}$	$1.228^{+0.006}_{-0.006}$	$1.568^{+0.008}_{-0.008}$
$40.51^{+0.123}_{-0.123}$	$47.60^{+0.140}_{-0.140}$	$33.57^{+0.114}_{-0.114}$	$340.2^{+0.62}_{-0.62}$	$79.9^{+0.243}_{-5.013}$	$1.175^{+0.005}_{-0.005}$	$1.418^{+0.006}_{-0.006}$
$50.41^{+0.132}_{-0.132}$	$57.61^{+0.156}_{-0.156}$	$43.23^{+0.134}_{-0.134}$	$340.3^{+0.63}_{-0.63}$	$99.5^{+0.260}_{-6.257}$	$1.143^{+0.004}_{-0.004}$	$1.332^{+0.005}_{-0.005}$
$59.88^{+0.157}_{-0.157}$	$67.15^{+0.177}_{-0.177}$	$52.56^{+0.137}_{-0.137}$	$340.6^{+0.64}_{-0.64}$	$118.2^{+0.310}_{-7.468}$	$1.121^{+0.004}_{-0.004}$	$1.278^{+0.005}_{-0.005}$
$70.42^{+0.173}_{-0.173}$	$77.73^{+0.192}_{-0.192}$	$62.96^{+0.153}_{-0.153}$	$340.7^{+0.60}_{-0.60}$	$138.9^{+0.341}_{-8.815}$	$1.104^{+0.004}_{-0.004}$	$1.235^{+0.004}_{-0.004}$
$80.67^{+0.186}_{-0.186}$	$88.01^{+0.203}_{-0.203}$	$73.11^{+0.172}_{-0.172}$	$340.9^{+0.63}_{-0.63}$	$159.2^{+0.366}_{-10.129}$	$1.091^{+0.004}_{-0.004}$	$1.204^{+0.004}_{-0.004}$
$90.51^{+0.195}_{-0.195}$	$97.85^{+0.215}_{-0.215}$	$82.87^{+0.185}_{-0.185}$	$341.2^{+0.65}_{-0.65}$	$178.6^{+0.386}_{-11.434}$	$1.081^{+0.003}_{-0.003}$	$1.181^{+0.004}_{-0.004}$
$100.9^{+0.214}_{-0.214}$	$107.7^{+0.298}_{-0.298}$	$93.21^{+0.212}_{-0.212}$	$341.3^{+0.60}_{-0.60}$	$199.1^{+0.423}_{-12.784}$	$1.068^{+0.004}_{-0.004}$	$1.156^{+0.004}_{-0.004}$
$197.3^{+2.400}_{-2.400}$	$206.6^{+2.445}_{-2.445}$	$190.5^{+2.358}_{-2.358}$	$341.5^{+0.60}_{-0.60}$	$389.2^{+4.736}_{-25.495}$	$1.047^{+0.018}_{-0.018}$	$1.085^{+0.019}_{-0.019}$
$510.0^{+1.732}_{-1.732}$	$521.7^{+1.728}_{-1.728}$	$504.1^{+1.683}_{-1.683}$	$341.9^{+0.72}_{-0.72}$	$1006^{+3.418}_{-65.366}$	$1.023^{+0.005}_{-0.005}$	$1.035^{+0.005}_{-0.005}$
$1001^{+2.745}_{-2.745}$	$1014^{+2.507}_{-2.507}$	$996.3^{+2.516}_{-2.516}$	$342.2^{+0.63}_{-0.63}$	$1975^{+5.417}_{-128.88}$	$1.012^{+0.004}_{-0.004}$	$1.017^{+0.004}_{-0.004}$

TAB. D.10 Measurements for $D_o/D_i = 1.4167$, $h_{cl,r} = 0.2\,\mathrm{mm}$ and $u_0 = 0.054^{+0.0001}_{-0.0017}$ at $T_{amb} = 294.8\,\mathrm{K}$ shown in Fig. 8.14.

p^*_{ch} [Pa]	p_{HP} [Pa]	p_{LP} [Pa]	T_B [K]	δ^* [−]	p_{HP}/p^*_{ch} [−]	p_{HP}/p_{LP} [−]
$0.60^{+0.056}_{-0.056}$	$1.67^{+0.114}_{-0.114}$	$0.51^{+0.074}_{-0.074}$	$302.3^{+1.80}_{-1.80}$	$1.2^{+0.113}_{-0.114}$	$2.800^{+0.327}_{-0.327}$	$3.240^{+0.517}_{-0.517}$
$0.70^{+0.055}_{-0.055}$	$1.74^{+0.096}_{-0.096}$	$0.53^{+0.074}_{-0.074}$	$304.6^{+1.62}_{-1.62}$	$1.4^{+0.109}_{-0.112}$	$2.489^{+0.239}_{-0.239}$	$3.280^{+0.492}_{-0.492}$
$0.80^{+0.068}_{-0.068}$	$1.85^{+0.068}_{-0.068}$	$0.56^{+0.059}_{-0.059}$	$306.1^{+1.17}_{-1.17}$	$1.6^{+0.136}_{-0.139}$	$2.305^{+0.212}_{-0.212}$	$3.318^{+0.372}_{-0.372}$
$0.91^{+0.059}_{-0.059}$	$2.00^{+0.068}_{-0.068}$	$0.60^{+0.063}_{-0.063}$	$307.1^{+0.98}_{-0.98}$	$1.8^{+0.117}_{-0.123}$	$2.187^{+0.159}_{-0.159}$	$3.330^{+0.367}_{-0.367}$
$1.02^{+0.055}_{-0.055}$	$2.16^{+0.080}_{-0.080}$	$0.65^{+0.069}_{-0.069}$	$308.2^{+0.92}_{-0.92}$	$2.0^{+0.110}_{-0.119}$	$2.126^{+0.139}_{-0.139}$	$3.316^{+0.371}_{-0.371}$
$1.26^{+0.056}_{-0.056}$	$2.49^{+0.073}_{-0.073}$	$0.76^{+0.062}_{-0.062}$	$309.0^{+0.91}_{-0.91}$	$2.5^{+0.112}_{-0.127}$	$1.981^{+0.106}_{-0.106}$	$3.286^{+0.287}_{-0.287}$
$1.50^{+0.055}_{-0.055}$	$2.84^{+0.081}_{-0.081}$	$0.88^{+0.062}_{-0.062}$	$309.4^{+0.80}_{-0.80}$	$3.0^{+0.111}_{-0.133}$	$1.886^{+0.088}_{-0.088}$	$3.227^{+0.247}_{-0.247}$
$1.74^{+0.058}_{-0.058}$	$3.17^{+0.068}_{-0.068}$	$1.01^{+0.067}_{-0.067}$	$309.9^{+0.81}_{-0.81}$	$3.5^{+0.115}_{-0.145}$	$1.818^{+0.072}_{-0.072}$	$3.142^{+0.218}_{-0.218}$
$2.04^{+0.064}_{-0.064}$	$3.57^{+0.066}_{-0.066}$	$1.17^{+0.062}_{-0.062}$	$310.5^{+0.75}_{-0.75}$	$4.1^{+0.128}_{-0.166}$	$1.755^{+0.064}_{-0.064}$	$3.050^{+0.170}_{-0.170}$
$2.49^{+0.056}_{-0.056}$	$4.17^{+0.068}_{-0.068}$	$1.43^{+0.063}_{-0.063}$	$310.9^{+0.75}_{-0.75}$	$5.0^{+0.111}_{-0.173}$	$1.677^{+0.046}_{-0.046}$	$2.908^{+0.136}_{-0.136}$
$3.01^{+0.059}_{-0.059}$	$4.84^{+0.065}_{-0.065}$	$1.75^{+0.061}_{-0.061}$	$311.3^{+0.59}_{-0.59}$	$6.0^{+0.119}_{-0.203}$	$1.607^{+0.038}_{-0.038}$	$2.765^{+0.103}_{-0.103}$
$4.01^{+0.060}_{-0.060}$	$6.06^{+0.067}_{-0.067}$	$2.41^{+0.073}_{-0.073}$	$311.7^{+0.80}_{-0.80}$	$8.0^{+0.121}_{-0.255}$	$1.512^{+0.028}_{-0.028}$	$2.512^{+0.081}_{-0.081}$
$5.04^{+0.061}_{-0.061}$	$7.27^{+0.065}_{-0.065}$	$3.16^{+0.068}_{-0.068}$	$312.2^{+0.68}_{-0.68}$	$10.1^{+0.121}_{-0.314}$	$1.441^{+0.022}_{-0.022}$	$2.304^{+0.054}_{-0.054}$
$6.07^{+0.062}_{-0.062}$	$8.43^{+0.074}_{-0.074}$	$3.95^{+0.079}_{-0.079}$	$312.5^{+0.71}_{-0.71}$	$12.1^{+0.123}_{-0.375}$	$1.389^{+0.019}_{-0.019}$	$2.135^{+0.047}_{-0.047}$
$6.98^{+0.062}_{-0.062}$	$9.44^{+0.068}_{-0.068}$	$4.66^{+0.071}_{-0.071}$	$312.9^{+0.60}_{-0.60}$	$14.0^{+0.125}_{-0.434}$	$1.352^{+0.015}_{-0.015}$	$2.028^{+0.034}_{-0.034}$
$8.06^{+0.066}_{-0.066}$	$10.57^{+0.073}_{-0.073}$	$5.53^{+0.078}_{-0.078}$	$313.2^{+0.68}_{-0.68}$	$16.1^{+0.132}_{-0.504}$	$1.312^{+0.014}_{-0.014}$	$1.912^{+0.030}_{-0.030}$
$9.00^{+0.069}_{-0.069}$	$11.58^{+0.077}_{-0.077}$	$6.32^{+0.082}_{-0.082}$	$313.4^{+0.62}_{-0.62}$	$18.0^{+0.137}_{-0.567}$	$1.287^{+0.013}_{-0.013}$	$1.832^{+0.027}_{-0.027}$
$10.03^{+0.069}_{-0.069}$	$12.66^{+0.077}_{-0.077}$	$7.20^{+0.077}_{-0.077}$	$313.8^{+0.73}_{-0.73}$	$20.1^{+0.138}_{-0.638}$	$1.263^{+0.012}_{-0.012}$	$1.758^{+0.022}_{-0.022}$
$12.48^{+0.078}_{-0.078}$	$15.39^{+0.079}_{-0.079}$	$9.51^{+0.085}_{-0.085}$	$314.0^{+0.64}_{-0.64}$	$25.0^{+0.156}_{-0.799}$	$1.233^{+0.010}_{-0.010}$	$1.618^{+0.017}_{-0.017}$
$15.14^{+0.082}_{-0.082}$	$18.16^{+0.088}_{-0.088}$	$11.94^{+0.089}_{-0.089}$	$314.2^{+0.71}_{-0.71}$	$30.3^{+0.164}_{-0.975}$	$1.200^{+0.009}_{-0.009}$	$1.521^{+0.014}_{-0.014}$
$17.80^{+0.083}_{-0.083}$	$20.91^{+0.091}_{-0.091}$	$14.44^{+0.088}_{-0.088}$	$314.4^{+0.68}_{-0.68}$	$35.6^{+0.166}_{-1.151}$	$1.174^{+0.007}_{-0.007}$	$1.448^{+0.011}_{-0.011}$
$19.98^{+0.089}_{-0.089}$	$23.14^{+0.095}_{-0.095}$	$16.51^{+0.090}_{-0.090}$	$314.5^{+0.59}_{-0.59}$	$40.0^{+0.178}_{-1.300}$	$1.158^{+0.007}_{-0.007}$	$1.402^{+0.010}_{-0.010}$
$25.38^{+0.098}_{-0.098}$	$28.63^{+0.107}_{-0.107}$	$21.69^{+0.107}_{-0.107}$	$314.7^{+0.66}_{-0.66}$	$50.8^{+0.197}_{-1.660}$	$1.128^{+0.006}_{-0.006}$	$1.320^{+0.008}_{-0.008}$
$30.05^{+0.105}_{-0.105}$	$33.35^{+0.112}_{-0.112}$	$26.23^{+0.101}_{-0.101}$	$314.9^{+0.58}_{-0.58}$	$60.1^{+0.210}_{-1.983}$	$1.110^{+0.005}_{-0.005}$	$1.272^{+0.006}_{-0.006}$
$40.27^{+0.124}_{-0.124}$	$43.64^{+0.130}_{-0.130}$	$36.22^{+0.114}_{-0.114}$	$315.1^{+0.65}_{-0.65}$	$80.6^{+0.248}_{-2.674}$	$1.083^{+0.005}_{-0.005}$	$1.205^{+0.005}_{-0.005}$
$50.11^{+0.139}_{-0.139}$	$53.49^{+0.143}_{-0.143}$	$45.90^{+0.126}_{-0.126}$	$315.3^{+0.57}_{-0.57}$	$100.3^{+0.278}_{-3.357}$	$1.067^{+0.004}_{-0.004}$	$1.165^{+0.004}_{-0.004}$
$59.90^{+0.168}_{-0.168}$	$63.27^{+0.170}_{-0.170}$	$55.56^{+0.148}_{-0.148}$	$315.5^{+0.58}_{-0.58}$	$119.9^{+0.336}_{-4.036}$	$1.056^{+0.004}_{-0.004}$	$1.139^{+0.004}_{-0.004}$
$70.20^{+0.183}_{-0.183}$	$73.56^{+0.184}_{-0.184}$	$65.76^{+0.163}_{-0.163}$	$315.6^{+0.66}_{-0.66}$	$140.5^{+0.366}_{-4.761}$	$1.048^{+0.004}_{-0.004}$	$1.119^{+0.004}_{-0.004}$
$80.50^{+0.208}_{-0.208}$	$83.84^{+0.214}_{-0.214}$	$75.98^{+0.187}_{-0.187}$	$315.9^{+0.67}_{-0.67}$	$161.1^{+0.416}_{-5.519}$	$1.041^{+0.004}_{-0.004}$	$1.103^{+0.004}_{-0.004}$
$90.60^{+0.220}_{-0.220}$	$93.90^{+0.225}_{-0.225}$	$86.00^{+0.201}_{-0.201}$	$316.0^{+0.64}_{-0.64}$	$181.3^{+0.440}_{-6.254}$	$1.036^{+0.004}_{-0.004}$	$1.092^{+0.004}_{-0.004}$
$99.73^{+0.218}_{-0.218}$	$102.5^{+0.294}_{-0.294}$	$95.07^{+0.215}_{-0.215}$	$316.2^{+0.70}_{-0.70}$	$199.6^{+0.436}_{-6.944}$	$1.028^{+0.004}_{-0.004}$	$1.078^{+0.004}_{-0.004}$
$125.1^{+0.346}_{-0.346}$	$130.0^{+0.344}_{-0.344}$	$121.7^{+0.292}_{-0.292}$	$316.4^{+0.56}_{-0.56}$	$250.3^{+0.692}_{-8.792}$	$1.040^{+0.004}_{-0.004}$	$1.069^{+0.004}_{-0.004}$
$150.2^{+0.613}_{-0.613}$	$155.4^{+0.618}_{-0.618}$	$147.0^{+0.590}_{-0.590}$	$316.6^{+0.64}_{-0.64}$	$300.6^{+1.227}_{-10.688}$	$1.034^{+0.006}_{-0.006}$	$1.057^{+0.006}_{-0.006}$
$196.9^{+1.597}_{-1.597}$	$202.4^{+1.627}_{-1.627}$	$193.9^{+1.610}_{-1.610}$	$316.8^{+0.65}_{-0.65}$	$393.9^{+3.195}_{-14.378}$	$1.028^{+0.012}_{-0.012}$	$1.044^{+0.012}_{-0.012}$
$307.7^{+1.243}_{-1.243}$	$314.1^{+1.238}_{-1.238}$	$305.3^{+1.214}_{-1.214}$	$317.0^{+0.58}_{-0.58}$	$615.8^{+2.486}_{-22.220}$	$1.021^{+0.006}_{-0.006}$	$1.029^{+0.006}_{-0.006}$
$408.6^{+1.210}_{-1.210}$	$415.7^{+1.218}_{-1.218}$	$406.6^{+1.207}_{-1.207}$	$317.2^{+0.59}_{-0.59}$	$817.7^{+2.421}_{-29.583}$	$1.017^{+0.004}_{-0.004}$	$1.022^{+0.004}_{-0.004}$
$506.5^{+1.126}_{-1.126}$	$514.2^{+1.153}_{-1.153}$	$504.8^{+1.115}_{-1.115}$	$317.3^{+0.65}_{-0.65}$	$1014^{+2.252}_{-36.808}$	$1.015^{+0.003}_{-0.003}$	$1.019^{+0.003}_{-0.003}$
$755.8^{+1.650}_{-1.650}$	$764.8^{+1.663}_{-1.663}$	$754.8^{+1.634}_{-1.634}$	$317.5^{+0.59}_{-0.59}$	$1512^{+3.302}_{-55.478}$	$1.012^{+0.003}_{-0.003}$	$1.013^{+0.003}_{-0.003}$
$1010^{+2.748}_{-2.748}$	$1016^{+2.641}_{-2.641}$	$1004^{+2.615}_{-2.615}$	$317.7^{+0.70}_{-0.70}$	$2022^{+5.499}_{-74.640}$	$1.006^{+0.004}_{-0.004}$	$1.013^{+0.004}_{-0.004}$